# Atomistic Computer Simulations of FePt Nanoparticles: Thermodynamic and Kinetic Properties

Vom Fachbereich

Material- und Geowissenschaften

der Technischen Universität Darmstadt

zur Erlangung des Grades Doktor-Ingenieur

genehmigte Dissertation


vorgelegt von

Dipl.-Ing. Michael Müller

geboren in Miltenberg



Referent: Prof. Dr. Karsten Albe

Korreferent: Prof. Dr. Horst Hahn

Tag der Einreichung: 5. Dezember 2006

Tag der mündlichen Prüfung: 7. Februar 2007

Darmstadt, 2007

D17

# Contents

# Abstract

The prospect of realizing nanometer sized hard magnetic particles for magnetic recording and medical applications has driven a large number of research activities on FePt nanoparticles in recent years. Different experimental techniques for preparing isolated FePt nanoparticles have been developed. The final goal of producing particles that combine all desired properties is, however, still hampered by a number of challenges: By condensation in the gas phase not only single-crystalline, but also multiply twinned particles are obtained that prohibit the existence of a single magnetization direction. Wet-chemically prepared particles, in contrast, are usually dominated by the substitutional random alloy phase without uniaxial magnetocrystalline anisotropy and even post-annealing processes do not always succeed in inducing the transition into the ordered structure. Until now, it is not clear whether the non-crystalline and the disordered particles are thermodynamic equilibrium structures, or whether they result from a kinetic trapping of the particles in metastable states during the processes of formation and growth.

For addressing these problems, a hierarchical multiscale approach for modeling FePt nanoparticles by atomistic simulations is developed in the present work. By describing the interatomic interactions on different levels of sophistication, various time and length scales can be accessed. Methods range from static quantum-mechanic total-energy calculations of small periodic systems to simulations of whole particles over an extended time by using simple lattice Hamiltonians.

In the first part, the energetic and thermodynamic stability of non-crystalline multiply twinned FePt nanoparticles is investigated. Then, the thermodynamics of the order-disorder transition in FePt nanoparticles is analyzed, including the influence of particle size, composition and modified surface energies by different chemical surroundings. In order to identify processes that reduce or enhance the rate of transformation from the disordered to the ordered state, the kinetics of the ordering transition in FePt nanoparticles is finally investigated by assessing the contributions of surface and volume diffusion.

The results from the atomistic modeling approach presented in the present work can lead to a more detailed understanding of FePt nanoparticles and help to explain the experimental findings related to twinning and ordering. In addition, means for optimizing process conditions of particle preparation and post-annealing steps can be identified.

# Part I.

# Introduction

# 1. Motivation

## 1.1. Properties of metallic nanoparticles

Metallic nanoparticles have attracted a considerable amount of scientific research interest motivated by the emergence of novel or modified electronic, optical, chemical and magnetic properties. With decreasing particle size, for example, the energy required for altering the magnetization direction of a magnetic particle reaches the order of the thermal energy and a transition from the ferromagnetic to the superparamagnetic state can be observed [1]. If the dimensions are reduced to objects containing less than about $10^3$ atoms, the confinement of electron wave functions leads to a discretization of electronic states, which alters the electronic, chemical and optical properties [2, 3]. As a result, the color of gold nanoparticles can change from red to blue, green and orange depending on particle size and shape [4]. As opposed to the inertness of their bulk material counterparts, nano-dispersed gold particles show a high catalytic activity [5].

Since the surface to volume ratio increases with reduced size, the behavior of small particles also becomes more and more influenced by surface properties. Size effects directly influence phase transitions such as melting [6–8], and can lead to modified lattice parameters in nanoparticles [9]. As will be demonstrated in this work, surface energy and surface tension terms also affect the vacancy formation and a depletion of vacancies in small metallic particles is found.

Furthermore, nanoparticles possess the tendency of forming a variety of structures absent in bulk materials [3, 7, 10]. The shape of nanoparticles is not restricted to crystalline structures that are merely cut from the bulk matter. Instead, owing to their finite size, the constraint of translational invariance on a lattice can be broken [7]. As a result, multiply twinned structures of fivefold symmetry in the form of icosahedral or decahedral shapes can occur. Although the presence of multiply twinned particles (MTPs) can be a result of non-equilibrium processes during particle formation [7], calculations show that MTPs can be energetically favored at very small sizes [11, 12]. A size dependent transition of the

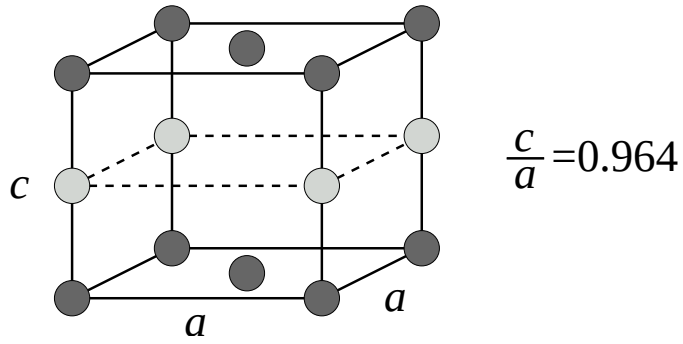


**Figure 1.1.:** *Tetragonal unit cell of the $L1_0$ ordered FePt structure. Pt atoms are displayed light grey, Fe atoms dark grey.*

stable shape from multiply twinned to single crystalline particles has been experimentally observed in the case of copper [12] and gold clusters [13].

## 1.2. FePt nanoparticles for magnetic recording applications - state of the art

Apart from exploiting novel properties, the interest in nanoparticles is also motivated by the need for miniaturization in technological applications, where a scaling of functional units to ever decreasing dimensions is attempted. In this case, it is desirable to *retain* the materials properties known from the bulk phase down to the nanometer scale. A prominent example is the attempt of employing the magnetization direction of individual nanoparticles as the information unit (bit) for increasing the areal density of magnetic data storage media [14–16].

For magnetic recording applications, *single crystalline* nanoparticles in the *ferromagnetic* state with an uniaxial alignment of spins are required. As a promising material for realizing such nanoparticles, equiatomic FePt alloys in the hard magnetic $L1_0$ phase have attracted a considerable amount of research interest [14, 16–18]. The unit cell of the face centered tetragonal $L1_0$ structure is depicted in Fig. 1.1. It is built from alternating layers of Fe and Pt atoms along the $\langle 001 \rangle$ direction, with a $c/a$ ratio of 0.964 [19]. Because of the tetragonal distortion, the magnetic properties of the $L1_0$ phase are characterized by a very high uniaxial magnetocrystalline anisotropy energy (MAE) [17]. This offers the prospect of reducing the particle dimension to a few nanometers, while maintaining a thermally stable magnetization direction [17]. If one assumes a storage time constant of 10 years

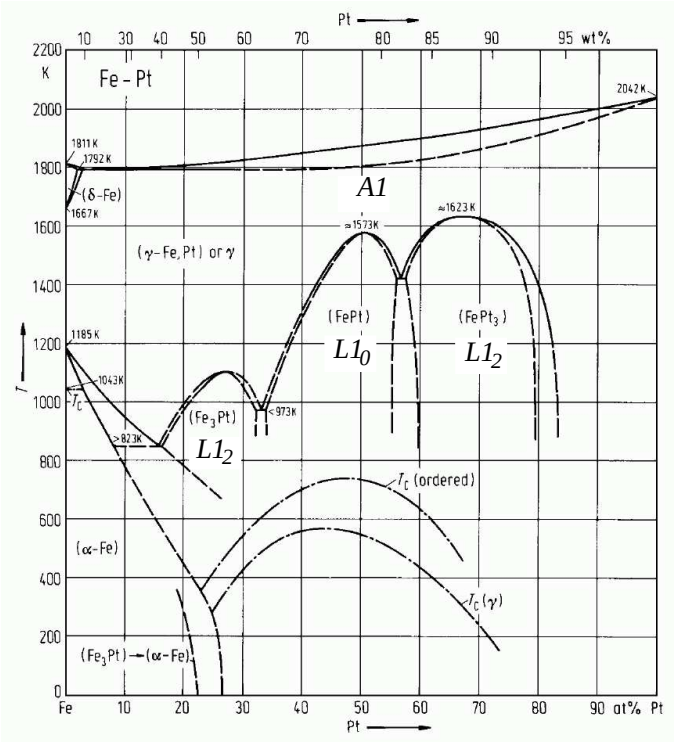


**Figure 1.2.:** *Phase diagram of the FePt alloy system, as taken from Ref. [19].*

and a MAE of $7 \times 10^7\,\mathrm{erg/cm^3}$ a stable magnetization can be conserved in spherical FePt particles as small as 4 nm in diameter.

For bulk materials, the phase diagram of the binary FePt alloy system (Fig. 1.2) shows that the $L1_0$ structure is the thermodynamically stable phase at low temperatures. At 1573 K, an order-disorder phase transition to the substitutional disordered $A1$ phase occurs [19]. In contrast to the $L1_0$ phase, the $A1$ phase is magnetically soft and has a face centered cubic (fcc) structure. Because of the considerably reduced MAE of $1.1 \times 10^6\,\mathrm{erg/cm^3}$ [17] FePt nanoparticles in the disordered phase are not suitable for magnetic recording applications.

To date, different synthesis routes for the preparation of single crystalline, $L1_0$ ordered FePt nanoparticles are discussed in literature, including the preparation by evaporation or sputtering techniques [20, 21], gas-phase preparation [18] and chemical synthesis from solution-phase [14, 16]. However, the production of FePt nanoparticles applicable as magnetic recording medium is still hampered by significant challenges, which are summarized in the following.

The solution phase synthesis route usually results in FePt particles that are single-crystalline [14, 22] and only a small fraction of multiply twinned particles (MTPs) in

decahedral or icosahedral shapes have been identified [23]. In the as-prepared particles, however, no chemical ordering is observed and a post-annealing process at high temperatures around 800 K is required for transforming the particles into the $L1_0$ phase [24]. Usually, post-annealing destroys the monodisperse size distribution, leading to coalescence and particle sintering [18, 24]. In contrast, isolated particles have been observed to remain in the disordered state even after heat treatment [21, 22, 25].

The preparation of FePt nanoparticles from the gas phase provides the possibility of a thermal annealing step prior to deposition on a substrate [18], which is regarded as an advantage over the solution phase synthesis. However, also here, the formation of $L1_0$ order can only be realized under processing conditions (high carrier gas pressure) where a coalescence of the particles is unavoidable [18]. For lower gas pressures, where isolated, monodisperse particles can be obtained, MTPs in icosahedral shapes are predominant [18]. Along with single crystalline particles, MTPs in icosahedral and decahedral shapes have also been observed in other gas-phase synthesis studies [26, 27].

In consequence, attention has been directed to the suppression of MTPs in the gas-phase synthesis route. Attempts include the suppression of twinning by increasing the oxygen partial pressure [18], and ion beam induced transformation from multiply twinned to single crystalline particles [28]. While both methods succeed in producing single crystalline particles, drawbacks are again particle agglomeration at a high oxygen supply and absence of $L1_0$ order in particles transformed by ion beam irradiation.

## 1.3. Open questions addressed in the present work

The challenges encountered in the various experimental works point to a number of open questions concerning the thermodynamics and kinetics of FePt nanoparticles:

- Is the strong tendency of forming MTPs in the gas-phase preparation process a result of the kinetics of the growth process, or is it a consequence of a thermodynamic favoring of non-crystalline morphologies at small particle sizes?

- The observation of disordered FePt particles even after thermal annealing is contradictory to the bulk FePt phase diagram, where the $A1$ phase is only stable at high temperatures above 1573 K. Is the difficulty of transforming the particles into the $L1_0$ phase due to a depression of the thermodynamic ordering temperature with decreasing particle size, or is the transformation hindered by kinetic limitations?

- Which factors do influence the ordering kinetics of the $A1$ to $L1_0$ transformation? Which processes do limit or enhance the rate of transformation?

- In substitutional alloys, the rate of phase transitions requiring a rearrangement of atomic species is controlled by vacancy assisted diffusion. The ordering kinetics in FePt nanoparticles are therefore expected to significantly depend on the vacancy concentration. This leads to the more general question: What is the influence of particle size on the concentration of thermal vacancies in metallic nanoparticles?

Answers to these questions would allow a more detailed understanding of the physics involved and could provide the necessary input for optimizing process conditions.

In the present work, atomistic simulation methods are applied for addressing the problems encountered in the experimental studies on FePt nanoparticles. In order to achieve a comprehensive treatment, a number of simulation techniques for investigating static, equilibrium and dynamic materials properties are employed. Depending on the required accuracy and numerical efficiency, these techniques rely on models for describing interatomic interactions on different levels of detail, ranging from simple lattice Hamiltonians over analytic potentials to density functional theory calculations. In addition to the actual simulations, the development of reliable interaction models for FePt alloys therefore takes a central part of this work.

In the following chapter, the methods of atomistic simulation applied in the present work are discussed in conjunction with their applicability to the questions defined above. In the second part of this work, the development of the interaction Hamiltonians is described. With these models, the thermodynamic stability of multiply twinned FePt nanoparticles and the thermodynamics of the ordering behavior are investigated. Finally, the kinetics of the $A1$ to $L1_0$ transition in FePt nanoparticles is analyzed.

# 2. Methodology

*This chapter describes the philosophy followed in the present work for investigating the properties of FePt nanoparticles by atomistic simulations. An outline of atomistic simulation methods is given and models for describing interatomic interactions are summarized.*

## 2.1. Modeling approach

In the domain of atomistic computer simulation, a number of methods are available for studying static, equilibrium and dynamic materials properties. These include molecular statics calculations for structural energy minimizations, the molecular dynamics (MD) method for integrating equations of motion, and Monte Carlo (MC) simulations for a random sampling of phase space. The key ingredient for all these methods are atomistic interactions models that allow to assess energies and forces in the system under consideration. On the level of highest accuracy, quantum-mechanical total energy calculations are available, a prominent example being the density functional theory (DFT), which is applied in this work. However, because of the high computational effort, DFT methods restrict simulations to small system sizes and short time scales, only.

For studying structural, equilibrium and dynamic properties of FePt nanoparticles, size ranges from approximately 2 to 10 nm in diameter have to be considered. As is illustrated by the following arguments, it is not possible to address this problem solely on the grounds of DFT calculations:

- Typical system sizes comprise a number of $10^3$ to $10^5$ atoms. These large systems exceed the limits of self-consistent methods for total energy calculations.

- For investigating equilibrium properties at finite temperature, it is not sufficient to only study energy terms. Instead, also the contributions of vibrational and configu-

| Atomic interaction model | Accuracy of | | Assessment of | |
|---|---|---|---|---|
| | Energies | Forces | Vibrational entropy | Configurational entropy |
| Quantum Mechanics | ✓✓✓ | ✓✓✓ | – | – |
| Interatomic potentials | ✓✓ | ✓✓ | ✓✓ | ✓ |
| Lattice Hamiltonians | ✓ | ⁄ | ⁄ | ✓✓ |

**Table 2.1.:** *Comparison of atomic interaction models in terms of their accuracy for calculating energies and forces and their applicability for assessing entropy contributions in MD and MC simulations.*

rational *entropy* to the free energy become decisive.* Even if small system sizes were considered, assessing entropy contributions requires to follow long trajectories or to sample an extensive number of configurations. Again, this is not possible if quantum mechanical Hamiltonians are applied.

Given these limitations of the quantum-mechanical methods, the philosophy of the present work is to follow a hierarchical multiscale approach for achieving a reliable description of FePt nanoparticles. In order to bridge the gap between system sizes and time scales accessible by DFT methods on the one hand, and extended simulations of up to $10^5$ atoms on the other hand, atomic interaction models of higher numerical efficiency are developed in this work. Increased efficiency, however, is always accompanied by a tradeoff in terms of accuracy as some details of atomic bonding have to be sacrificed. This is illustrated in Tab. 2.1, where the different interaction models used in this work are compared in terms of their accuracy and their capability of assessing the different entropy contributions in MD or MC simulations.

As can be seen in Tab. 2.1, in the first stage of coarse-graining, analytic interatomic potentials for the FePt system are developed, which treat an ensemble of atoms as classical interacting mass points, only. Interatomic potentials therefore allow MD or off-lattice MC simulations of large systems over long time scales, which makes the assessment of vibronic entropy contributions possible. Instead, as the phase space is still continuous in terms of atomic coordinates, the sampling of *configurational* entropy still requires a large amount of computing time. In a next step, the continuous nature of interatomic interactions is

*For clarity, in this case configurational entropy denotes the number of possibilities for distributing atoms in a substitutional alloy on the lattice.

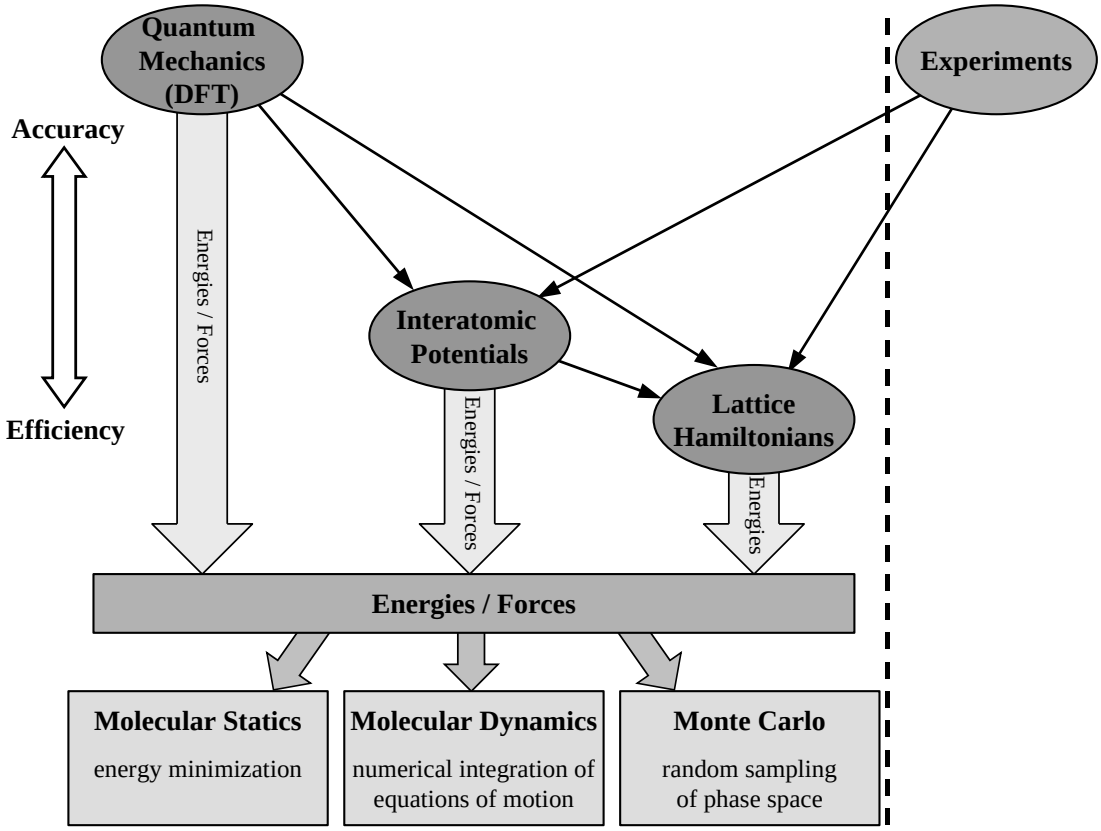


**Figure 2.1.:** *Illustration of the hierarchy of the atomic interaction models employed in this work.*

therefore neglected, leading to the development of lattice Hamiltonians for FePt alloys. These allow to assess the influence of configurational entropy at very low computational cost by lattice MC methods.

As illustrated in Fig. 2.1, the hierarchical character of the present approach is emphasized by conveying results obtained from the high-level calculations to the coarse-grained levels. This can serve to justify the approximations that enter in the more efficient models. Also, simulation results from DFT calculations serve as input for deriving FePt interatomic potentials and lattice Hamiltonians.

However, the present work will also demonstrate that fitting solely to reference data from high-level calculations is not necessarily the best choice. Instead, as indicated in Fig. 2.1, fitting directly to selected properties obtained from experiments can enhance the quality of an atomic interaction model.

In the following section, an outline of the molecular statics, molecular dynamics and Monte Carlo methods is given. Subsequently, the principles of the atomic interaction models at different levels of detail are summarized in short. A detailed description of the

FePt interatomic potentials and lattice Hamiltonians developed in this work can be found in Chapter 3.

## 2.2. Methods of atomistic simulation

### 2.2.1. Molecular Statics

In molecular statics calculations, the energy of a system composed of $N$ atoms is minimized with respect to the atomic positions in the zero temperature limit. Starting from an initial configuration, the information of the forces acting on the atoms is employed for solving the $3N$-dimensional problem of efficiently minimizing the energy function $E(\mathbf{r}_1, \mathbf{r}_2, \ldots \mathbf{r}_N)$. A typical numerical minimization algorithm is the conjugate gradient method [29]. In the present work, molecular statics calculations are applied for structural optimization of particles (see Chapter 5) and for determining the configuration and energy of defects in crystals (see Chapter 7).

### 2.2.2. Molecular Dynamics

The molecular dynamics (MD) method allows to simulate the dynamics of an ensemble of interacting atoms at finite temperatures by integrating Newton's equations of motion. This results in the system of coupled differential equations

$$m_i \frac{\partial^2 \mathbf{r}_i}{\partial t^2} = \mathbf{F}_i \left( \mathbf{r}_i \right), \qquad i = 1 \ldots N, \tag{2.1}$$

where $m_i$ is the mass of atom $i$, $\mathbf{r}_i$ its position and $\mathbf{F}_i$ the force acting on it. For $N > 3$, this system can not be solved analytically and one has to resort to numerical methods. In a MD simulation, this is achieved by regarding the forces as constant over a short time step $\Delta t$ and by integrating Eq. (2.1) iteratively.

In MD simulations, a measurable quantity $A$ of the system under consideration is calculated as a time average over the actual values of interest $A(t)$

$$\langle A \rangle = \lim_{\tau_{\mathrm{sim}} \to \infty} \frac{1}{\tau_{\mathrm{sim}}} \int_{\tau=0}^{\tau_{\mathrm{sim}}} A(t) \mathrm{d}t, \tag{2.2}$$

where $\langle \ldots \rangle$ indicates the time averaging, while $\tau_{\mathrm{sim}}$ is the simulation time. In practice, allowing an equilibration of the system, the initial time steps of the simulation have to be excluded from the averaging.

The time scales accessible by MD simulations are typically limited to a few nanoseconds, because of the need of resolving the vibrational motion of atoms occurring at typical time constants of picoseconds.

Possible applications of MD simulations are studies of point defect diffusion at sufficiently high temperatures (see Sec. 3.4) and the evaluation of vibrational contributions to the total energy (see Sec. 3.4 and Appendix A).

### 2.2.3. Monte Carlo

In materials modeling, methods that evolve an atomic system by generating a random sequence of states in phase space $\mathbf{\Gamma}$ are denoted Monte Carlo (MC) simulations. Basically, two different classes of MC simulations can be distinguished. In this work, MC simulations have been used mostly for determining equilibrium properties and analyzing phase transitions. For these tasks, importance sampling MC (often only MC) algorithms can be employed [30], where the states visited by the trajectory of the system through phase space are chosen solely on the grounds of their probability in the given ensemble. Therefore, the trajectory generally does not reflect a true time evolution of the system under consideration and the definition of a time scale or the treatment of non-equilibrium processes is not possible. Alternatively, the succession of states through phase space can be generated based on the transition probabilities between neighboring states. The corresponding algorithms are denoted kinetic MC (KMC) simulations, emphasizing their applicability for studying non-equilibrium and dynamic processes.

#### Importance sampling Monte Carlo

Statistical mechanics provides the possibility of determining equilibrium properties by calculating ensemble averages of the property of interest, $A$. For a system Hamiltonian $\mathcal{H}$ and constant number of atoms, volume and temperature, the (canonical) ensemble average is given by [31]

$$\langle A \rangle = \frac{\int \mathrm{d}\mathbf{\Gamma} A(\mathbf{\Gamma}) \exp\left(-\mathcal{H}(\mathbf{\Gamma})/k_\mathrm{B}T\right)}{\int \mathrm{d}\mathbf{\Gamma} \exp\left(-\mathcal{H}(\mathbf{\Gamma})/k_\mathrm{B}T\right)}, \tag{2.3}$$

where the integration is over all points in phase space $\mathbf{\Gamma}$. In general, the integrals in Eq. (2.3) can not be evaluated analytically and one has to resort to numerical integration schemes. Because of the high dimensionality of the integrals involved, conventional numerical integration relying on a uniform sampling of the integrand are not feasible. Instead, by realizing that only a limited region of phase space contributes significantly to Eq. (2.3),

preferentially sampling the integrand at points of high weight can reduce the numerical effort tremendously. MC algorithms provide efficient ways for solving Eq. (2.3) by employing the idea of *importance sampling*.

In the importance sampling MC algorithm proposed by Metropolis (Ref. [32]), a trajectory through phase space is constructed by starting from an initial configuration and randomly generating neighboring trial states. In the canonical ensemble, depending on the nature of the problem and the coarse graining level, trial states can be found by random displacements of atoms on a lattice or in continuum and by random exchanges of atom pairs. A transition is then accepted according to the Metropolis probability [32]

$$\omega = \begin{cases} 1 & \text{for} \quad \Delta E \leq 0 \\ \exp\left(-\dfrac{\Delta E}{k_\mathrm{B} T}\right) & \text{for} \quad \Delta E > 0, \end{cases} \tag{2.4}$$

where $\Delta E$ is the change of energy in the system associated with the transition. For sufficiently long trajectories generated by this algorithm, each state is visited a number of steps that is proportional to its weight in the canonical ensemble [32]. From a simulation with a total of $M$ trial steps (accepted or unaccepted), the estimate of the ensemble average is given by

$$\langle A \rangle = \frac{1}{M} \sum_{i=1}^{M} A(\mathbf{\Gamma}_i), \tag{2.5}$$

where $\mathbf{\Gamma}_i$ denotes the state visited in the $i^{\mathrm{th}}$ step. It is common to express the duration of a MC simulation by the number of "MC steps", which is usually defined as the number of trial steps divided by the number of atoms in the system.

For practical applications, the described MC algorithm is most efficient for an average acceptance probability of $\overline{\omega} = 1/2$, which allows to sample the maximum number of states with the correct frequency in a given simulation time [33]. For simulations where random atom displacements are attempted, a modification of $\overline{\omega}$ can easily be achieved by adapting the displacement lengths.

However, for some applications, controlling $\overline{\omega}$ is not possible and the efficiency of the above algorithm can be severely limited for very low average acceptances. In these cases, the more elaborate $n$-fold way algorithm can be beneficial, as it avoids the rejection of trial attempts [34]. In each step of a $n$-fold way simulation, *all* possible transitions $j$ to neighboring states have to be identified. The hierarchy of the transitions is established by calculating their weights $\omega_j$ according to Eq. (2.4). Out of the catalog of $n$ transitions, one transition is then selected randomly according to the normalized probability

$$\rho_j = \omega_j / Q, \tag{2.6}$$

with $Q = \sum_{k=1}^{n} \omega_k$. An internal time variable $t$ is incremented by

$$\Delta t = -\ln(r)/Q, \tag{2.7}$$

where $r$ is a random number between 0 and 1. The system is then evolved by carrying out the selected transition. From a $n$-fold way MC simulation, ensemble averages are obtained by

$$\langle A \rangle = \frac{\sum_{i=1}^{M} A(\mathbf{\Gamma}_i)\Delta t_i}{\sum_{i=1}^{M} \Delta t_i}. \tag{2.8}$$

It is important to stress that in an importance sampling $n$-fold way MC simulation, the variable $t$ is generally not related to a physical time. Instead, it serves for measuring the relative weights of the states visited during the simulation.

In the present work, in addition to canonical ensemble calculations, importance sampling MC simulations have also been carried out in the isothermal-isobaric $N, P, T$ ensemble. For a correct sampling of ensemble averages, $N, P, T$ calculations include random changes of cell shape and dimensions. The transition probabilities are then calculated by replacing $\Delta E$ in Eq. (2.4) by the change in enthalpy $\Delta H$.

Applications for importance sampling MC simulations with the classic Metropolis algorithm are calculations of free energies (see Sec. 3.4 and Appendix A) and investigations of order-disorder phase transitions (see Chapter 6). The $n$-fold way algorithm is a suitable method for determining the equilibrium vacancy concentration in nanoparticles (see Chapter 7).

### Kinetic Monte Carlo

For simulating non-equilibrium and dynamic processes, the trajectory through phase space generated by a MC algorithm has to reflect a true evolution of the system under consideration. Also, the possibility of correlating the number of MC steps to a real time scale is desirable. If coarse graining allows to reduce the time evolution of a system to a sequence of independent, thermally activated processes ("Poisson processes"), then the $n$-fold way algorithm provides a solution to this problem [35]. For every step of the simulation, the $n$-fold way algorithm now identifies all possible activated processes and calculates the transition rates $\nu_j$ according to

$$\nu_j = \nu_{0,j} \times \exp\left(-\frac{E_j^{\mathrm{a}}}{k_{\mathrm{B}}T}\right), \tag{2.9}$$

where $\nu_{0,j}$ is the attempt frequency of the $j^{\text{th}}$ process and $E_j^{\text{a}}$ its activation energy, i.e. the energy difference between the saddle point and the initial state. Accordingly, the normalized probability for selecting one of the processes is now given by

$$\rho_j = \nu_j / Q, \tag{2.10}$$

with $Q = \sum_{k=1}^{n} \nu_k$. The time increment $\Delta t$ as defined in Eq. (2.7) now has a physical meaning. It corresponds to the "residence time", i.e. the time that elapses on average until the next activated process occurs. Although off-lattice calculations with an on-the-fly identification of transition paths have been attempted [36], KMC simulations typically reduce the effort by restricting atomic positions to fixed lattice sites and by allowing only a predefined set of transition events to occur (e.g. single atom jumps by a vacancy mechanism). KMC is then a suitable method for studying the kinetics of atomic diffusion processes (see Chapter 8). Concerted motion of multiple atoms and the formation of lattice defects can be incorporated by extending the event database and by applying a refined lattice [37].

## 2.3. Modeling interatomic interactions

The basic ingredient for any of the above listed atomistic simulation methods is the ability of calculating the structural energy for an arbitrary configuration of atoms. For molecular statics and MD, as a derived quantity, the interatomic forces are obtained by the gradient of the energy with respect to the atomic coordinates. Because of a manifold of requirements on simulations in materials research in terms of accuracy, system size and time scale, methods for treating interatomic interactions on different levels of abstraction have been developed.

### 2.3.1. Density functional theory

In principle, the highest accuracy and transferability for calculating interatomic interactions provide quantum-mechanics based approaches that seek to solve Schrödinger's equation of the many particle, many electron system by applying a minimal number of simplifications. In condensed matter physics and materials science, a well established and widely used method is the density functional theory (DFT) [38]. DFT relies on the theorem that the total energy of a system can be expressed as a functional of the electron density and that the ground state electron density minimizes energy [39]. The most common energy functional is given by Kohn and Sham [40], reducing the many particle problem to a set of

effective one-particle equations. The challenge in DFT calculations is to solve the Kohn-Sham equations self-consistently, while applying a minimum number of approximations. For this task, a number of efficient computer codes are now widely available [38], including the program package VASP [41] applied in the present work. Although DFT calculations can provide very accurate structural energies, their drawback are the high computational costs. While a number of 150 to 200 atoms marks the upper bound for the system size, the computing time required for the self-consistent cycle in every step of a simulation restricts the time scale in MD to the order of picoseconds and forbids an extensive sampling of phase space in MC simulations

### 2.3.2. Analytic interatomic potentials

If larger system sizes and time scales are of interest that cannot be accessed by DFT calculations, one has to resort to more efficient interaction models. Here, analytic interatomic potentials provide a reasonable compromise between accuracy, transferability and computational efficiency. The advantage of interatomic potentials lies in an analytic description of the energy of a system solely as a function of atomic coordinates. The influence of the electron system is incorporated only implicitly by devising different functional forms and parameterizations specific to the character of the interatomic interactions (metallic, ionic, covalent, van der Waals) and atom types involved. For metallic bonding, the embedded atom method (EAM) [42] and the derived, angular dependent modified embedded atom method (MEAM) [43] have been applied successfully for describing a wide variety of metal and metal alloy interactions. An alternative approach is provided by the analytic bond-order potential (ABOP) formalism [44–47] The advantage of the ABOP over the MEAM method are a more compact functional form with lesser free parameters and a high modularity, allowing to describe even mixed metallic-covalent bonding [47, 48]. Analytic potentials allow to access system sizes of up to millions of atoms and time scales of microseconds in molecular dynamics simulations.

### 2.3.3. Effective lattice Hamiltonian

Analytic potentials extend the time and size scales of atomistic simulations significantly, but require a continuous spacial sampling of phase space. For further reducing the complexity of the model description, effective Hamiltonians that map the configurational energy of a system on a lattice can be employed. Methods that construct the lattice Hamiltonian by a series expansion over site energies, pair energies, three-body and higher order interac-

tion energies are usually denoted as cluster expansions [49]. By truncating the expansion so that it only includes pair energies and by restricting the interaction range to nearest or second nearest neighbor shells, classic Ising-type model descriptions are obtained [50]. The advantage of these models is that they allow a very efficient sampling of configurational degrees of freedom. They can therefore conveniently be used in MC simulations for investigating phase diagrams of substitutional alloy systems [50].

## 2.4. Summary

The philosophy of the present approach for modeling FePt nanoparticles has been described. Because of the typical system sizes of $10^3$ to $10^5$ atoms, high-level DFT calculations can not be employed directly for determining energies and forces in nanoparticles. Also, the assessment of entropy contributions to particle properties at finite temperatures is not feasible by the DFT method. For overcoming these restrictions, a multiscale approach has been chosen that relies on the development of more efficient interaction models at different levels of sophistication, including interatomic potentials and effective lattice Hamiltonians. By combining the results from these different models, this work seeks to provide a thorough understanding of the properties of FePt nanoparticles by atomistic simulations.

In the following part of this work, the development of interatomic FePt potentials based on the analytic bond-order formalism, and the parametrization of an Ising-type lattice Hamiltonian for FePt alloys is described.

# Part II.

# Model descriptions of the FePt system

# 3. Analytic bond-order potential

*In this chapter the development of an analytic bond-order potential for modeling interatomic interactions in FePt alloys is described. After a general introduction an outline of the functional form and the general fitting procedure is given. Then, the Fe-Fe, Pt-Pt and Fe-Pt interaction potentials are described, separately.*

## 3.1. Introduction

Numerically efficient models for describing interatomic interactions are indispensable for investigating the properties of FePt nanoparticles by atomistic computer simulations. On the detail level between total-energy density functional theory (DFT) calculations and simple lattice Hamiltonians, interatomic potentials describe an ensemble of atoms as classical interacting mass points.

In the present work, the analytic bond-order potential (ABOP) formalism has been applied for modeling interatomic interactions in the Fe-Pt alloy system, which has been chosen because of its compact functional form that allows, up to a certain degree, an intuitive control over the properties. In its original form, the ABOP formalism has been developed for describing covalently bonded systems such as silicon [45, 51] and carbon [52]. In covalent systems, binding is strongly directional dependent, which is accounted for by the inclusion of three-body angular terms. With the addition of angularity, the ABOP formalism has been shown to be formally equivalent to the second moment tight-binding method [53], making its application to metals and mixed metallic-covalent systems straightforward. In a slightly modified version [47], it has already proven valuable for modeling transition metals with a variety of crystal structures. Potentials exist for face centered cubic platinum [47], body centered cubic tungsten [48] as well as hexagonal close packed zinc [54]. For metal systems, the inclusion of angularity can also be important, as is exemplified by the inaptness of nearest-neighbor potentials for describing metals with highly isotropic shear moduli, such as platinum [47].

The analytic bond-order formalism follows a modular approach for describing both pure elements, as well as compounds: The potential energy of a system consisting of atom types A and B is given as a sum over individual bond energies, while for each bond type (A-A, B-B or mixed A-B bond) a separate parametrization is used. Therefore, once a potential for a pure element has been derived, it serves as a basis for modeling its compounds and alloys.

For modeling FePt alloy nanoparticles, the ABOP formalism therefore requires the development of three separate parameterizations, describing pure Fe, pure Pt and the mixed Fe-Pt interactions, respectively. Since the $L1_0$ structure exhibits direct next neighbor interactions of the pure constituents, the mixed FePt parameter set cannot be fitted independently. In order to provide a solid basis for the alloy interactions, a realistic description of the boundary phases is necessary. In the case of Fe, most notably this includes a reproduction of the structural transitions from bcc $\alpha$ over fcc $\gamma$ and bcc $\delta$-Fe to the liquid phase. Important benchmarks for the pure Pt parametrization are the high energy penalty for stacking-fault and twin boundary defects, as well as a nearly isotropic elastic behavior of fcc Pt.

In this chapter the functional form of the ABOP is first summarized and a brief outline of the general fitting procedure is given. In following three main parts the development of the Fe-Fe, Pt-Pt and Fe-Pt interaction potentials is described in detail.

## 3.2. Bond-order formalism

The functional form of the analytic bond-order potential is summarized in short by the following equations. A physical motivation based on the second moment tight-binding approximation is given in Refs. [44–47, 53]. In the bond-order formalism, the potential energy of a system is written as a sum over individual bond energies

$$E = \sum_{i<j} f_{ij}^{\mathrm{c}}(r_{ij}) \left[ V_{ij}^{\mathrm{R}}(r_{ij}) - \frac{b_{ij} + b_{ji}}{2} V_{ij}^{\mathrm{A}}(r_{ij}) \right]. \tag{3.1}$$

The pair-like repulsive and attractive terms are taken as Morse-like pair potentials

$$\begin{aligned} V^{\mathrm{R}}(r) &= \frac{D_0}{S-1} \exp\left(-\beta\sqrt{2S}(r-r_0)\right), \\ V^{\mathrm{A}}(r) &= \frac{SD_0}{S-1} \exp\left(-\beta\sqrt{2/S}(r-r_0)\right). \end{aligned} \tag{3.2}$$

Here, $S$ is an adjustable parameter, while $D_0$ denotes the dimer bond energy and $r_0$ the dimer bond length. The parameter $\beta$ can be determined from the ground-state oscillation frequency of the dimer. The interaction range is determined by the cutoff function

$$f^{\mathrm{c}}(r) = \begin{cases} 1, & r \leq R - D, \\ \frac{1}{2} - \frac{1}{2}\sin\left(\frac{\pi}{2}(r-R)/D\right), & |R - r| \leq D, \\ 0, & r \geq R + D. \end{cases} \tag{3.3}$$

where $R$ and $D$ are adjustable parameters. Three-body contributions and angularity enter the energy function via the bond-order parameter $b_{ij}$

$$b_{ij} = (1 + \chi_{ij})^{-\frac{1}{2}}, \tag{3.4}$$

$$\chi_{ij} = \sum_{k \neq i,j} f_{ik}^{\mathrm{c}}(r_{ik}) g_{ik}(\theta_{ijk}) \exp\left[2\mu_{ik}(r_{ij} - r_{ik})\right]. \tag{3.5}$$

The indices monitor the type-dependence of the parameters, which is important for describing compound systems. The angular dependence is described by

$$g(\theta) = \gamma\left(1 + \frac{c^2}{d^2} - \frac{c^2}{d^2 + [h + \cos\theta]^2}\right). \tag{3.6}$$

## 3.3. General fitting procedure

The general fitting methodology employed in the present work has already been applied successfully for deriving analytic bond-order potentials of numerous elements [47, 48, 55]. For achieving a high transferability, the aim is to match the properties of the potential with an extensive database of values obtained from experiment and total-energy DFT calculations. The complete set of reference data is divided into a fitting and a testing database [56, 57]. The fitting database encompasses structural properties like bond lengths, cohesive energies and elastic constants of structures covering the coordination range from the dimer up to the twelve-fold coordinated close packed fcc and hcp structures. Starting from an initial guess, the potential parameters are optimized by adjusting the properties predicted by the potential to the values contained in the fitting database using a conjugate gradient least-squares minimization algorithm as implemented in the program Pontifix [58]. Subsequently, the quality of a parameter set which has been identified as a good fit in this first step is evaluated by comparing to the testing database. This database comprises data on point defects like vacancy and interstitial formation energies and two dimensional defects such as surface and interface energies. Furthermore, thermal properties like the melting temperature and transitions between solid phases are also included. This procedure

allows to identify regions of parameter space where the potential shows a high transferability. Promising parameter sets can be used as a new starting point in the minimization algorithm. In iterating the fitting and testing steps, one eventually proceeds towards a parametrization that shows an overall satisfactory behavior regarding the complete set of reference data.

# 3.4. Fe-Fe interaction: analytic bond-order potential for bcc and fcc iron

## 3.4.1. Introduction

In this section the development of the pure Fe-Fe part of the analytic bond-order potential (ABOP) is described.

In the hierarchy of modeling techniques, atomistic simulations with analytic interatomic potentials close the gap between self-consistent quantum-mechanical calculations and coarse-grained methods based on quasi-particle or continuum models. Interatomic potentials are computationally very efficient, because the electronic degrees of freedom are not explicitly treated and the energy of a system is solely described by the positions of the constituting atoms. In the realm of metallic materials the embedded-atom method (EAM) [42] and its variants [43, 59] have been successfully applied for describing materials properties of various d-transition metals. Modeling of magnetic materials, including iron has, however, remained a true challenge. Iron exhibits a phase transition between bcc $\alpha$-iron and fcc $\gamma$-iron at $T_c^{\alpha\gamma} = 1184\,\mathrm{K}$, and a transition back to the bcc phase ($\delta$-iron) at $T_c^{\gamma\delta} = 1665\,\mathrm{K}$ before melting [60]. The origin of these phase transitions is well understood [61]: At zero Kelvin, the contribution of ferromagnetic energy to the total energy of the bcc phase stabilizes $\alpha$-iron over $\gamma$-iron. At finite temperatures, the degrees of freedom of the magnetic spins represent the decisive contributions to entropy that drive the structural phase transitions. In contrast, the vibronic contributions to entropy are only of secondary importance.

Therefore, by relying on interatomic potentials where the degrees of freedom of the electronic subsystem are missing, modeling these phase transitions is conceptually challenging.

In the past, a variety of interatomic potentials for Fe and some of its alloys have been proposed [62–68], most of them employing a central force description. Angular dependent potentials were developed within the modified EAM [69], the embedded-defect method (EDM) [70] and the angular dependent potential method (ADP) [71], which allow an improved description of properties as compared to standard EAM potentials. Interestingly, transitions between the $\alpha$- and $\gamma$-phases have only been considered in pure iron in Ref. [65] and in the context of martensite-austenite transitions in Fe-Ni alloys [64]. Recently, Dudarev and Derlet [67] proposed a potential in which magnetic energy contributions are included via a Stoner model. They present two separate parameterizations of their potential for magnetic and non-magnetic iron phases, but do not address the problem of how to switch from one to the other with increasing temperature.

Addressing the question of whether the characteristic $\alpha$–$\gamma$–$\delta$–liquid phase sequence can be reproduced would therefore be an important step in the theoretic description of iron by analytic potential methods.

As it has been argued above, the Gibbs free energy difference between the bcc and fcc phase is dominated by magnetic energy and entropy contributions. Since the latter are missing in a classic interatomic potential, the key idea of the present approach is to construct an Fe ABOP that is able to mimic the differences between bcc and fcc Fe by lattice energy and phonon contributions, only. This is done by adjusting the lattice energy difference of the bcc and fcc phases in a way that the calculated Gibbs free energies cross at the desired temperatures. The thus obtained potential is then applicable for problems where the bcc-fcc transition is of importance.

For benchmarking the Fe ABOP, a thorough comparison of its properties with four established iron potentials is provided. These include the embedded-atom-method potential by Simonelli *et al.* (potential "A" in Ref. [62]), the Fe part of the Fe-Cu potential by Ackland *et al.* [63], the Mendelev *et al.* potential (parametrization II) [66] and the "magnetic" potential of case study II of Dudarev and Derlet [67].

This section is organized as follows. First, total-energy DFT calculations of iron are described, which serve for extending the fitting database. After a detailed description of the fitting process, various bulk properties are compared including phonon dispersions and the Bain-path. Melting properties and calculations of Gibbs free energies for bcc and fcc iron are addressed, revealing the $\alpha$–$\gamma$–$\delta$–liquid transitions. Finally, point defect properties are discussed and a summary of the Fe ABOP is given.

## 3.4.2. Total-energy calculations

As described Sec. 3.3, the fitting procedure of the bond-order potentials relies on an extensive database that covers a variety of differently coordinated structures. The experimental data on iron available in literature is naturally constricted to phases that are experimentally accessible, like the ground state bcc phase or the high temperature fcc phase. For structures that do not appear in the iron phase diagram, density functional theory (DFT) calculations have been carried out in order to fill the fitting database with the required properties.

The DFT calculations have been performed using the Vienna *ab initio* simulation package VASP[41] employing the projector-augmented wave (PAW) method [72, 73]. The generalized gradient approximation (GGA) has been used in the parametrization by Perdew and Wang (PW91) [74]. The plane-wave cutoff energy was set to 348.3 eV. The number

of $k$-points in the irreducible Brillouin-zone was chosen to guarantee a convergence of the total energy better than 1 meV/atom. Typical values are 220 $k$-points for the bcc and fcc structures.

Total energies have been calculated for Fe in the fcc, hcp, bcc, sc and diamond structures. For each structure, the minimum energy, lattice constant, bulk modulus and pressure derivative of the bulk modulus have been determined by fitting the energy-volume data to the Birch-Murnaghan equation of state [75]. For the hcp structure, the $c/a$-ratio has been identified by calculating energy-volume curves for different fixed $c/a$-ratios and subsequently fitting a second order polynomial to the energy minima. This method proved to be more efficient and accurate than a relaxation of the cell shape controlled by the forces acting on the atoms within a single run of VASP. The results of the calculations are summarized in Tab. 3.2.

For identifying the magnetic ground state of a structure, non spin-polarized (non-magnetic, NM) as well as spin-polarized calculations with ferromagnetic (FM) and anti-ferromagnetic (AFM) alignment of the atomic spins have been performed. The magnetic ground states were found to be NM for the diamond structure, FM for simple cubic, FM for bcc, AFM for fcc and NM for hcp. As shown in Fig. 3.1, the calculations furthermore reveal the existence of two FM states in fcc Fe, namely a high-spin, high-volume (HS) and a low-spin, low-volume (LS) state separated from the AFM state by 45 meV and 29 meV, respectively. The results on bcc, fcc and hcp Fe are in qualitative agreement with *ab initio* calculations from Entel *et al.* [76, 77]. Experimental evidence for the AFM ground state of $\gamma$-Fe and the existence of the FM HS state is summarized in Ref. [78]. Depending on the number of electrons treated as valence states in the pseudo-potentials employed in their work, Entel *et al.* find a strong variation of the energies of the different magnetic fcc phases [77]: Pseudo-potentials that treat the $3p$ electrons as part of the pseudo core produced a false FM fcc ground state and only a self consistent treatment of the $3p$ states as valence states could lift this failure in favor of a AFM ground state. In light of these findings, the calculations for bcc and fcc Fe were conducted with two different kinds of PAW pseudo-potentials, treating the $3p$ electrons as core states (PAW1) and valence states (PAW2), respectively. As can be seen in Fig. 3.1, in the present work, the difference between the two pseudo-potentials is negligible and the computationally more efficient PAW1 potential can be used for extending the fitting database with *ab initio* data. The energy difference between FM bcc Fe and AFM fcc Fe calculated by this method is 0.11 eV/atom.

For bcc and fcc Fe, the complete set of second order elastic constants has been calculated. For this purpose, the deformation energy of the system was analyzed in response to different deformation modes (see Tab. 3.2). The GGA calculations provide an overall

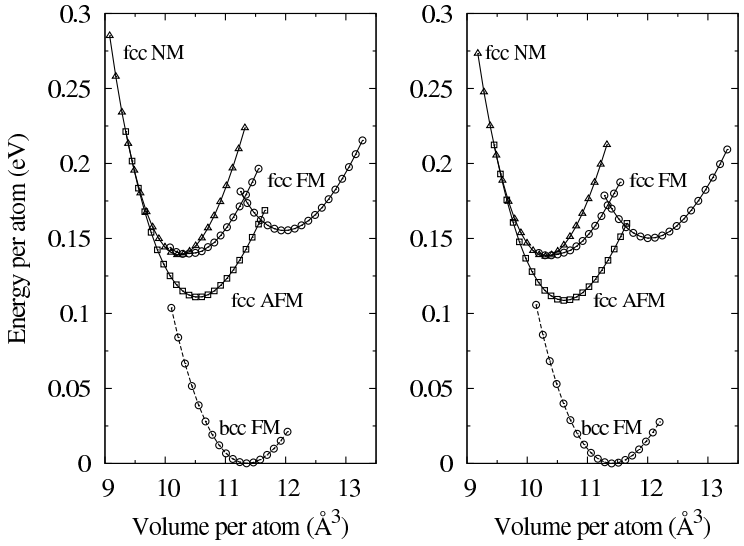


**Figure 3.1:** *Comparison of energy-volume curves at 0 K for bcc and fcc Fe in different magnetic states as obtained from DFT calculations with two different PAW potentials. Left panel: $3p$ electrons are included in the pseudo core of the PAW potential. Right panel: $3p$ electrons are treated as valence states. Energies are relative to the FM bcc ground state.*

good description of the elastic properties of bcc iron, with a bulk modulus being however 12 % larger than the reference value of 169 GPa and a somewhat too low $c_{44}$ elastic constant. The significance of the experimentally determined elastic constants of $\gamma$-iron for comparison with the results from DFT calculations is only limited. Since the experimental values have been obtained at 1428 K, a softening of the elastic constants with respect to the zero Kelvin calculations is to be expected. A deviation of the DFT results towards higher values is therefore reasonable. Furthermore, in agreement with the ground state of $\gamma$-iron, an anti-ferromagnetic alignment of spins was assumed in the DFT calculations. At the temperature of the experimental measurement, the magnetic ordering is, however, not preserved and its influence on the elastic constants cannot be assessed.

The DFT data represents a complement to the available experimental data in the fitting database. However, this introduces the problem that structural properties like the bond lengths obtained from DFT calculations can deviate from experimental values simultaneously used in the fitting database. For obtaining a consistent input data set, all atomic volumes obtained by DFT were scaled by a factor 1.03 that matches the volume of the bcc ground state to the experimental volume. The scaled volumes are given in brackets in Tab. 3.2.

### 3.4.3. Fitting of the Fe potential

On the basis of the extended fitting database, the parametrization of the Fe ABOP has been determined as described in the following.

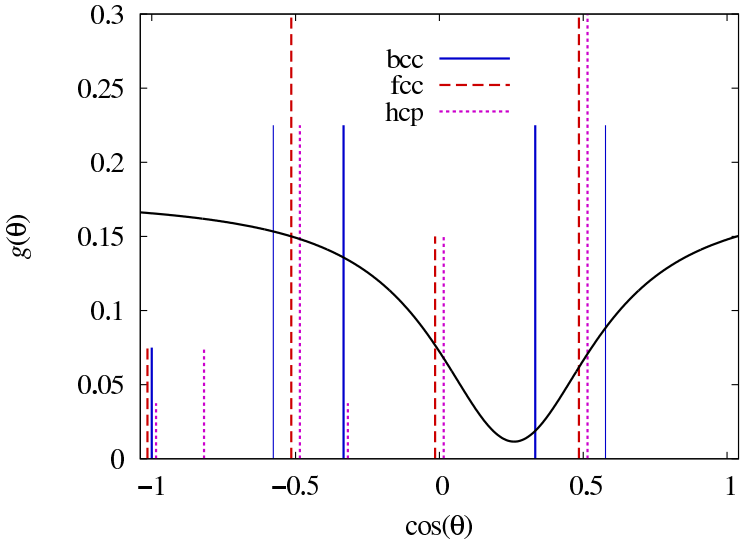


**Figure 3.2:** *Angular function $g(\theta)$ of the Fe potential. Angles appearing in different structures are indicated by vertical lines. The height of a line is proportional to the weight of the angle in the respective structure. The angles are shifted slightly so that structures having identical angles can be distinguished.*

For the sake of computational efficiency, it is generally desirable to keep the cutoff radius as small as possible, reducing it to nearest neighbor interactions only. However, the difference in bond length between the nearest and second nearest neighbors in the bcc structure is very small, and positioning the cutoff function between the two distances can lead to unpredictable cutoff effects. The cutoff radius of the ABOP was therefore chosen so that second nearest neighbors are included for the bcc structure, but are excluded for the fcc structure. (This approach has previously proven useful for describing tungsten [48]).

One quantity that proved to be decisive for the performance of the potential is the parameter $h$ determining the position of the minimum in the angular function $g(\theta)$ (see equation Eq. (3.6)). Atomic configurations exhibiting angles close to this minimum possess a higher bond-order than configurations with angles lying outside the minimum. Careful selection of the range of $h$ therefore easily allows to energetically favor the bcc structure over the close packed fcc and hcp structures. As shown in Fig. 3.2, the dominating nearest neighbor angles on a bcc lattice are 70.5° and 107.5°, which appear in Fig. 3.2 at positions $+1/3$ and $-1/3$. In contrast, the fcc lattice exhibits angles of 60°, 90° and 120°, corresponding to positions $1/2$, 0 and $-1/2$. A selection of $h$ with $|h|$ in the vicinity of $1/3$ therefore allows to create potentials where the bcc structure has a lower energy than the close packed structures.

However, positioning the minimum of $g(\theta)$ exactly on or too close to an angle appearing in a structure often deteriorates the elastic properties. In this case, the fitting routine is prone to the risk of stabilizing the structure by a minimum in the energy landscape arising solely from the presence of the selected angle which leads to large restoring forces when moving the atoms away from their equilibrium positions by shear deformations. Poor

elastic constants (a too high $c_{44}$) are also found for $|h| \geq 1/3$. These considerations restrict the range of $|h|$ to values close to, but lower than 0.3.

Changing the sign of the parameter $h$ alters the static properties of the bcc phase only slightly, since, apart from the 180° angle, the angles appearing in the bcc structure are symmetrically distributed around $\cos(\theta) = 0$. Parameter sets with a positive $h$ around 0.3 show, however, unrealistically low melting temperatures at approximately 1000 K. For this reason, the parameter $h$ has to be restricted to negative values.

Another restriction applies to the parameter $2\mu$. During the fitting procedure, it was found that the fcc Fe phase becomes thermally instable for $2\mu > 0$. It turned out that although the fcc structure is a local minimum in the potential energy landscape, the fcc phase spontaneously transforms into a twinned bcc structure at non-zero temperatures sometimes as low as 200 K. In contrast, the thermal stability of the fcc Fe phase is maintained with parameter sets having very low values for $2\mu$. This parameter has therefore been restricted to zero.

During the fitting process, incompatibilities between two desired properties can appear, i.e. fitting exactly to one property results in a bad performance of the potential for the other property. In some cases, this problem can be circumvented by restarting the fitting process in another region of parameter space. For the Fe potential an incompatibility between the correct dimer bond length and realistically high surface energies could, however, not be resolved. Fixing the dimer bond length at the experimental value of 2.0 Å results in very low surface energies, a finding that holds true for the entire range of parameter space sampled during the fitting process. A trade off between accurate dimer properties and sufficiently high surface energies therefore has to be accepted. The final parametrization of the Fe potential exhibits a 15 % too high dimer binding length of 2.3 Å but in turn yields acceptable surface energies.

An essential feature of the iron phase diagram is the $\alpha$-$\gamma$ transition. A correct description of this transition in classical molecular dynamics simulations is only possible, if the missing contributions of the magnetic entropy are accounted for. By following the method described in Appendix A, the temperature dependence of the Gibbs free energy difference $\Delta G$=$G$(fcc)-$G$(bcc) has been calculated for different trial parameterizations. The general shape of the $\Delta G$ curve was found to be universal for the region of parameter space sampled. It is plotted exemplarily for the final parametrization of the ABOP in Fig. 3.3, together with the contributions from enthalpy and entropy. After an initial decrease, $\Delta G$ reaches a minimum at intermediate temperatures and increases again up to the melting point. Although, in general, the $\Delta G$ curve does not give rise to a bcc-fcc phase transition for an arbitrary parametrization, this general shape suggests the following procedure for fitting

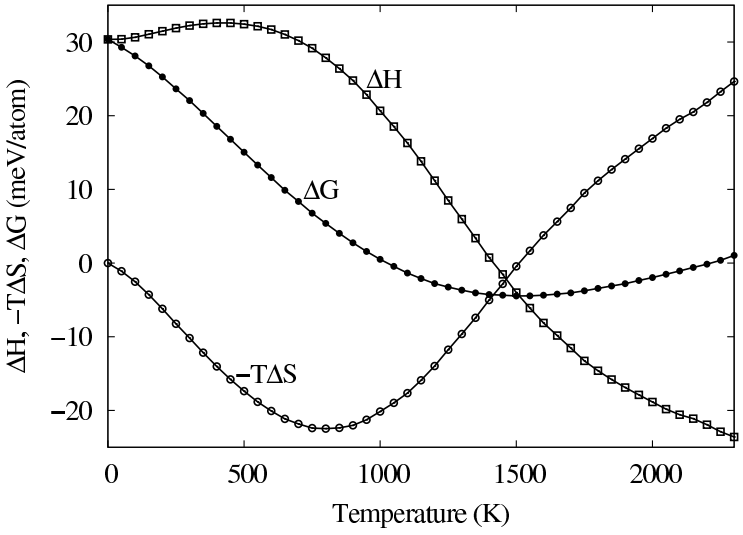


**Figure 3.3:** *Enthalpy and entropy contributions to the Gibbs free energy difference $\Delta G$=G(fcc)-G(bcc) between the fcc and bcc phases of the iron potential developed in this work.*

| Parameter | Value |
|---|---|
| $D_0$ (eV) | 1.5 |
| $r_0$ (Å) | 2.29 |
| $\beta$ (Å$^{-1}$) | 1.4 |
| $S$ | 2.0693109 |
| $\gamma$ | 0.0115751 |
| $c$ | 1.2898716 |
| $d$ | 0.3413219 |
| $h$ | −0.26 |
| $2\mu$ (Å$^{-1}$) | 0.0 |
| $R$ (Å) | 3.15 |
| $D$ (Å) | 0.2 |

**Table 3.1:** *Final parameter set of the analytic bond-order potential for iron.*

the potential to the $\alpha$-$\gamma$ transition: The missing contributions of the magnetic entropy can be compensated purely by vibronic contributions if the fcc-bcc energy difference $\Delta E$ is regarded as an adjustable parameter allowing to shift the $\Delta G$ curve until a phase transition is located in the correct temperature regime. The potential is then regarded as an effective energy function that best describes the behavior of the real iron system.

In practice, the fitting procedure proved to be more complex, since a change in $\Delta E$ does not only shift the $\Delta G$ curve, but the new parameter set can also lead to a change in the slope of $\Delta G$ over $T$. A trial and error process therefore had to be adopted. The final best-fit parameter set developed by this method is given in Tab. 3.1.

### 3.4.4. Characterization of the Fe potential and comparison with EAM potentials

In the following, the predictions of the ABOP for an extensive set of properties are compared to reference values from experiment and simulation. The performance of the ABOP is discussed in comparison with the EAM potentials by Simonelli [62], Ackland [63], Mendelev [66] and Dudarev [67].

#### Dimer and bulk properties

The dimer properties, cohesive energies and structural parameters of iron in the diamond, sc, bcc, fcc and hcp structures, as well as the elastic constants of the bcc and fcc structures as predicted by the ABOP and EAM potentials are compared in Tab. 3.2 with reference data from literature and total-energy calculations.

All potentials predict a dimer binding length higher than the experimental value of $r_\mathrm{b} = 2.0\,\text{Å}$ [79]. The values range from 2.11 Å for the Simonelli potential up to 2.35 Å for the Ackland potential. The ABOP also gives a rather high $r_\mathrm{b}$ of 2.29 Å. As mentioned in the description of the fitting process, this deviation is a necessity for obtaining acceptable surface energies with the ABOP. With 1.50 eV, the dimer binding energy is well reproduced by the ABOP, the reference values scatter between 1.04 and 1.65 eV [80, 81]. In contrast, all EAM potentials considered systematically overestimate the dimer binding energy by at least a factor 2.

The ABOP was fitted exactly to the experimental reference data on the cohesive energy, lattice constant and elastic constants of the ground-state bcc structure. These parameters are therefore reproduced with high accuracy, only the elastic constant $c_{44}$ is slightly too high. Deviations of the EAM potentials from this basic experimental data occur due to several reasons. No reference data for the cohesive energy of bcc iron is given in the paper by Ackland *et al.* instead, the reported value of $-4.316\,\text{eV/atom}$ is the cohesive energy obtained from their potential. [63] This value has then been used as a reference in the works of Dudarev *et al.* [67] and Mendelev *et al.* [66]. For achieving a better agreement of other parameters with experiment, the latter potential was fitted with only little weight on the cohesive energy, explaining the value of $-4.127\,\text{eV/atom}$. The deviations of the elastic constants of the EAM potentials from the experimental values given in Tab. 3.2 mainly arise from the utilization of different reference values. The deviations therefore give no indication on the quality of the potentials, they rather deliver insight on the scattering of the experimental data. Fitting the energy-volume curve of bcc Fe obtained from the

Table 3.2.: Comparison of structural and cohesive properties of Fe in various phases from calculation and experiment. Errors are given in round brackets. Values in square brackets are rescaled to the experimental atomic volume of bcc Fe. For the DFT calculations, the parameters are given for the lowest energy magnetic configuration, as indicated. $r_\mathrm{b}$: dimer bond distance (Å), $E_\mathrm{b}$: dimer binding energy (eV/atom), $\omega_0$: dimer vibration frequency ($\mathrm{cm}^{-1}$), $V$: equilibrium volume ($\mathrm{Å}^3$/atom), $a_0$: lattice constant (Å), $c/a$: axial ratio, $E_\mathrm{c}$: cohesive energy (eV/atom), $\Delta E$: energy difference (eV/atom) to ground state (FM bcc), $\Delta E_\mathrm{Bain}$: energy barrier (meV/atom) between fcc and bcc phase along Bain-path, $B$, $B'$: bulk modulus (GPa) and its pressure derivative, $c_{ij}$: elastic constants (GPa).

| | PAW GGA-DFT This work | Literature | Simonelli Ref. [62] | Ackland Ref. [63] | Mendelev Ref. [66] | Dudarev Ref. [67] | ABOP |
|---|---|---|---|---|---|---|---|
| Dimer | | | | | | | |
| $r_\mathrm{b}$ | | 2.02[a] | 2.11 | 2.35 | 2.19 | 2.24 | 2.29 |
| $E_\mathrm{b}$ | | 1.04[b], 1.14[c] | 4.12 | 2.86 | 3.01 | 4.44 | 1.50 |
| $\omega_0$ | | 299[d] | 350(10) | 293 | 305(5) | 510(10) | 239 |
| Diamond ($Fd\bar{3}m$), non-magnetic | | | | | | | |
| $V$ | 14.31 [14.74] | | 21.70 | 23.46 | 19.82 | 24.17 | 21.45 |
| $a_0$ | 4.856 [4.904] | | 5.578 | 5.726 | 5.413 | 5.783 | 5.557 |
| $\Delta E$ | 1.17 | | 1.43 | 1.69 | 1.42 | 1.48 | 2.13 |
| Simple Cubic ($Pm\bar{3}m$), ferromagnetic | | | | | | | |
| $V$ | 13.26 [13.66] | | 13.42 | 12.79 | 11.27 | 10.89 | 14.13 |
| $a_0$ | 2.367 [2.390] | | 2.376 | 2.339 | 2.24 | 2.216 | 2.417 |
| $\Delta E$ | 0.75 | | 0.80 | 1.08 | 0.71 | 0.81 | 1.15 |
| Body-centered cubic ($Im\bar{3}m$), ferromagnetic | | | | | | | |
| $V$ | 11.36 [11.70] | 11.70[f] | 11.78 | 11.77 | 11.64 | 11.78 | 11.70 |
| $a_0$ | 2.832 [2.860] | 2.860[f] | 2.866 | 2.866 | 2.855 | 2.866 | 2.860 |
| $E_\mathrm{c}$ | −4.28[g] | −4.28[h] | −4.280 | −4.316 | −4.127 | −4.316 | −4.280 |
| $B$ | 189 | 169 [i] | 178 | 178 | 178 | 173 | 169 |
| $B'$ | 5.1 | | 4.5 | 4.8 | 1.5 | −1 | 4.6 |
| $c_{11}$ | 277 | 226 [i] | 242 | 243 | 243 | 243 | 225 |
| $c_{12}$ | 147 | 140 [i] | 146 | 145 | 145 | 138 | 142 |
| $c_{44}$ | 96 | 116 [i] | 112 | 116 | 116 | 122 | 126 |

*Continued on next page.*

*(continued)*

| | PAW GGA-DFT This work | Literature | Simonelli Ref. [62] | Ackland Ref. [63] | Mendelev Ref. [66] | Dudarev Ref. [67] | ABOP |
|---|---|---|---|---|---|---|---|
| Face-centered cubic ($Fm\bar{3}m$), anti-ferromagnetic | | | | | | | |
| $V$ | 10.55 [10.87] | 11.30[f] | 12.07 | 12.45 | 12.24 | 11.74 | 11.77 |
| $a_0$ | 3.482 [3.516] | 3.562[f] | 3.641 | 3.680 | 3.658 | 3.608 | 3.611 |
| $\Delta E$ | 0.11 | 0.06[j] | 0.026 | 0.054 | 0.121 | 0.086 | 0.030 |
| $\Delta E_{\mathrm{Bain}}$ | | 45 [l] | 4 | 8 | 0.7 | 12 | 36 |
| $B$ | 199 | 133[k] | 140 | 144 | 49 | 130 | 164 |
| $B'$ | 5.5 | | 5.9 | 1.0 | 11 | 4.9 | 4.6 |
| $c_{11}$ | 309 | 154[k] | 160 | 187 | 67 | 175 | 204 |
| $c_{12}$ | 152 | 122[k] | 130 | 121 | 40 | 108 | 144 |
| $c_{44}$ | 201 | 77 [k] | 101 | 98 | 10 | 99 | 101 |
| Hexagonal close-packed ($P6_3/mmc$), non-magnetic | | | | | | | |
| $V$ | 10.18 [10.48] | | 12.07 | 12.43 | 12.24 | 11.75 | 11.77 |
| $a_0$ | 2.459 [2.484] | | 2.574 | 2.600 | 2.607 | 2.552 | 2.555 |
| $c/a$ | 1.58 | | 1.633 | 1.633 | 1.595 | 1.633 | 1.63 |
| $\Delta E$ | 0.06 | | 0.026 | 0.054 | 0.117 | 0.086 | 0.027 |

[a] Ref. [79]
[b] Ref. [80]
[b] Ref. [82]
[d] Ref. [83]
[e] Ref. [81]
[f] Ref. [78] Lattice constant extrapolated to 0 K.
[g] Value taken from experimental data.
[h] Ref. [84]
[i] Ref. [85]
[j] Ref. [86]
[k] Ref. [87] From phonon dispersion measurement at 1428 K.
[l] Ref. [88]

Dudarev potential to the Birch-Murnaghan equation of state reveals, however, a negative pressure derivative of the bulk modulus, which implies that an expansion of the bcc crystal from the equilibrium volume requires a higher energy than a compression. As shown in Sec. 3.4.4, the Dudarev potential consequentially possesses a negative expansion coefficient.

In the case of $\gamma$-iron, all potentials produce too high equilibrium atomic volumes. The ABOP (11.77 $\mathrm{Å}^3$) and the Dudarev (11.74 $\mathrm{Å}^3$) potential are closest to the reference value of 11.30 $\mathrm{Å}^3$. Also, only in the case of the Dudarev potential, the fcc structure has an at least slightly lower atomic volume than the bcc structure. In contrast, the Ackland (12.45 $\mathrm{Å}^3$) and Mendelev (12.24 $\mathrm{Å}^3$) potentials severely overestimate the atomic volumes. Here it is to be said that Mendelev *et al.* used a reference value of 3.6583 Å for the lattice constant of fcc iron at zero Kelvin, obtained from first-principles calculations performed as a part of their work in Ref. [66]. This value is, however, already larger than experimental results for

the lattice constant of $\gamma$-iron at room temperature (3.569 Å, see Ref. [78] and references therein).

The elastic constants of $\gamma$-iron predicted by the ABOP are 20 % to 30 % higher than the reference values extracted from phonon dispersion measurements at 1428 K [87]. On the other hand, the elastic constants remain markedly below the values obtained from DFT calculations. Considering the expected softening of the crystal at elevated temperatures, and taking into account that GGA-DFT calculations tend to overestimate the elastic constants of iron, it is reasonable to obtain elastic constants that lie between the high temperature experimental values and the *ab initio* data. Apart from the Mendelev potential, the EAM potentials also yield fcc elastic constants of roughly the same magnitude. The elastic constants of the Mendelev potential are undoubtedly too low. With a $c_{44}$ of only 10 GPa, the fcc structure is almost mechanically unstable.

The structural energy difference $\Delta E$ between fcc and bcc iron predicted by the potentials ranges from 0.026 eV/atom (Simonelli) and 0.030 eV/atom (ABOP) up to 0.121 eV/atom for the Mendelev potential. During the fitting process of the potentials, different strategies for determining $\Delta E$ have been applied. Consequentially, the significance of the final value for $\Delta E$ varies between the potentials. In the Simonelli and Ackland potentials, $\Delta E$ was not explicitly considered but merely served to render the bcc phase the ground state structure, i.e. care was taken that $\Delta E$ assumed a reasonably positive value. On the other hand, in the case of the Mendelev and Dudarev potentials, $\Delta E$ has been fitted to *ab initio* calculations, eventually leading to markedly higher values.* Finally, as discussed in Sec. 3.4.3, during the fitting process of the ABOP, $\Delta E$ is considered as an adjustable parameter providing the necessary flexibility to the effective energy function for reproducing the bcc to fcc phase transition in real iron. In consequence, the final value of $\Delta E = 0.03$ eV/atom is significantly lower than the reference value from DFT calculations (0.11 eV/atom), as well as the value estimated by a thermodynamic assessment of the Fe phase diagram (0.06 eV/atom) [86].

For the hcp structure, all potentials produce the same atomic volume as for the fcc structure. This represents a deviation from the total energy calculations, which yield an atomic volume that is smaller than in the case of fcc. Apart from the Dudarev potential, the atomic volume of the hcp structure is furthermore higher than the atomic volume of the bcc structure. Therefore, the hcp structure is not correctly reproduced as the high pressure equilibrium phase at 0 K. Instead, a negative pressure is required for realizing a transition

*The energy difference between the fcc and bcc structures of the Dudarev Fe potential calculated in this work and listed in Tab. 3.2 differs from the value given in Table 1 of Ref. [67]. It is however consistent with the energy difference extracted from Fig. 4 of Ref. [67]. It therefore appears that Table 1 of Ref. [67] does not contain the properties of the final parametrization of the Fe EAM potential.

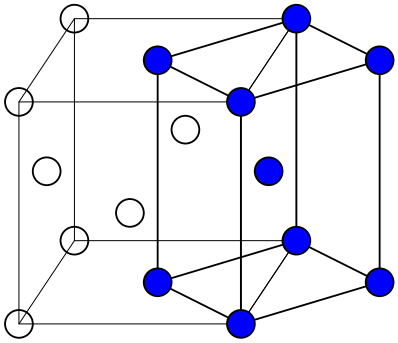

**Figure 3.4:** *Geometrical correlation between the fcc and bcc unit cells. The fcc structure (open circles) can be regarded as a tetragonally distorted bcc structure (filled circles) with an axial ratio of* $c/a = \sqrt{2}$.

from the bcc to the hcp phase. Also, the DFT calculations predict that, at zero Kelvin, the hcp structure is more stable than the fcc structure. Only the ABOP and the Mendelev potential yield cohesive energies for the fcc and hcp phases that are in consistency with this finding. For the remaining potentials, cohesive energies for fcc and hcp are identical.

At lower coordination, all potentials perform reasonably well in reproducing the cohesive energy and lattice constant of the sc structure. In contrast, for the diamond structure, all potentials significantly overestimate the lattice constant on one hand but underestimate the cohesive energy on the other hand. As previously discussed for the fcc and bcc structures, magnetic effects have an important influence on the cohesive energy and bond length. Considering the multiple changes of magnetic ground state in the DFT data when proceeding from high coordination up to the diamond structure, it is understandable that the potentials cannot grasp all the resulting effects and the deviations at low coordination are acceptable.

### Bain-path

As shown in Fig. 3.4, the bcc lattice can be regarded as a tetragonally distorted fcc lattice and vice versa. A possible transformation path from the bcc to the fcc structure is therefore the uniaxial expansion of the bcc unit cell along a [100] direction, which is also known as the Bain-path. In Fig. 3.5, the energetics of this transformation predicted by the analytic potentials is compared with results from GGA-DFT calculations on ferromagnetic iron taken from Ref. [88]. Fig. 3.5 visualizes the previously discussed energy differences between the fcc and bcc structures predicted by the analytic potentials. Furthermore, the energy barrier $\Delta E_{\mathrm{Bain}}$ that has to be overcome for a transition from fcc to bcc along the Bain-path can be extracted. The value for $\Delta E_{\mathrm{Bain}}$ estimated by the DFT calculations is 45 meV/atom. With $\Delta E_{\mathrm{Bain}}$=36 meV/atom, the ABOP is closest to this reference value. In contrast, all EAM potentials predict significantly lower transition barriers. The smallest barrier is

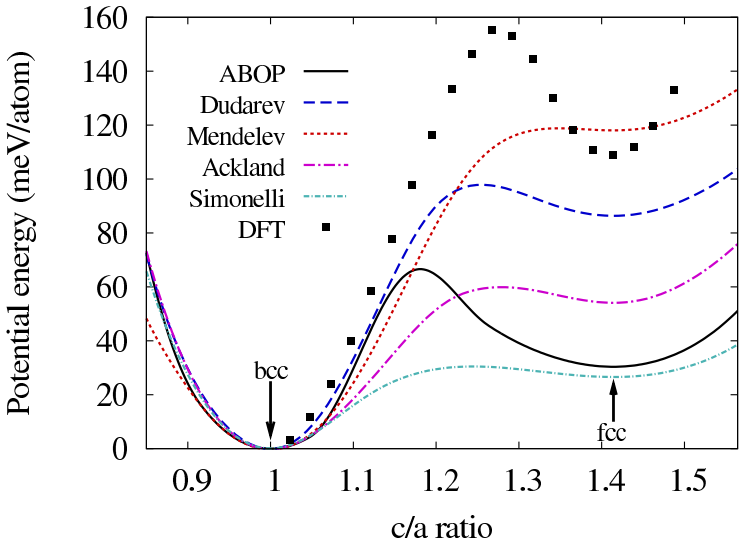


**Figure 3.5:** *Bain-path between fcc and bcc iron. The energy scale is relative to the ground state bcc structure of the respective potentials. Data from DFT calculations is taken from Ref. [88].*

given by the Mendelev potential, where $\Delta E_{\mathrm{Bain}}$ is less than 1 meV/atom. In this case, the transition requires almost no activation, making the fcc phase extremely unstable.

An apparent difference in the Bain-paths plotted in Fig. 3.5 is the much higher curvature of the local fcc minimum obtained from DFT calculations as compared to the ABOP. For small tetragonal distortions of a cubic lattice, the curvature of the energy-strain curve is proportional to the elastic constant $C'$, with $C' = (c_{11} - c_{12})/2$. GGA-DFT calculations predict a much higher $C'$ than justifiable by the experimental data on elastic constants of $\gamma$-iron (see Tab. 3.2). In contrast, $C'$ obtained from the ABOP is in reasonable agreement with the experimental data. The low curvature of the fcc minimum of the ABOP therefore appears to be more realistic. For the same reason, obtaining a somewhat smaller barrier $\Delta E_{\mathrm{Bain}}$ than the GGA-DFT reference value also seems to be reasonable.

### Melting properties and thermal expansion

For determining the melting point of Fe at zero pressure, molecular dynamics simulations of a solid-liquid interface in the $N$,$P$=0,$T$ ensemble have been performed. For different temperatures around the expected melting point, the position of the solid-liquid interface was monitored and the actual melting temperature was found for zero velocity of the interface, i.e. when the volume fractions of the solid and liquid phases remain constant over the simulation time of 0.5 ns. The melting point for the ABOP estimated by this method is 2270(20) K, which is distinctly higher than the experimental value of 1811 K [60]. The Ackland and Dudarev potentials give a similar overestimation of the melting

**Table 3.3.:** *Comparison of thermal, surface and stacking-fault properties of bcc and fcc Fe as obtained from analytic potentials with literature data. Errors are given in round brackets.* $T_m$*: melting point (K),* $\alpha_L$*: coefficient of linear thermal expansion (*$10^{-6}$*/K),* $\gamma_{(hkl)}$*: energy of* $(hkl)$*-surface (meV/Å*$^2$*),* $\gamma^{\mathrm{USF}}_{(hkl)[uvw]}$*: relaxed unstable stacking-fault energy for* $(hkl)[uvw]$ *slip system (J/m*$^2$*).*

| | Literature | | Simonelli | Ackland | Mendelev | Dudarev | ABOP |
|---|---|---|---|---|---|---|---|
| | Experiment | Theory | | | | | |
| $T_m$ | 1811[a] | | 1910(20) | 2340(20) | 1760(30) | 2160(20) | 2270(20) |
| Body-centered cubic ($Im\bar{3}m$) | | | | | | | |
| $\alpha_L$(RT) | 11.8[b] | | 8.4 | 9.4 | 8.4 | −6.0 | 2.1 |
| $\gamma_{(100)}$ | 150[c] | 143[d] | 102 | 113 | 111 | 112 | 104 |
| $\gamma_{(110)}$ | 150[c] | 142[d] | 90 | 99 | 103 | 101 | 85 |
| $\gamma_{(111)}$ | 150[c] | 157[d] | 112 | 125 | 125 | 125 | 115 |
| $\gamma_{(211)}$ | 150[c] | | 103 | 114 | 118 | 116 | 104 |
| $\gamma^{\mathrm{USF}}_{(010)[001]}$ | | 1.87[e], 1.79[f] | 2.09 | 2.35 | 1.85 | 2.20 | 2.15 |
| $\gamma^{\mathrm{USF}}_{(110)[001]}$ | | 1.43[e], 1.40[f] | 1.76 | 2.22 | 1.75 | 2.05 | 1.93 |
| $\gamma^{\mathrm{USF}}_{(110)[1\bar{1}1]}$ | | 0.59[e], 0.47[f] | 0.74 | 0.90 | 0.66 | 0.90 | 0.90 |
| Face-centered cubic ($Fm\bar{3}m$) | | | | | | | |
| $\alpha_L$(RT) | 24.5[g] | | 9.0 | 2.0 | | | 10.5 |
| $\alpha_L$(1500 K) | 23.3[g] | | 10.1 | 6.9 | | | 7.7 |
| $\gamma_{(100)}$ | | | 94 | 104 | 98 | 102 | 103 |
| $\gamma_{(110)}$ | | | 102 | 112 | 107 | 109 | 115 |
| $\gamma_{(111)}$ | | | 82 | 88 | 90 | 90 | 87 |

[a] Ref. [60]
[b] Ref. [85]
[c] Liquid surface tension measurements, Ref. [89].
[d] Ref. [90]
[e] spin-polarized LDA, Ref. [91]
[f] spin-polarized GGA, Ref. [91]
[g] Ref. [78]

point, only the Simonelli and Mendelev potentials produce melting temperatures of the correct magnitude.

The room temperature (RT) linear expansion coefficient $\alpha_L$ of bcc iron predicted by the Simonelli, Ackland and Mendelev EAM potentials is lower, but reasonably close to the experimental value of $11.8 \times 10^{-6}\,1/\mathrm{K}$ [85]. In accordance with a negative pressure derivative of the bulk modulus (see Tab. 3.2), the Dudarev potential possesses a negative linear thermal expansion coefficient of $-6\times10^{-6}\,1/\mathrm{K}$. The ABOP features a rather low $\alpha_L$ of only $2.1\times10^{-6}\,1/\mathrm{K}$. This shortcoming of the ABOP is a compromise that has to be accepted for fitting the potential to the bcc to fcc phase transition. Preliminary parameterizations of the Fe potential having a higher fcc to bcc energy difference $\Delta E$ than the final potential, and consequently not showing a transition between the two phases, displayed expansion coefficients closer to the experimental value. A reduction of $\Delta E$, while remaining in the same region of parameter space is then observed to be accompanied by a lowering of $\alpha_L$.

The expansion coefficient for $\gamma$-iron has been evaluated at RT and 1500 K, the last temperature lying within the stability region of the fcc phase. Compared to the experimental values, the potentials underestimate the thermal expansion by more than a factor of two. Interestingly, in qualitative agreement with experiment [78], the ABOP shows a smaller expansion coefficient for $\gamma$-iron at high temperatures than at room temperature.

A deficiency of the potentials by Dudarev and Mendelev in describing fcc iron is revealed when simulating the fcc structure at finite temperatures. At temperatures as low as 200 K, the fcc structure does not remain stable. Instead, a transition to a twinned bcc structure is observed after just a few picoseconds. In consequence, thermal properties of the fcc phase cannot be evaluated for these potentials. In general, such a behavior would not present a failure of the potentials, if restricted to the low temperature regime where the bcc phase is the thermodynamically stable phase in the real iron system. The instability of the fcc phase remains, however, intact up to the respective melting points of the potentials. In the case of the Mendelev potential, this instability can be explained both by the low elastic constants of the fcc structure (see Tab. 3.2) as well as by the almost non-existent barrier between the fcc and bcc phases when following the Bain-path (see Fig. 3.5). Instead, the Dudarev potential possesses a distinctive barrier of 12 meV in the Bain-path. This barrier is larger than in the case of the Simonelli and Ackland potentials, both showing a thermally stable fcc structure. The Bain-path does therefore not provide an explanation for the thermal instability of the fcc structure in the Dudarev potential. Also, the elastic constants of the fcc phase are reasonably high and do not give an indication for an instability. The energy function of the Dudarev potential therefore has to provide another artificially low energy path connecting the fcc phase with the bcc phase.

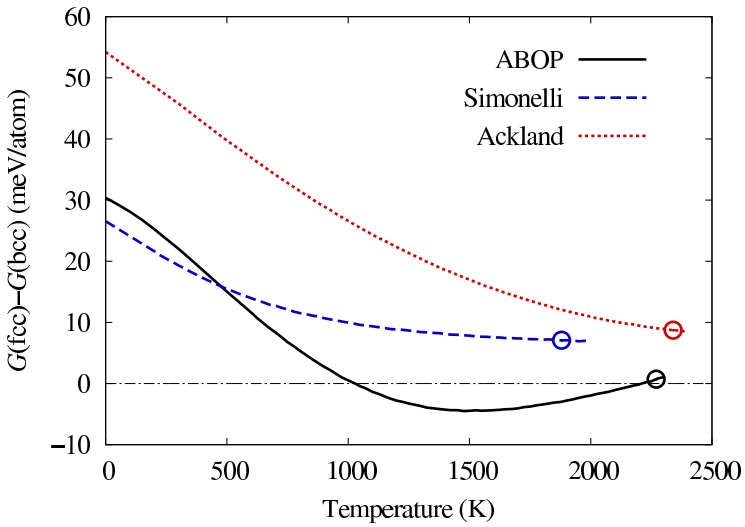


**Figure 3.6:** *Gibbs free energy difference between the fcc and bcc phases of iron, as obtained from different interatomic potentials. Open circles indicate the melting points of the respective potentials.*

### BCC to FCC phase transition

Whether the analytic iron potentials reproduce the bcc $\alpha$-iron to fcc $\gamma$-iron phase transition has been examined by calculating the fcc to bcc Gibbs free energy difference up to the melting point of the respective potentials. As described in Appendix A, Gibbs free energies of both phases at a temperature $T_0$ can be determined by the coupling parameter method [33]. The temperature dependence of the Gibbs free energy is then obtained by integrating the Gibbs-Helmholtz equation.

The lack of a thermally stable fcc phase makes these calculations redundant for both the Mendelev and Dudarev potentials. For the remaining potentials, the fcc to bcc Gibbs free energy difference $\Delta G$ is plotted in Fig. 3.6. Starting from the respective 0 K structural energy difference $\Delta E$, all potentials feature an initial decrease of $\Delta G$ with increasing temperature. However, a bcc to fcc phase transition is absent for both the Simonelli and the Ackland EAM potentials, with $\Delta G$ remaining positive up to the melting temperature.

In the case of the Ackland potential Gibbs free energy calculations have already been published by Lopasso and coworkers in Ref. [92]. The same methods for calculating free energies as in the present work were used, only with the coupling parameter method implemented in a MD instead of a Monte Carlo (MC) simulation. Their results slightly differ from the calculations performed in this work: The calculations of Lopasso *et al.* do predict the presence of a bcc to fcc transition at 2343 K, located just below the somewhat higher melting temperature of 2396 K found by their method. However, applying their increased melting temperature to the $\Delta G$ curve in Fig. 3.6 would still not give rise to a thermodynamic stability of fcc iron from the present calculations. According to the Gibbs free energy calculations performed in this work, the Ackland potential gives a $\Delta G$ that is still

larger than 8 meV/atom at 2400 K. As described in the appendix, by double checking the results, any presence of systematic errors in the implementation of the coupling parameter method or the integration of the Gibbs-Helmholtz equation in this work can be ruled out. In contrast, a possible source for the discrepancies between both calculations can be finite size effects. In Ref. [92], the simulation cells consist of 686 atoms for the bcc structure and 500 atoms for the fcc structure. The simulations in the present work are performed with 1024 atoms for the bcc structure and 1008 atoms for the fcc structure. However, it should be noted that an analysis of finite size effects performed as part of this work gives a difference of less than 1 meV/atom for $\Delta G$ at 2100 K when applying both sets of cell sizes. Finite size effects might, however, be of a different magnitude in an MD implementation of the coupling parameter method, as done in Ref. [92].

The same authors also recently published calculations of Gibbs free energies for the Simonelli EAM potential [93]. Here, they find in agreement with the present results that the bcc phase remains the stable solid phase up to the melting point. The melting point obtained from their Gibbs free energy calculations of 2103 K is, however, significantly higher than the value found by the solid-liquid interface method of 1910(20) K. Also, their finding that the fcc structure is thermally unstable in simulations above room temperature (identical to the thermal instability of fcc iron found for the Mendelev and Dudarev potentials) cannot be confirmed from the simulations of the present work. The sources for these discrepancies remain unclear.

As shown in Fig. 3.6, only the ABOP succeeds in reproducing the alternating phase stability of bcc and fcc iron. Here, the bcc to fcc phase transition is located at 1030 K, which is in good agreement with the real transition temperature of 1184 K [60]. A remarkable feature of the ABOP is furthermore the rise of $\Delta G$ at temperatures above 1500 K. This increase eventually leads to a stabilization of the bcc over the fcc phase again at 2210 K, just before the potential reaches its melting point at 2270 K. This behavior is consistent with the $\gamma$-iron to $\delta$-iron phase transition in the real iron system, located however at 1665 K [60].

The contributions of entropy and enthalpy to the temperature evolution of $\Delta G$ are plotted in Fig. 3.7, in comparison with data obtained from a thermodynamic assessment of the iron phase diagram [86]. The 0 K structural energy difference between fcc and bcc iron of $\Delta E$=60 meV/atom obtained by the latter method is twice as high as the value from the ABOP. For a better visualization of the general trends obtained from both methods, all energies in Fig. 3.7 are therefore scaled by a factor $1/\Delta E$. For the absolute values, see Fig. 3.3 and Ref. [86]. The qualitative agreement between both methods is remarkable. The ABOP not only reproduces the phase transitions in itself, but also the correct

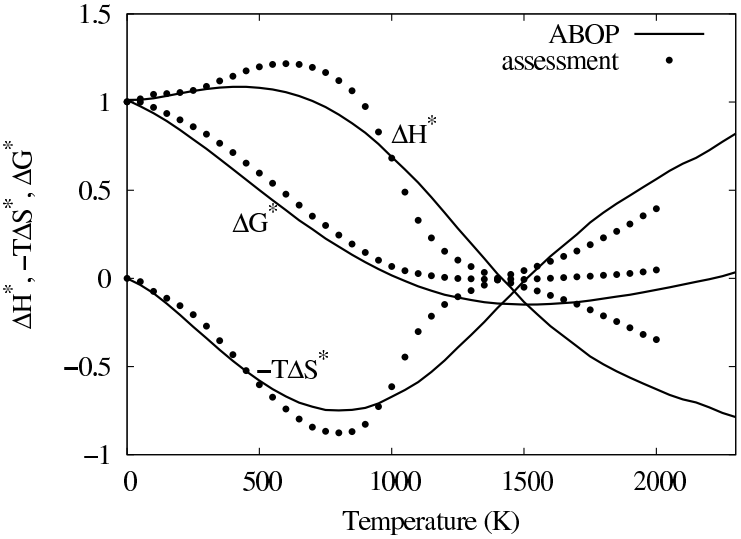


**Figure 3.7:** *Variation of reduced enthalpy, entropy and Gibbs free energy difference between fcc and bcc iron with temperature, as obtained from the ABOP and from a thermodynamic assessment of the Fe phase diagram [86]. For better qualitative comparison, all energies are scaled by the reciprocal 0 K structural energy difference between the fcc and bcc phases.*

ratios of the entropy and enthalpy contributions to $\Delta G$: After a slight increase at lower temperatures, the enthalpy difference $\Delta H$ decreases up to the melting point, eventually becoming negative. At the $\alpha$ to $\gamma$ transition temperature, however, $\Delta H$ preserves a positive value. Instead, it is the excess of entropy of the fcc phase that accounts for the phase transition. After an initial decrease, the entropy contribution $-T\Delta S$ reaches a minimum around 800 K and finally assumes positive values at temperatures above 1500 K. Again, it is this contribution to $\Delta G$ that overcompensates the negative $\Delta H$, leading to the renewed stability of the bcc phase in the temperature regime just below the melting point.

The excellent performance of the ABOP in reproducing the alternating relative thermodynamic stabilities of the bcc and fcc phases shows that analytic interatomic potentials can be successfully applied for describing complicated systems. Care must, however, be taken to identify shortcomings of the potential function in describing all contributions to energy and entropy present in the real system. As is shown in the present case of magnetic iron, a compensation of missing contributions is possible by regarding the potential as an effective energy function, which requires a consistent scaling of structural energy differences.

### Surfaces and stacking-faults

The energies of planar defects like low index surfaces and stacking-fault configurations obtained from the ABOP and EAM potentials are compared with reference values from experiment and theory in Tab. 3.3.

The different potentials produce very similar results for the relaxed low-index surface energies of bcc, as well as fcc iron. For bcc iron, surface energies are available both from

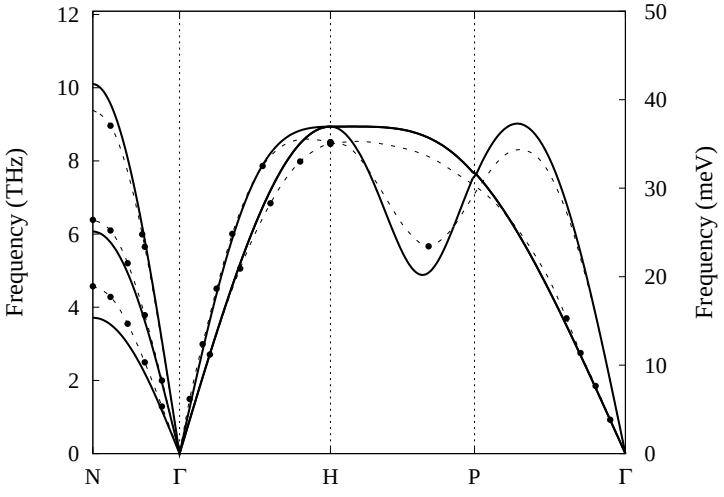


**Figure 3.8:** *Phonon dispersion of bcc $\alpha$-Fe as calculated from the ABOP potential developed in this work. Black dots denote experimental data points [94].*

experiment [89] and theory [90]. Compared to these reference values, it is evident that the surface energies of the potentials are on average 30–40 % too small.

The unstable generalized stacking fault energy $\gamma^{\mathrm{USF}}$ has been examined for different slip systems. The fault energies are in good overall agreement with data from first-principles calculations [91]. The lowest activation for slip is found in the $(110)[1\bar{1}1]$ system. However, all potentials overestimate the value for the respective $\gamma^{\mathrm{USF}}$.

### Phonon dispersions

The phonon dispersions for bcc as well as fcc Fe predicted by the ABOP are shown in figures 3.8 and 3.9 together with data points from experiment [87, 94]. An inspection of Fig. 3.8 reveals an excellent agreement of the bcc phonon dispersion with the reference data.

The phonon dispersion of fcc iron has been measured at 1428 K [87]. For consistency, the phonon dispersion of fcc iron of the ABOP has been calculated at the 1428 K atomic volume of 12.27 $\mathrm{Å}^3$/atom. As shown in Fig. 3.9, the phonon frequencies are somewhat higher than the experimental reference data. This difference can be attributed to the fact that the phonon softening is underestimated because of the weak lattice expansion predicted by the potential.

Not shown are the phonon dispersions of the EAM potentials. In general, all EAM potentials perform well in reproducing the phonon dispersion of the bcc phase. Also, similar to the ABOP, higher phonon frequencies than in the 1428 K reference data are found for the fcc phase. The only exception is the Mendelev potential, where, in line with the low elastic constants, phonon frequencies of the fcc phase are significantly underestimated.

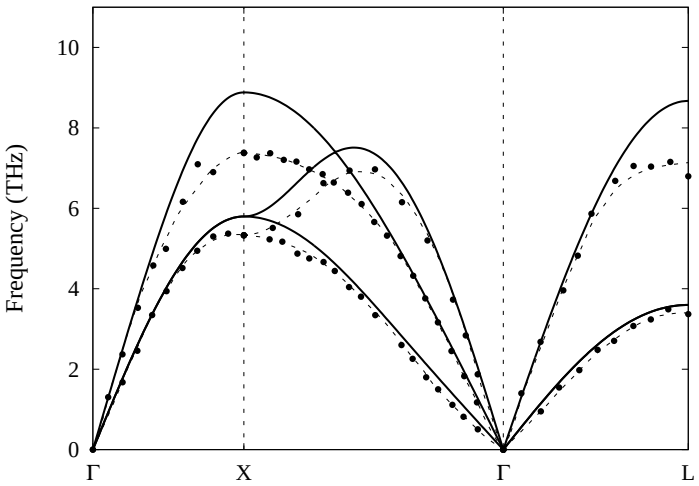


**Figure 3.9:** *Phonon dispersion of fcc $\gamma$-Fe as obtained from the ABOP at the 1428 K atomic volume of 12.27 Å$^3$/atom. Black dots denote experimental data points measured at 1428 K [87].*

### Point Defects

Properties of point defects in bcc and fcc iron as predicted by the analytic potentials are listed in Tab. 3.4, together with reference values from literature.

**Static properties** *BCC $\alpha$-iron:* The bcc vacancy formation energies of all potentials considered in this work lie roughly within the scattering range of the experimental data between 1.59 and 1.89 eV [60], with the ABOP (1.56 eV) marking the lower and the Dudarev (1.86 eV) potential marking the upper boundary.

The energetic ordering of self-interstitial (SI) configurations represents a peculiarity of the bcc Fe system compared to other bcc transition metals [104]. In consistency with experimental findings [60], *ab initio* calculations predict the $\langle 110 \rangle$ dumbbell configuration as the most stable SI defect in bcc iron [95, 96]. Both calculations concordantly estimate the energy difference to the next stable $\langle 111 \rangle$ dumbbell configuration to be 0.7 eV. With the *ab initio* data at hand, the more recent Fe EAM potentials by Mendelev and Dudarev have been fitted to reproduce these interstitial properties [66, 67]. Both potentials yield the $\langle 110 \rangle$ as the most stable configuration with the formation energy close to the reference values. The energy difference to the $\langle 111 \rangle$ dumbbell is 0.5 and 0.6 eV, respectively. The Ackland potential also reproduces the correct ordering of interstitial configurations, the formation energies are however significantly higher than the *ab initio* data. Finally, the Simonelli potential falsely predicts the $\langle 111 \rangle$ dumbbell as the energetically most favorable configuration.

Regarding energetics only, the Dudarev EAM potential seems to provide a good description of SI defects. However, this potential yields negative formation volumes for all

**Table 3.4.:** *Comparison of point defect properties of bcc and fcc Fe as obtained from analytic potentials with literature data. Curly brackets denote values taken from the original publications deviating from the present calculations. $\Delta E_v^f$: vacancy formation energy (eV), $\Delta V_v$: vacancy relaxation volume (in units of atomic volume), $\Delta E_v^m$: vacancy migration energy, $\Delta E_i^f$: interstitial formation energy (eV), $\Delta V_i^f$: formation volume of the lowest energy interstitial (in units of atomic volume), $\Delta E_i^m$: interstitial migration energy (eV), $E^{\mathrm{d}}_{\langle uvw\rangle}$: threshold displacement energy in direction $\langle uvw\rangle$ (eV), $E^{\mathrm{d}}_{\mathrm{av}}$: threshold displacement energy averaged over all directions (eV),*

| | Literature | | Simonelli | Ackland | Mendelev | Dudarev | ABOP |
|---|---|---|---|---|---|---|---|
| | Experiment | Theory | | | | | |
| Body-centered cubic ($Im\bar{3}m$) | | | | | | | |
| $\Delta E_v^f$ | 1.59 – 1.89[a] | | 1.63 | 1.70 | 1.71 {1.84} | 1.86 {1.97} | 1.56 |
| $\Delta V_v$ | | | −0.19 | −0.18 | −0.23 | −0.41 | −0.37 |
| $\Delta E_v^m$ | 0.55 [a] | | 0.46 | 0.63 | 0.47 | 0.58 | 0.57 |
| $\Delta E^f_{i,\langle 110\rangle}$ | | 3.41[b], 3.64[c] | 3.67 | 4.87 | 3.50 | 3.65 | 4.19 |
| $\Delta E^f_{i,\langle 111\rangle}$ | | 4.11[b], 4.34[c] | 3.54 | 5.01 | 3.99 | 4.24 | 4.59 |
| $\Delta E^f_{i,\langle 100\rangle}$ | | 4.37[b], 4.64[c] | 4.57 | 6.10 | 4.32 | 4.58 | 5.51 |
| $\Delta V_i^f$ | 1.1[a] | | 0.2 | 0.76 | 0.22 | −0.57 | 0.37 |
| $\Delta E_i^m$ | 0.25 – 0.30[a] | | 0.03 | 0.04 | 0.18 | 0.15 | 0.17 |
| $E^{\mathrm{d}}_{\langle 100\rangle}$ | 17[d], 20[e] | | 15[f g] | 17[f] | 15[f] | | 15[h] |
| $E^{\mathrm{d}}_{\langle 110\rangle}$ | >30[d], 30[e] | | 27[f g] | 31[f] | 27[f] | | 23[h] |
| $E^{\mathrm{d}}_{\langle 111\rangle}$ | 20[d] | | 19[f g] | 35[f] | 25[f] | | 19[h] |
| $E^{\mathrm{d}}_{\mathrm{av}}$ | | | 42.4[f g] | 44.8[f] | 36.9[f] | | 36.7[h] |
| Face-centered cubic ($Fm\bar{3}m$) | | | | | | | |
| $\Delta E_v^f$ | 1.71[i] | | 1.78 | 1.92 | 1.75 | 1.95 | 1.92 |
| $\Delta V_v^f$ | | | −0.11 | +0.91 | −0.37 | −0.10 | −0.26 |
| $\Delta E_v^m$ | | | 0.27 | 0.30 | | | 0.32 |
| $\Delta E^f_{i,\langle 100\rangle}$ | | | 3.18 | 3.63 | | 3.03 | 3.35 |
| $\Delta E^f_{i,\langle 111\rangle}$ | | | 3.28 | 3.85 | | 2.98 | 3.80 |
| $\Delta V_i^f$ | | | 0.38 | 0.10 | | 0.56 | 0.58 |
| $\Delta E_i^m$ | | | 0.13 | 0.21 | | | 0.40 |

[a] Ref. [60]
[b] Ref. [95]
[c] Ref. [96]
[d] Ref. [97]
[e] Ref. [98]
[f] Ref. [99]
[g] Repulsive part by Becquart *et al.*, Ref. [100, 101].
[h] Ref. [102]
[i] Ref. [103]

interstitial configurations considered. This finding puts into question whether this potential is able to give a physically meaningful description of the relaxation properties.

The ABOP developed in the present work reproduces the correct ordering of SI configurations. With 4.19 eV, the formation energy of the ⟨110⟩ dumbbell is somewhat higher than the reference values of 3.41 (Ref. [95]) or 3.64 eV (Ref. [96]), but still lower than the value obtained from the Ackland potential. The energy difference to the ⟨111⟩ dumbbell is 0.4 eV. For the ⟨110⟩ dumbbell, the ABOP yields an SI formation volume of 0.37 atomic volumes.

*FCC $\gamma$-iron:* For fcc iron, experimental data is only available for the vacancy formation energy, which has been determined by Kim and Buyers by positron annihilation spectroscopy [103]. Their result for the formation energy is 1.71 eV. The magnitude of this value is well reproduced by all Fe potentials.

For SI defects in fcc iron, the ABOP as well as the Simonelli and Ackland potentials predict the ⟨100⟩ dumbbell as the lowest energy configuration. In contrast, with the Dudarev potential the ⟨111⟩ dumbbell has a slightly lower energy than the ⟨100⟩ dumbbell. The SI formation energy predicted by the potentials varies between 2.98 eV and 3.63 eV, with the ABOP lying in the middle of this interval. For the Mendelev potential, the fcc structure does not remain stable when inserting a SI atom and no values can be given.

**Dynamic properties** The diffusivity of point defects has been calculated using MD simulations and monitoring the mean square displacement over an extended temperature range. The simulations were carried out in the $N, V, E$ ensemble, because the scaling of velocities and positions by the utilization of thermostats and barostats can falsify the dynamics of the atoms. Therefore, for each temperature, the size of the simulation box was first equilibrated in a $N$,$P$=0,$T$ ensemble calculation. Fixed at the equilibrated volume, the kinetic energy of the atoms was then equilibrated in a $N, V, T$ run. Finally, the mean square displacements $\langle R^2 \rangle$ were followed over a period of time $\tau$ in the $N, V, E$ ensemble. The diffusivity $D$ is given by the Einstein-Smoluchowski equation in three dimensions $\langle R^2 \rangle = 6D\tau$. Migration energies have been obtained by fitting Arrhenius laws to the accumulated diffusivity data. Exemplarily, the diffusivities of the ABOP are plotted in Fig. 3.10.

*BCC $\alpha$-iron:* The vacancy migration energy $\Delta E_v^m$ in bcc Fe obtained by this method is 0.57 eV for the ABOP, in perfect agreement with the experimental value of 0.55 eV. The vacancy migration energies of the EAM potentials have approximately the same magnitude, the Simonelli potential (0.46 eV) giving the lowest and the Ackland potential (0.63 eV) giving the highest values. The migration energies obtained by the dynamical method are significantly lower than the values given by the authors of the EAM potentials in

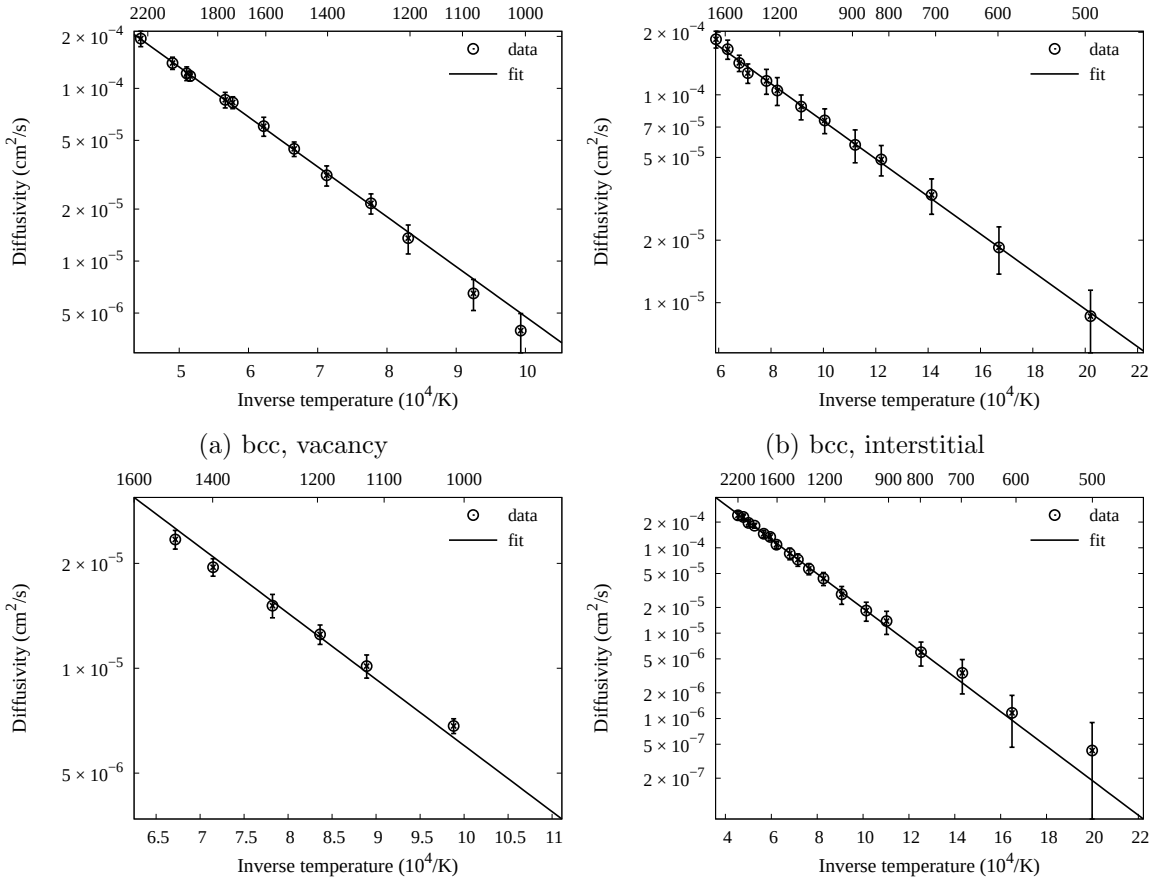


(a) bcc, vacancy (b) bcc, interstitial

(c) fcc, vacancy (d) fcc, interstitial

**Figure 3.10.:** *Temperature dependence of vacancy and interstitial diffusivities in bcc and fcc iron as predicted by the analytic bond-order potential for iron developed in this work. The simulations were carried out in the $N, V, E$ ensemble using periodic cells containing one defect in $8 \times 8 \times 8$ or $7 \times 7 \times 7$ unit cells for bcc and fcc, respectively.*

the respective publications (0.78 eV, 0.62 eV and 0.84 eV, for the Ackland, Mendelev and Dudarev potential). The reason for this is that in the original publications, $\Delta E_v^m$ has been determined by employing purely static calculations, where an atom is displaced from its original position to the position of the vacancy and the maximum energy along this path is taken as the migration barrier. It is noteworthy that the dynamical approach for calculating $\Delta E_v^m$ is usually more reliable and, in the present case, consistently leads to a better agreement with experiment for all potentials.

For the migration energy of SI atoms in bcc iron, the Simonelli and Ackland potentials give very low values of only 0.03 eV and 0.04 eV, respectively. In contrast, the Mendelev and Dudarev potentials as well as the ABOP predict higher migration energies of 0.18, 0.15 and

0.17 eV, respectively. These values are closer, but still below the experimentally determined SI migration energies of 0.25 to 0.3 eV [60]. Again, the migration energies calculated by the dynamic method are lower than those from static calculations: In Ref. [105], Willaime and coworkers calculated the migration energies for the Ackland and Mendelev potentials and obtained values of 0.18 eV and 0.31 eV, respectively.

Direction-specific threshold displacement energies needed for displacing an atom in bcc iron in order to create a stable Frenkel pair have been calculated for the Simonelli, Ackland and Mendelev potentials by Nordlund *et al.* [99]. Using the same method as in Ref. [99], the threshold displacement energies predicted by the ABOP have also been analyzed by Nordlund [102]. The results are summarized in Tab. 3.4 together with reference data from experiment [97, 98]. Although the $\langle 110 \rangle$ is somewhat underestimated, a good agreement of the ABOP with experiments is achieved: While the minimum threshold is in the $\langle 100 \rangle$ direction, a clearly higher threshold in the $\langle 110 \rangle$ than in the $\langle 111 \rangle$ direction is obtained. A similar accordance is only provided by the Simonelli potential. Note however that the latter predicts the wrong $\langle 111 \rangle$ dumbbell as the most stable interstitial configuration.

*FCC $\gamma$-iron:* Owing to the thermal instability of the fcc phase in the Mendelev and Dudarev potentials, no point defect migration parameters can be calculated for these potentials. The Simonelli and Ackland potentials as well as the ABOP show very similar behavior concerning the vacancy migration in fcc Fe. The diffusivity data is best fitted by migration energies of 0.27, 0.30 and 0.32 eV, respectively. For the SI diffusion in fcc Fe, migration energies of 0.13, 0.21 and 0.40 eV are obtained.

In summary, the ABOP provides an overall excellent description of point defects in bcc iron. The agreement with respect to static and dynamic interstitial properties is even more remarkable when considering that none of the SI properties have been used for the fitting procedure of the potential. For fcc, too little experimental data exists for a quantitative comparison of the potentials with the real $\gamma$-iron system. All potentials featuring a thermally stable fcc phase give, however, a description of point defect properties that is consistent amongst each other.

### 3.4.5. Conclusions

In conclusion, the bond-order formalism has been applied for devising an interatomic potential for iron. The new Fe ABOP provides an excellent description of iron both in the bcc and fcc phases. This marks an improvement over many analytic potentials fitted solely to the bcc structure, as these often exhibit an instability of fcc iron at elevated temperatures. Moreover, in order to mimic the magnetic contributions to phase stability in the form of

energy and entropy effects, the static lattice energy difference between bcc and fcc iron has been considered as an adjustable quantity that is used for fitting the difference in Gibbs free energies between the corresponding phases. The present ABOP therefore properly reproduces the $\alpha$–$\gamma$–$\delta$–liquid phase transition sequence in iron.

Despite these improvements, the complexity of the iron phase diagram still provides room for further enhancements. In particular, this concerns the description of the hcp phase. The higher atomic volume of the hcp structure compared to the bcc structure leads to an incorrect pressure dependence of the iron phase diagram obtained from the ABOP. Note however that, apart from the Dudarev potential, this problem holds equally true for the other EAM potentials. Also, since all potentials predict identical atomic volumes for the fcc and hcp structures, the vibrational entropy contributions to the Gibbs free energies of the fcc and hcp phases are almost identical.

In addition to the phase diagram, the new potential also performs well in describing a large variety of properties of iron in the bcc and fcc phases. The calculated phonon dispersion curves for bcc and fcc iron are in good agreement with experimental values. The formation energies of various point defects compare very well to literature data with the $\langle 110 \rangle$-interstitial as most stable configuration in bcc iron. Diffusivities obtained from MD simulations are in line with experimental results. The same holds true for the threshold displacement energy. The Bain-path exhibits an energy barrier for the fcc-bcc transition that is comparable to DFT results, while all central-force potentials considered here have a lower barrier.

# 3.5. Pt-Pt interaction: analytic bond-order potential for platinum

## 3.5.1. Introduction

In this section the parametrization of the Pt potential is developed. The fcc transition metal Pt is characterized by a very large energy penalty for stacking-fault defects, amounting to $E_{\mathrm{SF}} = 20\,\mathrm{meV/\AA^2}$ [106]. This quantity has a significant influence on the plastic behavior of Pt, as a large $E_{\mathrm{SF}}$ prevents the splitting of a dislocation into partial dislocations. Furthermore, Pt possesses a low tendency for deformation twinning, since the twinning-energy $\gamma_{\mathrm{twin}}$ is also related to $E_{\mathrm{SF}}$ by $2\gamma_{\mathrm{twin}} \approx E_{\mathrm{SF}}$ [106]. As another characteristic property of Pt, an almost isotropic elastic behavior is determined by the small ratio of the two principle shear moduli $c_{44}$ and $C' = (c_{11} - c_{12})/2$, with $c_{44}/C' = 1.47$ [107]. For short ranged interatomic potentials, reproducing a $c_{44}/C'$ smaller than two is generally challenging and can only be resolved by including angular dependencies in the energy functional [47, 108], if only next neighbor interactions are considered.

For achieving a solid description of the element Pt, the large stacking-fault energy and the small $c_{44}/C'$ have been central elements during the development of the Pt ABOP. Total-energy calculations on Pt and the procedure for fitting the potential are described in the following. Subsequently, the properties of the final parametrization are discussed and a summary is given.

## 3.5.2. Total-energy calculations

In order to extend the fitting database, density functional theory (DFT) calculations in the generalized gradient approximation (GGA) have been performed, employing the same techniques as described in Sec. 3.4.2 for the Fe potential. In the Pt calculations, the plane-wave cutoff energy was set to 299.3 eV and converged energies better than 1 meV/atom have been achieved by a typical number of 220 $k$-points in the irreducible Brillouin-zone for the fcc structure. The results of the DFT calculations on Pt are summarized in Tab. 3.6. For combining data from DFT calculations and experiment in the fitting database, all atomic volumes from DFT were again scaled by a factor that matches the values in case of the fcc structure. The scaled values are given in brackets in Tab. 3.6. When compared to experimental data [107], the elastic constants of fcc Pt are poorly described by the GGA method, being generally too small: the predicted bulk modulus is 15 % lower than the reference of 288 GPa and the $c_{44}$ shear elastic constant estimated by GGA is only

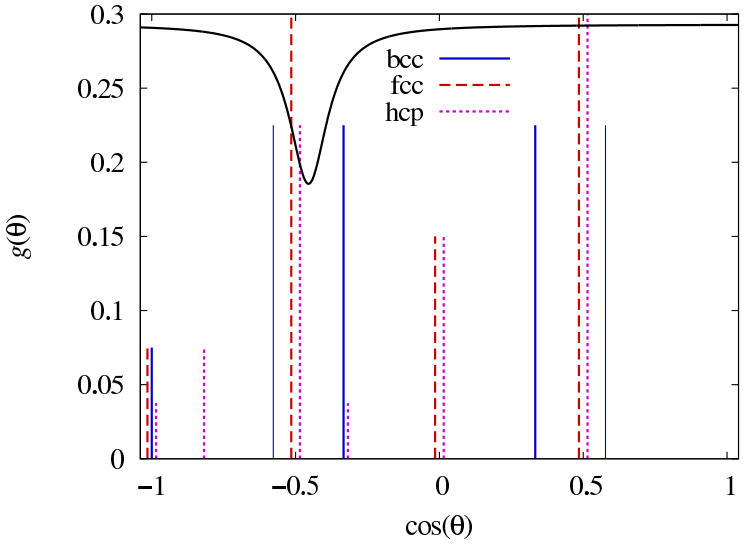


**Figure 3.11:** *Angular function $g(\theta)$ of the Pt bond-order potential. Angles appearing in different structures are indicated by vertical lines. The height of a line is proportional to the weight of the angle in the respective structure. The angles are shifted slightly so that structures having identical angles can be distinguished.*

56 GPa, as compared to 77 GPa from experiments. For comparison, the calculations on fcc Pt have therefore also been conducted within the local density approximation (LDA) [109, 110], which resulted in a markedly better agreement for the elastic constants. With both methods, however, the small $c_{44}/C'$ ratio of Pt is correctly reproduced.

### 3.5.3. Fitting of the Pt potential

For fitting the pure Pt potential, the general procedure described in Sec. 3.3 has been followed.

In order to describe the large stacking-fault energy by the bond-order potential, the hcp structure of Pt has to possess a considerably smaller cohesive energy than the fcc ground state. This is also reflected by the DFT calculations, which give an energy difference of 56 meV/atom. Furthermore, DFT predicts a non-ideal $c/a$-ratio of the hcp Pt phase of approximately 1.73. For interatomic potentials that restrict the interaction range to nearest or second nearest neighbors only it is challenging to realize structural energy differences between the fcc and hcp phases, since the bonding characteristics in both phases are very similar. Therefore, as in the case of bcc and fcc Fe, the position of the minimum in the angular function $g(\theta)$ (Eq. (3.6)) plays a key role for obtaining a reliable potential. As shown in Fig. 3.11, the nearest neighbor angles in the fcc and hcp phases are almost identical. Only the 120° angle ($\cos\theta = -0.5$) allows to increase the bond-order of the fcc over the hcp phase, as it appears four times per atom in the cubic but only three times per atom in the hexagonal close-packed structure. On the contrary, parameterizations of the Pt potential that do not possess a minimum in the $g(\theta)$ function around $\cos\theta = -0.5$

**Table 3.5:** *Final parameter set of the analytic bond-order potential for platinum.*

| Parameter | Value |
|---|---|
| $D_0$ (eV) | 3.2 |
| $r_0$ (Å) | 2.42 |
| $\beta$ (Å$^{-1}$) | 1.61 |
| $S$ | 2.2955906 |
| $\gamma$ | 0.1854649 |
| $c$ | 0.0609071 |
| $d$ | 0.08 |
| $h$ | 0.455 |
| $2\mu$ (Å$^{-1}$) | 1.5856477 |
| $R$ (Å) | 3.75 |
| $D$ (Å) | 0.2 |

in unison show at least a slight preference for the hcp structure. For the Pt potential, the parameter $h$ was therefore restricted to a narrow range around the value 0.5. With this choice, the experimental stacking fault energy of fcc Pt and the $c/a$ ratio of hcp Pt obtained from DFT calculations could be reproduced.

Also similar to the Fe bond-order potential, an exact reproduction of the experimental dimer bond length ($r_\mathrm{b} = 2.33\,\text{Å}$, Ref. [111]) resulted in somewhat too low surface energies. By slightly increasing $r_\mathrm{b}$ to 2.42 Å, a good compromise could, however, be achieved.

The final parameter set of the Pt bond-order potential is listed in Tab. 3.5. Its properties are discussed in the following.

## 3.5.4. Characterization of the Pt potential

### Dimer and bulk properties

In Tab. 3.6, results of the ABOP on dimer properties, cohesive energies and structural parameters of Pt in different phases and on the elastic constants of fcc Pt are compared with reference data from literature and total-energy calculations.

The Pt ABOP gives a quantitatively accurate description of $Pt_2$ dimer properties. The dimer binding energy and the vibration frequency are reproduced almost exactly. For the bond length, a slightly increased value of 2.42 Å is obtained. This, however, corresponds to a deviation of only 4 % compared to the experimental value of 2.33 Å.

The potential has been fitted with a high weight on the lattice constant, cohesive energy and elastic properties of the fcc structure. In consequence, the respective reference values

**Table 3.6.:** *Comparison of structural and cohesive properties of Pt in various phases from calculation and experiment. Errors are given in round brackets. Values in square brackets are rescaled to the experimental atomic volume of fcc Pt.* $r_\mathrm{b}$*: dimer bond distance (Å),* $E_\mathrm{b}$*: dimer binding energy (eV/atom),* $\omega_0$*: dimer vibration frequency (cm*$^{-1}$*),* $V$*: equilibrium volume (Å*$^3$*/atom),* $a_0$*: lattice constant (Å),* $c/a$*: axial ratio,* $E_\mathrm{c}$*: cohesive energy (eV/atom),* $\Delta E$*: energy difference (eV/atom) to ground state (fcc),* $B$*,* $B'$*: bulk modulus (GPa) and its pressure derivative,* $c_{ij}$*: elastic constants (GPa),* $C'$*: shear elastic constant* $(c_{11}-c_{12})/2$ *(GPa).*

| | PAW GGA-DFT | PAW LDA-DFT | Literature | | Pt ABOP |
|---|---|---|---|---|---|
| | | | Experiment | Theory | |
| Dimer | | | | | |
| $r_\mathrm{b}$ | | | 2.33 [a] | 2.34 [b] | 2.42 |
| $E_\mathrm{b}$ | | | 3.14 [a] | 3.12 [b], 3.18 [b] | 3.2 |
| $\omega_0$ | | | 222 [a] | 224 [b], 223 [b] | 215 |
| Diamond (Fd$\bar{3}$m) | | | | | |
| $V$ | 24.30 [23.06] | | | | 26.08 |
| $a_0$ | 5.793 [5.693] | | | | 5.931 |
| $\Delta E$ | 1.048 | | | | 1.93 |
| Simple Cubic (Pm$\bar{3}$m) | | | | | |
| $V$ | 18.26 [17.33] | | | | 17.27 |
| $a_0$ | 2.633 [2.588] | | | | 2.585 |
| $\Delta E$ | 0.428 | | | | 1.21 |
| Body-centered cubic (Im$\bar{3}$m) | | | | | |
| $V$ | 16.01 [15.19] | | | | 15.26 |
| $a_0$ | 3.176 [3.120] | | | | 3.125 |
| $\Delta E$ | 0.090 | | | | 0.27 |
| Face-centered cubic (Fm$\bar{3}$m), anti-ferromagnetic | | | | | |
| $V$ | 15.83 [15.02] | 14.90 [15.02] | 15.02 [d] | | 15.03 |
| $a_0$ | 3.986 [3.917] | 3.906 [3.917] | 3.917 [d] | | 3.917 |
| $E_\mathrm{c}$ | −5.77 [c] | −5.77 [c] | −5.77 [d] | | −5.770 |
| $B$ | 244 | 304 | 288.4 [e] | | 286 |
| $B'$ | 5.5 | 5.4 | | | 6.0 |
| $c_{11}$ | 292 | 373 | 358 [e] | | 356 |
| $c_{12}$ | 220 | 270 | 253 [e] | | 251 |
| $c_{44}$ | 56 | 79 | 77.4 [e] | | 81 |
| $C'$ | 36 | 51.5 | 52.5 [e] | | 52.5 |
| $c_{44}/C'$ | 1.56 | 1.53 | 1.47 [e] | | 1.54 |
| Hexagonal close-packed (P6$_3$/mmc), non-magnetic | | | | | |
| $V$ | 15.94 [15.12] | | | | 15.11 |
| $a_0$ | 2.773 [2.724] | | | | 2.714 |
| $c/a$ | 1.727 | | | | 1.75 |
| $\Delta E$ | 0.056 | | | | 0.036 |

[a] Ref. [111]
[b] Ref. [112]
[c] Value taken from experimental data.
[d] Ref. [113]
[e] Ref. [107]

**Table 3.7:** *Comparison of thermal properties, point-defects, surfaces and planar faults of Pt as obtained from the ABOP potential with literature data. $T_m$: melting point (K), $\alpha_L$: coefficient of linear thermal expansion at 300 K ($10^{-6}$/K), $\Delta E_v^f$: vacancy formation energy (eV), $\Delta V_v$: vacancy relaxation volume (in units of atomic volume), $\gamma_{(hkl)}$: energy of $(hkl)$-surface (meV/Å$^2$), $E_{\mathrm{SF}}$: stacking-fault energy (meV/Å$^2$), $\gamma_{\mathrm{twin}}$: (111) twin boundary energy (meV/Å$^2$).*

| | Literature | | Pt ABOP |
|---|---|---|---|
| | Experiment | Theory | |
| $T_{\mathrm{m}}$ | 2045 [a] | | 2700(20) |
| $\alpha_L$ | 8.8 [b] | | 6.5 |
| $\Delta E_v^f$ | 1.35 [a] | | 1.7 |
| $\Delta V_v$ | −0.2 [c] | | −0.27 |
| $\gamma_{(100)}$ | 156 [d] | 114 [e] | 107 |
| $\gamma_{(111)}$ | 156 [d] | 92 [e] | 83 |
| $\gamma_{(110)}$ | 156 [d] | 121 [e] | 113 |
| $E_{\mathrm{SF}}$ | 20 [f] | 17 [f] | 19.7 |
| $\gamma_{\mathrm{twin}}$ | 10 [f] [g] | | 10.4 |

[a] Ref. [60]
[a] Ref. [85]
[c] Ref. [114]
[d] Liquid surface tension measurements, Ref. [89].
[e] Ref. [115]
[f] Ref. [106]
[g] Half the value of $E_{\mathrm{SF}}$.

are reproduced almost exactly. In particular, with $c_{44}/C' = 1.54$, an elastic anisotropy ratio smaller than 2 could be realized, which is in close agreement with the experimental value of 1.47 [107].

For the hcp structure, the Pt ABOP also gives an accurate description of lattice constants, and especially the non-ideal $c/a$-ratio larger than 1.633 is reproduced. Likewise, the structural energy difference $\Delta E$ to the fcc phase is reasonably large. The exact value of $\Delta E$ has been used as an adjustable parameter so that the stacking-fault energy in fcc Pt is correctly reproduced by the ABOP (see next section).

For lower coordinated structures, the ABOP potential also performs well in describing the respective bond lengths. The cohesive energies of the diamond and sc phases are, however, somewhat underestimated.

### Planar defects: surfaces, stacking-faults and twin boundaries

Properties of two-dimensional defects in fcc Pt are given in Tab. 3.7. Compared to the values from DFT calculations [115], a reasonable agreement for the low-index surface ener-

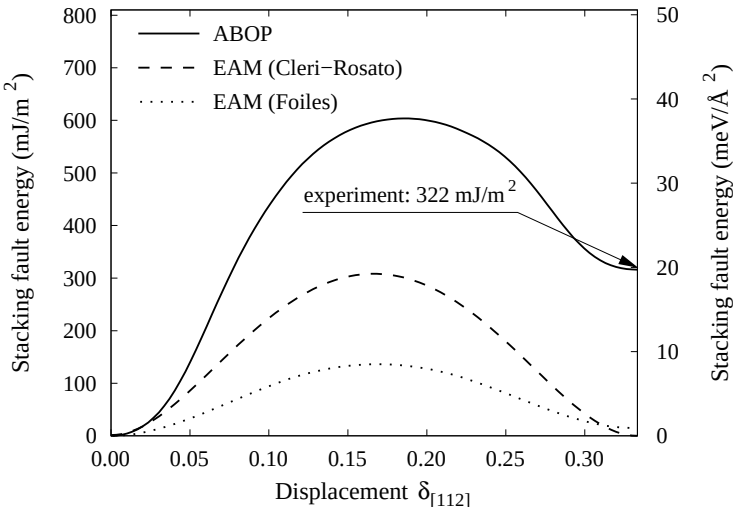


**Figure 3.12:** *Generalized stacking-fault energy of fcc Pt as obtained from the Pt ABOP. The displacement along the [112]-direction is given relative to a full displacement that restores the perfect stacking. The experimental value indicated by the arrow is taken from Ref. [106]. For comparison, results from two EAM potentials (Cleri and Rosato [59], Foiles et al. [116]), are also shown.*

gies has been achieved. The maximum deviation is obtained for the (111)-surface energy, which is underestimated by $-10\,\%$.

In contrast, as the energy difference between the hcp and fcc phases has been employed for fitting the stacking-fault energy $E_{\mathrm{SF}}$, the ABOP reproduces the experimental value for $E_{\mathrm{SF}}$ almost exactly. A stacking-fault can be created by displacing the upper half of a fcc crystal parallel to a {111}-plane in [112]-direction. The energy along this path is denoted as the generalized stacking-fault (GSF) energy curve or $\gamma$-surface [117]. The GSF-curve predicted by the Pt ABOP is plotted in Fig. 3.12. For illustrating the difficulty of constructing an interatomic potential that reproduces a large value for $E_{\mathrm{SF}}$, the GSF curves obtained from two embedded-atom method (EAM) potentials (Cleri and Rosato [59], Foiles *et al.* [116]) are also shown. In both Pt EAM potentials the energy content of stacking-faults is essentially zero.

In addition to the energy of the stable stacking-fault ($E_{\mathrm{SF}}$), the maximum of the GSF curve also represents an important parameter for plastic deformation. This unstable stacking-fault energy $E_{\mathrm{USF}}$ determines the activation barrier for splitting a full dislocation in two partial dislocations. The ABOP predicts a value of $E_{\mathrm{USF}} = 38\,\mathrm{meV/\AA^2}$. An experimental reference for $E_{\mathrm{USF}}$ is not available, but a distinctly larger value than for $E_{\mathrm{SF}}$ can be anticipated. In the case of the EAM potentials, $E_{\mathrm{USF}}$ not even reaches the experimental value of the stable fault and splitting of dislocations therefore requires too small activation.

A property related to stacking-faults is the twinning energy $\gamma_{\mathrm{twin}}$ and often the relation $2\gamma_{\mathrm{twin}} \approx E_{\mathrm{SF}}$ holds true [106]. This is also the case for the Pt ABOP, where a value of $10.4\,\mathrm{meV/\AA^2}$ is obtained for $\gamma_{\mathrm{twin}}$. The low tendency of Pt for plastic deformation by deformation twinning [106] should therefore be reproduced by the ABOP.

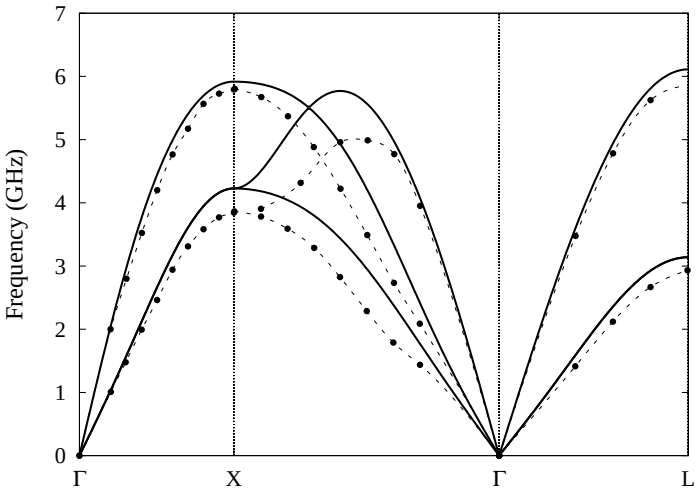


**Figure 3.13:** *Phonon dispersion curves of fcc Pt obtained from the Pt ABOP potential developed in this work. Black dots indicate experimental data points as compiled in Ref. [118].*

#### Thermal properties, vacancies and phonon dispersion

Thermal and vacancy properties of the Pt ABOP are also listed in Tab. 3.7. For determining the melting temperature, molecular dynamics simulations of a solid-liquid interface have been performed as described in Sec. 3.4.4. The melting point of the Pt ABOP estimated by this method is 2700(20) K, which is clearly above the experimental value of 2045 K [60]. Also, the formation energy for vacancies is somewhat overestimated.

The phonon dispersion of fcc Pt as predicted by the ABOP has been derived by diagonalization of the dynamical matrix at different $k$-points [119]. The result is shown in Fig. 3.13 together with data points from experiment [118]. A comparison of both data sets reveals an overall good agreement, with somewhat too high frequencies of the ABOP potential along the Γ-X direction.

### 3.5.5. Conclusions

In conclusion, the development of a bond-order potential for fcc Pt has been described. The comparison of materials properties calculated by the ABOP with reference data from literature and total-energy calculations show that structural and elastic properties of Pt can be properly described. This includes the small anisotropy ratio of the shear elastic constants, the structural energy difference between the hcp and fcc phases and the high $c/a$-ratio of the hcp structure. Furthermore, the ABOP could be fitted exactly to the large experimental values of stacking-fault and twinning energies, which are quantities influencing the plastic deformation behavior. For the application of the Pt ABOP to the

FePt alloy system in the present work, the large $\gamma_{\text{twin}}$ becomes important for analyzing the stability of multiply twinned morphologies in FePt nanoparticles (see Chapter 5).

# 3.6. Fe-Pt interaction: cross interaction potential for iron-platinum

## 3.6.1. Introduction

Based on the pure Fe-Fe and Pt-Pt potentials presented in the foregoing sections, the parametrization of a Fe-Pt cross interaction potential is developed in the following. The structural $L1_0$ to $A1$ order-disorder transition in stoichiometric FePt alloys at 1573 K is preceded by a transition from the ferromagnetic to the paramagnetic state at 750 K [19]. Internal magnetic degrees of freedom therefore contribute to the free energies of the competing structural phases, which are missing in molecular dynamics and Monte Carlo simulations that apply an analytic potential description. Following the same idea as for the Fe potential, the structural energy difference between the $L1_0$ and $A1$ phases is therefore considered as an adjustable parameter. In order to reproduce the order-disorder transition, this energy difference is then fitted explicitly to the bulk ordering temperature in stoichiometric FePt alloys.

In this section, the total-energy calculations for extending the fitting database are described first, then the fitting procedure is outlined. Finally, the properties of the final parametrization are analyzed.

## 3.6.2. Total-energy calculations

For complementing the fitting database with quantities not available from experiments, total-energy calculations in the framework of the density functional theory (DFT) have been carried out, as described in the following. The calculations were performed using the same techniques as described in Sec. 3.4.2. The generalized gradient approximation (GGA) [74] has been employed. As GGA showed to produce relatively low elastic constants for fcc Pt (see Sec. 3.5.3), calculations on $L1_0$ ordered FePt have also been performed within the local density approximation (LDA) [109, 110]. The plane-wave cutoff energy was set to 348.3 eV. The number of $k$-points in the irreducible Brillouin-zone was chosen to guarantee a convergence of the total energy better than 1 meV/atom. A typical value is 360 $k$-points for $L1_0$ ordered FePt. Magnetic ground states were identified by performing non spin-polarized (non-magnetic, NM) as well as spin-polarized calculations with ferromagnetic (FM) and anti-ferromagnetic (AFM) alignment of the atomic spins. The results of the calculations are summarized in Tab. 3.9.

The DFT calculations predict FM ground states for FePt alloys in all the $L1_0$ and $L1_2$ ordered structures. Note, however, that for $L1_2$-$FePt_3$ the energy difference between the FM and AFM state is only 4 meV/atom and contrarily to the present study, a AFM ground state has been reported in Ref. [120].

For the $L1_0$ ordered compound, the total-energy calculations give a formation energy of $-224$ meV/atom. This is in good agreement with the first principles calculations reported in Ref. [120], where a value of $-287$ meV/atom is found. In contrast, a thermodynamic assessment of the FePt phase diagram provides a much higher formation energy of $-730$ meV/atom [121, 122].

The elastic constants of the $L1_0$ FePt phase estimated by LDA and GGA differ from each other, with LDA giving distinctly higher values than GGA. However, the order of the $L1_0$ elastic constants is conserved when switching between the two methods, with $c_{11}<c_{33}$, $c_{12}>c_{13}$ and $c_{44}<c_{66}$. Also, the elastic constants fulfill the stability criteria for the tetragonal symmetry in both cases [123]. As GGA underestimates the elastic constants of pure Pt but at the same time gives somewhat increased values for pure Fe (see Sec. 3.4.2), an averaging effect can be expected for FePt compounds. Therefore, the GGA elastic constants can represent a reasonable reference for fitting the FePt bond-order potential.

### 3.6.3. Fitting of the Fe-Pt cross potential

The principle steps of the fitting procedure are described in Sec. 3.3 and are identical to the development of the pure Fe and Pt potentials. In the case of the Fe-Pt cross potential, the fitting database extends over FePt in the stoichiometric $L1_0$ ordered structure and the ordered structures at compositions $Fe_3Pt$ and $FePt_3$ ($L1_2$). Additionally, special quasirandom structures [124] have been included for fitting the energy difference between the ordered and disordered phase.

#### Long-range order parameter

In order to fit the Fe-Pt ABOP to the experimental order-disorder transition temperature $T_c$, the Monte Carlo method has been applied for determining $T_c$ of various trial parameterizations. For doing so, the amount of ordering has been measured by the long-range order (LRO) parameter defined in the following.

For a quantitative description of chemical ordering on face centered cubic and face centered tetragonal derived lattices, a three component LRO parameter $\underline{\Psi}$ has been employed

[50]. It is defined as follows: The face centered lattice can be decomposed into a set of four sublattices $\nu$ with a single-atomic basis. A sublattice occupation $m_\nu$ is then defined as

$$m_\nu = 1/N \sum_{k \in \nu} s_k, \qquad \nu = 1, 2, 3, 4, \tag{3.7}$$

where the variable $s_k$ is defined to have the value 1 if site $k$ is occupied by an Fe atom and -1 if site $k$ is occupied by a Pt atom. The summation in Eq. (3.7) runs over all sites of the sublattice $\nu$ and $N$ is the number of atoms in the system. The components of the order parameter are then defined as

$$\underline{\psi} = \begin{pmatrix} \psi_1 \\ \psi_2 \\ \psi_3 \end{pmatrix} = \begin{pmatrix} m_1 + m_2 - m_3 - m_4 \\ m_1 - m_2 - m_3 + m_4 \\ m_1 + m_2 + m_3 - m_4 \end{pmatrix}. \tag{3.8}$$

The LRO parameter takes the values $(\pm 1\ 0\ 0), (0\ \pm 1\ 0), (0\ 0\ \pm 1)$ for complete $L1_0$ ordering in $x$-, $y$- and $z$-direction, respectively. By taking the ordering direction ($c$-axis of the $L1_0$ phase) parallel to the $z$-axis of the coordinate system, it is finally sufficient to only monitor the $z$-component of $\underline{\psi}$ for analyzing $L1_0$ to $A1$ order-disorder transitions. For these transitions, the LRO parameter discussed in the remainder of this work is therefore identical to $\psi_3$.

In addition, the vector $\underline{\psi}$ can also be employed for measuring chemical ordering in the $Fe_3Pt$ and $FePt_3$ phases. In these cases, complete $L1_2$ order is indicated by the values $(\pm\frac{1}{2}\ \pm\frac{1}{2}\ \pm\frac{1}{2})$, $(\pm\frac{1}{2}\ \mp\frac{1}{2}\ \pm\frac{1}{2})$, $(\mp\frac{1}{2}\ \pm\frac{1}{2}\ \mp\frac{1}{2})$ and $(\mp\frac{1}{2}\ \mp\frac{1}{2}\ \pm\frac{1}{2})$.

### Fitting of the order-disorder transition temperature

For fitting the potential to the order-disorder transition temperature $T_c$ at equiatomic composition, it is desirable to include a disordered random structure in the fitting database. This allows to control the energy difference between the ordered and the disordered alloy. In order to be representative for the bonding characteristics of infinite, perfectly random alloys, a large number of atoms have to be included in a finite, periodic cell. However, too large structures would significantly reduce the efficiency of the fitting procedure. A good compromise between low computational cost and an exact description of a random alloy is provided by the so-called special quasirandom structures (SQS's) [124]. They are specially designed in order to match the first few radial correlation functions of a perfectly random alloy by a small number of atoms. Therefore, a SQS allows to efficiently capture the most important bonding characteristics in random alloys. The SQS added to the fitting database for the mixed FePt potential consists of 16 atoms (SQS16) and is taken from Ref. [125].

The $L1_0$ and SQS16 structures are only representative for the ordered phase at 0 K and the disordered phase at infinite temperature, respectively. At finite temperatures, a certain degree of disorder in form of anti-site defects is present in the $L1_0$ phase. On the other hand, the $A1$ phase is not perfectly random, but is characterized by a temperature dependent presence of short range order. The degree of order in both phases at the transition temperature is *a priori* unknown. Additionally, a transition from the ferromagnetic to the paramagnetic state occurs at approximately 750 K [19] and internal magnetic degrees of freedom contribute to phase stability. For these reasons, the static energy difference between the fully ordered and disordered structures cannot be used for the potential fitting. In order to reproduce the correct $L1_0$ to $A1$ transition temperature, the target energy difference $\Delta E$ between the SQS16 and the $L1_0$ was taken as an adjustable parameter and has been determined as described in the following.

For parameterizations of the mixed FePt potential fitted to different values of $\Delta E$, the transition temperature was calculated by a series of off-lattice MC simulations in the $N, P{=}0, T$ ensemble. Trial steps consisted of exchanges of two randomly chosen atoms, small random displacements of individual atoms and random changes of cell dimensions independently in $x$, $y$ and $z$ direction. System sizes were chosen from $6 \times 6 \times 6$ unit cells (864 atoms) up to $12 \times 12 \times 12$ unit cells (6912 atoms). By running simulations at different temperatures and by monitoring the LRO parameter over an extended interval of MC steps, the transition temperature of a given parametrization has been determined and $\Delta E$ was then adjusted accordingly. For the final parametrization, the variation of LRO over temperature is plotted in Fig. 3.15.

One important side effect of these MC simulations is that they allow the detection of unwanted minima in the potential energy landscape that stabilize other configurations over the desired $L1_0$ ground state structure. Because of the complexity of the energy function, structures stabilized by erroneous energy minima can be quite complex and in general can therefore not be guessed beforehand. This also renders the addition of a few selected candidate structures (e.g. $L1_1$ or $B2$) to the fitting database ineffective, since assuring a high energy for these structures does not exclude the existence of other low energy structures. Instead, the procedure chosen in this work was to expand the fitting database iteratively by the corresponding structure, each time the MC simulations revealed an erroneous global energy minimum. During subsequent fitting steps, a higher formation energy has then been assigned to these structures. A consequence of these calculations is that the cutoff radius of the Fe-Pt cross interactions had to be increased to fully include the second nearest neighbor sphere. For only nearest neighbor interactions, the $B2$ structure was always favored over the desired $L1_0$ ground state.

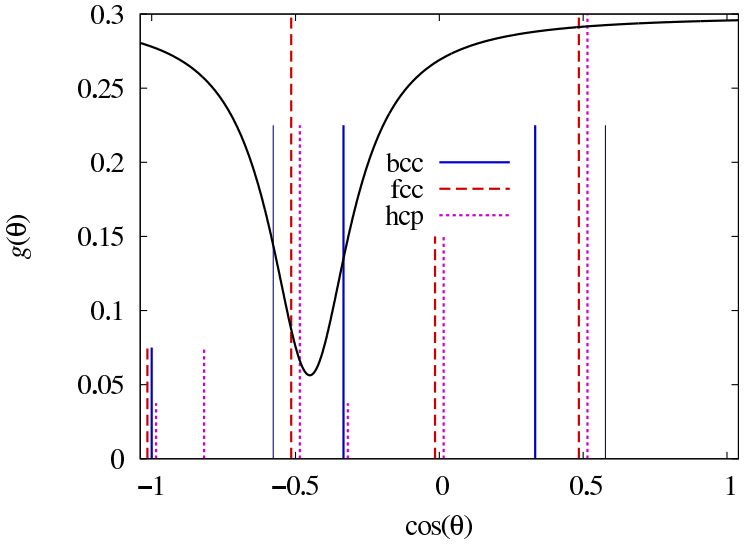


**Figure 3.14:** *Angular function $g(\theta)$ of the FePt potential. Angles appearing in different structures are indicated by vertical lines. The height of a line is proportional to the weight of the angle in the respective structure. The angles are shifted slightly so that structures having identical angles can be distinguished.*

### Twinning energy

An important value for structure formation in FePt alloys is the twinning energy $\gamma_{\text{twin}}$, as it determines for example the tendency of twinning in nanoparticles. A target value for $\gamma_{\text{twin}}$ in the $L1_0$ phase is available from electronic structure calculations, which predict an energy of $\gamma_{\text{twin}} = 6.5\,\text{meV/Å}^2$ [126]. For the case of Pt, which has a high twinning energy of $\gamma_{\text{twin}} = 10\,\text{meV/Å}^2$ [106] it has been show in Sec. 3.5.3 that the magnitude of $\gamma_{\text{twin}}$ can be tuned by carefully positioning the minimum of the function $g(\theta)$ (Eq. (3.6)) through the parameter $h$.

For the Fe-Pt cross potential, however, it was found that $h$ has to be restricted to a narrow range around the value 0.5. For other values of $h$, an orthogonal distortion of the $L1_0$ structure with $a \neq b \neq c$ occurred.

The angular dependence of the $g(\theta)$ function of the final Fe-Pt cross potential is shown in Fig. 3.14. For clarity, bond angles that appear in different structures such as fcc, hexagonal close packed (hcp) and body centered cubic (bcc) are also indicated. The position of the minimum of $g(\theta)$ implies an increased bond-order in a fcc compared to a hcp environment. Therefore, the hcp structure is disfavored, leading to a high twinning energy in FePt alloys in the present potential, similar to the pure Pt interactions.

The final best-fit parameter set for the Fe-Pt cross potential is given in Tab. 3.8. For convenience, the parameterizations of the pure Fe and Pt interactions are also repeated in Tab. 3.8. The properties of the FePt ABOP are discussed in the following.

| Parameter | Interaction type | | |
|---|---|---|---|
| | Fe-Fe | Pt-Pt | Fe-Pt |
| $D_0$ (eV) | 1.5 | 3.2 | 2.64759104 |
| $r_0$ (Å) | 2.29 | 2.42 | 2.36130052 |
| $\beta$ (Å$^{-1}$) | 1.4 | 1.61 | 1.45616698 |
| $S$ | 2.0693109 | 2.2955906 | 2.26243642 |
| $\gamma$ | 0.0115751 | 0.1854649 | 0.05633499 |
| $c$ | 1.2898716 | 0.0609071 | 0.35073555 |
| $d$ | 0.3413219 | 0.08 | 0.16902364 |
| $h$ | $-0.26$ | 0.455 | 0.45035775 |
| $2\mu$ (Å$^{-1}$) | 0.0 | 1.5856477 | 0.95780361 |
| $R$ (Å) | 3.15 | 3.75 | 4.20 |
| $D$ (Å) | 0.2 | 0.2 | 0.20 |

**Table 3.8:** *Parameter sets for the Fe-Fe, Pt-Pt and Fe-Pt analytic bond-order potentials.*

## 3.6.4. Characterization of the Fe-Pt potential

### Structural properties

In Tab. 3.9, structural properties of FePt in ordered and disordered phases as obtained from the ABOP are compared with literature data and results from DFT calculations. For comparison, the recent modified embedded-atom method (MEAM) potential for FePt by Kim *et al.* is also included [122]. All crystallographic parameters like lattice constant and $c/a$-ratio are in excellent agreement with reference values from literature. For fitting the formation energies of the ordered compounds, the reference values from total-energy calculations have been employed. For obtaining a better agreement of the elastic constants, a deviation of the formation energies towards higher values has been accepted. The final values are, however, still well below the MEAM potential, where formation energies from a thermodynamic assessment of the FePt phase diagram were taken as reference. The bulk moduli and elastic constants predicted by the ABOP are in good agreement with the target values. Moreover, the ordering of the elastic constants of the $L1_0$ structure ($c_{11}<c_{33}$, $c_{12}>c_{13}$ and $c_{44}<c_{66}$) as obtained from the total-energy calculations is reproduced by the ABOP.

### Order-disorder transition

From experimental studies on the FePt phase diagram, a $L1_0$ to $A1$ order-disorder transition temperature of $T_c = 1573\,\mathrm{K}$ is reported [19]. For the nature of the transition, strong

**Table 3.9.:** *Comparison of structural and cohesive properties of FePt in various phases from calculation and experiment. For the DFT calculations, the parameters are given for the lowest energy magnetic configuration, as indicated.* $a_0$*: lattice constant (Å),* $c/a$*: axial ratio,* $E_\mathrm{c}$*: cohesive energy (eV/atom),* $\Delta E_f$*: energy of formation (eV/atom),* $B$*,* $B'$*: bulk modulus (GPa) and its pressure derivative,* $c_{ij}$*: elastic constants (GPa).*

| | PAW GGA-DFT | PAW LDA-DFT | Literature | ABOP | MEAM Ref. [122] |
|---|---|---|---|---|---|
| $L1_0$ FePt, ferromagnetic | | | | | |
| $a_0$ | 3.872 | 3.772 | 3.85 [a] | 3.862 | 3.81 |
| $c/a$ | 0.973 | 0.975 | 0.964 [a] | 0.963 | 0.963 |
| $\Delta E_f$ | −0.224 | −0.140 | −0.730 [b], −0.287 [c] | −0.320 | −0.604 |
| $E_\mathrm{c}$ | −5.249 | −5.165 | | −5.345 | |
| $B$ | 200 | 251 | | 217 | 232 |
| $B'$ | 5.0 | 4.2 | | 5.9 | |
| $c_{11}$ | 261 | 360 | | 258 | 304 |
| $c_{33}$ | 299 | 371 | | 293 | 242 |
| $c_{12}$ | 169 | 229 | | 203 | 223 |
| $c_{13}$ | 151 | 185 | | 185 | 197 |
| $c_{44}$ | 103 | 143 | | 141 | 107 |
| $c_{66}$ | 133 | 192 | | 182 | 41 |
| $A1$ random FePt | | | | | |
| $a_0$ | | | 3.80 [a] | 3.819 | 3.78 |
| $\Delta E_f$ | | | | −0.169 | −0.440 |
| $E_\mathrm{c}$ | | | | −5.194 | |
| $B$ | | | | 214 | 234 |
| $B'$ | | | | 5.5 | |
| $c_{11}$ | | | | 257 | 291 [d] |
| $c_{12}$ | | | | 193 | 205 [d] |
| $c_{44}$ | | | | 132 | 95 [d] |
| $L1_2$ $Fe_3Pt$, ferromagnetic | | | | | |
| $a_0$ | 3.740 | | 3.72 [a] | 3.73 | 3.70 |
| $\Delta E_f$ | −0.068 | | | −0.234 | −0.422 |
| $E_\mathrm{c}$ | −4.720 | | | −4.886 | |
| $B$ | 174 | | | 201 | 202 |
| $B'$ | 3.5 | | | 6.0 | |
| $c_{11}$ | | | | 259 | 239 |
| $c_{12}$ | | | | 172 | 184 |
| $c_{44}$ | | | | 145 | 95 |
| $L1_2$ $FePt_3$, ferromagnetic | | | | | |
| $a_0$ | 3.924 | | 3.87 [a] | 3.876 | 3.84 |
| $\Delta E_f$ | −0.188 | | | −0.236 | −0.461 |
| $E_\mathrm{c}$ | −5.585 | | | −5.634 | |
| $B$ | 222 | | | 246 | 256 |
| $B'$ | 5.1 | | | 5.3 | |
| $c_{11}$ | | | | 305 | 326 |
| $c_{12}$ | | | | 217 | 230 |
| $c_{44}$ | | | | 127 | 90 |

[a] Ref. [19]
[b] Thermodynamic assessment, Ref. [121].
[c] First principles calculations, Ref. [120].
[d] Ref. [127]

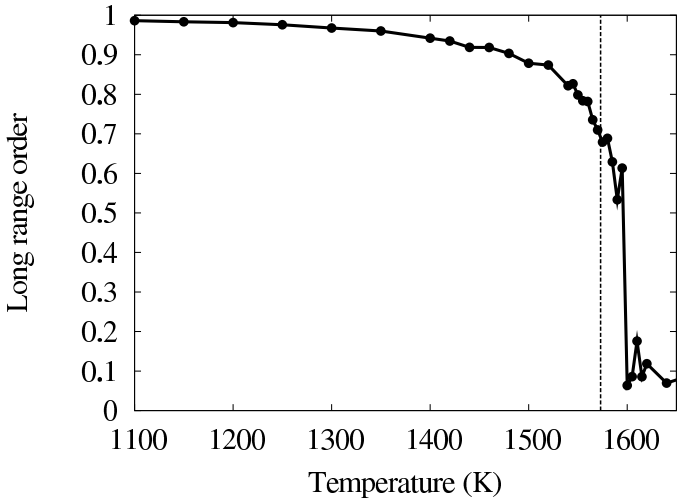


**Figure 3.15:** *Variation of the LRO parameter for the $L1_0$ to $A1$ transition with temperature, as obtained by MC simulations for the FePt ABOP. The dashed line indicates the transition temperature of $T_c = 1573$ K reported from experiments [19].*

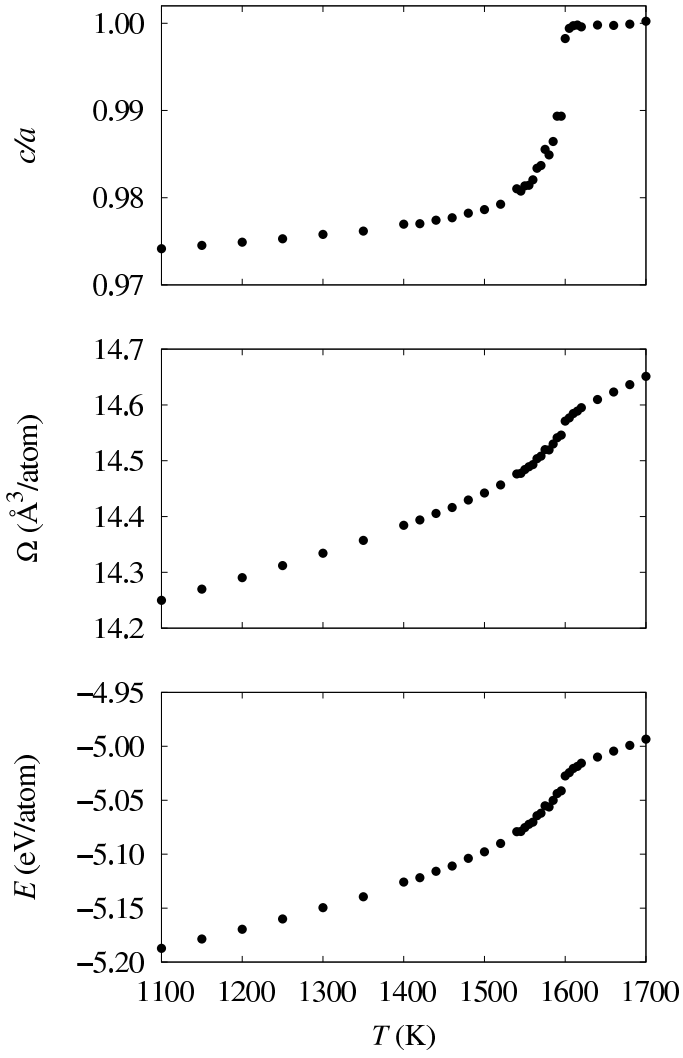


**Figure 3.16:** *Evolution of energy ($E$), atomic volume ($\Omega$) and $c/a$-ratio with temperature for the $L1_0$ to $A1$ order-disorder transition, as calculated for the FePt ABOP.*

experimental evidence exists for a first-order phase transition: The derivative of the LRO parameter has a discontinuity at $T_c$ [128], and the transitions between both phases proceed via nucleation and growth [128–130]. Also, two phase regions separating the $L1_0$ and $A1$ phases have been identified [128–130].

For characterizing the $L1_0$ to $A1$ transition of the FePt ABOP, the evolutions of LRO parameter, energy and structural properties with temperature have been determined by the off-lattice MC method described in Sec. 3.6.3. Close to the transition temperature, the MC data has been sampled with a resolution of 5 K using system sizes up to $12 \times 12 \times 12$ unit cells. The resulting evolution of the LRO parameter is shown in Fig. 3.15. The variations of energy, atomic volume and $c/a$-ratio across the order-disorder transition are plotted in Fig. 3.16. From the drop of the LRO parameter in Fig. 3.15, the order-disorder transition of the ABOP description can be located at 1595(5) K, which is only a slight overestimation of the experimental $T_c$ (1573 K).

However, the quality of the obtained MC data does not allow to draw a definite conclusion on the order of the phase transition predicted by the ABOP. Although the LRO parameter shows a clear drop, only a very small jump in energy and atomic volume at the transition temperature is visible. Instead, the plots shown in Fig. 3.16 appear smeared around $T_c$, indicating a continuous transition.

On the other hand, this smearing effect can also be a consequence of the finite system size, which appears in MC studies on phase transitions if the correlation length exceeds the size of the simulation cell close to the transition temperature [131]. In addition, a reduction of transition barriers between stable and metastable states in finite systems increases the smearing effect [131]. The possibility of finite size smearing in the present MC data is indicated by the non-vanishing, fluctuating LRO parameter beyond $T_c$. In systems of a limited number of atoms, small variations of the atomic configuration can lead to relatively high amplitudes in the LRO parameter.

Several methods for handling finite size effects in MC studies on phase transitions have been derived, including finite size scaling or evaluating the distribution function of the order parameter for identifying metastable states [131]. However, as opposed to simple models like Ising-type lattice Hamiltonians, it was found that these methods are not applicable for off-lattice MC simulations in conjunction with continuous interatomic potentials, such as the ABOP. The increased computational effort for evaluating the complex energy function and the inclusion of atom displacements as well as cell shape variations do not allow to sample larger systems over the necessary number of MC steps within reasonable computing times.

| | Literature | ABOP |
|---|---|---|
| $T_m$ | 1873 [a] | 2050(50) |
| Ordered $L1_0$ phase | | |
| $\gamma_{100}$ | 132 [b] | 109 |
| $\gamma_{001}$ (average) | 136 [b] | 134 |
| $\gamma_{111}$ | 109 [b] | 89 |
| $\gamma_{\text{twin}}$ | 6.5 [c] | 11.7 |
| Disordered $A1$ phase | | |
| $\gamma_{100}$ | | 104 |
| $\gamma_{110}$ | | 109 |
| $\gamma_{111}$ | | 81 |
| $\gamma_{\text{twin}}$ | | 11.7 |

**Table 3.10:** *Comparison of the melting point, surface properties and twinning energies in FePt predicted by the ABOP with literature data. $T_m$: melting point (K), $\gamma_{(hkl)}$: energy of $(hkl)$-surface (meV/Å$^2$), $\gamma_{\text{twin}}$: (111) twin boundary energy (meV/Å$^2$).*

[a] Ref. [19].
[b] DFT calculations, Ref. [132]
[c] Electronic-structure calculations, Ref. [126].

### Melting temperature

The melting point of an equiatomic FePt alloy predicted by the ABOP has been determined by molecular dynamics simulations of a solid-liquid interface in the $N$,$P$=0,$T$ ensemble. For increasing temperatures, the position of the solid-liquid interface has been monitored and the melting temperature was found for zero velocity of the interface, i.e. when the volume fractions of the solid and liquid phases remained constant over the simulation time of 1 ns. As listed in Tab. 3.10, the melting point estimated by this method is 2050(50) K, which is about 200 K higher than the experimental value of 1873 K [60]. Considering that the potentials for the pure Fe and Pt boundary phases also overestimate the melting temperature, an increased value can be expected and the agreement is still reasonable.

### Surface and twin boundary energies

In the $L1_0$ ordered phase, a (111) surface consists of an equal number of Fe and Pt atoms. By cleaving the crystal perpendicular to the $c$ direction, (100) or (010) surfaces are generated, which also possess an equiatomic composition. In contrast, a cleavage parallel to the $c$ direction leads to the formation of two (001) surfaces, one being occupied solely by Fe and the other solely by Pt atoms. In a computational cell with equiatomic composition and open boundaries along the $c$ direction, always both types of (001) surfaces are contained.

Their energies can therefore not be separated and an average value is given in Tab. 3.10. Reference values for surface energies in the $L1_0$ ordered phase are available from DFT calculations [132]. On average, a good performance of the ABOP in describing surface energies is obtained. While the potential reproduces the average (001) surface energy in the $L1_0$ phase, the values for the (111) and (100) surfaces are approximately 18 % lower as compared to the results obtained from DFT calculations. Thus, for the random phase, where no reference values are available, a small underestimation of surface energies can also be expected.

For the twin boundary energies ($\gamma_{\text{twin}}$) in the $L1_0$ ordered and $A1$ disordered FePt phases, identical values of $\gamma_{\text{twin}} = 11.7\,\text{meV/Å}^2$ are obtained. Considering the equally high twin-boundary energy of $10\,\text{meV/Å}^2$ in pure Pt [106], a high energy penalty for twinning can indeed be expected for FePt alloys. As discussed in Sec. 3.6.3, in consequence of the constraint applying to the parameter $h$, the Fe-Pt cross-interaction potential gives a considerable contribution to $\gamma_{\text{twin}}$ in mixed phases. Therefore, twinning energies with a magnitude similar to pure Pt are obtained. However, as a reference, electronic-structure calculations give only a value of $\gamma_{\text{twin}} = 6.5\,\text{meV/Å}^2$ for the $L1_0$ ordered phase [126]. These calculations therefore suggest that $\gamma_{\text{twin}}$ in FePt alloys rather scales linearly with the Pt content. In the current potential description, the twinning energy might therefore be overestimated by roughly a factor 2.

### 3.6.5. Conclusions

Based on the parameterizations for the boundary phases, a Fe-Pt cross-interaction potential in the analytic bond-order formalism has been developed. Characteristic for the Fe-Pt ABOP is a good reproduction of structural properties of FePt in the chemically ordered $L1_0$ and $L1_2$ phases, as well as in the $A1$ random alloy phase. The ABOP also gives a reasonable description of surface energies, while by comparison with first principles calculations, the energy content of twin-boundaries is overestimated approximately by a factor 2.

The $L1_0$ to $A1$ order-disorder transition temperature at equiatomic composition is well reproduced. While it could be located within approximately 20 K deviation compared to the experimental transition temperature, a determination of the order of the transition turned out to require larger system sizes and longer simulation runs than feasible with MC simulations in conjunction with a continuous interatomic potential.

## 3.7. Summary

In this chapter, a model description for FePt alloys based on analytic bond-order potentials has been developed. This included the fitting of three separate parameterizations, corresponding to the pure Fe-Fe, pure Pt-Pt and the mixed Fe-Pt interactions, respectively. By comparing the properties of the potentials with an extensive database of reference values both from experiment and first principles calculations, a solid description of the Fe and Pt boundary phases by the pure interaction potentials could be demonstrated. Most notably, this includes the structural transitions of Fe from the $\alpha$ to the $\gamma$ and $\delta$ phase with increasing temperature. For pure Pt, a correct reproduction of the high twinning energy and the low elastic anisotropy ratio could be verified.

Based on the potentials for the constituents, a parametrization of the Fe-Pt cross-interaction potential has been developed. It provides an accurate description of the $L1_0$ ordered and $A1$ disordered structures. By explicitly fitting to the order-disorder transition temperature, the chosen parametrization to some extent accounts for magnetic energy and entropy contributions and is able to mimic the FePt phase diagram. The FePt bond-order potential therefore represents an adequate tool for investigating size dependent structural properties (see Chapter 5) and the ordering behavior of FePt nanoparticles (Chapter 6).

However, for applications that require large system sizes and a very thorough sampling of configurational entropy, the problems encountered for characterizing the order-disorder transition in FePt (Sec. 3.6.4) already point to the necessity of models that provide an even higher numerical efficiency than analytic potentials. At the next degree of coarse-graining, lattice-based Hamiltonians that neglect the continuous nature of interatomic interactions allow the calculation of configurational energies at very low computational cost, while still conserving atomic resolution. Therefore, the development of a lattice-based Ising-like Hamiltonian for FePt alloys will be described in the next chapter.

# 4. Ising-type lattice Hamiltonian

*In this chapter an outline of the Ising-type lattice Hamiltonian model for studying order-disorder transitions in FePt alloys is given. The fitting procedure employed for parameterizing the model is described.*

## 4.1. Introduction

Because of their high computational efficiency, Ising-type lattice Hamiltonians are a convenient choice for studying the thermodynamics and kinetics of fcc based binary ordering alloys [50, 133–138]. These models describe the energy of a system by a set of additive pair interaction energies that only depend on the pair type. The interactions can be restricted to include only nearest neighbor pair energies, or can be extended to atom pairs in higher neighbor shells. In this chapter, the development of an Ising-type Hamiltonian for investigating the $L1_0$ to $A1$ phase transition in FePt alloys is described. For properly describing the FePt phase diagram and the energetics of the $L1_0$ structure, extending the pair interactions to second-nearest neighbors proves necessary (see Sec. 4.2).

As atomic positions are restricted to sites of a rigid fcc lattice, changes in crystal symmetry accompanying configurational phase transitions can not be resolved by the lattice Hamiltonian. The tetragonal distortion of the $L1_0$ structure will therefore be ignored in the following. However, with a $c/a$-ratio of 0.964 [19], the distortion is only small and its neglect can be justified. Additionally, with the analytic bond-order potential at hand, the effect of the tetragonal distortion of the $L1_0$ structure on the phase transition in FePt nanoparticles will be assessed separately in Chapter 6. Only small differences to the predictions of the lattice Hamiltonian are found and the applicability of the Ising-type model is confirmed.

In the following, the configurational energy function of the Ising-type Hamiltonian applied for studying FePt alloys is summarized. Subsequently, the procedure adopted for parameterizing the model is described.

## 4.2. Configurational energy function

In the Ising-type Hamiltonian, Fe and Pt atoms are distributed on a rigid fcc lattice. Atom-atom interactions are restricted to nearest neighbor (NN) and next nearest neighbor (NNN) pairs and are described by the pair interaction energies $\varepsilon_1^{\mathrm{FeFe}}, \varepsilon_1^{\mathrm{PtPt}}, \varepsilon_1^{\mathrm{FePt}}$ (for NN pairs) and $\varepsilon_2^{\mathrm{FeFe}}, \varepsilon_2^{\mathrm{PtPt}}, \varepsilon_2^{\mathrm{FePt}}$ (for NNN pairs). The configurational energy of a system is then given by

$$E = \sum_i \left( \sum_{\mathrm{NN}j} \frac{1}{2} \varepsilon_1^{ij} + \sum_{\mathrm{NNN}j} \frac{1}{2} \varepsilon_2^{ij} \right), \tag{4.1}$$

where the outer summation is over all atoms $i$, and the inner sums run over all nearest and next-nearest neighbors of atom $i$, respectively. The ordering properties of this model do not depend on the absolute values of the individual pair interaction energies, but only on a number of linear combinations between them [133]. At the end, the number of adjustable parameters is reduced to the following quantities:

$$\begin{aligned} J_1 &= \frac{1}{4}\varepsilon_1^{\mathrm{FeFe}} + \frac{1}{4}\varepsilon_1^{\mathrm{PtPt}} - \frac{1}{2}\varepsilon_1^{\mathrm{FePt}}, \\ J_2 &= \frac{1}{4}\varepsilon_2^{\mathrm{FeFe}} + \frac{1}{4}\varepsilon_2^{\mathrm{PtPt}} - \frac{1}{2}\varepsilon_2^{\mathrm{FePt}}, \\ h &= 3\varepsilon_1^{\mathrm{FeFe}} - 3\varepsilon_1^{\mathrm{PtPt}} + \frac{3}{2}\varepsilon_2^{\mathrm{FeFe}} - \frac{3}{2}\varepsilon_2^{\mathrm{PtPt}}. \end{aligned} \tag{4.2}$$

For a bulk system with fixed composition, only the parameters $J_1$ and $J_2$ determine the ordering behavior, as these define the energy change for exchanging pairs of Fe and Pt atoms. For a system with free surfaces, the difference between the interaction energies of like atoms ($\varepsilon_1^{\mathrm{FeFe}} - \varepsilon_1^{\mathrm{PtPt}}$ and $\varepsilon_2^{\mathrm{FeFe}} - \varepsilon_2^{\mathrm{PtPt}}$) also plays an important role. Depending on whether Fe-Fe or Pt-Pt bonds are stronger, Pt or Fe atoms tend to segregate on the surface, respectively. Therefore, the parameter $h$ can be viewed as a surface segregation potential determining the segregation behavior of the system [138].

The complete analogy of this model to an Ising model is established by describing the occupation of the lattice by a variable $s_k$. The variable is defined to have the value 1 if site $k$ is occupied by an Fe atom and -1 if site $k$ is occupied by a Pt atom. For a bulk system, a Hamiltonian $\mathcal{H}_{\mathrm{Ising}}$ can then be expressed by

$$\mathcal{H}_{\mathrm{Ising}} = J_1 \sum_{\mathrm{NN}\langle k,l\rangle} s_k s_l + J_2 \sum_{\mathrm{NNN}\langle k,l\rangle} s_k s_l + h \sum_k s_k. \tag{4.3}$$

Here, the first two sums run over all pairs of NN and NNN sites, respectively. The last sum is over all sites of the lattice. For a system with free surfaces, the Hamiltonian in

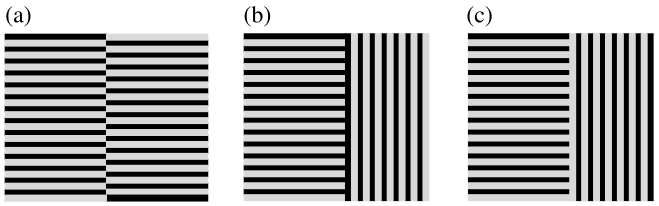


**Figure 4.1:** *Illustration of antiphase boundaries in the $L1_0$ ordered phase: (a) conservative antiphase boundary (b) and (c) non-conservative antiphase boundary. Black stripes denote Fe layers, grey stripes denote Pt layers.*

| APB | $\gamma \cdot a_0^2$ |
|---|---|
| conservative (Fig. 4.1a) | $-8J_2$ |
| non-conservative (Fig. 4.1b) | $4J_1 - 4J_2 + \frac{2}{3}h$ |
| non-conservative (Fig. 4.1c) | $4J_1 - 4J_2 - \frac{2}{3}h$ |

**Table 4.1:** *APB energies ($\gamma$) expressed by the model parameters. $a_0$ is the lattice parameter of the fcc unit cell.*

the spin-like notation becomes more complex, since additional summations over all sites in surface layers have to be included. Therefore, Eq. (4.1) is preferred in this work.

As depicted in Fig. 4.1, conservative and non-conservative antiphase boundaries (APBs) can occur on an $L1_0$ ordered lattice. The energy contents of the APBs resulting from the Ising-type model are listed in Tab. 4.1. For $J_2 = 0$, the conservative APB has no energy penalty, since the number of NN bonds between like and unlike atoms does not change when introducing a conservative APB into an ordered structure. In result, the ground state of the Ising model without NNN interactions is highly degenerate. Therefore, the inclusion of NNN interactions is an indispensable feature for modeling order-disorder transitions in single domain particles of FePt that possess little or no APBs. For keeping the model as simple as possible, it is sufficient to restrict the NNN interactions to unlike atoms only. In the following, the parameters $\varepsilon_2^{\mathrm{FeFe}}$ and $\varepsilon_2^{\mathrm{PtPt}}$ are therefore ignored and only $\varepsilon_2^{\mathrm{FePt}}$ is allowed to assume non-zero values.

## 4.3. Fitting of the model parameters

Interestingly, simultaneously with the work presented in this dissertation, effective Ising-type Hamiltonians have also been applied by other groups for investigating the ordering behavior in FePt nanoparticles [139–141]. Parameterizations of these models have been obtained by fitting the interaction parameters completely (Ref. [140]), or in part (Ref. [139]) to energies determined by *ab initio* calculations.

In the present work, a different approach has been pursued: The Ising-type Hamiltonian is applied for studying order-disorder phase transitions in Monte Carlo simulations by

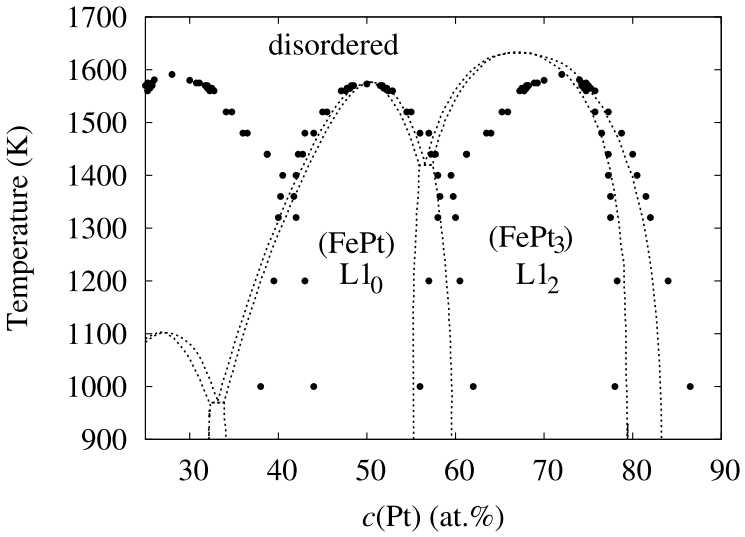


**Figure 4.2:** *Comparison of the phase diagrams of the Ising-type Hamiltonian (full circles) with the experimentally determined FePt phase diagram (dashed lines). The latter is plotted using data from Ref. [19].*

sampling the configurational entropy contributions. In a real FePt alloy, however, apart from this configurational entropy, the phase stability is also influenced by vibronic entropy contributions and by the degrees of freedom of the electronic spin system. This also includes the ferromagnetic-paramagnetic transition in the $L1_0$ ordered phase at 740 K [19]. As has already been shown in this work by the Gibbs free energy calculations of $\alpha$- and $\gamma$-iron in the analytic bond-order description (see Chapter 3.4), a fitting of effective Hamiltonians to zero Kelvin structural energies will in general not lead to a correct description of phase transitions. In this work, the interaction parameters have therefore been determined by fitting the Hamiltonian directly to the FePt phase diagram and to experimental results on the segregation behavior at free surfaces.

For determining equilibrium properties of the Ising-type Hamiltonian, a standard particle exchange Monte Carlo scheme has been applied. At each elementary step of the MC simulations, a pair of two neighboring atoms is picked randomly and the energy change for an exchange of the two atoms is calculated. The exchange is then accepted or declined according to the Metropolis algorithm. After the system has reached equilibrium from an arbitrarily chosen initial configuration, properties of interest (e.g. ordering, segregation) are sampled over a large number of MC steps. One MC step corresponds to N attempted exchanges of neighboring atoms, where N is the total number of atoms.

### 4.3.1. FePt Phase diagram

The model parameters $J_1$ and $J_2$ have been determined by adjusting the phase diagram of the Ising-type Hamiltonian to the bulk phase diagram of FePt. In doing so, a bulk

fcc lattice with 13500 sites (15x15x15 unit cells) and periodic boundary conditions in $x, y$ and $z$ direction have been applied. For fixed ratios $\alpha = J_2/J_1 = 0, 0.05, 0.1, 0.15, 0.2$, the parameter $J_1$ was varied until the correct ordering temperature of 1573 K is reproduced at the stoichiometric composition of $Fe_{50}Pt_{50}$: Starting with a completely disordered lattice, the simulation was run for 300000 MC steps at 1585 K and the temperature was then lowered by steps of 5 K to 1500 K. The final structure of each simulation was used as input structure for the simulation at the next lower temperature *. The transition from the disordered to the ordered state was detected by monitoring a long-range order (LRO) parameter as defined in Sec. 3.6.3. $J_1$ was then varied until the transition is situated in the temperature interval between 1570 K and 1575 K. Independence of the results from the input structures was verified by repeating the temperature series for the best fit with completely ordered as well as disordered input structures at each temperature.

Subsequently, the boundaries of the $L1_0$ ordered ($Fe_{50}Pt_{50}$) and $L1_2$ ordered ($Fe_{25}Pt_{75}$) phases have been determined for the given values of $\alpha$ and $J_1$: Close to the stoichiometric compositions, the ordering temperature was determined by running simulations with fixed composition at different temperatures following the same procedure as described before. The phase boundaries at compositions farther away from stoichiometry were determined by MC simulations in the grand-canonical ensemble, a method described in detail in Ref. [50]. The best fit was obtained for $\alpha = 0.2$, $J_1 = 0.0465\,\text{eV}$, which gives $J_2 = -0.0093\,\text{eV}$. A comparison of the experimentally determined phase diagram and the phase diagram of the Ising-type model is shown in Fig. 4.2.

An intrinsic feature of the Ising-type model with pair interaction energies is the symmetry of the phase diagram relative to the $Fe_{50}Pt_{50}$ composition [142]. Therefore, the model cannot reproduce all details of the asymmetric FePt phase diagram for all three ordered phases. Reproducing the asymmetry would require the inclusion of many-body interactions [143]. However, in the composition range that will be considered in this work (46 at. % Pt to 54 at. % Pt), the stability region of the $L1_0$ ordered phase is matched very well by the pair-interaction model. The lattice Hamiltonian also reproduces the two phase region separating the $L1_2$ ordered $FePt_3$ phase from the disordered substitutional Pt-rich solid solution. This feature is important, since the surface segregation behavior of the model has been fitted at the composition $Fe_{20}Pt_{80}$, as described in the next section.

*Since the equilibrium structures at two successive temperatures only differ slightly in general, this procedure reduces the number of MC steps needed to initially equilibrate the system at each temperature.

### 4.3.2. Order of the $L1_0$ to $A1$ phase transition

For the $L1_0$ to $A1$ order-disorder transition in FePt alloys, strong experimental evidence pointing to a first-order phase transition exists: The derivative of the LRO parameter has a discontinuity at the transition temperature of 1573 K [128], the $L1_0$ and $A1$ phases are separated by a two phase region and transitions between both phases proceed via nucleation and growth [128–130].

The order of phase transitions for Ising-type Hamiltonians has been investigated in several studies [134, 142, 144]. For second-nearest neighbor models with $\alpha = J_2/J_1 < 0.25$, the transition is of first order. In the present parametrization of the Hamiltonian derived by a fitting to the phase boundaries, this feature of the experimental phase diagram is therefore reproduced.

In contrast, for higher ratios $\alpha$, the transition becomes continuous in the Ising-type description [134, 144]. This is the case for the parametrization of the Hamiltonian derived by partly fitting to zero Kelvin structural energies from ab initio calculations in Ref. [139], where a very high ratio of $\alpha = 0.73$ was obtained. A continuous phase transition is also obtained for the Hamiltonian fitted purely to *ab initio* data of Ref. [140], where interactions up to third nearest neighbors have been included.

The fact that the latter two studies fail in describing the correct order of the transition supports the approach taken in this work that a fitting of effective Hamiltonians to experimental data leads to a physically more meaningful model description of the real system.

### 4.3.3. Surface segregation

With $J_1$ and $J_2$ fixed, the parameter $h$ has been determined by fitting the lattice Hamiltonian to experimental results on surface segregation in thin films. Quantitative studies of the segregation behavior of FePt systems exist for the (111) surface of an $Fe_{20}Pt_{80}$ alloy [145, 146]. It was found that at 1200 K, the (111) surface is enriched with Pt: the first layer consists of almost pure Pt (with a concentration of $96 \pm 4$ at. % [145]). The Pt concentration in the second and third layer is also increased ($84 \pm 7$ at. % and $85 \pm 15$ at. %, respectively [145]).

The dependence of Pt segregation on the parameter $h$ has been analyzed by using an fcc lattice with free (111) surfaces in the z-direction and periodic boundaries in x- and y-direction. The lattice consisted of 150 (111) layers with 1920 atoms per layer. The large number of (111) layers was necessary for making the two surfaces independent from

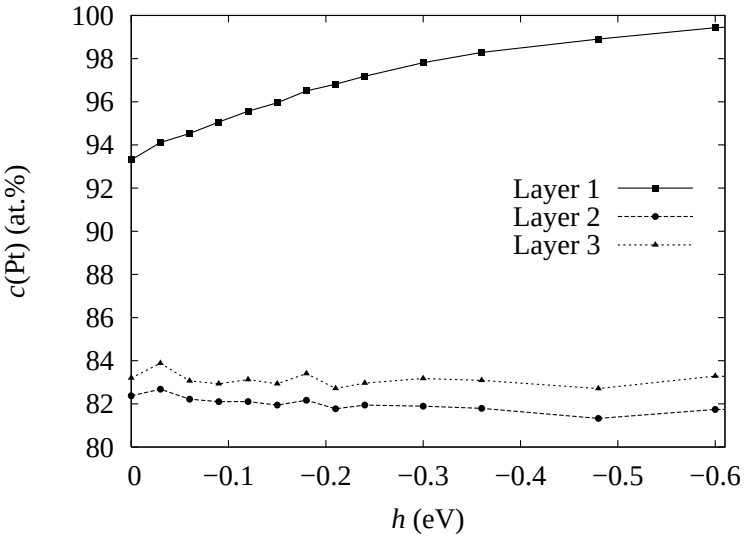


**Figure 4.3:** *Influence of the model parameter $h$ on the segregation of Pt at the (111) surface of a $Fe_{20}Pt_{80}$ alloy at 1200 K.*

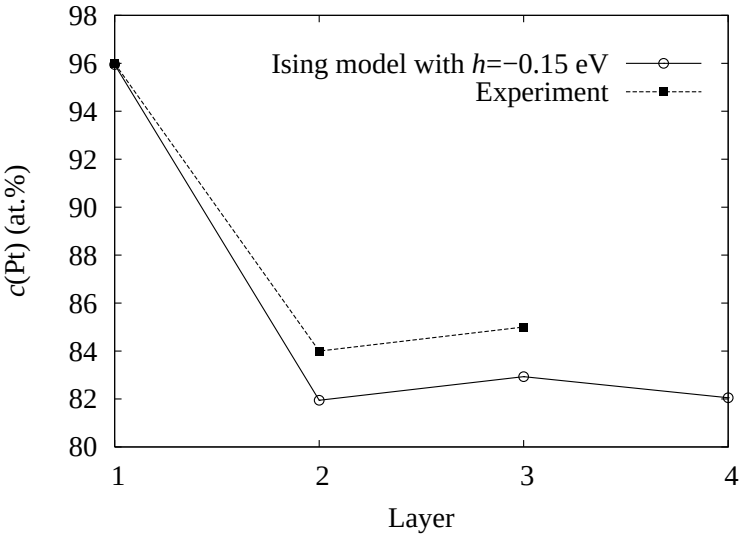


**Figure 4.4:** *Depth profile of the Pt concentration at the (111) surface of an $Fe_{20}Pt_{80}$ alloy at 1200 K. Comparison of experiments with the results of the Ising-type model for $h = -0.15\,\mathrm{eV}$.*

each other. For each value of the parameter $h$, the lattice was initialized with a random distribution of Fe and Pt atoms in the ratio 20/80. The concentration profile was then determined by taking the average over 90000 MC steps, after discarding the first 10000 MC steps. In all simulations, the temperature was set to 1200 K. Fig. 4.3 shows the Pt concentration in the first three surface layers as a function of the parameter $h$. As an effect of the ordering of the system [146], Pt is enriched in the first surface layer to approximately 93 at. % even without a driving force for surface segregation ($h = 0$). With increasing $h$, the Pt concentration in the first layer increases to almost 100 at. %. In contrast to the first layer, the Pt concentrations in the second and third layer hardly depend on the parameter $h$. However, Pt is enriched to approx. 82 at. % in the second and 83 at. % in the third layer. The experimental result of 96 at. % Pt in the first surface layer is reproduced best

**Table 4.2:** *Parameters of the Ising-type Hamiltonian.*

| Parameter | Value (eV) | Parameter | Value (eV) |
|---|---|---|---|
| $J_1$ | 0.0465 | $\varepsilon_1^{\mathrm{FeFe}}$ | 0 |
| $J_2$ | −0.0093 | $\varepsilon_1^{\mathrm{PtPt}}$ | 0.05 |
| $h$ | −0.15 | $\varepsilon_1^{\mathrm{FePt}}$ | −0.068 |
| | | $\varepsilon_2^{\mathrm{FeFe}}$ | 0 |
| | | $\varepsilon_2^{\mathrm{PtPt}}$ | 0 |
| | | $\varepsilon_2^{\mathrm{FePt}}$ | 0.0186 |

with the parameter $h = -0.15\,\mathrm{eV}$. The concentration profile corresponding to this best fit is compared to the experimentally determined profile in Fig. 4.4. The model exactly reproduces the Pt segregation in the first surface layer. It is also very reasonable for the second and third layers, where the calculated concentrations deviate from the experimental values by less than 2 at. %.

Interestingly, the same value for the parameter $h$ has been derived independently by Yang and coworkers [139, 141], applying the difference in surface energy of the two elements as a reference. This indicates that the chosen value represents a solid estimate of the driving force for surface segregation in FePt alloys.

The final parameter set of the Ising-type Hamiltonian is presented in Tab. 4.2.

## 4.4. Summary

In summary, an Ising-type Hamiltonian on a fcc lattice has been parameterized for studying order-disorder phase transitions in the FePt alloy system. In order to properly account for antiphase boundary energies, interactions have been extended to second-nearest neighbors. This also provides the necessary flexibility for fitting the effective lattice Hamiltonian to the bulk phase diagram of FePt. In particular, the temperature and the order of the $L1_0$ to $A1$ transition can be reproduced. The model parameter $h$, which is independent of the bulk phase diagram, has been fitted to segregation experiments on free FePt surfaces. The parametrization presented in Tab. 4.2 can therefore be applied for studying the interplay of surface segregation and ordering in FePt nanoparticles in the gas phase (Sec. 6.5.1). Alternatively, depending on the preparation process, FePt particles may also be dispersed in a matrix or coated by organic ligands, which can significantly alter the surface segregation behavior. The virtue of the Ising-type Hamiltonian is that simply by adjusting the surface segregation potential $h$, these different chemical surroundings can be accounted for without altering the characteristics of the order-disorder transition in the bulk phase (see Sec. 6.5.4).

# Part III.

# Structural properties of FePt nanoparticles

# 5. Structural stability of multiply twinned FePt nanoparticles

*In this chapter the structural stability of FePt nanoparticles in multiply twinned and single crystalline morphologies is investigated by means of molecular statics calculations based on the FePt bond-order potential. The results obtained from the atomistic calculations are used for validating a continuum model which allows to assess the contributions of elastic strain, surface and twin boundary energies, separately. The static model calculations predict a strong energetic preference for single crystalline morphologies in the ordered $L1_0$ and disordered $A1$ phases. If estimates of vibrational entropy contributions are taken into account, however, icosahedral particles can become thermodynamically stable at elevated temperatures. Based on these results, experimental observations of icosahedral FePt nanoparticles prepared by inert gas condensation are discussed.*

## 5.1. Introduction

FePt nanoparticles prepared by gas-phase synthesis exhibit non-crystalline multiply twinned structures under certain process conditions. For low carrier gas pressures, where a monodisperse size distribution can be obtained, icosahedral MTPs are predominant [18]. Single crystalline particles can only be obtained at higher gas pressures where a coalescence of the particles is unavoidable [18]. The same experiments also indicate that a size dependent transition from icosahedral to single crystalline structures may be present in FePt nanoparticles: The mean diameter of the icosahedral particles was 5.9 nm, while a larger size of 7.6 nm has been reported for the single crystalline particles [18].

For interpreting the experimental findings on the preference for multiply twinned or single crystalline FePt particles under different processing conditions, a detailed knowledge of the energetics of particles in the various conformations is essential. In order to establish

whether FePt nanoparticles exhibit a stability range for MTPs, the most stable particle morphology as a function of size has to be identified. Also, energy differences between the various shapes determine the driving force for transitions between the structural motives.

Energy considerations show that MTPs optimize the surface energy at the expense of elastic strain in the volume and twin boundary energies [11, 12]. In consequence, MTPs can be energetically favored over single crystalline shapes at small or intermediate particle sizes where the surface to volume ratio is sufficiently high. For elemental systems, this size dependent transition from multiply twinned to single crystalline particles has been shown for copper [12] and gold particles [13].

In the present chapter, the structural stability of FePt nanoparticles is investigated by atomic scale and continuum model descriptions. The size dependent energies of the different structural motives are calculated by atomistic simulations employing the FePt analytic bond-order potential (ABOP) described in Chapter 3. The results from atomistic calculations are then used for testing a continuum model which allows to assess the contributions of elastic strain, surface and twin boundary energies, separately. Based on these calculations, the energetic stability of multiply twinned FePt particles is predicted. Moreover, it is discussed to what extent entropy contributions to the free energy affect the structural stability.

## 5.2. Particle shapes

### 5.2.1. Single crystalline particles

In the case of single crystalline metal particles, the thermodynamically stable shape is determined by a Wulff-construction. If $d_{hkl}$ denotes the distance from the particle center of a $\{hkl\}$-facet with surface energy per unit area $\gamma_{hkl}$, then the Wulff construction states that the energy minimizing shape is characterized by a constant ratio $\gamma_{hkl}/d_{hkl}$ [147]. For many fcc metals the low index surface energies obey the ordering sequence $\gamma_{111} < \gamma_{100} < \gamma_{110}$.

In the limit of strong facetting ($\gamma_{110}/\gamma_{111} \geq \sqrt{3/2}$), the Wulff shape is a truncated octahedron surrounded by $\{111\}$ and $\{100\}$ facets [11], only. This shape is schematically depicted in Fig. 5.1.

In the strong facetting limit and for a given ratio $\Gamma = \gamma_{100}/\gamma_{111}$, the Wulff polyhedron for single crystalline particles can be constructed starting from a regular octahedron of side length $a$ with only $\{111\}$ facets, which are at a distance $d_{111} = a/\sqrt{6}$ from the center. By truncating the vertices of the octahedron at a distance $d_{100} = \Gamma a/\sqrt{6}$ from the center, six square $\{100\}$ facets of side length $l_{100} = a(1 - \Gamma/\sqrt{3})$ are laid open. The hexagonal $\{111\}$

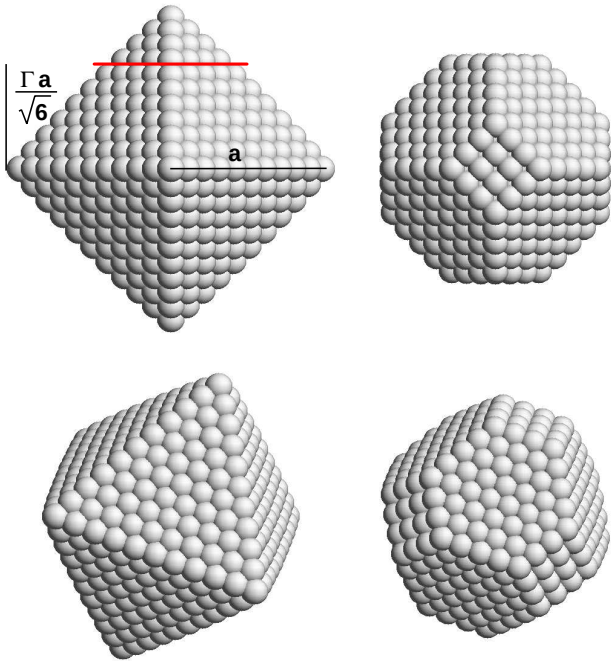


**Figure 5.1:** *Construction of a Wulff polyhedron from a regular octahedron in the strong facetting model.* $\Gamma$ *denotes the ratio of the* $\{100\}$ *to* $\{111\}$ *surface energies.*

facets are limited by three edges of length $l_{100}$ and three edges of length $l_{111} = a(2\Gamma/\sqrt{3}-1)$. For $\Gamma = \sqrt{3}/2$, $l_{111}$ becomes zero and the Wulff shape is a cuboctahedron. For $\Gamma = 2/\sqrt{3}$, the edge lengths are equal ($l_{100} = l_{111} = a/3$) and a regular truncated octahedron is obtained. For $\Gamma = \sqrt{3}$, $l_{100}$ vanishes and the octahedron remains uncut. For the following considerations, $\Gamma$ therefore has to obey the constraint $\sqrt{3}/2 \leq \Gamma \leq \sqrt{3}$.

The volume $V$ and the total area of $\{111\}$ and $\{100\}$ facets of the Wulff polyhedron can be expressed by

$$V = d_{111}^3 4 \left(\Gamma^3 - 3\sqrt{3}\Gamma^2 + 9\Gamma - 2\sqrt{3}\right) \tag{5.1}$$

$$A_{111} = d_{111}^2 \sqrt{3} \left(3\sqrt{3}\Gamma - \frac{3}{2}\Gamma^2 - 3\right) \tag{5.2}$$

$$A_{100} = d_{111}^2 2 \left(\Gamma^2 - 2\sqrt{3}\Gamma + 3\right). \tag{5.3}$$

For a Wulff polyhedron consisting of $N$ atoms with atomic volume $\Omega$, the volume is given by $V = N\Omega$, which leads to the condition

$$d_{111}(N) = (N\Omega/4g)^{1/3}, \tag{5.4}$$

with the geometry factor

$$g = \Gamma^3 - 3\sqrt{3}\Gamma^2 + 9\Gamma - 2\sqrt{3}. \tag{5.5}$$

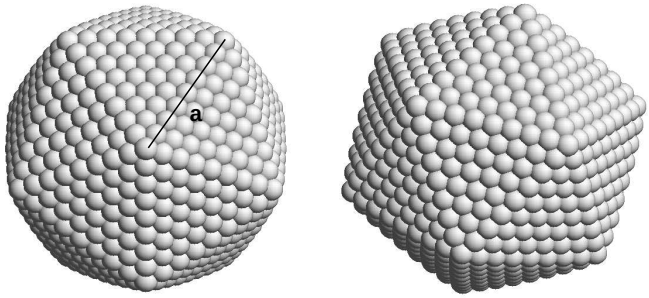


**Figure 5.2:** *Representation of an icosahedral MTP. With $a$, the edge length of a tetrahedral building block in the unstrained state is denoted.*

For distinguishing the various structures, two indices $(n_l, n_{\mathrm{cut}})$ are sufficient according to Baletto and Ferrando [7], where $n_l$ is the edge length (in number of atoms) of the uncut octahedron and $n_{\mathrm{cut}}$ is the number of layers cut from the vertices.

## 5.2.2. Icosahedral MTPs

The icosahedron is a possible shape for a MTP which has a low surface to volume ratio and is solely terminated by {111} facets [148]. It is depicted schematically in Fig. 5.2. An icosahedral particle can be built from 20 regular tetrahedra sharing a common vertex. For each of the tetrahedra, one of the {111} facets is on the surface, while the remaining facets form twin boundaries with the neighboring tetrahedra. In an icosahedral MTP this leads to 30 internal twin boundaries. Since this construction does not fill the volume and leads to a geometric gap, the tetrahedra have to be elastically strained. In general, icosahedral MTPs only occur if strain and twinning energies are smaller than the energy gain achieved by the formation of only low energy {111} facets. Icosahedral MTPs are therefore only energetically favored over single crystalline particles at very small particle sizes where the surface to volume ratio is sufficiently large [7, 10, 11, 149].

The size of a MTP can be related to the number of atoms $N$ if the particle volume is taken from the unstrained state. The volume, surface area and twin boundary area are then given by the following relations

$$V = \frac{5\sqrt{2}}{3}a^3, \tag{5.6}$$

$$A_{111} = 5\sqrt{3}a^2, \tag{5.7}$$

$$A_{\mathrm{twin}} = \frac{15\sqrt{3}}{2}a^2, \tag{5.8}$$

where $a$ is the edge length of an undistorted tetrahedral building block of the icosahedron.

With the replacement $V = N\Omega$, this leads to the condition

$$a(N) = \left(3N\Omega/5\sqrt{2}\right)^{1/3}. \tag{5.9}$$

The strain energy density $W_{\mathrm{Ic}}$ in icosahedral particles has been estimated by Ino [11], assuming homogeneous strains and linear displacements of the atoms. A refined estimate was proposed by Howie and Marks [149]. They consider angular and radial inhomogeneities of internal strain and find a smaller strain energy density $W_{\mathrm{Ic}}$ as compared to the result of Ino. For an elastically isotropic material with shear modulus $\mu$ and Poisson's ratio $\nu$, the strain energy density as derived by Howie and Marks is

$$W_{\mathrm{Ic}} = \epsilon_{\mathrm{d}}^2 \frac{2\mu(1+\nu)}{(1-\nu)\Omega}, \tag{5.10}$$

with $\epsilon_{\mathrm{d}} = 0.0205$ [149]. For modeling an elastically anisotropic cubic material, this relation will be used by replacing $\mu$ with the effective Voigt average of the two principal shear moduli $(c_{11} - c_{12} + 3c_{44})/5$ [150].

In addition to $W_{\mathrm{Ic}}$, Howie and Marks also introduce a surface stress term that is supposed to correct the surface energy of the strained particle [10, 149]. However, an analytic expression for this term is not available from literature.

According to Ref. [7], an icosahedron can be formally identified by a single index $k$, denoting the number of atomic shells building the particle.

### 5.2.3. Decahedral MTPs

Another family of MTPs is derived from a decahedron in the form of a pentagonal bipyramid. A decahedron is constructed by five regular tetrahedra sharing a common edge in $\langle 110 \rangle$ direction and each contributing two $\{111\}$ facets to the surface of the decahedron. Again, the tetrahedra have to be distorted for joining the remaining two $\{111\}$ facets with the neighboring tetrahedra. The strain energy density is considerably smaller than in the case of an icosahedron [149]. Because of their lower strain energy density, decahedral particles are often found to be the energetically most stable shape at intermediate particle sizes, between the stability ranges of icosahedral and single crystalline particles [7, 10, 11, 149].

A regular decahedron is surrounded by $\{111\}$ facets only, but its shape is far from being spherical and has a rather large surface to volume ratio. As depicted in Fig. 5.3, energetically more favorable shapes can therefore be obtained by truncating the decahedron along the edges, which exposes $\{100\}$ facets, and from the vertices, exposing reentrant $\{111\}$ facets. The corresponding star-like shapes are designated as Marks decahedra [7].

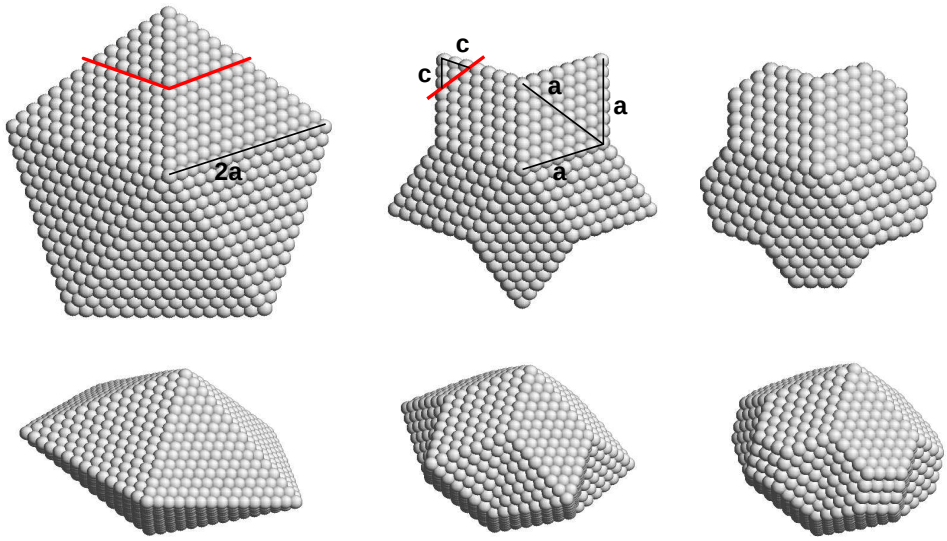


**Figure 5.3.:** *Construction of a Marks multiply twinned decahedron with reentrant* $\{111\}$ *facets and square* $\{100\}$ *facets starting from a regular decahedron. Lengths* $a$ *and* $c$ *are measured in the unstrained state.*

Following Ref. [7], Marks decahedra can be characterized by a triplet of integers $(m, n, p)$, where $m$ and $n$ are the number of atoms along the edges of the $\{100\}$ facets perpendicular and parallel to the fivefold $\langle 110 \rangle$ symmetry axis and $p$ is the depth of the reentrant $\{111\}$ facets.

Building analytic expressions for the volume, surface and twin boundary area in Marks decahedra that cover the whole range of possible index combinations in the triplet $(m, n, p)$ renders the treatment unnecessarily complex. The following considerations are therefore restricted to Marks decahedra with fixed reentrant size and square $\{100\}$ facets. The corresponding particles can be constructed from a decahedron as illustrated in Fig. 5.3. Starting from a regular decahedron composed of tetrahedra of edge length $2a$, 10 tetrahedra of edge length $a$ are cut from the corners, giving rise to a star-like shape with pointed tips having only $\{111\}$ facets. By furthermore truncating the tips of the star at a distance $c$ along the edge, square $\{100\}$ facets are exposed and the surface to volume ratio is

significantly reduced. For a given ratio $\lambda = c/a$, the volume, surface and twin boundary area of the Marks decahedron can now be given by

$$V = \frac{5\sqrt{2}}{2}a^3\left(1-\lambda^3/3\right) \tag{5.11}$$

$$A_{111} = 5\sqrt{3}a^2\left(\frac{3}{2}-\lambda^2\right) \tag{5.12}$$

$$A_{100} = 5a^2\lambda^2 \tag{5.13}$$

$$A_{\text{twin}} = \frac{15\sqrt{3}}{4}a^2. \tag{5.14}$$

$$\tag{5.15}$$

Matching the volume of $N$ atoms with the volume of the Marks decahedron gives

$$a(N) = \left(\frac{2N\Omega}{5\sqrt{2}(1-\lambda^3/3)}\right)^{1/3}. \tag{5.16}$$

In the remainder of this section $\lambda$ is fixed at 1/2, describing Marks decahedra of equal indices ($m = n = p$), which were found to best minimize energy in the atomistic calculations.

According to Howie and Marks, the strain energy density in decahedral particles is given by [149]

$$W_{\text{Dh}} = \epsilon_{\text{d}}^2\frac{\mu}{4(1-\nu)\Omega}. \tag{5.17}$$

with $\epsilon_{\text{d}} = 0.0205$.

## 5.3. Atomistic simulations

The molecular statics method has been employed for calculating the fully relaxed energy of FePt nanoparticles in single crystalline, multiply twinned icosahedral and multiply twinned decahedral morphologies. Interatomic interactions have been modeled by the FePt analytic bond-order potential developed in Chapter 3. Structural properties, surface and twin boundary energies of FePt in the $L1_0$ ordered and $A1$ disordered phases as described by the ABOP are summarized in Tab. 3.9 and Tab. 3.10. Notably, the twin boundary energy is comparably high and of the same order as in pure Pt [106]. The surface energies of the random $A1$ phase fulfill the condition of strong facetting ($\gamma_{110}/\gamma_{111} = 1.35$). The Wulff polyhedron is therefore only terminated by {111} and {100} facets.

For each structural motive, closed shell particles in the size range from 500 to 10000 atoms, corresponding to a diameter from 2.4 to 6.4 nm, have been generated by systematically scanning through all feasible combinations of integer indices (see Sec. 5.2) while the

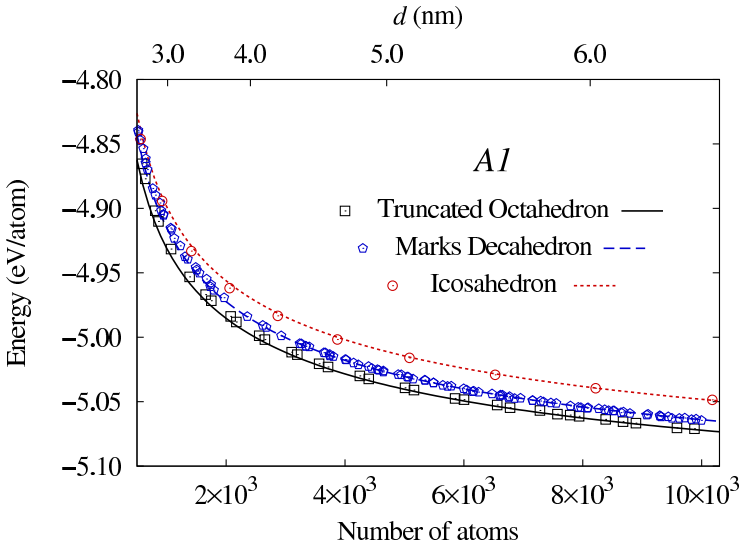


**Figure 5.4:** *Average potential energy for $A1$ disordered particles in different morphologies. Data points denote molecular statics calculations, curves are predictions of the continuum model Eq. (5.18).*

stoichiometry of Fe and Pt is fixed to a 1:1 composition. In case of disordered particles in $A1$ structure, energy fluctuations arising from a statistical distribution of atoms within the particle are minimized by averaging the energies of at least 20 different configurations.

In chemically ordered particles, the layered structure of the $L1_0$ phase leads to a deviation from the equiatomic composition of Fe and Pt (see Chapter 6, Ref. [151]). For comparing energies of different structural motives, particles of equal composition have to be considered. Therefore, an equiatomic composition is enforced by randomly distributing a corresponding number of anti-site defects within the ordered particles.

Furthermore, the icosahedron, which is composed of tetrahedral units with different orientations, does not allow the adjustment of $L1_0$ order without introducing additional anti-phase boundaries.

For identifying lowest energy configurations, ordered icosahedral particles have been generated by simulated annealing, employing a Metropolis Monte Carlo algorithm where atom displacements as well as atom exchanges are attempted and the temperature is lowered from 1200 to 0 K over a large number of $2 \times 10^4$ Monte Carlo steps. The structure proposed by the Monte Carlo simulation has then been further relaxed by the molecular statics method.

The particle energy as a function of cluster size is shown in Fig. 5.4 for single crystalline, decahedral and icosahedral particles in the random $A1$ phase. Since the particle energies vary with the shape of each structural motive, only the lowest energetic particles of each sequence are shown. For single crystalline particles in the random phase, truncated octahedra with relatively small $\{100\}$ facets are observed, described by the indices $n_{\mathrm{cut}} \approx 0.26 n_{\mathrm{l}}$. The ratio $d_{100}/d_{111}$ is then close to 1.284, which corresponds to the Wulff polyhedron de-

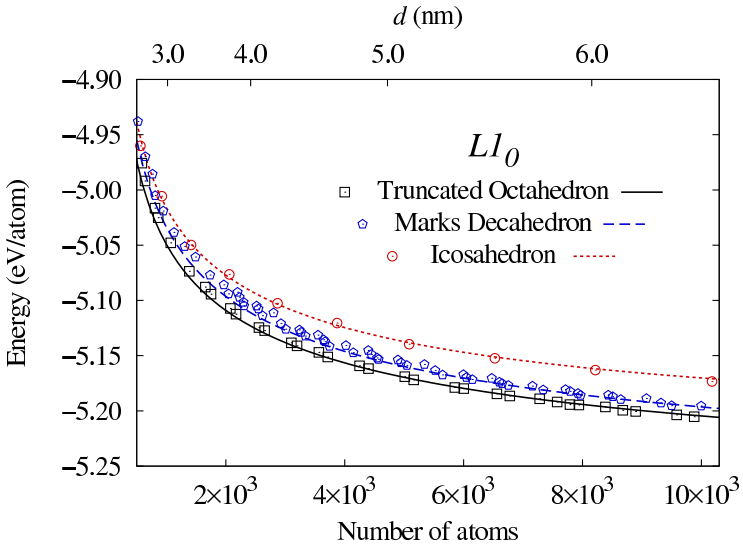


**Figure 5.5:** *Average potential energy for $L1_0$ ordered particles in different morphologies. Data points denote molecular statics calculations, curves are predictions of the continuum model Eq. (5.18).*

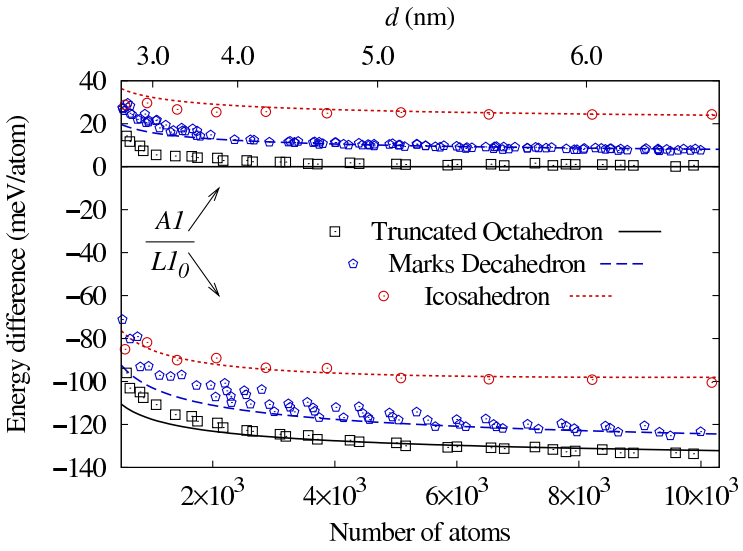


**Figure 5.6:** *Average potential energies for disordered and $L1_0$ ordered FePt particles in different morphologies, plotted relative to Eq. (5.18) applied to single crystalline particles in the $A1$ disordered phase.*

fined by the surface energies for the $A1$ phase listed in Tab. 3.10. In experiments, truncated octahedra with small {100} facets have indeed been found in as prepared particles from gas-phase synthesis [27]. For decahedral particles, the atomistic calculations predict that shapes with approximately equal indices $(m, n, p)$ are most favorable. These resemble the Marks decahedron depicted in Fig. 5.3 and have also been observed in gas-phase synthesis studies [27]. In general, even for the smallest particle sizes studied, the single crystalline shapes are energetically favored over MTPs by at least 10 meV/atom. Icosahedral particles exhibit a much higher energy than decahedral ones because of their higher internal strain and larger twin boundary areas. The same holds true if particles in the $L1_0$ structure are compared. As shown in Fig. 5.5, again it is observed that the single crystalline particles

are favored over both multiply twinned shapes. As a result of the anti-phase boundaries in icosahedral particles, their energy difference to the other morphologies is even increased compared to the disordered state.

A comparison between ordered and disordered particles is shown in Fig. 5.6. Here, the particle energies are plotted relative to a reference energy obtained from the continuum model for single crystalline particles, which is described in the next section (Eq. (5.18)). As expected, the ordered structures are energetically favored over the disordered ones in the $T = 0\,\mathrm{K}$ regime.

The results based on the atomistic calculations by means of an analytic bond-order potential do not provide evidence for an energetic stability of multiply twinned FePt nanoparticles. However, the large energy differences between icosahedral and decahedral particles on the one hand and single crystalline particles on the other hand can mainly be a consequence of the large twin boundary energy predicted by the FePt ABOP. Since calculations based on a potential description do not allow to assess the influence of single parameters (such as $\gamma_{\mathrm{twin}}$) independently, a more versatile continuum description of the particle energies is presented in the next section, which in return is benchmarked by the atomic scale simulations presented here.

## 5.4. Continuum model calculations

In the following a continuum model is applied that provides the possibility to assess the strain, twin boundary and surface energy contributions to the structural energy of the particles, separately. The model allows to investigate the influence of surface and twin boundary energies on the stability of MTPs beyond the values defined by the ABOP. As described in the last section, this becomes especially interesting considering that the comparison with electronic structure calculations suggest that the ABOP overestimates the twin boundary energy approximately by a factor 2, while it may somewhat underestimate the surface energies (see Tab. 3.10).

### 5.4.1. Model description

The energy of a nanoparticle can be approximated by the sum of volume, surface and twin boundary energy terms, if excess energies of edges and vertices are neglected:

$$E(N) = N(E_{\mathrm{c}} + W) + A_{\mathrm{twin}}(N)\gamma_{\mathrm{twin}} + \sum_{hkl} A_{hkl}(N)\gamma_{hkl}. \tag{5.18}$$

Here, $E_c$ is the cohesive energy per atom in the bulk phase and $W$ is an average strain energy per atom, which is zero for single crystalline particles. $A_{\text{twin}}$ and $\gamma_{\text{twin}}$ denote the twin boundary area and its energy. Furthermore, $A_{hkl}$ and $\gamma_{hkl}$ denote the total area and energies of the $hkl$ facets terminating the particle surface. For MTPs, Eq. (5.18) assumes that the only necessary correction due to the distortion of the tetrahedral building blocks is the additional volume strain energy density. The values of surface and twin boundary energies are considered unchanged as compared to the unstrained crystal.

Cleveland and Landman [12] validated this model for metallic nanoparticles without considering the energies of the twinning planes. They found a good agreement for single crystalline and decahedral nanoparticles, but failed to describe icosahedral particles with Ino's model [11] for the strain energy.

For describing FePt nanoalloys, the continuum model is extended by the excess energy contributions of the twin boundaries and the improved estimate for the strain energy in MTPs by Howie and Marks [149] is used. For the different morphologies, the size of surface and twin boundary areas as well as expressions for the strain energy density are given in Sec. 5.2.

### 5.4.2. Comparison with atomistic calculations

For validating the continuum model by comparison with the atomistic calculations, values for cohesive energies, elastic constants, surface and twin boundary energies predicted by the FePt ABOP are substituted into Eq. (5.18). For the random $A1$ phase, the values from Tab. 3.9 and Tab. 3.10 can be employed directly. However, for taking the anti-site defects in ordered particles into account, a volume term in addition to the $L1_0$ cohesive energy has to be considered. Also, the anti-phase boundaries in ordered icosahedral particles have to be modeled by an energy penalty that scales with $N^{2/3}$.

In Fig. 5.4, Fig. 5.5 and Fig. 5.6, the results from Eq. (5.18) are compared with the atomistic calculations. For disordered particles, where the continuum model can be applied without any adjustable parameters, an excellent agreement is found for all morphologies at particle sizes larger than 4 nm in diameter. In particular, it is evident that the refined estimate of strain energies by Howie and Marks (Ref. [149]) also allows to apply the model to icosahedral particles. Moreover, the agreement suggests that correction terms due to the strain in the surface of icosahedral particles are negligible. For ordered particles, accounting for anti-site defects by increasing the cohesive energy of the $L1_0$ phase by 6 meV/atom also leads to a good agreement between atomistic and continuum calculations. Furthermore, the

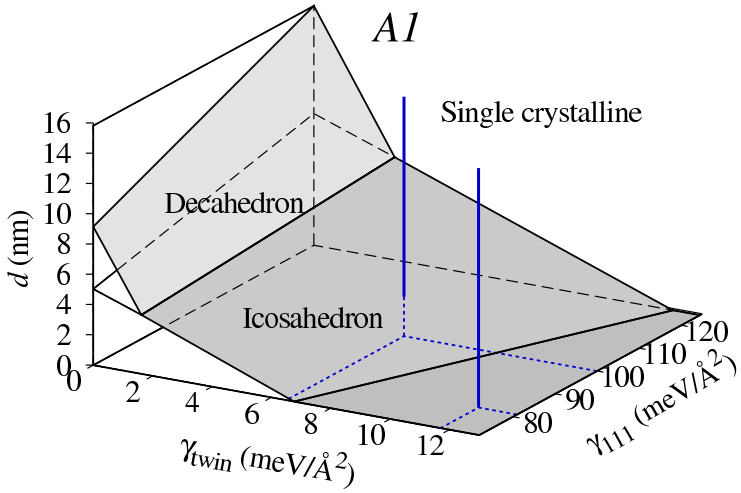


**Figure 5.7.:** *Stability of $A1$ disordered FePt particles in multiply twinned and single crystalline morphologies as obtained from Eq. (5.18) by varying surface and twin boundary energies. Shown are the boundary planes between stability domains of the various structural motives. Single crystalline particles are stable for particle sizes above the grey shaded area. The vertical lines indicate the $\gamma_{\mathrm{twin}}$ and $\gamma_{111}$ values predicted by the FePt ABOP and values estimated on the basis of first principles calculations [126, 132].*

anti-phase boundaries in icosahedral particles have been modeled by the term $2\times10^{-5}N^{2/3}$ added to Eq. (5.18).

For $d < 4\,\mathrm{nm}$, small deviations between the continuum model and the atomistic calculations occur. These can be attributed to the neglect of edge and vertex atom contributions in the continuum model, which become more important as the size reduces. As the size limit for a quantitative applicability of Eq. (5.18) coincides with the superparamagnetic limit in FePt nanoparticles, restrictions of the continuum model are negligible for applications where the hard-magnetic properties of the particles are of interest.

### 5.4.3. Assessment of surface and twin boundary energy contributions

Given the quantitative character of the continuum model, it can now be applied for investigating the stability of MTPs for surface and twin boundary energies beyond the values defined by the ABOP. For the $A1$ disordered phase, the energy of twinned and single crystalline particles have been calculated from Eq. (5.18) for twin boundary energies ranging from 0 to $13\,\mathrm{meV/\AA^2}$. The surface energy has been varied by adjusting $\gamma_{111}$ between 72 and $125\,\mathrm{meV/\AA^2}$ and keeping the ratio $\Gamma = \gamma_{100}/\gamma_{111}$ constant at the value predicted by the ABOP ($\Gamma = 1.284$). The data is used for evaluating the phase boundaries between

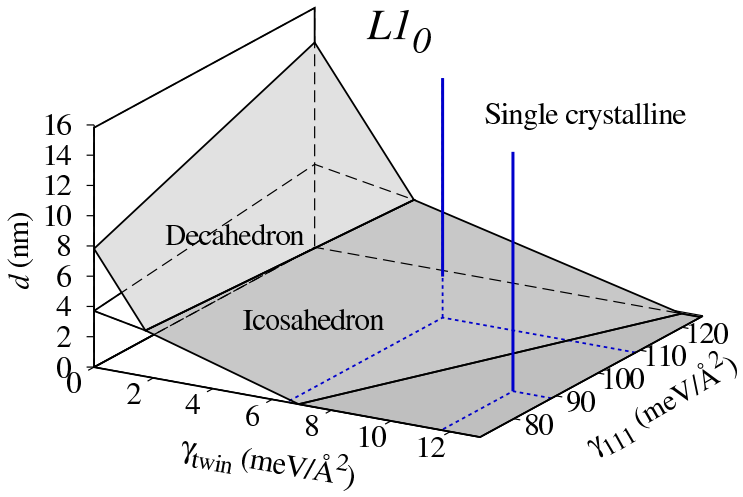


**Figure 5.8:** *Same as Fig. 5.7, except that the stability domains of $L1_0$ ordered particles are plotted.*

stability domains of decahedral, icosahedral and single crystalline particles. In Fig. 5.7, the most stable morphology for disordered particles is indicated as a function of twin boundary energy, surface energy and particle size.

Random FePt alloys described by the FePt ABOP are located in the region of parameter space where single crystalline particles are most stable at any size. However, Fig. 5.7 shows that a rather small reduction of $\gamma_{\text{twin}}$ and/or an increase of $\gamma_{111}$ leads to the stability of icosahedral particles at small sizes. In contrast, decahedral particles become stable at intermediate size ranges only for low twinning energies less than 3 to 4 meV/Å$^2$. Because of their larger twin boundary area, a reduction of $\gamma_{\text{twin}}$ has a higher impact on the stability of icosahedral than decahedral particles. Also, because of the lowest surface to volume ratio, an increase of surface energy favors the icosahedral shape over the competing morphologies.

Following the same procedure, a phase diagram has also been calculated for particles in the $L1_0$ ordered phase, as shown in Fig. 5.8. The features of this phase diagram are qualitatively the same as in Fig. 5.7. However, the different ratio of low-index surface energies and the additional incorporation of anti-phase boundaries in icosahedral particles restrict the stability of MTPs to lower sizes as compared to the disordered phase.

For estimating which set of $\gamma_{\text{twin}}$ and $\gamma_{111}$ energies best describes reality, reference values from first principles calculations have been considered for $L1_0$ FePt (see Tab. 3.10) [126, 132]. With 109 meV/Å$^2$, the (111) surface energy from DFT calculations is 22 % higher than the value given by the ABOP (89 meV/Å$^2$). In the case of $\gamma_{\text{twin}}$, the reference value only amounts to almost half the value predicted by the ABOP (6.5 as compared to 11.7 meV/Å$^2$). As shown in Fig. 5.8, for this combination of $\gamma_{\text{twin}}$ and $\gamma_{111}$ energies, the continuum model gives rise to the stability of icosahedral morphologies in the $L1_0$ ordered phase at very small particle sizes of $d < 2.7$ nm.

Furthermore, presuming that the relative deviations of the ABOP compared to these methods remain constant, a simple scaling may provide reasonable estimates also for reference values in the disordered phase. This procedure gives $\gamma_{111} \approx 100\,\mathrm{meV/\AA^2}$ (a $\approx 22\,\%$ increase of the ABOP value of $81\,\mathrm{meV/\AA^2}$) and $\gamma_{\mathrm{twin}} \approx 6.5\,\mathrm{meV/\AA^2}$ (the ABOP produces identical results for the twin boundary energy in the $A1$ and $L1_0$ phase). For this set of energies, the maximum diameter for stable icosahedrons in the disordered phase is 2.6 nm, as indicated in Fig. 5.7.

## 5.5. Role of Temperature

In the present study, stabilities of single crystalline and multiply twinned particles were discriminated solely by energy considerations and are therefore strictly valid only at zero Kelvin. It is well known from literature, however, that vibrational entropy contributions can lead to a crossover between structural motives at finite temperatures [152], because twinned particles exhibit softer vibration modes than single crystalline ones. Therefore, the effect of vibrational contributions to free energies can change the stability regions for FePt nanoparticles. In the following, we restrict ourselves to a simple estimate of the vibrational entropy contributions in FePt nanoparticles of 4 nm in diameter, which are the most relevant for the prospective applications. If we take surface and twinning energies from first principles calculations, the continuum model predicts a static lattice energy difference between the icosahedral structure and the truncated octahedron in the disordered phase of $\Delta E^{A1}_{fcc-ico} = 5.9\,\mathrm{meV/atom}$ and in the ordered phase of $\Delta E^{L1_0}_{fcc-ico} = 11.9\,\mathrm{meV/atom}$. The transition temperature can then be estimated by the relation [152]

$$T \approx \frac{\Delta E_{fcc-ico}}{3k_{\mathrm{B}} \ln \frac{\bar{\nu}_{ico}}{\bar{\nu}_{fcc}}}, \tag{5.19}$$

where $\bar{\nu}_{ico}$ and $\bar{\nu}_{fcc}$ are the average vibrational frequencies in the icosahedral and single crystalline particle. By adopting the value of $\bar{\nu}_{ico}/\bar{\nu}_{fcc} = 0.9798$ as reported by Doye and Calvo [152] for Lennard-Jones particles, a transition temperatures of 1100 K in the disordered phase and 2250 K in the ordered phase are predicted, if the size dependence of the frequencies is neglected. For comparison, the melting point is 1873 K and the order-disorder transition temperature $T_c$ is 1573 K [19].

From these simple estimates at $d = 4\,\mathrm{nm}$, ordered single crystalline particles should always be thermodynamically stable up to the order-disorder transition temperature. At $T_c$, the order-disordered transition is then accompanied by a simultaneous change of particle morphology, and disordered icosahedral shapes become stable up to the melting point.

For disordered particles with a diameter of 6 nm ($\Delta E^{A1}_{fcc-ico} = 9.6\,\mathrm{meV/atom}$), the estimated transition between single crystalline and icosahedral particles is about 1820 K, which is close to the melting point. This size should therefore approximately define the limit from which on MTPs are unstable in both the $L1_0$ and the $A1$ phase at all temperatures.

In the case of decahedral particles, smaller energy differences to single crystalline shapes are obtained from the continuum model. However, as the ratio of vibrational frequencies is close to one ($\bar{\nu}_{deca}/\bar{\nu}_{fcc} = 0.99826$), Eq. (5.19) predicts transition temperatures between single crystalline and decahedral particles well above the melting point. In this context, the decahedral morphology can therefore be disregarded.

## 5.6. Discussion

The considerations on particle energies and temperature effects provide a reasonable explanation for the predominance of icosahedral FePt nanoparticles prepared by inert gas condensation [18].

Since icosahedral particles are energetically most stable for small sizes below $d = 2.6\,\mathrm{nm}$, it is likely that icosahedral seeds evolve during the nucleation stage of inert gas condensation. When growing further, kinetic trapping of the particles in the metastable morphology can then lead to the presence of icosahedral particles even at larger sizes. According to Baletto and Ferrando, kinetic trapping is mainly responsible for the formation of large icosahedral MTPs during solid-state growth of metal systems [7].

Moreover, as the free energy difference between single crystalline and multiply twinned particles diminishes with increasing temperature, annealing processes at high temperatures will not have the desired effect of inducing the transformation towards single crystalline particles. The particles will remain in the disordered state, since icosahedral morphologies can be the thermodynamical stable structure at elevated temperatures.

For particles larger than 6 nm, the calculations suggest that single crystalline particles remain stable up to the melting point both in the ordered, as well as disordered state. This estimate is consistent with the crossing from icosahedral to single crystalline particles at $d > 6\,\mathrm{nm}$ in the gas-phase preparation process reported in Ref. [18].

The predominance of single crystalline morphologies from the solution phase synthesis route [14, 22] can be explained by the reduced surface energy of particles in solution. As is evident from Fig. 5.7 and Fig. 5.8, smaller surface energies extend the stability range of single crystalline particles.

## 5.7. Summary

The structural stability of FePt nanoparticles has been investigated by atomistic and continuum model calculations. The molecular statics method has been employed in conjunction with the FePt bond-order potential for calculating the energies of FePt nanoparticles in single crystalline as well as multiply twinned icosahedral and decahedral morphologies.

The results of the atomistic calculations have further been used for verifying the accuracy of a continuum model, describing particle energies solely by volume and surface energy contributions. In addition to previous applications [12], and owing to its importance in Pt alloys, the excess twin boundary energy has been included in the continuum model. Furthermore, an improved description of volume strain contributions in MTPs has been employed [149]. With these expansions, the applicability of the continuum model now extends to the icosahedral morphology. For particle sizes larger than $d = 4\,\mathrm{nm}$, an accurate agreement with particle energies from atomistic calculations could be demonstrated.

With the continuum model, the influence of surface and twin boundary energies on the relative stabilities of multiply twinned and single crystalline particles has been assessed. By employing $\gamma_{\mathrm{twin}}$ and $\gamma_{111}$ energies based on first principles calculations [126, 132], the calculations suggest that for particle sizes larger than 2.6 nm, single crystalline structures are energetically preferred. Simple estimates of temperature dependent entropy contributions [152], however, provide evidence that the icosahedral motive is becoming thermodynamically stable in the disordered state at elevated temperatures.

Based on these considerations, the observation of icosahedral particles in gas-phase condensation can be explained by the formation of stable twinned structures during nucleation that are kinetically trapped up to larger sizes. Because of the larger vibrational entropy in icosahedra, annealing processes at high temperatures fail to induce a transformation to single crystalline structures. Furthermore, the crossing of the predominant structural motive observed in experiments at $d > 6\,\mathrm{nm}$ (Ref. [18]) coincides with the estimated size limit from which on single crystalline particles are stable up to the melting point. Instead, the predominance of crystalline particles from solution phase synthesis is a result of the reduced surface energy contributions.

# Part IV.

# Thermodynamics of ordering in FePt nanoparticles

# 6. Thermodynamics of the ordering transition in FePt nanoparticles

*In this chapter the thermodynamics of ordering in FePt nanoparticles is investigated by Monte Carlo simulations. By applying both the FePt bond-order potential and the Ising-type lattice Hamiltonian for analyzing the size dependence of the ordering temperature, the validity of the simple lattice model for describing ordering phenomena in small particles is verified. With the efficient Ising-type Hamiltonian, the influence of composition and surface segregation on the $L1_0$ to $A1$ transition is discussed. Owing to its flexibility, different chemical surroundings can be imitated by adjusting the segregation tendencies of the elements, leading to the observation of the most pronounced effects on ordering.*

## 6.1. Introduction

An intriguing finding by various experimental studies on FePt nanoparticles is that the disordered phase is still predominant even after heat treatment at temperatures where the chemically ordered structure represents the equilibrium phase in bulk materials. It is not clear whether the difficulties in transforming isolated particles into the ordered $L1_0$ phase are due to kinetic limitations, or whether size effects lead to a depression of the thermodynamic ordering temperature.

In the present chapter this problem is addressed by describing a series of Monte Carlo (MC) simulations, aimed at giving a detailed insight into the thermodynamics of the $L1_0$ to $A1$ transition in FePt nanoparticles. In order to investigate the influence of particle size on the ordering transition, the numerically efficient Ising-type lattice Hamiltonian described in Chapter 4 has been applied. For selected particle sizes, the predictions of the Ising-type model are compared to simulations employing the FePt analytic bond-order potential (ABOP) from Chapter 3. This procedure allows to assess the influence of strain

in particles arising from the tetragonal distortion of the $L1_0$ structure, separately. Only small differences between the two models are found. This verifies the validity of the simple lattice Hamiltonian for describing ordering phenomena in small particles.

Given the numerical efficiency of the Ising-type model, the influence of a wide parameter space on the ordering behavior can now be encompassed, including variations of particle size and composition. Additionally, the Ising-type Hamiltonian provides the flexibility for modifying the surface segregation potential $h$ without affecting the bulk phase diagram (see Chapter 4). Therefore, the influence of different chemical surroundings that alter the preference for surface segregation can also be examined.

In the following sections, the particle shape assumed in the simulations is discussed and an outline of the simulation method is given. Subsequently, the comparative study between the ABOP and Ising-type models is presented. Finally, an extended study on the ordering behavior in FePt nanoparticles using the Ising-type model is given and the results are discussed in the context of experimental findings.

## 6.2. Particle shape

In the present work, equilibrium shapes of FePt nanoparticles have already been investigated in Chapter 5. In the case of particles prepared by solution phase synthesis, lowered surface energy contributions stabilize the crystalline morphologies. For FePt nanoparticles from the gas phase, the calculations in Chapter 5 demonstrate that only in disordered particles up to 6 nm, vibrational entropy contributions can lead to a crossing of the equilibrium structural motive to icosahedrons. Based on thermodynamic considerations, accounting for twinned shapes is therefore only relevant for $d \lessapprox 6\,\mathrm{nm}$. On the other hand, if a particle has once been prepared in the crystalline state, kinetic arguments render a transformation into the icosahedral shape unlikely, since it requires the nucleation of partial dislocations. For investigating equilibrium *ordering*, it is therefore a reasonable assumption to consider single crystalline particles only.

In the Ising-type Hamiltonian, surface energies are determined simply by the number of broken bonds on a given facet. For a face centered cubic lattice, the ratio of {100} to {111} low index surface energies is then given by $\gamma_{100}/\gamma_{111} = 2/\sqrt{3}$ and from the Wulff construction (see Sec. 5.2.1) it follows that the energy minimizing shape is a regular truncated octahedron (TO).

In Fig. 6.1, an ideally $L1_0$ ordered regular TO with 9201 atoms (diameter $d = 6.3\,\mathrm{nm}$) is depicted. The surface of the TO consists of 8 {111} and 6 {100} facets. If the $L1_0$

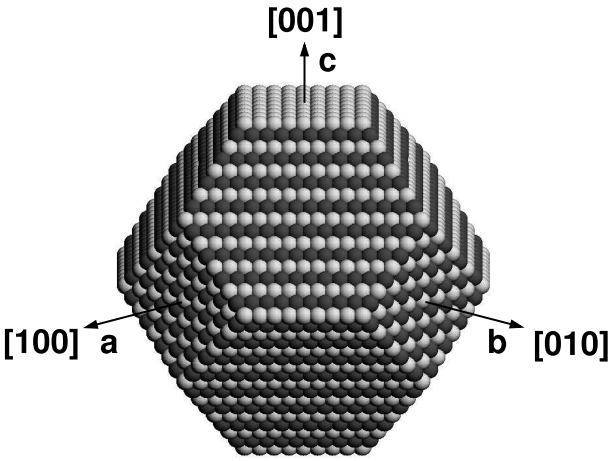


**Figure 6.1:** *Illustration of a completely $L1_0$ ordered regular truncated octahedron with 9201 atoms ($d = 6.3$ nm).*

structure is ordered along the crystallographic $c$ direction, then the two (001) facets are occupied by either pure Fe or pure Pt, depending on whether the ordered structure starts with an Fe or Pt layer. The (100) and (010) facets are occupied by the same number of Fe and Pt atoms (not counting the edges). An edge at the junction of two facets can also be occupied by either pure Fe or pure Pt, or can be alternately occupied by Fe and Pt atoms.

The composition of an ideally $L1_0$ ordered regular TO deviates from perfect stoichiometry because of constrictions imposed by the lattice structure and particle shape. Depending on whether the (001) facets are pure Fe or Pt, the overall concentration of Fe (Pt) is 51.54 at. % for a TO with 586 atoms ($d = 2.5$ nm). With increasing size, this deviation decreases and the concentration of Fe (Pt) reaches 50.31 at. % for a TO with 23178 atoms ($d = 8.5$ nm).

In order to analyze the dependence of ordering on particle size and composition, particles of truncated octahedral shape containing 586 to 23178 atoms have been considered, corresponding to diameters of 2.5 to 8.5 nm. The correlation between diameter and number of atoms in FePt particles is listed in Tab. 6.1.

## 6.3. Simulation method

For determining equilibrium properties of FePt particles described by the Ising-type Hamiltonian a particle exchange Monte Carlo scheme has been applied. At each elementary step of the MC simulations, a pair of two neighboring atoms is picked randomly and the energy change for an exchange of the two atoms is calculated. The exchange is then accepted or declined according to the Metropolis algorithm.

**Table 6.1:** *Correlation between particle size and number of atoms for regular truncated octahedral shaped FePt particles.*

| Diameter (nm) | Number of atoms |
|---|---|
| 2.5 | 586 |
| 3.3 | 1289 |
| 4.0 | 2406 |
| 4.8 | 4033 |
| 5.5 | 6266 |
| 6.3 | 9201 |
| 7.0 | 12934 |
| 7.8 | 17561 |
| 8.5 | 23178 |

For each particle size and composition, a series of MC simulations at temperatures ranging from 300 K to 1575 K has been run. Each series was started at the highest temperature, using a completely disordered particle as input structure. The output of the simulation was then handed over as input for the next lower temperature. At each temperature configurations were sampled at least over 90000 MC steps after discarding the first 10000 MC steps. In simulations employing the FePt ABOP, trial steps in the MC algorithm additionally include small displacements of atomic coordinates.

## 6.4. Comparison of the Ising-type Hamiltonian and ABOP models

In order to evaluate the differences between the Ising-type and ABOP models, particles with diameters of 4 and 4.8 nm have been considered. For enabling a direct comparison, a regular truncated octahedral shape of the particles has also been assumed in the simulations employing the ABOP. Note, however, that from the high ratio of the (100) to (111) surface energies of the FePt $A1$ phase listed in Tab. 3.10, the Wulff construction for the ABOP predicts an equilibrium shape with smaller (100) facets than in the regular TO. For assuring that changes in the facet sizes do not alter the results significantly, particles with the correct Wulff shape have also been included in the ABOP calculations. Within the statistical error, however, these calculations have led to the same results and are therefore not discussed in the following.

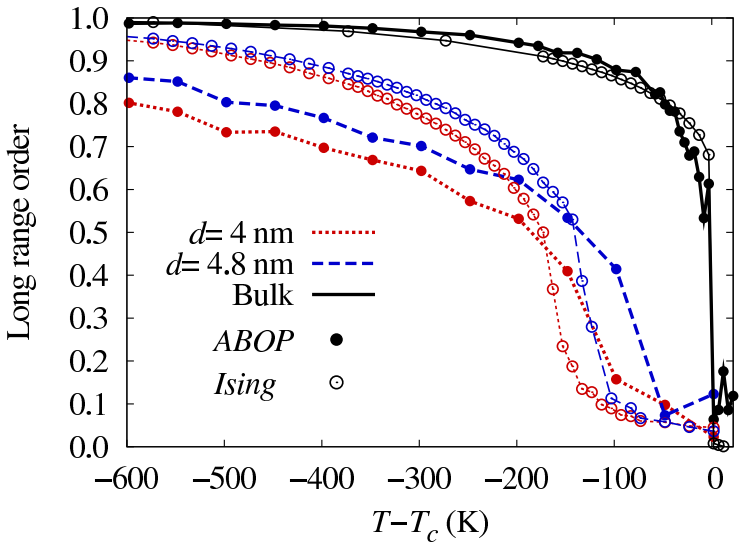


**Figure 6.2:** *Variation of LRO parameter with temperature in FePt nanoparticles compared to the bulk phase. Data obtained from the ABOP and from the Ising-type lattice Hamiltonian is plotted. The temperature axis is taken relative to the order-disorder transition temperature in the bulk phase ($T_c$).*

### 6.4.1. Transition temperature

The order-disorder transition in FePt nanoparticles has been investigated for both models by off-lattice and lattice based MC calculations monitoring the long-range order (LRO) parameter defined in Sec. 3.6.3 over a wide temperature range. The results are plotted in Fig. 6.2. Two general trends, both in the Ising model and the ABOP description are clearly visible: With decreasing particle size, the transition from the ordered to the disordered phase is shifted towards lower temperatures and becomes continuous. At moderate temperatures, the amount of ordering in particles is clearly reduced as compared to the bulk FePt phase.

Interestingly, in the continuum ABOP description, the shift of the order-disorder transition temperature with decreasing particle size is even less pronounced than for the Ising-type lattice Hamiltonian. By taking the highest slope of the curves in Fig. 6.2 as a measure for the transition temperature, the depression of ordering temperature is roughly 80 K for the 4.8 nm particle and 120 K for the 4 nm particle. For the Ising-type Hamiltonian, the values are 120 K at 4.8 nm and 160 K at 4 nm, respectively. These small differences between the two models indicate that the lattice strain that arises from the tetragonal distortion of the $L1_0$ structure does not significantly affect the depression of ordering temperature.

Although the ABOP predicts a slightly less pronounced depression of the transition temperature, Fig. 6.2 shows that the equilibrium degree of order at moderate temperatures predicted by the ABOP is lower than in the Ising-type model. At 1000 K (which is approx. 600 K below the bulk transition), with only 85 % in particles of 4.8 nm and only 80 % in particles of 4 nm, the degree of ordering is clearly reduced in the ABOP. In contrast, with

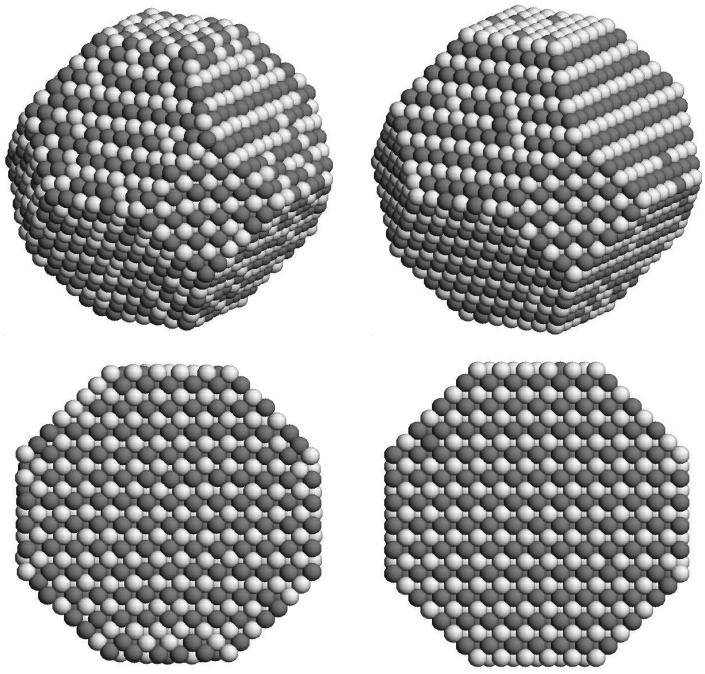

(a) ABOP (b) Ising-type Hamiltonian

**Figure 6.3:** *Snapshots of approx. 4.8 nm particles from MC simulations at 1000 K for a) the ABOP and b) the Ising-type Hamiltonian. In the bottom row, cross sections through particle centers are shown.*

more than 95 % ordering for both particle sizes, the Ising-type model predicts significantly higher values for the LRO parameter at the same temperature. As demonstrated in the following, this difference arises from surface contributions to the disorder, which are of different magnitude in the two models.

## 6.4.2. Surface induced disorder

In Fig. 6.3, snapshots of 4.8 nm particles from simulation runs at 1000 K are compared. The cross sections through the particle centers in the bottom row of Fig. 6.3 demonstrate that, for the ABOP as well as the Ising-type model, complete order is preserved in the particle volume. In both cases, the reduced LRO parameter can therefore only be explained by a certain degree of disorder at the particle surface. As can be seen in the top row of Fig. 6.3, MC simulations employing the ABOP result in a large number of surface anti-site defects, leading to an overall reduced LRO parameter. In contrast, the Ising-type Hamiltonian only gives rise to a small amount of surface disorder at 1000 K, which explains the higher value of the overall LRO parameter in this case.

Reduced ordering at the particle surface as compared to the volume can be explained by the lower coordination of surface atoms. In the Ising-type Hamiltonian, each broken bond decreases the driving force of an atom to occupy the correct sublattice, while the

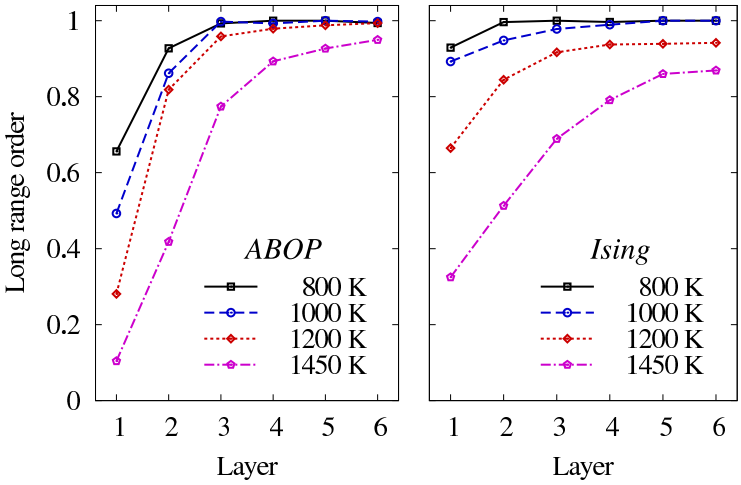


**Figure 6.4:** *Profiles of LRO parameter for particles of approx. 4.8 nm in diameter. Following Ref. [141], a particle is divided into layers based on the distance $r$ from the particle center. Layer 1 contains atoms for which $r \geq 2.2$ nm. The subsequent layers 2 to 5 are shells of width 0.3 nm, each. Finally, layer 6 contains the atoms in the particle core with $r < 1$ nm.*

particle can gain configurational entropy by increasing the disorder. In addition to this, vibrational displacements of surface atoms contribute to the particles free energy within the more refined simulations based on the ABOP. A possible explanation for the larger surface disorder in the ABOP is that the average frequencies of the soft surface phonons are lower for the disordered than for the ordered structure, providing an additional driving force for surface induced disorder (SID).

In a recent theoretical study of FePt nanoparticles based on a lattice Monte-Carlo scheme, Yang and coworkers [141] also identified the presence of SID at temperatures where the particle bulk still remains ordered. They demonstrated that SID is responsible for the pronounced continuous nature of the order-disorder transition in small particles. In the SID mechanism, the disordered layer initiated at the surface grows continually with increasing temperature, eventually transforming the whole particle.

Considering the even higher amount of SID at moderate temperatures together with the slightly higher transition temperature in the ABOP description, it is interesting to compare how the disorder evolves with temperature in both models. For doing so, LRO parameter profiles of 5 nm particles are plotted for different temperatures in Fig. 6.4. Following Ref. [141], particles have been divided into layers defined by spherical concentric shells around the particle center. From this plot the differences between the ABOP and the Ising-type model are clearly visible. While the ABOP predicts a higher amount of disorder in surface near regions at all temperatures, the progression of disorder through the particle volume occurs at a lower rate with increasing temperature. At 1450 K, where the average LRO parameter is identical in both models (see Fig. 6.2), the central layers still remain highly ordered in the ABOP model. In contrast, a somewhat reduced ordering is predicted

by the Ising-type Hamiltonian within the whole particle, which explains that the transition is completed at somewhat lower temperatures.

### 6.4.3. Conclusions

There are only small differences between the predictions of the ABOP and the Ising-type model on the ordering behavior in FePt nanoparticles. Most notably, the ABOP predicts a higher amount of surface induced disorder, reducing the overall LRO parameter by up to 20 % at a moderate temperature of 1000 K. This difference can be attributed to the vibrational entropy contributions. On the other hand, including strain effects by the tetragonal distortion of the $L1_0$ phase does not have a significant influence on the results. In the investigated 4 nm and 4.8 nm particles, the ordering transition is even located at slightly higher temperatures when investigated by the ABOP.

The close agreement between the results obtained from the more sophisticated ABOP and the coarse grained Ising-type model proves that simple lattice-based Hamiltonians are an appropriate model for investigating size effects in alloy nanoparticles. Therefore, the Ising-type model is employed in the next section for a more detailed analysis of the thermodynamic ordering behavior in FePt nanoparticles.

## 6.5. Ising-type lattice Hamiltonian study

As the Ising-type lattice Hamiltonian allows a very efficient calculation of configurational energies, it allows to sample a wide parameter space by Monte Carlo simulations. In the following, the influence of temperature, composition, size and surface segregation potential on the ordering behavior of FePt nanoparticles is investigated.

### 6.5.1. Ordering and surface segregation behavior

To begin with, the dependence of particle structure on composition at 300 K has been studied. At this point, only results for a 7 nm (12934 atoms) particle are reported. These are representative for all other particle sizes, too. Typical configurations for varying compositions at 300 K are shown in Fig. 6.5. At all compositions, $L1_0$ ordered single domain particles free of antiphase boundaries (APBs) have been obtained.

If the $c$-axis of the $L1_0$ structure is taken parallel to the [001] direction, then (001) planes are occupied alternatingly by Fe and Pt atoms. Because of the tendency of Pt atoms to segregate on the surface (surface segregation potential $h < 0$, see Sec. 4.3.3), the

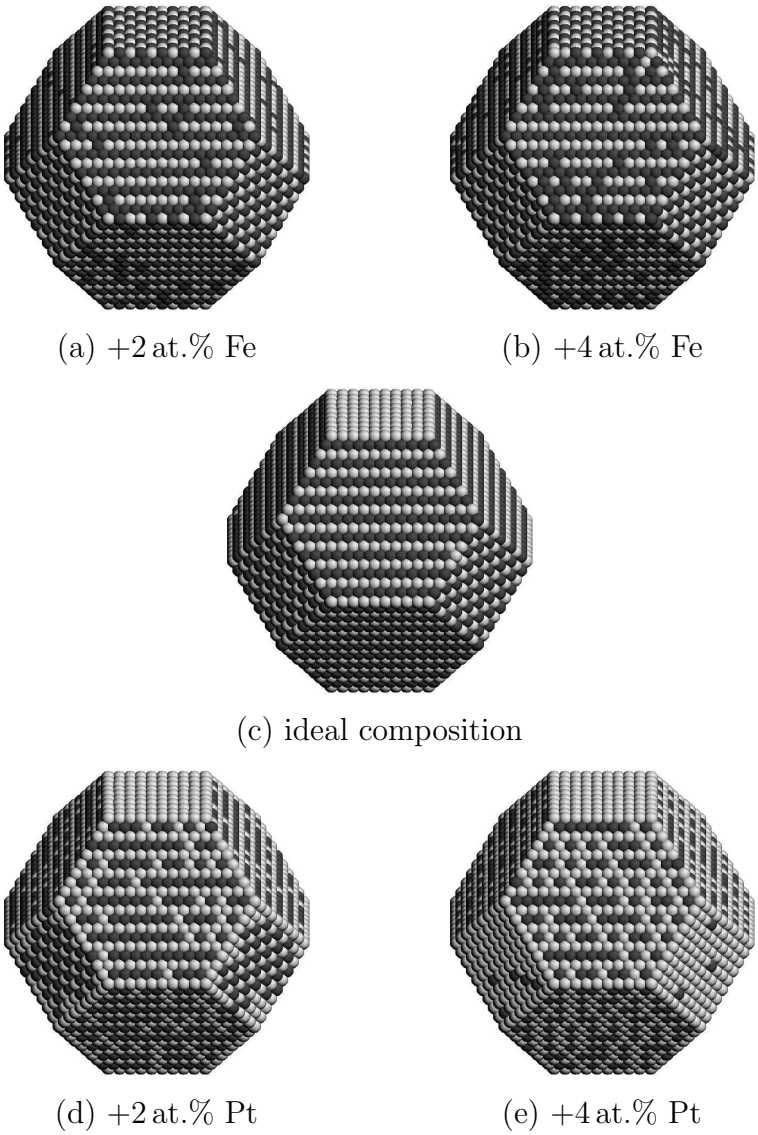

(a) +2 at.% Fe (b) +4 at.% Fe

(c) ideal composition

(d) +2 at.% Pt (e) +4 at.% Pt

**Figure 6.5:** *Structure of particles with $d$=7.0 nm (12934 atoms) after simulation at 300 K. The particle concentration varies from* $+4\,\mathrm{at.\,\%}$ *Fe to* $+4\,\mathrm{at.\,\%}$ *Pt relative to the concentration of an ideally ordered TO. Pt atoms are displayed light grey, Fe atoms dark grey.*

outer (001) facets of the particle are either fully occupied by Pt atoms (Figs. 6.5 c,d) or are enriched with Pt, even if Fe atoms are available in excess (Figs. 6.5 a,b). Therefore, independent of composition, the ordered structure of all particles exhibits a Pt-Fe-...-Fe-Pt stacking sequence in [001] direction.

As can be seen in Fig. 6.5, a large fraction of excess atoms in particles with non-ideal composition segregate on the particle surface. For particles with an excess of Fe atoms Fe segregates preferentially on the Pt (001) facets, forming an ordered superstructure corresponding to the (100) and (010) facets (Fig. 6.5 a and b). Segregation of Pt in particles with an excess of Pt atoms (Fig. 6.5 d and e) starts at the edges of the TO. Once the edges are occupied almost entirely by Pt atoms, segregation can also be observed on

**Table 6.2:** *Energies for replacing an Fe atom by an excess Pt atom at different sites of an ideally $L1_0$ ordered regular TO.*

| Site | $\Delta E$ | $\Delta E$ (eV) |
|---|---|---|
| Volume | $8J_1 - 2h - 12J_2$ | 0.7836 |
| (111) Surface | $6J_1 - \frac{3}{2}h - 6J_2$ | 0.5598 |
| (100) Surface | $8J_1 - \frac{4}{3}h - 10J_2$ | 0.665 |
| (111)/(111) Edge | $6J_1 - \frac{7}{6}h - 4J_2$ | 0.4912 |
| (100)/(111) Edge | $6J_1 - \frac{7}{6}h - 4J_2$ | 0.4912 |
| Corner | $4J_1 - h - 4J_2$ | 0.3732 |

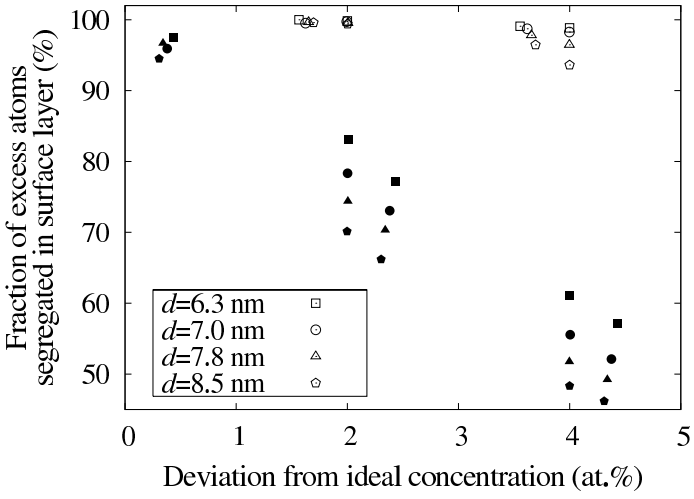


**Figure 6.6:** *Analysis of the surface segregation behavior in FePt nanoparticles. The fraction of excess atoms segregating on the surface is plotted over the deviation of the particle composition from the respective ideal composition. Open symbols: particles with excess Pt; Solid symbols: particles with excess Fe.*

the (111) and (100) facets, the last showing an almost complete coverage with Pt for high Pt concentrations (Fig. 6.5 e).

The energies for replacing an Fe atom by an excess Pt atom at various sites of an ordered particle are listed in Tab. 6.2. From this table, it is evident why excess Pt atoms first segregate on the edges of Pt rich particles: Replacing an Fe atom by a Pt atom at an edge site costs the least amount of energy. However, the tabulated energies cannot explain why Pt occupies only every second site on the (111) facets, while the (100) facets are almost completely covered with Pt. The reason for this is that Tab. 6.2 only lists the energies for replacing an Fe atom that has a completely ordered surrounding. If the atom already has a Pt atom occupying a wrong lattice site in its neighborhood, the energy for replacing this atom increases for the case of the (111) facet to $10J_1 - \frac{3}{2}h - 6J_2 = 0.7485\,\mathrm{eV}$, while it decreases for the (100) facet to $8J_1 - \frac{4}{3}h - 6J_2 = 0.6278\,\mathrm{eV}$. Therefore, it becomes more favorable for Pt atoms to occupy (100) facets with increasing level of segregation.

The amount of surface segregation for both Fe and Pt atoms is analyzed quantitatively in Fig. 6.6, where the fraction of excess atoms segregated on the surface layer is plotted over

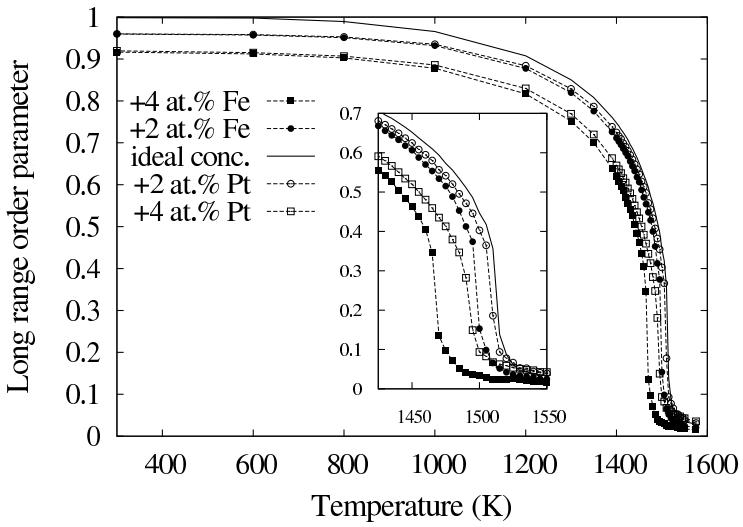


**Figure 6.7:** *Variation of LRO parameter with temperature for 7 nm particles with different composition. The inset shows a magnification of the region around the order-disorder transition.*

the deviation of the overall particle from the ideal composition. It is shown that virtually all excess Pt atoms are located at the surface, leaving the bulk of the particle free of antisite defects. The situation is different for particles enriched with Fe, where the surface can only accommodate a small number of excess Fe atoms. For larger deviations from the ideal composition, a considerable number (up to approx. 50 %) of excess Fe remains in the volume of the particles.

### 6.5.2. Influence of particle composition on the ordering behavior

In Fig. 6.7, the ordering behavior of 7 nm particles with Pt concentrations deviating from the ideal composition is depicted. For all other particle sizes, the composition dependence of ordering is qualitatively the same and is therefore not shown here.

Excess atoms in ordered particles with non-ideal composition have to occupy sites of a wrong sublattice and therefore inevitably lead to disorder in the particle. In effect, particles with non-ideal composition cannot attain a completely ordered structure at low temperatures, as can be seen in Fig. 6.7.

Also, Fig. 6.7 shows that the transition from the disordered to the ordered phase is shifted towards lower temperatures with increasing deviation from the ideal composition. For a quantitative comparison, the ordering temperatures of the particles have been determined and are shown in Fig. 6.8. Since the order-disorder transition in the particles is continuous, the ordering temperature has been defined by the highest slope in the LRO over temperature plots. From Fig. 6.8, it is apparent that the reduction of ordering temperature is more pronounced for particles enriched with Fe than for particles enriched with Pt.

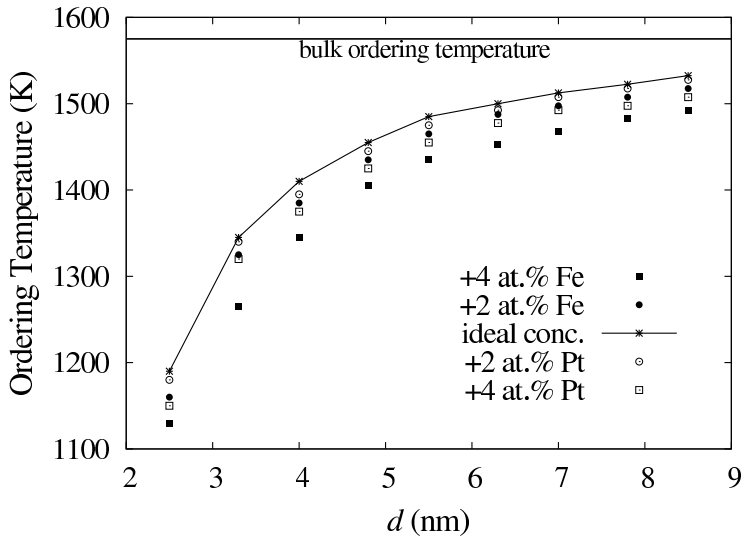


**Figure 6.8:** *Variation of ordering temperature with particle size and composition.*

For example, the ordering temperature of particles with 2 at. % excess of Pt atoms is only slightly decreased compared to particles with ideal composition. In contrast, the particles with an excess of Fe atoms of 2 at. % show a clear reduction of ordering temperature, which is about 20 K.

The fact that particles with an excess of Fe atoms exhibit a stronger reduction of ordering temperature can be explained by the different surface segregation behaviors of Fe and Pt. As was demonstrated in the last section, almost all excess Pt atoms segregate on the particle surface, while a considerable fraction of excess Fe remains in the volume of Fe rich particles. From the definition of the LRO parameter in Sec. 3.6.3, it follows that the amount of disorder introduced by an excess atom itself is independent from whether it occupies a surface or a bulk site. However, an atom occupying a wrong lattice site favors the introduction of additional disorder in its surrounding. As a consequence of its higher coordination, an excess Fe atom in the volume facilitates the exchange of a larger number of pairs than an excess Pt atom on the surface. It will therefore lead to a higher degree of disorder, which explains the larger reduction of ordering temperature.

At low temperatures, the energy required for exchanging a pair of atoms even in the neighborhood of an excess atom is large enough to efficiently suppress the exchange. Therefore, the ordering in the particles tends towards the maximum possible amount at the given composition and the residual disorder at low temperatures is independent from the type of the excess atoms, as can be seen in Fig. 6.7.

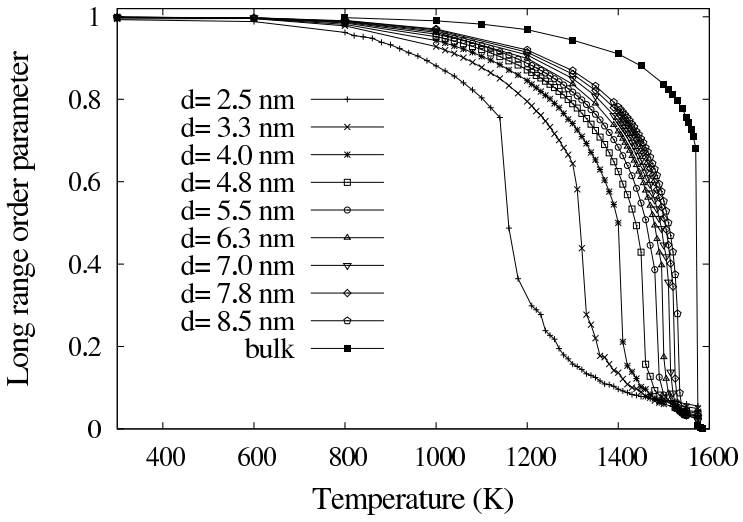


**Figure 6.9:** *Variation of LRO parameter with temperature for different sized particles. All particles possess the respective ideal composition of an ordered regular TO. For comparison, the curve of the $Fe_{50}Pt_{50}$ bulk sample is also shown.*

### 6.5.3. Influence of particle size on the ordering behavior

For investigating size effects on the ordering behavior, particles of different diameters and respective ideal composition have been compared. In Fig. 6.9, the dependence of long-range order on temperature for nanoparticles and for a $Fe_{50}Pt_{50}$ bulk sample is depicted. Independent from size, all particles reach complete ordering at low temperatures. The order-disorder transition of the particles, however, is shifted towards lower temperatures with decreasing particle size as shown in Fig. 6.8. The ordering temperature of the largest particle (8.5 nm, 1530 K) is lowered by approx. 40 K compared to the bulk sample (1573 K). The ordering temperature of the smallest particle (2.5 nm, 1190 K) is lowered by approx. 380 K.

As has been discussed in Sec. 6.4, the decrease of ordering temperature when going from the bulk to small particles is due to the under-coordination of surface atoms. Their driving force for occupying ordered lattice sites is reduced and disorder is introduced more easily in the system. When proceeding to even smaller particles, the surface to volume ratio increases. Additionally, the mean coordination of the surface atoms is further reduced. Both effects explain the larger decrease of ordering temperature with decreasing particle size.

The lowering of ordering temperature for nanometer sized particles in the simulations is comparatively small. Even for the smallest particles considered (2.5 nm), the order-disorder transition occurs at a temperature as high as $T_c = 1190$ K. A typical annealing temperature for inducing a transformation from the disordered to the $L1_0$ ordered phase in 6 nm FePt nanoparticles is 800 K [24]. As the annealing processes are performed well below the observed $T_c$, the present simulations give no evidence that the lack of ordering

found in FePt nanoparticles even after thermal treatment originates from a thermodynamic stability of the $A1$ phase.

### 6.5.4. Influence of the degree of surface segregation on the ordering behavior

As described in Sec. 4.3, the parameter $h$ of the Ising-type Hamiltonian has been fitted against an experimental value for Pt surface segregation in an $Fe_{20}Pt_{80}$ alloy. The uncertainty of this value ($96 \pm 4$ at. %) in principle allows for a wide range of parameters $h$, spanning from $h = 0$ (no driving force for surface segregation) to high values of $h$ that would correspond to an almost complete coverage of the (111) surface of the $Fe_{20}Pt_{80}$ alloy with Pt. Furthermore, depending on the preparation process, FePt particles can also be dispersed in a matrix or coated by organic ligands. These different chemical surroundings can significantly alter the surface segregation behavior, which can be reflected by a modified parameter $h$. Preferential segregation of one element distorts the stacking sequence imposed by the $L1_0$ order on the surface and depletes the bulk of the particle of the segregating element. Therefore, a strong interplay between surface segregation and ordering can be expected.

In the following, the influence of the parameter $h$ on the ordering behavior is investigated in order to study the effect of surfactants on wet chemically prepared particles that are coated by organic ligands consisting of oleic acid molecules [14]. By assuming that the oleic acid molecules bind more strongly to Fe than to Pt atoms by partial oxidization, a reversal of the surface segregation behavior towards a preferential segregation of Fe atoms can be expected. For the Ising-type Hamiltonian, this implies a positive sign of the parameter $h$. Also, by replacing oleic acid with other molecules, the degree of Fe surface segregation should in principle be tunable.

For a particle with a diameter of 4 nm (2406 atoms) and corresponding ideal composition (50.71 at. % Fe), the degree of Fe surface segregation is controlled by varying $h$ between 0 and 2.4 eV (see Fig. 6.10). For $h \leq 0.3$ eV, the driving force for ordering overcomes the tendency for surface segregation and the Fe concentration in the surface corresponds to a completely ordered particle. With increasing $h$, the content of Fe in the surface layer is raised. For $h \geq 2.1$ eV, the tendency for surface segregation becomes large enough that the entire surface of the particle is covered with Fe atoms. For each value of $h$, the degree of order in the particle is analyzed by counting the fraction of atoms whose nearest neighbor

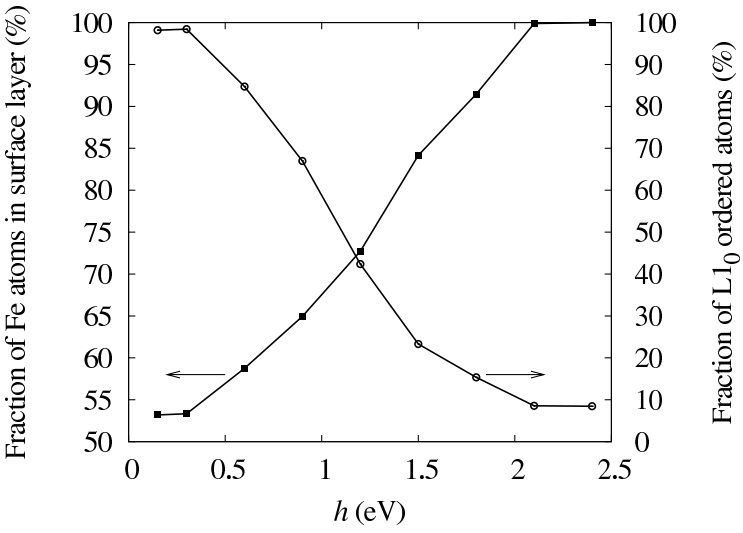


**Figure 6.10:** *Suppression of $L1_0$ ordering with increasing surface segregation. The degree of surface segregation and $L1_0$ ordering is plotted in dependence on the parameter $h$ for a 4 nm particle with ideal composition and $T$ =300 K.*

sites are occupied according to the $L1_0$ structure.* The results are shown in Fig. 6.10. Starting with an almost completely ordered particle for low values of $h$, the amount of $L1_0$ ordering decreases with increasing surface segregation of Fe. In the limiting case of a completely Fe terminated particle surface, only 9 % of the atoms can order in the $L1_0$ structure.

Out of the 2406 atoms of the 4 nm particle, 752 atoms are at the surface. If all the surface sites are occupied by Fe atoms, the composition of the remaining particle bulk is shifted towards approximately 72 at. % Pt. This leads to a suppression of $L1_0$ ordering in the particle, as the bulk composition lies outside the stability region of the $L1_0$ phase. Instead, a simultaneous evolution of $L1_2$ ordered domains can be expected. This is confirmed by analyzing the structure of completely Fe terminated particles in more detail, as shown in Fig. 6.11. In the left column of Fig. 6.11, cross sections of different sized completely Fe terminated particles are presented. Beneath the surface Fe layer, all particles exhibit a layer almost completely occupied by Pt atoms. In the remaining bulk of the particles, $L1_0$ and $L1_2$ ordered domains can easily be identified, as indicated by the light and dark grey patches in the right column of Fig. 6.11. The bulk of the smallest particle presented (3.3 nm) is completely $L1_2$ ordered. Here, the shift of the bulk composition is most important. In the 4 nm particle, the main fraction of bulk atoms are still $L1_2$ ordered. However, small $L1_0$ ordered domains evolve in the center and at the (100) surfaces of the particle. With further increasing particle size, an $L1_0$ ordered domain spans over the whole particle in

*The LRO parameter introduced in Sec. 3.6.3 is not appropriate for describing the degree of $L1_0$ order in particles with a high tendency for surface segregation. The shift of the bulk composition leads to a partial $L1_2$ ordering (see Fig. 6.11), which also has a non-zero contribution to the LRO parameter.

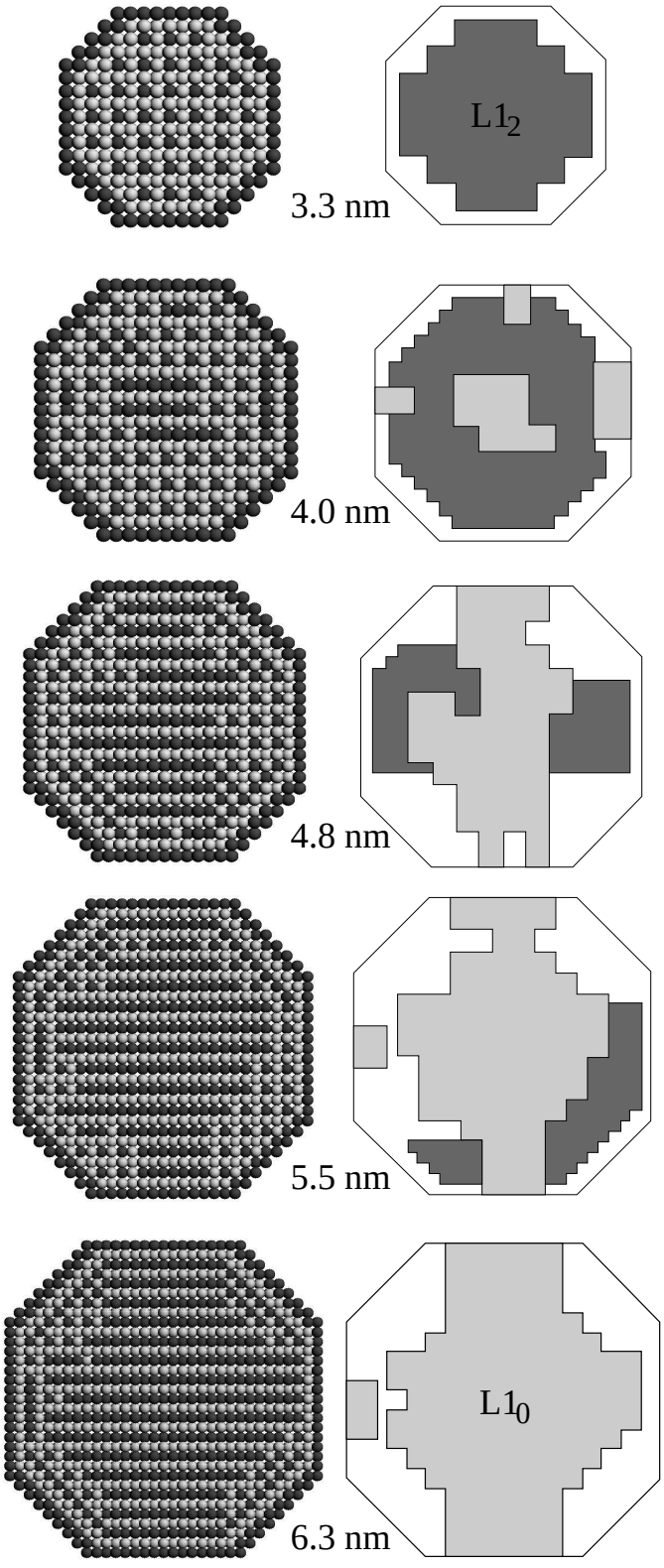


**Figure 6.11:** *Left column: Cross sections of completely Fe terminated particles with overall composition close to stoichiometry ($T$=300 K, $h$=2.4 eV). Right column: Dark grey patches indicate $L1_2$ ordered domains, light grey patches indicate $L1_0$ ordered domains.*

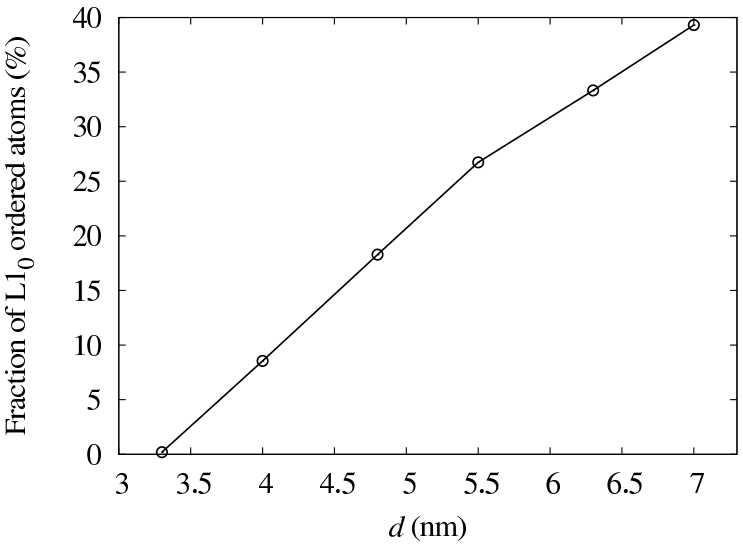


**Figure 6.12:** *Dependence of the amount of $L1_0$ ordering on particle size in completely Fe terminated particles with overall composition close to stoichiometry.*

[001] direction and grows at the expense of the $L1_2$ ordered areas. In the largest particle displayed (6.3 nm), the bulk is almost completely $L1_0$ ordered and no $L1_2$ domains can be identified.

The amount of $L1_0$ ordering in particles with complete Fe surface segregation is analyzed quantitatively in Fig. 6.12. As has already been observed in Fig. 6.11, the surface segregation suppresses the $L1_0$ ordering completely in particles with diameter $d \leq 3.3$ nm. In contrast, in the largest particle analyzed (7.0 nm), 40 % of the atoms are found to be $L1_0$ ordered. The value of 40 % ordering in the 7 nm particle seems to be rather small when compared to the large $L1_0$ ordered domain visible even in the 6.3 nm particle of Fig. 6.11. However, in the quantitative analysis, only atoms with a completely ordered nearest neighborhood are counted as ordered. This excludes all atoms at the boundaries of a domain and explains the apparent discrepancy.

The reduction of $L1_0$ ordering by surface segregation is largely due to the shift of the bulk composition. Therefore, an increase of the overall concentration of the segregating element can restore the stoichiometric composition in the bulk and can thus promote the ordering in the particles. The effect of increasing Fe content in Fe terminated 4 nm particles on the degree of $L1_0$ ordering is shown in Fig. 6.13. As expected, the amount of ordering increases with increasing Fe concentration. The fraction of the particle that is $L1_0$ ordered reaches its maximum of approx. 44 % at a composition of 62 at. % Fe. This value is conserved up to a composition of 65 at. % Fe. For higher concentrations of Fe, the order is again reduced.

For restoring the stoichiometric composition in the bulk of a completely Fe terminated 4 nm particle, an overall concentration of approx. 65 at. % Fe is needed. Therefore, instead of the observed plateau, a distinct maximum of ordering at 65 at. % Fe should be expected.

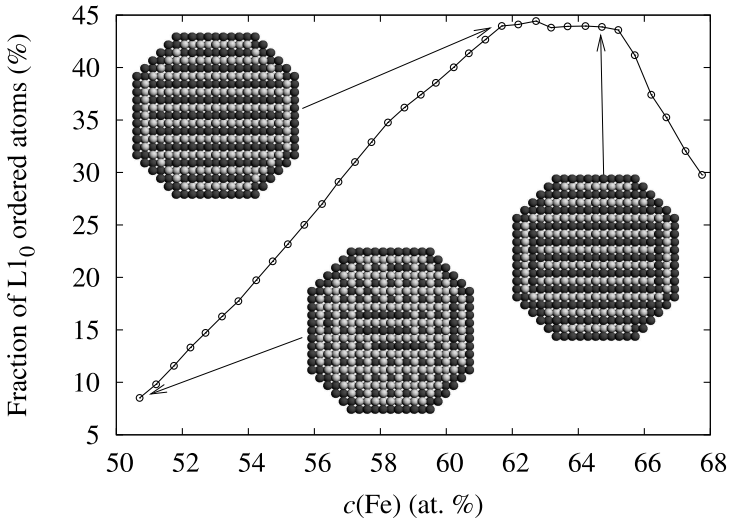


**Figure 6.13:** *Dependence of $L1_0$ ordering on composition in completely Fe terminated particles with a diameter of 4 nm. The insets show cross sections of particles at distinct compositions.*

The presence of the plateau can be explained by examining the cross sections of the particles at the limits of the plateau, as shown in the insets of Fig. 6.12. At 62 at. % Fe, the particle consists of an outer Fe shell, followed by a complete Pt shell. The remaining bulk of the particle is a single $L1_0$ ordered domain. For increasing the order by further addition of Fe atoms, the Fe layers of the ordered domain would have to penetrate the surrounding Pt shell. At 65 at. % Fe, this is only observed at the (111) facets of the particle. At the (100) facets perpendicular to the ordered direction, Fe is incorporated into the third layer and an antiphase boundary is developed. The disorder introduced by the antiphase boundary keeps the overall order in the particle at a constant level when increasing the Fe content from 62 to 65 at. %.

The simulations with varying $h$ show a strong interplay between the degree of surface segregation and the amount of order attainable. For stoichiometric particles smaller than approx. 4 nm, complete segregation of one element suppresses the formation of $L1_0$ order entirely. This observation therefore provides another possible explanation for the suppression of ordering in matrix embedded particles observed e.g. by Hono *et al.* [21], or in the solution phase synthesis route as reported e.g. by Stahl and coworkers [22]. For validating this assumption, further investigations of the particles with regard to concentration profiles would be interesting. By increasing the concentration of the segregating element and thus restoring the stoichiometric composition in the bulk, the order in the particles could then be enhanced.

## 6.6. Summary

The thermodynamics of ordering in nanometer sized FePt particles has been investigated by Monte Carlo simulations.

By comparing off-lattice MC simulations based on the analytic bond-order potential and lattice-based simulations using the Ising-type Hamiltonian, only small differences in the depression of ordering temperature have been found. This indicates that strain effects arising from the tetragonal distortion of the $L1_0$ structure do not have a significant influence on the size effects. On the other hand, the interatomic potential predicts a higher amount of surface induced disorder (SID) at moderate temperatures, which has been attributed to the vibrational entropy contributions. SID has also been shown to be responsible for the continuous nature of the ordering transition in nanoparticles [141].

Supported by the agreement between the two models, the computationally more efficient Ising-type Hamiltonian has been employed for a more detailed analysis of the ordering behavior. In particular, the influence of particle size, composition and surface segregation has been analyzed. The key findings of these simulations can be summarized as follows:

1. A reduction of thermodynamic ordering temperature $T_c$ with decreasing particle size has been observed. However, even for the smallest particle size studied ($d = 2.5\,\mathrm{nm}$, $T_c = 1190\,\mathrm{K}$), $T_c$ still remains well above the typical annealing temperatures employed in experiments for attempting to induce the $A1$ to $L1_0$ transformation. The simulations therefore suggest that the lack of chemical ordering found in FePt particles under a critical size cannot be attributed to a thermodynamic stability of the $A1$ phase. Instead, a kinetic trapping in the metastable disordered phase is expected.

2. In contrast to the symmetric bulk phase diagram (see Chapter 4), an asymmetry of the ordering temperature for compositions deviating from stoichiometry has been observed in free particles. The reduction of $T_c$ is found to be more pronounced for Fe-rich than for Pt-rich particles. This observation can be explained by the strong surface segregation tendency of excess Pt atoms, while a large number of excess Fe atoms were found to remain in the particle volume.

3. A strong dependence of ordering on the degree of surface segregation has been demonstrated. If complete surface segregation of one element is assumed, a growing amount of disorder and the formation of $L1_2$ domains is observed with decreasing particle size. Ordering can be restored, however, by increasing the concentration of the segregating element. This observation may provide an explanation for the lack of ordering in matrix-embedded or solution phase synthesis particles.

# Part V.

# Kinetics of ordering in FePt nanoparticles

# 7. Concentration of thermal vacancies in metallic nanoparticles

*The influence of particle size on the concentration of thermal vacancies in metallic nanoparticles is investigated. By analyzing the contributions of surface energies and surface stresses to the vacancy formation energy, a particle size dependent model is derived. The vacancy concentration in metallic nanoparticles is predicted to be smaller than the bulk value. The results are verified by Monte Carlo simulations using a broken bond model and by molecular statics calculations with embedded atom method potentials. The combination of both methods allows to study the influence of surface energies and stresses, separately, and to verify the proposed model description. The impact of the results on the ordering kinetics in FePt nanoparticles is discussed.*

## 7.1. Introduction

In the foregoing chapter, the thermodynamics of ordering in FePt nanoparticles has been investigated. Independent from the model description, only a small depression of ordering temperature with decreasing particle size has been found. At typical annealing temperatures in experiments, the ordered $L1_0$ structure still represents the thermodynamically stable phase. The difficulty of transforming the metastable disordered phase to the ordered structure therefore has to be attributed to kinetic effects that limit the transition rate.

In substitutional alloys such as FePt, phase transitions that require a rearrangement of atomic species are controlled by the vacancy assisted diffusion mechanism [153]. In this mechanism, the diffusivity of atoms is proportional to the vacancy concentration $C_\mathrm{v}$ [154], which leads to a strong dependence of the transition rate on $C_\mathrm{v}$. Therefore, investigating the more general question of the size dependence of the thermal vacancy concentration in metallic nanoparticles can provide valuable insights on the ordering kinetics in FePt nanoparticles.

In this chapter analytic expressions for the concentration of thermal vacancies in metallic nanoparticles are derived. Their validity is verified by atomistic simulations on copper nanoparticles, which serve as a representative model system. A depletion of vacancies at small sizes is found and is explained in detail. The chapter is concluded by an estimation of the effect in FePt nanoparticles.

## 7.2. Vacancy concentration at small sizes

The prevailing point defect in crystalline metallic solids is the vacancy, which affects many physico-chemical properties (electrical resistance, heat capacity, self-diffusion, catalytic activity,...) and determines the behavior of metals under processing conditions (alloying, sintering, creep, order-disorder kinetics,...). Although understanding the role of thermal vacancies in metallic particles becomes vital for controlling the above listed properties and processes on the nanoscale, very little is known about the size dependence of the vacancy concentration. For sufficiently large systems ($N > 10^3$ atoms) the concentration of thermal vacancies at a given temperature $T$ and pressure $P$ follows an Arrhenius law

$$C_\mathrm{v} = \exp\left(-\frac{G_\mathrm{v}^\mathrm{f}(T,P)}{k_\mathrm{B}T}\right), \tag{7.1}$$

where $G_\mathrm{v}^\mathrm{f} = E_\mathrm{v}^\mathrm{f} - TS_\mathrm{v}^\mathrm{f} + PV_\mathrm{v}^\mathrm{f}$ is the Gibbs free energy of vacancy formation. If only a small size dependence of the formation entropy $S_\mathrm{v}^\mathrm{f}$ and the formation volume $V_\mathrm{v}^\mathrm{f}$ is assumed, the problem of determining the vacancy concentration in small particles reduces to the question of how the vacancy formation energy $E_\mathrm{v}^\mathrm{f}$ varies with particle size.

In the past, several studies have tried to estimate this quantity in small particles by extrapolating empirical relationships established for the bulk vacancy formation energy down to the nanometer scale [155–158]. Gladkikh and Kryshtal, for example, used a proportionality between $E_\mathrm{v}^\mathrm{f}$ and the melting temperature [155]. Since the melting temperature is lowered for small particles [6], their result is that the vacancy formation energy is also reduced. Alternatively, Qi and Wang employ a proportionality between $E_\mathrm{v}^\mathrm{f}$ and the cohesive energy to come to the same conclusion [156–158]. Since $E_\mathrm{v}^\mathrm{f}$, cohesive energy and melting temperature can all be considered as a measure for the bond strength, a proportionality between these parameters occurs naturally in the case of a bulk material. However, this concept cannot be transferred to nanoparticles. If one considers (as in Refs. [156–158]) a simple broken bond model which assigns a fixed energy to each bond, the cohesive energy per atom of a particle is calculated as the average over the surface and volume atoms. This

average decreases with decreasing particle size and, as a consequence, a higher vacancy concentration in small particles is predicted. This result is counterintuitive, since the binding energy of an atom located in the particle volume remains unchanged and, consequently, breaking the bonds for creating a vacancy costs an amount of energy independent of particle size. Furthermore, the surface should be an efficient sink for vacancies and therefore lead to a reduced vacancy concentration within the particle.

In the following, it is shown that surface energy effects neglected in previous studies lead to an increasing $E_\mathrm{v}^\mathrm{f}$ with decreasing particle size.* An analytic expression for the size dependence of the vacancy formation energy in small particles is developed. The model is verified by means of computer simulations of Cu nanoparticles, which serve as a representative model system. Although Cu nanoparticles preferentially twin if the particle radius is smaller than approximately 1.9 nm [159], only single crystalline particles are studied in order to illustrate the principal effects.

## 7.3. Size dependent vacancy formation energy

For investigating the vacancy formation in small particles, it is helpful to start from the definition of the vacancy formation energy in bulk materials. The process of vacancy creation in a crystalline solid of $N$ atoms consists of removing an atom from the volume of the crystal and inserting it in a reservoir of a certain chemical potential $\mu$. Denoting the cohesive energy per atom in the undisturbed crystal by $E_\mathrm{c}$ and the excess energy of the crystal containing the vacancy by $\chi^0$, the vacancy formation energy $E_\mathrm{v}^\mathrm{f}$ is given by

$$\begin{aligned} E_\mathrm{v}^\mathrm{f} &= \underbrace{(N-1)E_\mathrm{c} + \chi^0 + \mu}_{\text{Defective System}} - \underbrace{NE_\mathrm{c}}_{\text{Ideal System}} \\ &= \chi^0 + \mu - E_\mathrm{c}. \end{aligned} \tag{7.2}$$

In practice, the reservoir for the removed atom is the crystal surface and $\mu$ is the chemical potential of the crystal. In the case of a bulk crystal, $\mu$ therefore equals the cohesive energy $E_\mathrm{c}$. This can be rationalized by regarding the surface of a crystal not as perfectly smooth, but as disturbed by surface steps and kinks. By adding atoms to kink positions of the surface, the crystal grows and the energy gain for each atom necessarily equals the cohesive energy, $E_\mathrm{c} = \mu$. Therefore, the vacancy formation energy in a bulk crystal

*Effects of surface energy $\gamma$ in particles or droplets are customarily expressed by the Laplace term $2\gamma/R$. Therefore, the radius $R$ is used in this chapter for denoting particle sizes, contrary to the diameter $d$ employed in the remainder of this work.

simplifies to $E_\mathrm{v}^\mathrm{f} = \chi^0$. In the case of metallic nanoparticles, however, the size dependence of the parameters $\chi$ and $\mu$ has to be considered, which is primarily given by surface energy and surface stress effects.

The surface energy $\gamma$ is defined as excess energy per unit surface area. It determines the amount of work $\mathrm{d}w = \gamma \mathrm{d}A$ required for creating an additional amount of surface $\mathrm{d}A$ [9, 160, 161]. As a consequence of curvature, adding an atom to the surface of a particle leads to a net increase of the surface area. If a spherical particle of radius $R$ is assumed, the area increase can be estimated as follows. By adding the atom to the surface, the volume of the particle increases by the atomic volume $\Omega$ corresponding to an increment of particle radius by $\mathrm{d}R = \Omega/4\pi R^2$. In consequence, the increase of particle surface area is given by $\mathrm{d}A = 2\Omega/R$. The chemical potential of the particle surface is reduced by the amount of work required for increasing the surface area, which gives

$$\mu(R) = E_\mathrm{c} + \frac{2\gamma\Omega}{R}. \tag{7.3}$$

The effect of surface energy is therefore to increase the vacancy formation energy in small particles.

On the other hand, the surface stress $f_{ij}$ is a tensor quantity that determines the work $\mathrm{d}(\gamma A) = A f_{ij} \mathrm{d}e_{ij}^s$ required for stretching an existing surface elastically [9], where $e_{ij}^s$ denotes the strain in the surface. In this work, the surface stress is considered as a scalar quantity $f$, which can be viewed as an effective average of the true stress $f_{ij}$. In fact, for the low index (100) and (111) surfaces of an fcc metal, $f_{ij}$ reduces to a scalar value [9]. The definition of $f$ is then given by $f = \gamma + \mathrm{d}\gamma/\mathrm{d}e^s$ [9]. For positive values of $f$, a compression of the surface leads to a reduction of the surface energy. This compression induces an elastic strain $e$ in the interior of the particle which is proportional to a pressure $P = -3eB$, where $B$ describes the bulk modulus [9]. If a vacancy is created by removing an atom from the particle, this leads to a volume change $\Delta V_\mathrm{v}^\mathrm{rel} = V_\mathrm{v}^\mathrm{f} - \Omega$. The work associated with this volume change against the pressure $P$ adds to the excess energy of vacancy formation and one obtains

$$\chi = \chi^0 - 3eB\Delta V_\mathrm{v}^\mathrm{rel}. \tag{7.4}$$

For $V_\mathrm{v}^\mathrm{f} < \Omega$ and compressive bulk strain $e < 0$, $\chi$ is therefore reduced compared to $\chi^0$. For a spherical particle with radius $R$ the pressure $P$ is assumed to be isotropic. It is then given by the Laplace pressure $2f/R$, leading to

$$\chi(R) = \chi^0 + \frac{2f\Delta V_\mathrm{v}^\mathrm{rel}}{R}. \tag{7.5}$$

Another effect of the surface stress is a reduction of the cohesion in the particle volume by $E_\mathrm{c} = {E_\mathrm{c}}^0 + 9e^2B\Omega/2$, where ${E_\mathrm{c}}^0$ is the cohesive energy in a bulk crystal [162]. Since

this effect only scales with $e^2$, it can safely be ignored compared to the contribution of Eq. (7.4).

Inserting the obtained size dependencies of $\chi$ and $\mu$ in Eq. (7.2) leads to the following result for the vacancy formation energy in small spherical particles:

$$E_{\mathrm{v}}^{\mathrm{f}}(R) = \chi^0 + \frac{2(\gamma\Omega + f\Delta V_{\mathrm{v}}^{\mathrm{rel}})}{R}. \tag{7.6}$$

In consequence, the vacancy concentration can be written as

$$C_{\mathrm{v}}(R) = C_{\mathrm{v}}^0 \exp^{-\frac{2(\gamma\Omega + f\Delta V_{\mathrm{v}}^{\mathrm{rel}})R^{-1}}{k_{\mathrm{B}}T}}, \tag{7.7}$$

where $C_{\mathrm{v}}^0$ is the vacancy concentration of a bulk material at the same temperature. In general, Eq. (7.7) can give rise to a decreasing, as well as increasing vacancy concentration with particle size, depending on the magnitude of the surface energy and surface stress terms. However, an average value for the vacancy relaxation volume appropriate for most fcc metals is $\Delta V_{\mathrm{v}}^{\mathrm{rel}} \approx -0.25\Omega$ [60], meaning that $f$ has to surmount $\gamma$ by approximately a factor four in order to overcompensate the surface energy term and for leading to an increased vacancy concentration. Although for many metals the calculated surface stress exceeds the surface energy, the ratio $f/\gamma$ is rarely larger than two [9]. In consequence, the most probable scenario from Eq. (7.7) is a considerable depletion of vacancies for particles in the nanometer scale, a finding that is clearly in contrast to the postulated linear decrease of $E_{\mathrm{v}}^{\mathrm{f}}$ with $1/R$ in Refs. [155–158].

In the derivation of equations (7.6) and (7.7), the assumption of a spherical particle shape led to the specific $1/R$ dependence of the surface energy and surface stress terms. However, a sphere is not the energetically most favorable shape for single crystalline particles. Instead, facetting of the surface occurs which exposes only low energy, low index faces and the energy minimizing polyhedron can be determined by the Wulff construction (see Chapter 5). In the remainder of this article, the transferability of equations (7.6) and (7.7) to particles of Wulff shape is analyzed in detail. In section 7.4 an analytic expression for the size dependence of $\mu$ in particles of Wulff shape is derived and it is demonstrated that Eq. (7.3) is directly transferable to this class of facetted particles. In Sec. 7.4.2, Monte Carlo (MC) simulations are carried out with a broken bond model. Within this model only surface energy terms are considered and the calculated vacancy concentrations are compared to the theoretical result.

Finally, in section 7.5, the variation of the excess energy $\chi$ in particles of Wulff shape is analyzed exemplarily for the element copper by molecular statics calculations. It is

shown that inhomogeneous stress distributions, which are caused by the facetting and large elastic anisotropy, are the reason for varying excess energies of vacancy formation within the particle.

## 7.4. Surface energy effects in particles of Wulff shape

In the foregoing section it was argued that the chemical potential of the surface, which acts as reservoir for the atom removed from the particle volume is $\mu = E_c$ in case of a bulk crystal and $\mu = E_c + 2\gamma\Omega/R$ in case of a spherical particle. In the following, a formal derivation of $\mu$ for the case of a nanoparticle with Wulff shape is presented and it is shown that the obtained results can be confirmed by numerical Monte-Carlo simulations.

### 7.4.1. Chemical potential of a facetted particle

Given the energy $E(N)$ of a particle of $N$ atoms, the chemical potential can be written as

$$\mu = \frac{\partial G}{\partial N} \approx \frac{\partial E(N)}{\partial N}. \tag{7.8}$$

In order to identify the size dependence of the chemical potential, the function $E(N)$ is developed in the following.

In the limit of strong facetting (only (111) and (100) facets, see Fig. 5.1), the Volume $V$ and the total area of (111) and (100) faces ($A_{111}$ and $A_{100}$) of the Wulff polyhedron have been given in Sec. 5.2.1:

$$V = d_{111}^3 4 \left(\Gamma^3 - 3\sqrt{3}\Gamma^2 + 9\Gamma - 2\sqrt{3}\right) \tag{7.9}$$

$$A_{111} = d_{111}^2 \sqrt{3} \left(3\sqrt{3}\Gamma - \frac{3}{2}\Gamma^2 - 3\right) \tag{7.10}$$

$$A_{100} = d_{111}^2 2 \left(\Gamma^2 - 2\sqrt{3}\Gamma + 3\right), \tag{7.11}$$

where $\Gamma$ is the ratio of the (100) to (111) surface energies ($\gamma_{100}/\gamma_{111}$) and $d_{111}$ is the distance of the (111) facets from the particle center.

For a particle of $N$ atoms with atomic volume $\Omega$, the volume is expressed by $V = N\Omega$, leading to the condition

$$d_{111}(N) = (N\Omega/4g)^{1/3}, \tag{7.12}$$

with the geometry factor

$$g = \Gamma^3 - 3\sqrt{3}\Gamma^2 + 9\Gamma - 2\sqrt{3}. \tag{7.13}$$

The energy of a Wulff polyhedron can then be expressed as the sum of volume and surface terms (Eq. (5.18)):

$$\begin{aligned} E(N) &= NE_\mathrm{c} + A_{111}\gamma_{111} + A_{100}\gamma_{100} \\ &= NE_\mathrm{c} + 3g^{1/3}\left(2N\Omega\right)^{2/3}\gamma_{111}. \end{aligned} \tag{7.14}$$

For the derivative with respect to the number of atoms one obtains

$$\frac{\partial E}{\partial N} = E_\mathrm{c} + 2(2\Omega)^{2/3}\gamma_{111}\left(g/N\right)^{1/3}, \tag{7.15}$$

and using Eq. (7.12) for expressing $N$ by $d_{111}$ yields

$$\mu = \frac{\partial E}{\partial N} = E_\mathrm{c} + \frac{2\gamma_{111}}{d_{111}(N)}\Omega = E_\mathrm{c} + \frac{2\gamma_{hkl}}{d_{hkl}(N)}\Omega. \tag{7.16}$$

Since $\gamma_{hkl}/d_{hkl}$ is a constant for any Wulff polyhedron, this result is independent of the assumption of strong facetting with only (100) and (111) facets. Compared to the bulk case, the energy gain when adding an atom to a Wulff particle is decreased by the quantity $2\gamma_{hkl}\Omega/d_{hkl}$. Therefore, the term $\gamma_{hkl}/d_{hkl}$ plays the equivalent role of the ratio $\gamma/R$ found for spherical particles in Eq. (7.3) and $2\gamma_{hkl}\Omega/d_{hkl}$ represents the energy needed for generating an additional amount of surface averaged over all facets.

For practicable application of Eq. (7.16), it is therefore convenient to replace the $hkl$ surface energies by an appropriately chosen average surface energy $\gamma$ and by expressing the size of the particle by the radius $R$ of a sphere that encloses the volume $N\Omega$. For the strong facetting model with known geometry factor $g$ and $\gamma_{111}$, equating the surface energies of the Wulff polyhedron and the sphere yields

$$\gamma = \left(3g/\pi\right)^{1/3}\gamma_{111}. \tag{7.17}$$

In the presented derivation of Eq. (7.16) it is assumed that any particle with an arbitrary number of $N$ atoms can be assembled into a Wulff polyhedron with perfectly flat faces. However, this is only the case for certain *magic* numbers of $N$ [7]. In consequence, Eq. (7.16) only gives an averaged energy gain for an additional atom and, depending on $N$, the true amount of energy gained fluctuates around Eq. (7.16). Consider, for example, a particle with a magic number of atoms and only flat faces. Adding an extra atom to this particle will lead to a much higher increase of surface area and lower energy gain, since the lowest energetic particle with $N+1$ atoms will most certainly not be surrounded by only flat faces. Particles with magic numbers are therefore expected to have a higher vacancy formation energy than predicted by Eq. (7.6). In contrast, for $N$ deviating from the magic numbers,

stepped faces on the particle surface already exist and the area increase for an additional atom is smaller. Particles with non-magic numbers will therefore have a lower vacancy formation energy than predicted by Eq. (7.6). With increasing temperature however, a thermal roughening of the surface of all particles diminishes this effect and the energy gain for an extra atom approaches the average value predicted by Eq. (7.16) for particles with any number of atoms.

In the following, Eq. (7.16) is verified by calculating $C_\mathrm{v}(R)$ from results of Monte-Carlo simulations of a simple model system which includes the tendency for facetting.

## 7.4.2. Monte Carlo calculations

As a model system for single crystalline fcc nanoparticles a broken bond model with nearest neighbor interactions on a rigid fcc lattice is assumed, where an energy $\varepsilon$ is assigned to each interatomic bond. In this model, contributions of surface stress are excluded, with $V_\mathrm{v}^\mathrm{f} = \Omega$ and $\chi(R) = \chi^0 = -6\varepsilon$. The ratio of the (100) to (111) surface energies equals $\Gamma = 2\sqrt{3}/3$ and the Wulff polyhedron is a regular truncated octahedron (TO) with geometry factor $g = 8\sqrt{3}/9$. The series of magic numbers is defined by $N_\mathrm{regTO} = 16k^3 + 15k^2 + 6k + 1$, with integer number $k$ [7]. The averaged surface energy $\gamma$ is given by

$$\gamma = -\frac{4\varepsilon}{a_0^2}\left(\frac{3}{\pi}\right)^{1/3}, \tag{7.18}$$

where $a_0$ is the lattice constant. The size of a particle of $N$ atoms is described by the radius

$$R = \frac{a_0}{2}\left(\frac{3N}{2\pi}\right)^{1/3}. \tag{7.19}$$

Without loss of generality the model parameters were chosen to mimic the bulk vacancy formation energy and lattice constant of Cu, with $E_\mathrm{v}^\mathrm{f} = 1.28\,\mathrm{eV}$ and $a_0 = 3.615\,\text{Å}$ [60, 116]. In consequence, the bond energy and averaged surface energy equal to $\varepsilon = -0.213\,\mathrm{eV}$ and $\gamma = 64.2\,\mathrm{meV/Å}^3$, respectively. As it is demonstrated in the following, the equilibrium vacancy concentration of this model system has been analyzed by MC simulations for particle sizes up to 10 nm in a temperature range from 800 K to 1300 K.

The simulations are started with a compact spherical particle of size $R$ positioned at the center of a cubic fcc lattice. Particles with both non-magic and magic numbers of atoms are generated. In each step $i$ of the simulation all possible exchanges $j$ of atoms with

neighboring empty lattice sites are identified and their respective exchange probabilities $\omega_j$ are determined by the Metropolis algorithm Eq. (2.4):

$$\omega_j = \begin{cases} 1 & \text{for} \quad \Delta E_j \leq 0 \\ \exp\left(-\dfrac{\Delta E_j}{k_\mathrm{B}T}\right) & \text{for} \quad \Delta E_j > 0. \end{cases} \tag{7.20}$$

Here, $\Delta E_j$ is the change in energy of the system associated with exchange $j$. In line with the assumptions made by Kozubski in Ref. [163] for calculating vacancy concentrations in ordering alloys, vacancy exchange jumps that lead to a desorption of atoms into the vacuum are explicitly not considered. Assuming the particle in equilibrium with its surrounding, the rates of desorption and adsorption are balanced and the total number of atoms in the particle remains constant.[†]

In order to calculate the time average of the vacancy concentration in a particle, a standard n-fold way MC algorithm is applied ([34], see Sec. 2.2.3). At every step an exchange $j$ with probability $\omega_j$ is accepted and an internal time variable $t$ is incremented by $\Delta t = -\ln r / \sum \omega_j$, where $r$ is a random number uniformly distributed between 0 and 1. During the simulations, the particles can freely equilibrate into their thermodynamic equilibrium configuration. The initially spherical particles rapidly evolve into a strongly facetted shape closely resembling the expected Wulff polyhedron of a regular TO. Also the diffusion of atoms leads to a statistical generation and annihilation of vacancies in the particles. The concentration of bulk vacancies is analyzed by determining for every residence time interval $\Delta t_i$ the number of empty sites $n_\mathrm{v}$ and the total number of volume sites $N_\mathrm{vol}$ with fully occupied next neighbor positions. The vacancy concentration is then given as time average of the actual vacancy concentration $c(t)$:

$$\begin{aligned} c = \langle c(t) \rangle &= \frac{1}{\tau} \int_0^\tau \frac{n_\mathrm{v}(t)}{N_\mathrm{vol}(t)} dt \\ &= \frac{1}{\sum_i \Delta t_i} \sum_i \frac{n_{\mathrm{v},i}}{N_{\mathrm{vol},i}} \Delta t_i \ . \end{aligned} \tag{7.21}$$

The vacancy concentrations obtained from MC simulations for different particle sizes and temperatures are plotted in Fig. 7.1 together with the corresponding bulk values and predictions from Eq. (7.7). In quantitative agreement with Eq. (7.7) the MC data shows an obvious depletion of the vacancy concentration with decreasing particle size for particles

[†]The small change of vapor pressure accompanied with the increase of surface area when a vacancy is formed can be neglected.

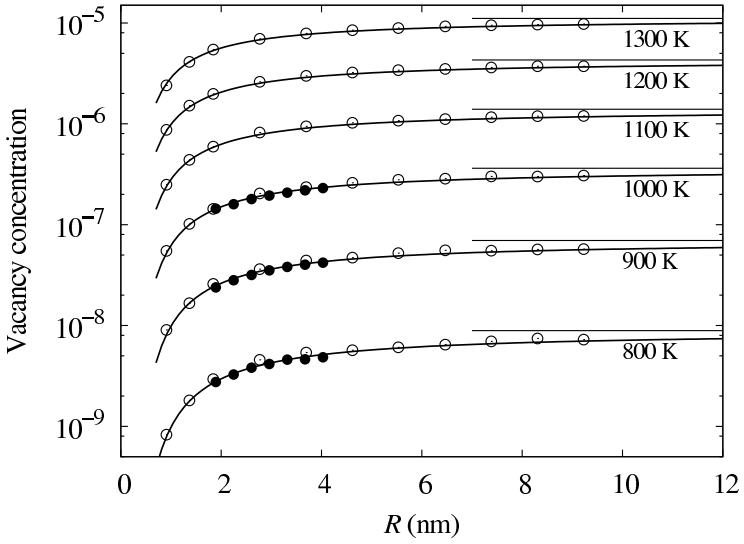


**Figure 7.1:** *Dependence of vacancy concentration on particle size for the broken bond model. Horizontal lines indicate the equilibrium bulk concentrations, curves are the predictions of Eq. (7.7). The data points are results from MC simulations. Open circles: particles with an arbitrary number of atoms. Closed circles: particles with magic number of atoms.*

of both non-magic and magic number of atoms. By taking the calculated data points and deriving from the Arrhenius law

$$C_{\mathrm{v}}(R) = \exp\left(-\frac{E_{\mathrm{v}}^{\mathrm{f}}(R)}{k_{\mathrm{B}}T}\right) \tag{7.22}$$

a particle size dependent formation energy $E_{\mathrm{v}}^{\mathrm{f}}(R)$, a linear increase of $E_{\mathrm{v}}^{\mathrm{f}}(R)$ with $1/R$ (see Fig. 7.2) is obtained, also in quantitative accordance with Eq. (7.6). The increase of $E_{\mathrm{v}}^{\mathrm{f}}$ for particles with a radius of 1 nm is approximately 150 meV.

A closer inspection of Fig. 7.2 reveals that $E_{\mathrm{v}}^{\mathrm{f}}(R)$ tends to lie above the line defined by Eq. (7.6) in particles with a magic number of atoms, while particles with a non-magic number of atoms possess a slightly lower $E_{\mathrm{v}}^{\mathrm{f}}(R)$. This is clarified in Fig. 7.3, where the difference of the MC data to Eq. (7.6) is plotted. As discussed in the previous section, this deviation arises from the difference in the chemical potential $\mu$ of the particle surface for particles with magic and non-magic numbers of atoms, while only an averaged $\mu$ enters Eq. (7.6). In the analyzed temperature range, the difference is less then 10 meV. Compared to the overall effect of up to 150 meV, this deviation is small and Eq. (7.6) gives a good approximation for $E_{\mathrm{v}}^{\mathrm{f}}(R)$ for all particles. However, the simulations can not establish a low temperature limit for the applicability of Eq. (7.6), since going to even lower temperatures would increase the required sampling time tremendously.

Provided that surface stress contributions are excluded, the MC calculations show that Eq. (7.7) correctly describes the depletion of vacancies in small particles.

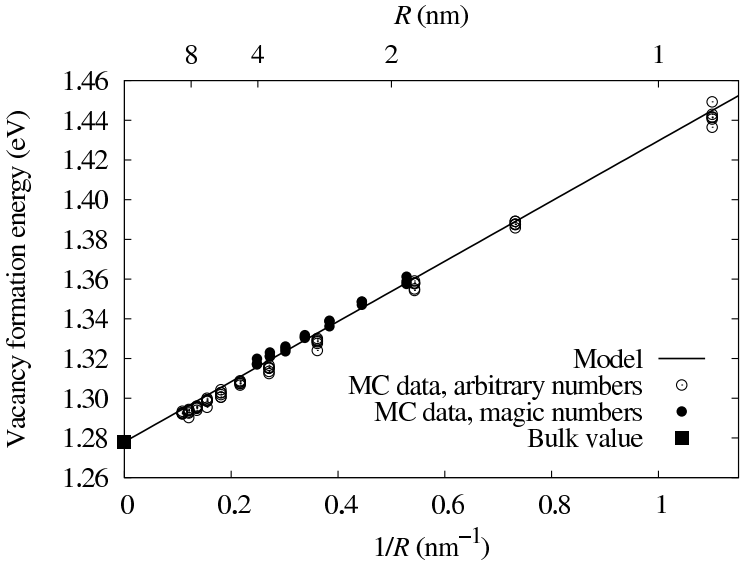


**Figure 7.2:** *Dependence of the vacancy formation energy on particle size for the broken bond model. Results from MC simulations are compared with the prediction of Eq. (7.6).*

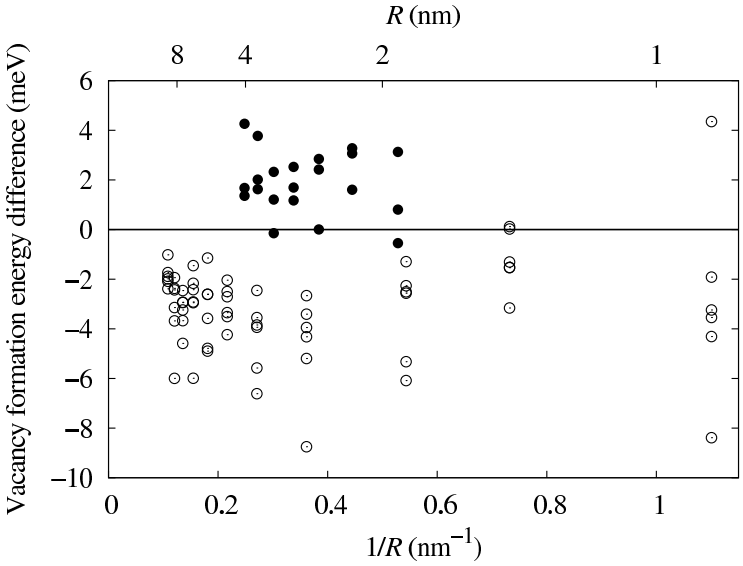


**Figure 7.3:** *Difference of the MC data on $E_{\mathrm{v}}^{\mathrm{f}}(R)$ to the predictions of Eq. (7.6). Open circles: particles with an arbitrary number of atoms. Closed circles: particles with magic number of atoms.*

**Table 7.1:** *Structural, defect and surface properties of Cu as predicted by the Foiles EAM potential [116].*

| Property | Value | Property | Value |
|---|---|---|---|
| $a_0$ (Å) | 3.615 | $\gamma_{111}$ (meV/Å$^2$) | 73.6 |
| $\Omega$ (Å$^3$/atom) | 11.816 | $\gamma_{100}$ (meV/Å$^2$) | 80.3 |
| $E_\mathrm{c}$ (eV/atom) | −3.538 | $\gamma_{110}$ (meV/Å$^2$) | 88.1 |
| $E_\mathrm{v}^\mathrm{f}$ (eV) | 1.283 | $\gamma$ (average) (meV/Å$^2$) | 82.4 |
| $\Delta V_\mathrm{v}^\mathrm{rel}$ ($\Omega$) | −0.264 | $f_{111}$ (meV/Å$^2$) | 53.7 [164] |
| $B$ (GPa) | 139 | $f_{100}$ (meV/Å$^2$) | 86.1 [164] |

## 7.5. Surface stress effects in particles of Wulff shape

Surface stress contributions to the excess energy $\chi$ in particles of Wulff shape are investigated in the following exemplarily for the element Cu by molecular statics calculations. Interatomic interactions are described by the embedded atom method (EAM) potential by Foiles *et al.* [116].

The EAM potential predicts the structural properties and defect energies for Cu listed in Tab. 7.1, with the vacancy formation energy in bulk crystalline Cu $E_\mathrm{v}^\mathrm{f} = \chi^0 = 1.283\,\mathrm{eV}$. The ratio $\gamma_{110}/\gamma_{111} = 1.20$ is only marginally smaller than $\sqrt{3/2}$ and the equilibrium shape of a Cu particle can well be described by the strong facetting model with only (100) and (111) faces. Given the ratio $\Gamma = 1.09$ of the (100) to (111) surface energies, the Wulff polyhedron closely resembles a regular TO. According to Eq. (7.17), the average surface energy amounts to $\gamma = 82.4\,\mathrm{meV/Å^2}$.

In equations (7.6) and (7.7), surface stress effects are included by assuming that the excess pressure within the particle is given by the surface stress via the Laplace pressure $2f/R$ and that it is homogeneous in the whole particle volume. For testing whether these assumptions hold true for particles of Wulff shape, the distribution of strain in fully relaxed defect free particles has been analyzed by calculating the average nearest neighbor distance $\overline{r}_\mathrm{NN}$ for each atom. The local strain is then given by $e = \overline{r}_\mathrm{NN}\sqrt{2}/a_0$. For comparison, the strain distribution has also been calculated in spherical particles of equal volumes. In Fig. 7.4, the results of these calculations are depicted exemplarily for a Wulff shaped and a spherical particle of $R = 3.7\,\mathrm{nm}$. As expected, the effect of surface stress leads to an almost homogeneous distribution of strain in the volume of the spherical particles. From the strain, an average value for the surface stress of $f = 65 \pm 0.4\,\mathrm{meV/Å^2}$ can be extracted, which compares reasonably well with the stresses of the low index (100) and (111) surfaces listed in Tab. 7.1. In contrast, the Wulff shaped particles exhibit an inhomogeneous distribution of strain. In accordance with the higher surface stress of the (100) surface compared to

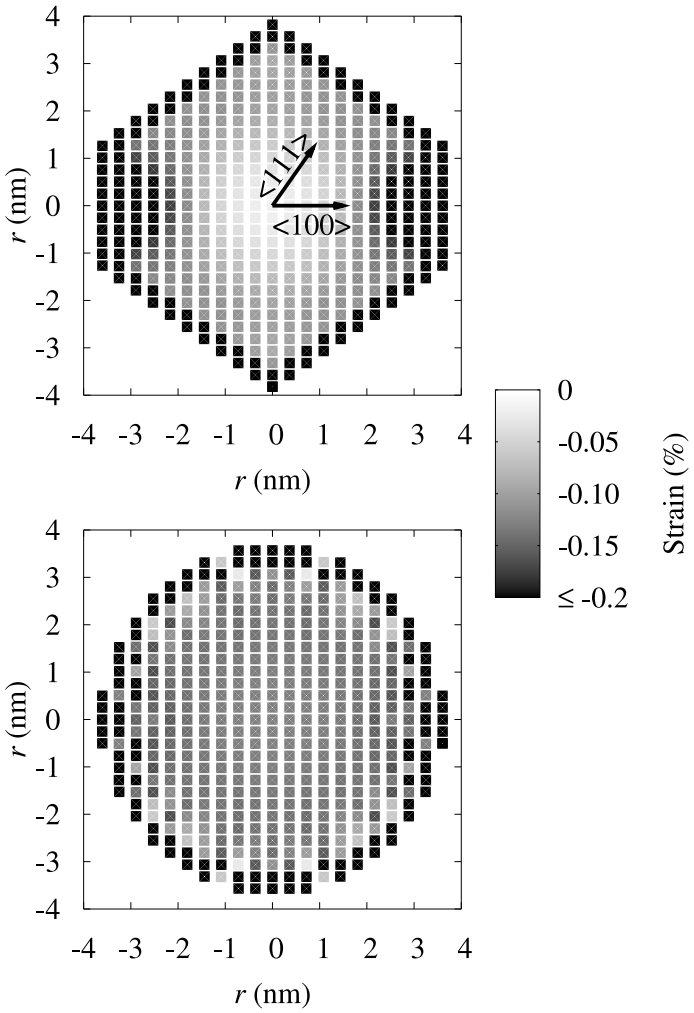


**Figure 7.4:** *Cross sections through single crystalline particles of $R = 3.7$ nm. Upper panel: Wulff shape, regular TO; Lower panel: spherical shape. Squares denote individual atoms, the grey shade scales with the local strain. Arrows indicate crystallographic directions.*

the (111) surface, high strain contributions arise from the (100) facets, while lower strain contributions arise from the (111) facets. Also, the local strain in the center of the Wulff polyhedron almost completely vanishes.

Combining Eq. (7.4) with the above results on the local strain, an inhomogeneous distribution of the vacancy excess energy $\chi$ within a Wulff shaped particle can be anticipated. The distribution of $\chi$ within a particle has been calculated by molecular statics calculations which comprise first the relaxation of defect free particles with $R$ ranging from approximately 1 to 5 nm. Subsequently, single atoms are removed at a distance $r$ along the $\langle 100 \rangle$ and $\langle 111 \rangle$ directions from the particle center. The maximum value of $r$ is chosen so that only vacancies in layers beneath the atomic layer forming the surface of the particle are created. Given the energy $E(N)$ of the defect free particle and the fully relaxed energy $E(N-1)$ of the particle containing a vacancy, $\chi$ is determined by $\chi = E(N-1) + E_c - E(N)$.

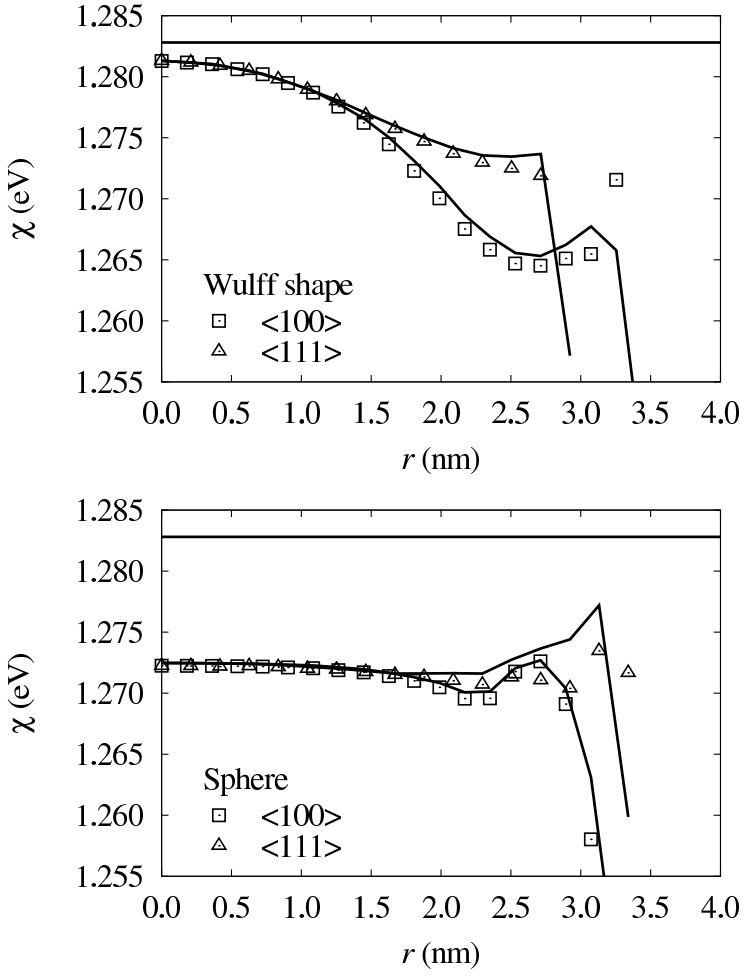


**Figure 7.5:** *Excess energy $\chi$ of vacancy formation as a function of distance $r$ from the center of a particle along the $\langle 100 \rangle$ and $\langle 111 \rangle$ directions. The particle size is $R = 3.7$ nm. Data points are direct calculations of $\chi$ by the molecular statics method. Solid lines are predictions from Eq. (7.4), using data on local strain from Fig. 7.4. The horizontal line indicates the bulk value $\chi^0$.*

For comparison, the same calculations have been performed for a crystal with periodic boundaries in two directions and free (100), respectively (111), surfaces in the remaining direction.

In Fig. 7.5, the calculated values of $\chi$ for a spherical and a Wulff shaped particle of $R = 3.7\,\mathrm{nm}$ are compared with the predictions of Eq. (7.4) using the local strain data from Fig. 7.4. As expected, a strong variation of $\chi$ within the Wulff shaped particle is found, whereas $\chi$ remains nearly constant in the volume of the spherical particle. Furthermore, the accordance of the directly calculated $\chi$-values with the values derived from the local strain shows that Eq. (7.4) provides a quantitatively correct description for the lowering of $\chi$ due to surface stress effects.

As can be better visualized in Fig. 7.6, this accordance does not hold true for vacancies in the first two monolayers beneath the surface: Although the absolute value of the strain further increases, the excess energy of surface near vacancies is clearly increased. This

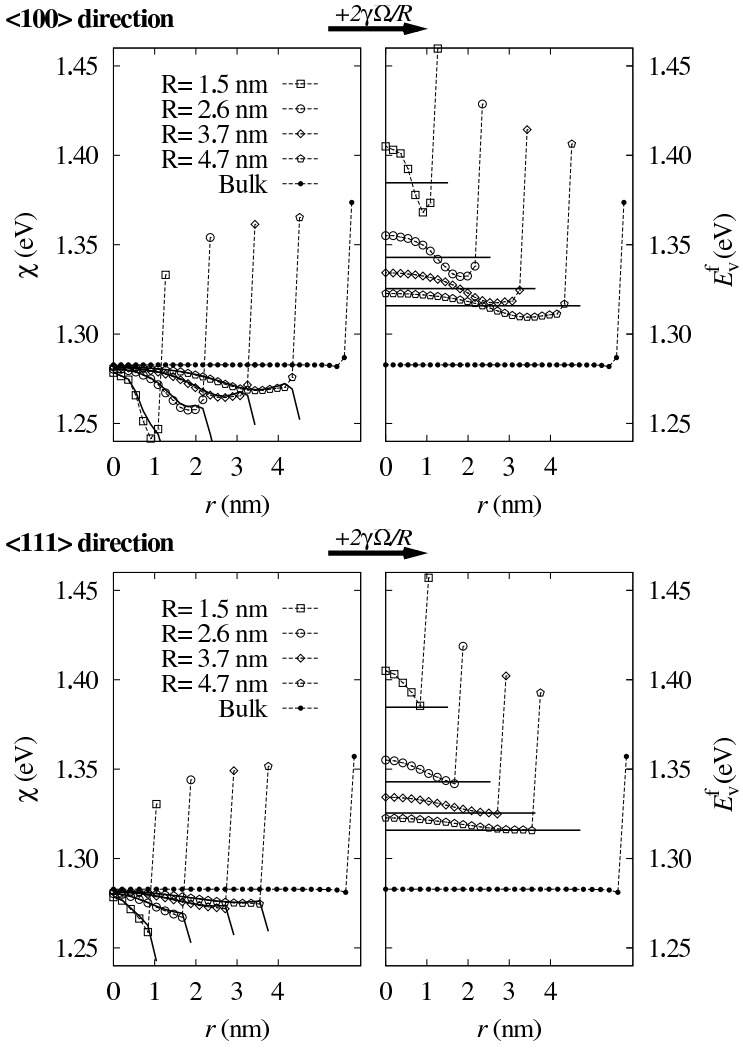


**Figure 7.6:** *Dependence of the excess energy $\chi$ and vacancy formation energy $E_\mathrm{v}^\mathrm{f}$ on the distance $r$ from the particle center along the $\langle 100 \rangle$ (top panel) and $\langle 111 \rangle$ (lower panel) directions. Data points denote direct calculations of $\chi$. The solid lines on the left hand side denote values for $\chi$ derived from local strain data using Eq. (7.4). The horizontal lines on the right hand side denote vacancy formation energies calculated from Eq. (7.6) with averaged values for surface energy and surface stress.*

simply reflects the fact that the behavior of surface near atoms cannot be quantified by parameters defined for a bulk material, as e.g. the bulk modulus. Instead, the higher excess energy in subsurface layers is attributed to an increased electron density arising from the decreased interlayer spacing at the surface. As shown in Fig. 7.5, with the same order of magnitude, this effect is also present in the subsurface layers of the periodic crystal samples.

While the molecular statics calculations demonstrate that the assumption of homogeneous strain implicit in Eq. (7.6) does not hold generally true, it nevertheless remains interesting to verify whether Eq. (7.6) can give a reasonable estimate for the average increase of the vacancy formation energy in small particles. For this purpose, by weighing the (100) and (111) surface stresses listed in Tab. 7.1 by the relative size of the (100) and (111) faces of the regular TO, an average surface stress of $f = 61\,\mathrm{meV/\AA^2}$ is obtained.

Using this value and the averaged surface energy $\gamma = 82.4\,\mathrm{meV/Å^2}$, Eq. (7.6) predicts the increased vacancy formation energies for small particles indicated by the horizontal lines in Fig. 7.6. Comparison with the values including the direct calculation of $\chi$ reveals a good agreement for the average effect.

## 7.6. Application to FePt nanoparticles

Given the possibility of a considerably reduced vacancy concentration in metallic nanoparticles demonstrated in this section, it is now interesting to estimate the effect of increased vacancy formation energy in FePt nanoparticles. This is done in the following for a particle size of 4 nm in *diameter* and a typical annealing temperature of 800 K.

Based on results from density functional theory calculations [132] and on the analytic bond-order potential for FePt, the low index surface energies of disordered FePt alloys have been estimated in Sec. 5.4.3, giving $\gamma_{111} = 100\,\mathrm{meV/Å^2}$ and $\gamma_{100} = 128\,\mathrm{meV/Å^2}$. From Eq. (7.17), an averaged surface energy of $\gamma = 116\,\mathrm{meV/Å^2}$ is therefore obtained. Given the lattice constant of 3.8 Å (Tab. 3.9), the atomic volume is $\Omega = 13.7\,\mathrm{Å^3}$. For the vacancy relaxation volume, $-0.25\Omega$ is assumed.

In order to estimate the reduction of vacancy concentration from Eq. (7.7), the largest uncertainty lies in the value for the surface tension $f$. If $f$ is taken equal to the surface energy $\gamma$, the vacancy concentration in a 4 nm diameter particle at 800 K only amounts to 20 % of the concentration in a bulk material. As an upper limit, a value of $f$ twice as high as $\gamma$ can be assumed. According to Eq. (7.7), the vacancy concentration in the 4 nm particle is then reduced to 30 % of the bulk concentration.

Given the proportionality between diffusivity and vacancy concentration [154], this estimate indicates that annealing times in 4 nm FePt particles should be 3 to 5 times longer than in bulk materials for achieving the same amount of transformation from the $A1$ disordered to the $L1_0$ ordered phase. The reduced vacancy concentration in nanoparticles can therefore represent a mechanism that considerably contributes to a kinetic limitation of the ordering transition.

## 7.7. Summary

In summary, by considering effects of surface energy and surface stress, an analytic expression for the vacancy formation energy in metallic nanoparticles has been derived. Because of the higher pressure in the particle volume, the surface stress generally tends to decrease

the excess energy of vacancy formation. The typically more important contribution, however, is the energy needed for increasing the particle surface that acts as a reservoir for the atom removed from the particle bulk. In consequence, a higher vacancy formation energy and a depletion of vacancies in small particles as compared to bulk materials is expected. These results have been verified by MC and molecular statics calculations for the element Cu using atomic interaction models that allow to investigate the surface energy and surface stress effects separately. The molecular statics calculations reveal that surface stresses can lead to an inhomogeneous distribution of strain in facetted particles, resulting in a vacancy formation energy dependent on the position within the particle.

By estimating the effect of the increased vacancy formation energy in FePt nanoparticles of 4 nm in diameter, it has been identified as a possible mechanism that limits the ordering kinetics. Vacancy concentrations of only 20 to 30 % of the value in bulk materials are expected at 800 K. Therefore, considerably increased annealing times are needed for achieving a complete transformation of the particle volume from the disordered to the ordered structure.

The simple estimate of annealing time scales based solely on the vacancy concentration in the particle volume is, however, incomplete. In particular, the contributions of surface diffusion mechanisms have been neglected. In the following chapter, these contributions are addressed by kinetic Monte Carlo simulations on the ordering transition in FePt nanoparticles.

# 8. Kinetics of the ordering transition in FePt nanoparticles

*In this chapter kinetic Monte Carlo simulations based on the Ising-type lattice Hamiltonian are employed to investigate the kinetics of ordering processes in FePt nanoparticles. In free particles, the $A1$ to $L1_0$ transition proceeds with a higher rate in surface near layers than in the volume of the particles, which demonstrates the important influence of surface diffusion. Because of the statistical nucleation of the ordered phase, however, no single domain particles are obtained and an elimination of the antiphase boundaries can not be observed within the time scales accessible by the simulations. Based on these findings, possibilities for increasing the transition rate in supported nanoparticles are investigated. By systematically modifying interface energetics, surface diffusion can be increased and a preferential ordering direction in the particle can be induced.*

## 8.1. Introduction

In the last chapter the concentration of thermal vacancies in metallic nanoparticles was analyzed and a depletion of vacancies at small sizes was demonstrated. As a result, the diffusivity of atoms in the volume of FePt nanoparticles is reduced and annealing times longer than in bulk materials are required for completely transforming the $A1$ disordered into the $L1_0$ ordered structure. This estimate, however, does not take into account the increased mobility of atoms at the particle surface. Because of the high surface to volume ratio in nanoparticles, surface diffusion can significantly contribute to the kinetics of the ordering transition.

In the present chapter kinetic Monte Carlo simulations based on an Ising-type lattice Hamiltonian are employed for investigating the ordering process in FePt nanoparticles. First, a description of the simulation method is given and a modified parametrization of

**Table 8.1:** *Modified parameters of the Ising-type Hamiltonian. Vacancy formation energies $E_\mathrm{v}^\mathrm{f}$ predicted in various surroundings.*

| Parameter | Value (eV) | Vacancy configuration | $E_\mathrm{v}^\mathrm{f}$ (eV) |
|---|---|---|---|
| $\varepsilon_1^{\mathrm{FeFe}}$ | $-0.269$ | Vacancy in fcc Fe | 1.61 |
| $\varepsilon_1^{\mathrm{PtPt}}$ | $-0.219$ | Vacancy in fcc Pt | 1.31 |
| $\varepsilon_1^{\mathrm{FePt}}$ | $-0.337$ | Fe site in $L1_0$ FePt | 1.89 |
| $\varepsilon_2^{\mathrm{FeFe}}$ | 0 | Pt site in $L1_0$ FePt | 1.79 |
| $\varepsilon_2^{\mathrm{PtPt}}$ | 0 | Fe site in $A1$ FePt | 1.85 |
| $\varepsilon_2^{\mathrm{FePt}}$ | 0.0186 | Pt site in $A1$ FePt | 1.70 |

the Ising-type Hamiltonian is presented that takes into account the vacancy formation energy. By comparing the simulations with experiments on sputtered FePt thin films, the choice of model parameters is validated. Subsequently, the influence of surface diffusion on the ordering kinetics in free FePt nanoparticles is investigated. Based on these results, possibilities for increasing the transition rate in supported particles are analyzed.

## 8.2. Simulation method and modified Ising-type Hamiltonian

The ordering kinetics in FePt nanoparticles is investigated by an $n$-fold way kinetic Monte Carlo algorithm (see Sec. 2.2.3). The simulations are started with a random distribution of Fe and Pt atoms on a fcc lattice. In each step of the simulation, all possible jumps of atoms to neighboring empty lattice sites are identified. In order to allow for a dynamical interpretation of the simulations, for each jump $j$ the transition rate $\nu_j$ is calculated by

$$\nu_j = \nu_0 \times \begin{cases} \exp\left(-\dfrac{E^\mathrm{mig}}{k_\mathrm{B}T}\right) & \text{for} \quad \Delta E_j \leq 0 \\ \exp\left(-\dfrac{\Delta E_j + E^\mathrm{mig}}{k_\mathrm{B}T}\right) & \text{for} \quad \Delta E_j > 0. \end{cases} \tag{8.1}$$

Here, $\Delta E_j$ is the change of energy in the system associated with transition $j$, which is calculated by the Ising-type Hamiltonian described in Chapter 4. For simplicity, the attempt frequency $\nu_0$ and the migration barrier $E^\mathrm{mig}$ are assumed independent of the type of the jumping atom or its chemical surrounding. According to these rates, one of the transitions is accepted in each step and a time variable is incremented by $\Delta t = -\ln r / \sum_j \nu_j$, where $r$ is a random number between 0 and 1.

This kinetic Monte Carlo algorithm allows to study ordering processes in bulk materials as well as nanoparticles. If a single vacancy is introduced in a lattice with periodic boundary conditions, a rearrangement of atoms by the vacancy diffusion mechanism in bulk materials is simulated. Instead, by initializing the simulation with a particle in the center of an otherwise empty lattice, surface diffusion occurs naturally. Identical to the algorithm applied in Sec. 7.4.2, the random generation and annihilation of vacancies at the surface then gives rise to a thermal concentration of vacancies in the volume of the particle. In order to apply the Ising-type lattice Hamiltonian to the studies of the present chapter, the absolute values of the interaction energies listed in Tab. 4.2 therefore have to be adjusted to reproduce reasonable values for the vacancy formation energy. In doing so, the phase diagram and the segregation behavior of the model presented in Chapter 4 remain unchanged. The set of modified parameters and the resulting vacancy formation energies $E_{\mathrm{v}}^{\mathrm{f}}$ in various chemical surroundings are listed in Tab. 8.1. With these values, the vacancy formation energies in the pure fcc Fe and fcc Pt phases agree well with the experimental values of 1.71 eV for Fe [103] and 1.35 eV for Pt [60], respectively.

Due to a lack of reference values for the FePt alloy system, experimental data on Pt self-diffusion has been employed in order to define the parameters $\nu_0$ and $E^{\mathrm{mig}}$. In Ref. [60], an attempt frequency of $\nu_0 = 4 \times 10^{13}\,1/\mathrm{s}$ and an activation energy for Pt self-diffusion of $Q = E_{\mathrm{v}}^{\mathrm{f}} + E^{\mathrm{mig}} = 2.8\,\mathrm{eV}$ is reported. From the values listed in Tab. 8.1, the average formation energy of a vacancy in FePt alloys predicted by the Ising-type Hamiltonian is 1.8 eV. An attempt frequency $\nu_0 = 4 \times 10^{13}\,1/\mathrm{s}$ and a migration energy $E^{\mathrm{mig}} = 1\,\mathrm{eV}$ should therefore provide realistic estimates for the present simulations.

## 8.3. Kinetics of ordering in bulk FePt alloys

In order to validate the choice of model parameters, the ordering kinetics of a FePt bulk crystal predicted by the simulations have been compared to annealing experiments on sputtered FePt thin films at a temperature of 973 K [165].

The bulk crystal has been modeled by periodic boundary conditions applied to a lattice of $70 \times 70 \times 70$ fcc unit cells, which corresponds to $N = 1,372,000$ lattice sites. By randomly distributing Fe and Pt atoms and introducing a single vacancy, the lattice has been initialized and the $n$-fold way algorithm described above was used for simulating the dynamics of ordering. In the simulation of a bulk material, the vacancy concentration is fixed at $C_{\mathrm{v}}^{\mathrm{sim}} = 1/N$, while in a real system a temperature dependent vacancy concentration of $C_{\mathrm{v}}^{\mathrm{real}}(T) \approx \exp\left(-1.8\,\mathrm{eV}/k_{\mathrm{B}}T\right)$ would be observed. In the latter case, the average vacancy

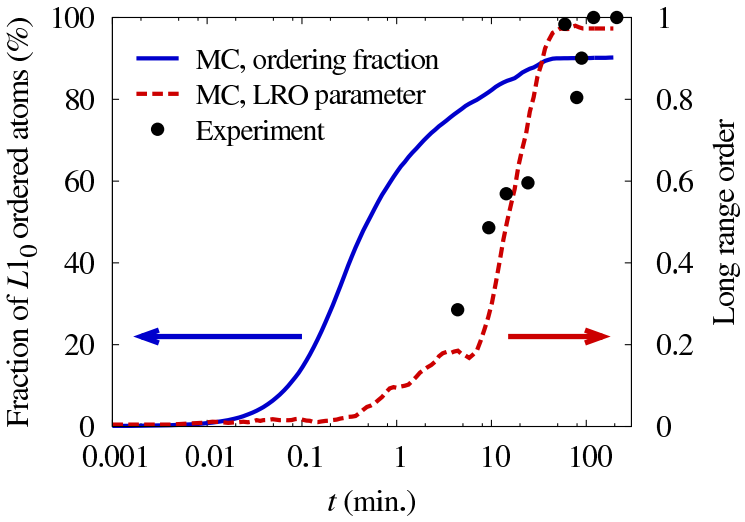


**Figure 8.1:** *Comparison of simulated ordering kinetics in bulk FePt alloys with results from annealing experiments on sputtered thin films [165]. The temperature in both experiments and simulation is 973 K.*

formation energy in FePt alloys predicted by the Ising-type Hamiltonian is assumed. In order to relate the time variable of the $n$-fold way algorithm to a real time, it therefore has to be scaled by the factor $C_{\mathrm{v}}^{\mathrm{sim}}/C_{\mathrm{v}}^{\mathrm{real}}(T)$.

At each step of the simulation, the amount of order has been analyzed by calculating the long range order (LRO) parameter defined in Sec. 3.6.3 and, additionally, by counting the fraction of atoms that possess a completely ordered nearest neighborhood, as introduced in Sec. 6.5.4. The time evolution of both order parameters is plotted in Fig. 8.1 in comparison to experiments on sputtered FePt films of 10 nm thickness [165]. Because of the large number of atoms, the simulations did not result in a single-domain ordered crystal. Instead, ordered domains with different $c$-axis orientation have been observed. For providing a correct description of the amount of order, the LRO parameter plotted in Fig. 8.1 has been calculated by summing over the individual domains and a value close to 1 is obtained after approximately one hour of real time. Instead, the parameter describing the fraction of $L1_0$ ordered atoms initially rises on a much shorter time scale, reflecting the presence of local order, only. Also, it stays at a value well below 1.0 at the end of the simulation, which indicates the fraction of atoms that reside in anti-phase boundaries.

In experiments, the presence of different domains has also been observed by dark-field (DF) transmission electron microscopy [165]. In consequence, the total ordered volume fraction has been determined by combining DF images from three independent directions. The degree of order reported in Ref. [165] therefore corresponds to the LRO parameter plotted in Fig. 8.1 and an excellent agreement between the simulations and the experiments can be observed.

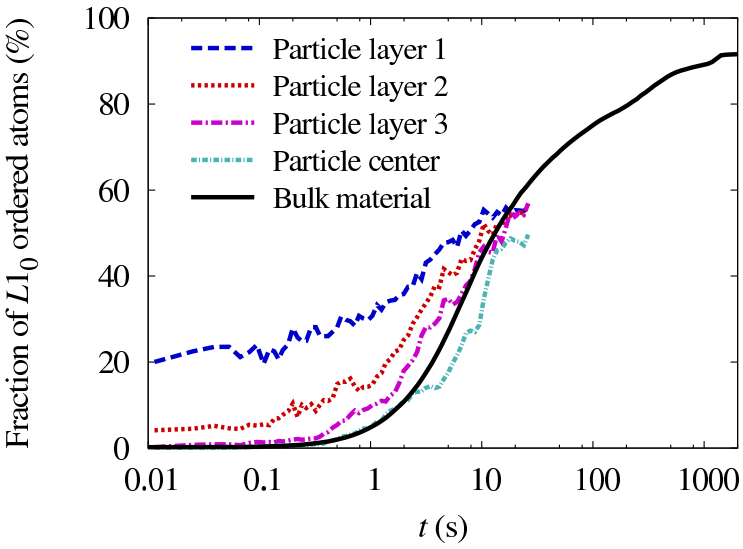


**Figure 8.2:** *Evolution of ordering fraction in a free FePt nanoparticle of $d = 5$ nm compared to the case of a bulk material. For analyzing the contribution of surface and volume effects, the particle has been divided into a spherical core of diameter 3.2 nm, followed by three layers of thickness 0.3 nm, with layer 1 denoting the surface. The temperature is 1000 K. Initially, the fraction of ordering was zero in all layers.*

Given the simplicity of the model and the uncertainties of the parameters $\nu_0$, $E^{\mathrm{mig}}$ and the vacancy formation energy, such an exact agreement is certainly to some extent coincidental. It shows, however, that the chosen values for $\nu_0$ and $E^{\mathrm{mig}}$ represent at least a reasonable estimate for diffusion parameters in FePt alloys.

## 8.4. Free FePt nanoparticles

In Chapter 7, a depletion of vacancies in the volume of metallic nanoparticles has been demonstrated. Therefore, the ordering transition should occur at a lower rate in the volume of a nanoparticles than in the corresponding bulk material. On the other hand, it is expected that surface diffusion can increase the rate of transformation in layers near the surface of the particle. In order to investigate both effects, the evolution of the ordering fraction at 1000 K in a FePt particle with 5 nm diameter has been analyzed. The particle has been divided into a spherical core of diameter 3.2 nm, followed by three layers of thickness 0.3 nm each. This way, the rate of the transition can be separated into surface near and volume contributions, as shown in Fig. 8.2. Note that all layers in the particle were initially completely disordered.

The effect of surface diffusion is clearly visible: a given amount of ordering is reached within a shorter time scale the closer a layer is positioned to the surface. By comparing to the simulations on a periodic lattice also shown in Fig. 8.2, it is also clear that the ordering in surface near layers proceeds at a higher rate than in a bulk material.

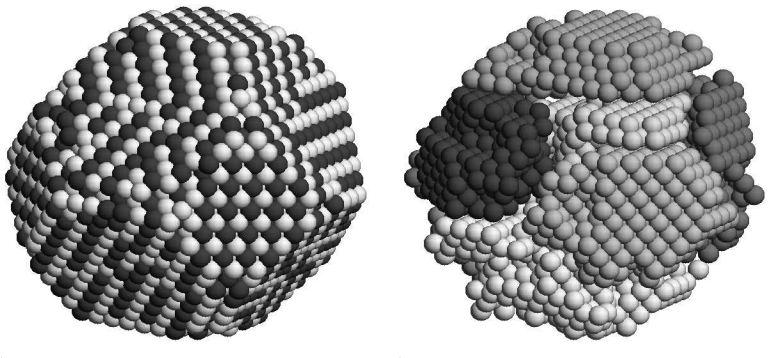

**Figure 8.3:** *Structure of a free 5 nm particle after 30 s of annealing time at 1000 K. Left: Pt atoms are displayed light grey, Fe atoms dark grey. Right: Atoms in anti-phase boundaries have been removed and the grey scale visualizes atoms that belong to the same ordered domain.*

In contrast, the core of the particle possesses the lowest rate of transformation from the disordered to the ordered phase. In accordance with the reduced vacancy concentration, the ordering process in the particle core requires longer annealing times than in the bulk material.

The kinetic MC simulations of the free FePt nanoparticles were terminated after approximately 30 s of real annealing time, which corresponds to one month of computing time. Within this time scale, the ordering fraction plotted in Fig. 8.2 indicates that only 50 % of the particle has been transformed. In Fig. 8.3, the structure of the particle at the end of the simulation run was analyzed and it can be seen that a high degree of order has been achieved. Because of the statistical nucleation of the $L1_0$ phase, however, the whole particle is divided into several ordered domains with different $c$-axis orientation. Approximately 50 % of the atoms reside in anti-phase boundaries, explaining the low value of the ordering fraction.

For the same reason, the ordering fraction in the bulk material has also reached a value of only 60 % after 30 s of annealing time. For eliminating most of the anti-phase boundaries, the annealing process has to be continued for up to 30 minutes in real time. Reaching these time scales in the particle simulations, however, would require computing times of up to 5 years and is therefore not feasible.

Although the kinetic MC simulations do not allow to study the ordering process in free FePt nanoparticles up to the final stage, possibilities for increasing the rate of transformation can be extracted. On the one hand, the important contribution of surface diffusion to atomic mobility has been demonstrated. Therefore, by increasing the amount of surface diffusion, it should be possible to enhance the transformation. Furthermore, a random nucleation of $L1_0$ ordered domains with different $c$-axis orientation occurs in free particles. Therefore, long annealing times are needed for obtaining a single domain structure.

By providing nucleation sites for the $L1_0$ phase, a preferential $c$-axis orientation could be induced, efficiently reducing the number of domains. In the following, the possibility for realizing enhanced surface diffusion and a preferential ordering direction in supported FePt nanoparticles is investigated. This scenario is at the same time relevant for the intended application and thus can provide guidelines on what substrate would be an appropriate choice.

## 8.5. Supported FePt nanoparticles

In order to model the energetics of supported FePt nanoparticles, the lattice Hamiltonian is extended by nearest neighbor bond energies of Fe and Pt atoms to a substrate, denoted $\varepsilon^{\mathrm{FeSub}}$ and $\varepsilon^{\mathrm{PtSub}}$, respectively. The relative strength of the atom interactions with the substrate is measured by the ratios $\varphi^{\mathrm{Fe}} = \varepsilon^{\mathrm{FeSub}}/\varepsilon_1^{\mathrm{FeFe}}$ and $\varphi^{\mathrm{Pt}} = \varepsilon^{\mathrm{PtSub}}/\varepsilon_1^{\mathrm{PtPt}}$. The lattice Hamiltonian restricts the investigations to an epitaxial relation between the substrate and the nanoparticles. Furthermore, only the (100) surface of the substrate is considered.

By varying the strength of the interactions with the substrate, the interface energetics of the supported particles can be modified. Two general cases are considered. First, the relative strength of the interactions with the substrate are assumed identical for both elements. The parameters $\varphi^{\mathrm{Fe}} = \varphi^{\mathrm{Pt}}$ then determine the wetting angle of the particle in equilibrium with the substrate. As a second case, it is assumed that only Pt has a significant binding energy to the substrate, with $\varphi^{\mathrm{Fe}} = 0$ and $\varphi^{\mathrm{Pt}} > 0$. In addition to wetting, the parameters then provide a driving force for segregation of Pt at the interface to the substrate.

### Identical Fe-substrate and Pt-substrate interactions

All kinetic MC simulations have been started with a spherical particle of 5 nm in diameter positioned on top of the substrate, as illustrated in the top row of Fig. 8.4. In the second row of Fig. 8.4, the outcome of simulations after a short annealing time of 0.4 s at 1000 K is depicted for particles with identical Fe-substrate and Pt-substrate interactions. For relatively weak interactions with the substrate ($\varphi^{\mathrm{Fe}} = \varphi^{\mathrm{Pt}} = 2/8$ and $3/8$, particles A and B, respectively), truncated octahedral particles are obtained that possess only a small degree of visible ordering. Instead, for a strong interaction with the substrate ($\varphi^{\mathrm{Fe}} = \varphi^{\mathrm{Pt}} = 5/8$, particle C), substantial wetting is observed and ordered domains are clearly visible. The degree and the mechanism of ordering in these particles is analyzed quantitatively in Fig. 8.5. For particles A and B Fig. 8.5 shows that the LRO parameter remains almost

Initial configuration of a supported spherical particle.

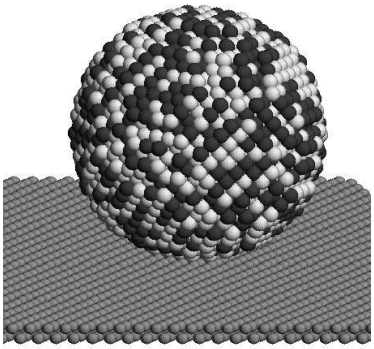

Final configurations, identical Fe-substrate and Pt-substrate interactions.

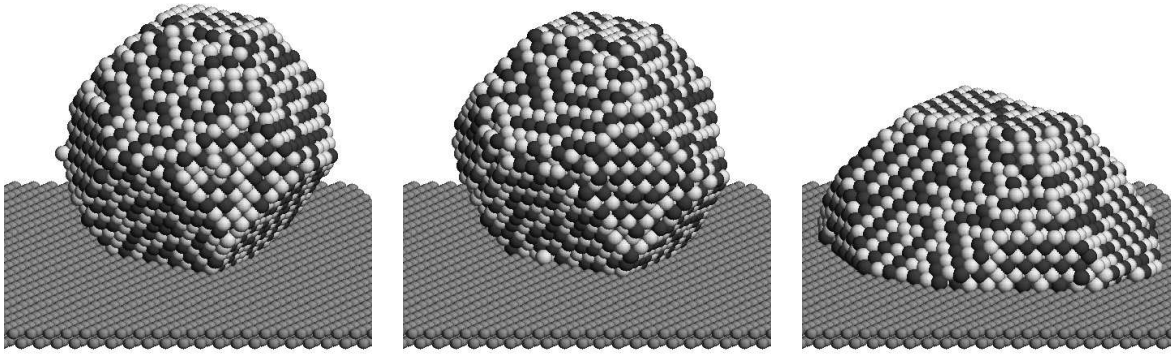

**A**: $\varphi^{\mathrm{Fe}} = \varphi^{\mathrm{Pt}} = 2/8$ **B**: $\varphi^{\mathrm{Fe}} = \varphi^{\mathrm{Pt}} = 3/8$ **C**: $\varphi^{\mathrm{Fe}} = \varphi^{\mathrm{Pt}} = 5/8$

Final configurations, only Pt-substrate interactions.

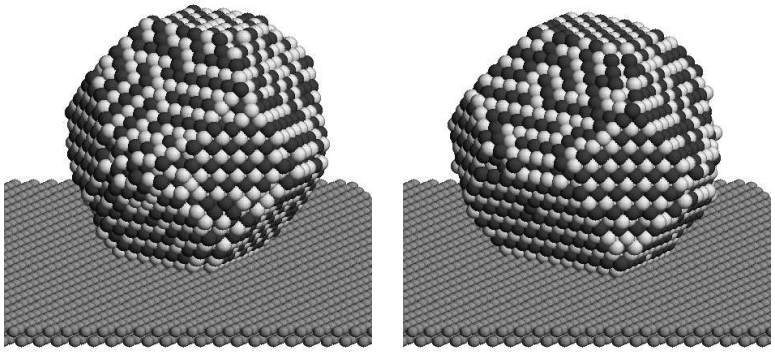

**D**: $\varphi^{\mathrm{Fe}} = 0;\ \varphi^{\mathrm{Pt}} = 2/8$ **E**: $\varphi^{\mathrm{Fe}} = 0;\ \varphi^{\mathrm{Pt}} = 3/8$

**Figure 8.4.:** *Snapshots of supported FePt nanoparticles illustrating the different interface energetics investigated in the MC simulations. Pt atoms are displayed light grey, Fe atoms dark grey. Top row: a disordered, spherical particle of 5 nm in diameter used as input structure in all simulations. Second row: Outcome of simulations with identical Fe-substrate and Pt-substrate interactions. Third row: Outcome of simulations with only Pt-substrate interactions.*

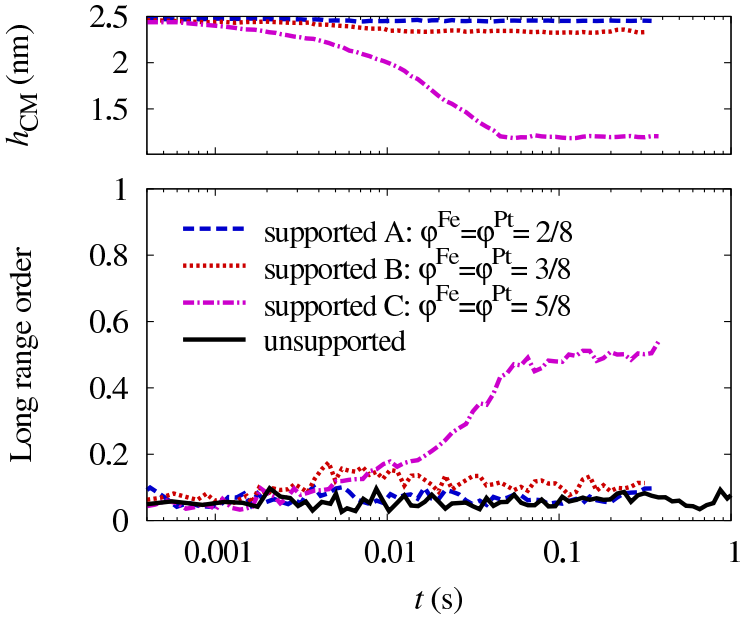


**Figure 8.5:** *Bottom panel: Evolution of LRO parameter with annealing time at 1000 K in a free and in supported FePt nanoparticles with identical Fe-substrate and Pt-substrate interactions. Top panel: Position of the center of mass of supported FePt nanoparticles, measured in height over the substrate* $h_{\mathrm{CM}}$.

zero within the annealing time of 0.4 s, identical to the unsupported particle. In contrast, for particle C, a rapid increase of LRO up to a value of 0.5 is observed. By monitoring the height of the center of mass of particle C over the substrate (top panel in Fig. 8.5), this increase in ordering can clearly be related to the wetting process. The mass transport over the particle surface towards the substrate is accompanied by a simultaneous adjustment of order.

### Pt-substrate interactions only

In the bottom row of Fig. 8.4, the outcome of simulations after an annealing time of 8 s at 1000 K is depicted for particles with only Pt-substrate interactions. For both particle D ($\varphi^{\mathrm{Pt}} = 2/8$) and particle E ($\varphi^{\mathrm{Pt}} = 3/8$), a truncated octahedral shape is obtained and Pt clearly segregates at the interface to the substrate. This segregation imposes a preferential ordering direction with $c$-axis perpendicular to the substrate. For particle E, where the driving force for segregation and the wetting area are larger, a large domain with this preferential orientation is clearly visible. The ordering is quantified in Fig. 8.6, where the variation of LRO parameter with annealing time for particles D and E is compared to an unsupported nanoparticle. After a short annealing time of 8 s, the LRO parameter of the free particle still indicates zero ordering, which can be attributed to the presence of multiple ordered domains as demonstrated in Sec. 8.4. Instead, a high degree of ordering (LRO = 0.8) is obtained for particle E within the same annealing time. In this particle, the randomness of the ordering process has been reduced by imposing a preferential $c$-axis

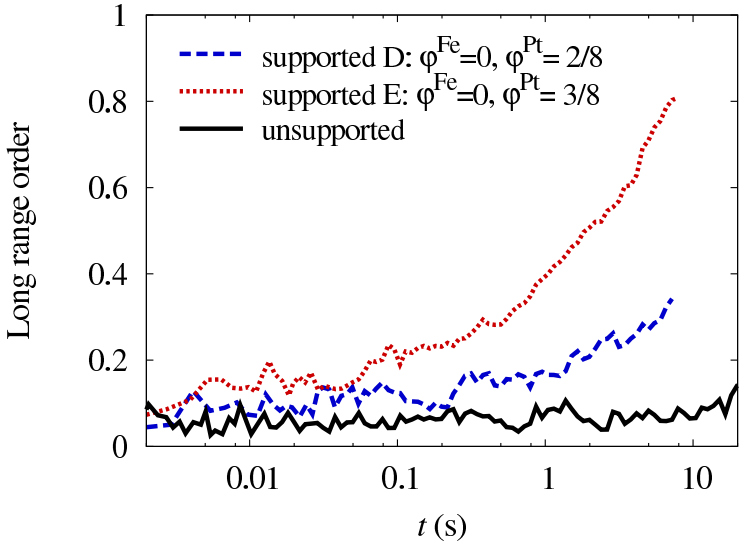


**Figure 8.6:** *Evolution of LRO parameter with annealing time at 1000 K in a free and in supported FePt nanoparticles with only Pt-substrate interactions.*

orientation through the segregation of Pt. In consequence, a single domain that extends almost through the whole particle could be realized within the short annealing time of 8 s.

## 8.6. Summary

The kinetics of ordering processes in FePt nanoparticles were investigated by kinetic Monte Carlo simulations based on the Ising-type lattice Hamiltonian with modified bond energies. In order to validate the choice of attempt frequencies and migration barriers for atomic diffusion, the variation of ordering with annealing time in a FePt bulk alloy was compared to annealing experiments on sputtered thin films.

In simulations of free nanoparticles, an important influence of surface diffusion on the ordering transition was identified. In surface near layers, the $A1$ to $L1_0$ transformation proceeds at a higher rate than in the particle core. Because of the statistical nucleation of the ordered phase, however, no single domain particles have been obtained and an elimination of the antiphase boundaries could not be observed within the time scales accessible by the simulations.

By systematically modifying the energetics of the particle-substrate interactions, possibilities for increasing the rate of transformation in supported nanoparticles have been investigated. If the interface energetics lead to a strong wetting of the substrate by the particle, the surface diffusion directed towards the substrate is accompanied by a simultaneous adjustment of order. Furthermore, if segregation of one element at the interface to the substrate occurs, a preferential $c$-axis orientation perpendicular to the substrate can be

induced. In result, random nucleation of multiple ordered domains is reduced and single domain particles can be obtained after short annealing times.

These observations can serve as a guideline for selecting appropriate substrates for FePt nanoparticles in magnetic recording applications. While the enhanced ordering by strong wetting should be independent from the epitaxial relation between particle and substrate, the effectivity of the segregation mechanism relies on a preferential $\langle 001 \rangle$ orientation of the particles. This orientation is, however, also a prerequisite for the applicability of FePt nanoparticles as a magnetic recording medium.

# Conclusions

In the present dissertation, thermodynamic and kinetic properties of FePt nanoparticles are investigated by atomistic computer simulations.

In the first part, atomistic model descriptions of the FePt alloy system have been developed by following a hierarchical multiscale approach: Quantum-mechanic total-energy calculations in the framework of the density functional theory have served as input for parameterizing an interatomic analytic bond-order potential (ABOP) for the FePt system. The interatomic potential, in turn, has been used in order to verify the adequacy of a lattice-based Ising-type Hamiltonian for investigating size effects in alloy nanoparticles.

In developing the ABOP, parameterizations for Fe-Fe, Pt-Pt and mixed Fe-Pt interactions have been devised. For pure Fe, it has been shown that the treatment of the structural phase transitions from the $\alpha$- to the $\gamma$- and $\delta$-phase neglected by previous classic interatomic potentials is possible. In order to compensate for the magnetic energy and entropy contributions to the free energy, the static lattice energy difference between bcc and fcc iron has been considered as an adjustable parameter. Calculations of the Gibbs free energy difference between the corresponding phases have then been carried out in order to verify the presence of the phase transitions. For pure Pt, a correct reproduction of the large stacking-fault and twin boundary energies has been achieved, which is essential for describing the plastic deformation behavior. Also, the potential accounts for the low anisotropy-ratio of the fcc Pt elastic shear moduli. Based on the potentials for the pure constituents, a parametrization of the Fe-Pt cross-interaction potential has been developed that provides an accurate description of the $L1_0$ ordered and $A1$ disordered structures. By conducting MC simulations of the ordering transition, the potential has explicitly been fitted to the order-disorder transition temperature.

By using the atomistic model descriptions developed in the first part, the size dependent structure and the ordering behavior of FePt nanoparticles have been investigated. The results are summarized in the following.

- By determining the energy of different structural motives and by estimating vibrational entropy contributions, the predominance of multiply twinned icosahedral particles in the gas-phase preparation process can been explained.
  - Because of an energetic preference of icosahedral shapes at particle sizes smaller than 2.6 nm in diameter, stable twinned structures are likely to be formed during the nucleation stage and are then kinetically trapped up to larger sizes.
  - In addition, for particles up to 6 nm in diameter the larger vibrational entropy contributions in icosahedral particles lead to a crossing of the thermodynamically stable structure from single crystalline to multiply twinned at elevated temperatures. The estimated size limit for this crossing coincides with experimental observations that show a predominance of single crystalline particles for diameters larger than 6 nm.
  - In contrast to the gas-phase preparation process, the presence of surfactants in solution-phase synthesis leads to reduced surface energy contributions and single crystalline particles occur.
- By applying the bond-order potential and the Ising-type Hamiltonian in importance sampling Monte Carlo simulations, the thermodynamics of ordering in FePt nanoparticles has been analyzed.
  - Both model descriptions yield only small differences concerning the size dependence of ordering. Most notably, the bond-order potential predicts a higher amount of surface induced disorder at moderate temperatures, which has been attributed to vibrational entropy contributions. On the other hand, the depression of ordering temperature with decreasing particle size is almost identical for the interatomic potential and the lattice Hamiltonian. This indicates that strain effects arising from the tetragonal distortion of the $L1_0$ structure do not have a significant influence on the ordering behavior. Therefore, it has been demonstrated that the Ising-type Hamiltonian is an appropriate model for studying size effects of ordering in FePt nanoparticles.
  - The Monte Carlo simulations predict only a small depression of ordering temperature $T_c$ with decreasing particle size. Therefore, the $L1_0$ structure remains the thermodynamically stable phase in FePt nanoparticles. Even for the smallest considered particle size of 2.5 nm, $T_c$ remains well above the typical annealing temperatures of 800 K employed in experiments. Thus, a kinetic trapping of the

particles in the metastable $A1$ phase is the most likely mechanism that inhibits the $A1$ to $L1_0$ transformation.

  - The strongest variations of ordering have been found for strong surface segregation potentials. If the energetics of the particle surface lead to a strong preferential segregation of one element, the composition of the particle volume is shifted away from stoichiometry and $L1_0$ ordering is suppressed. This effect can provide an explanation for the lack of ordering in matrix-embedded or solution phase synthesis particles. By increasing the concentration of the segregating element, the ordering can then be partially restored.

- Based on the finding that the $L1_0$ structure remains the stable phase in FePt nanoparticles, mechanisms that kinetically limit the $A1$ to $L1_0$ transformation have been investigated and process conditions that provide the possibility of increasing the transformation rate in supported nanoparticles have been analyzed.

  - By considering surface energy and surface stress effects, the vacancy formation energy in metallic nanoparticles was found to increase with decreasing particle size. Estimates for a 4 nm FePt nanoparticle give a vacancy concentration of only 20 to 30 % of the corresponding bulk value at typical annealing temperatures of 800 K. Annealing times increased by a factor three to five are therefore needed for completing the $A1$ to $L1_0$ transformation in the particle core.
  - The kinetics of ordering processes in free FePt nanoparticles have been investigated by kinetic Monte Carlo simulations. An increased atomic mobility at the surface of free particles leads to a gradient of the transformation rate, which proceeds faster in surface near layers than in the particle core. However, a statistical nucleation of multiple ordered domains leads to the presence of metastable anti-phase boundaries that can only be eliminated after long annealing times.
  - Given the important contribution of surface diffusion and the problem of statistical nucleation in free nanoparticles, possibilities for optimizing the transformation kinetics in supported FePt nanoparticles have been examined. If the energetics of the interface lead to a strong wetting of the substrate by the particle, the increased surface diffusion was found to be accompanied by a faster adjustment of order than in unsupported particles. Furthermore, a strong segregation of one element at the interface between the particle and the substrate can induce a preferential $c$-axis orientation which efficiently reduces the number of domains in the particle.

# A. Appendix: Phase stability

*In this chapter the methods used for calculating the Gibbs free energies of the bcc and fcc iron phases of various interatomic potentials are described.*

## A.1. Thermodynamic integration

In order to determine which of two phases is stable under given conditions, the phase with the lower Helmholtz free energy (at constant $V$ and $T$) or lower Gibbs free energy (constant $P$ and $T$) has to be identified. However, the calculation of entropy related properties like Helmholtz of Gibbs free energies is a non trivial task in computer simulations. In contrast to mechanical quantities like energy, pressure or temperature, the entropy cannot be written as an average of a function of the phase space coordinates of a system. Therefore, it cannot be calculated directly in a simulation by taking ensemble or time averages [33].

A method to circumvent this problem is to identify a thermodynamic relation that connects a derivative of the thermal property of interest with an easily measurable mechanical quantity. For example, the Gibbs-Helmholtz equation relates the temperature derivative of the Gibbs free energy with the enthalpy of the system:

$$\left(\frac{\partial}{\partial T}\left(\frac{G}{T}\right)\right)_P = -\frac{H}{T^2}. \tag{A.1}$$

Since the enthalpy can directly be obtained from a simulation, the Gibbs free energy of a system at a given temperature $T$ and pressure $p$ can be computed by measuring the enthalpy along a reversible path at constant pressure that links the system to a reference state of known Gibbs free energy $G_0$ at temperature $T_0$. The Gibbs free energy difference between the system at temperature $T$ and $T_0$ is then obtained by thermodynamic integration, i.e. by integrating Eq. (A.1) along the reversible path:

$$\frac{G(T)}{T} = \frac{G(T_0)}{T_0} - \int_{T_0}^{T} \frac{H(\tau)}{\tau^2} \mathrm{d}\tau. \tag{A.2}$$

## A.2. Coupling parameter method

In a simulation, the thermodynamic integration method is not limited to integration paths that could also be realized in a real world experiment. Instead, any parameter of the potential energy function can be used as integration variable [33]. A method that makes use of this possibility is the coupling parameter method.

In this method, an energy function $\tilde{U}$ is constructed by coupling the potential energy function that describes the interatomic interactions of the system of interest $U$ to the potential energy function of a reference system $U_{\mathrm{ref}}$ whose entropy can be calculated analytically:

$$\tilde{U}(\lambda) = (1-\lambda)U + \lambda U_{\mathrm{ref}}. \tag{A.3}$$

The coupling parameter $\lambda$ allows a gradual switching between the energy functions contributing to $\tilde{U}$. For $\lambda = 0$, the interactions of the original solid of interest are recovered, while for $\lambda = 1$, the reference system is obtained.

In the canonical $N, V, T$ ensemble, the partition function of a system described by Eq. (A.3) is given by [33]

$$Z(N,V,T,\lambda) = \frac{1}{\Lambda^{3N} N!} \int \mathrm{d}\mathbf{r}^N \exp\left(-\beta \tilde{U}(\lambda)\right) \tag{A.4}$$

with $\Lambda = \sqrt{\hbar 2\pi / m k_{\mathrm{B}} T}$ and $\beta = 1/k_{\mathrm{B}}T$. The derivative of the free energy $\tilde{F}(\lambda) = -1/\beta \ln Z(N,V,T,\lambda)$ with respect to $\lambda$ is given by

$$\begin{aligned}
\left(\frac{\partial \tilde{F}(\lambda)}{\partial \lambda}\right)_{N,V,T} &= -\frac{1}{\beta}\frac{\partial}{\partial \lambda} \ln Z(N,V,T,\lambda) \\
&= -\frac{1}{\beta Z(N,V,T,\lambda)} \frac{\partial Z(N,V,T,\lambda)}{\partial \lambda} \\
&= \frac{\int \mathrm{d}\mathbf{r}^N \frac{\partial \tilde{U}(\lambda)}{\partial \lambda} \exp\left(-\beta \tilde{U}(\lambda)\right)}{\int \mathrm{d}\mathbf{r}^N \exp\left(-\beta \tilde{U}(\lambda)\right)}.
\end{aligned} \tag{A.5}$$

Eq. (A.5) has the form of an ensemble average of the quantity $\partial \tilde{U}(\lambda)/\partial \lambda$:

$$\left(\frac{\partial \tilde{F}(\lambda)}{\partial \lambda}\right)_{N,V,T} = \left\langle \frac{\partial \tilde{U}(\lambda)}{\partial \lambda} \right\rangle_{\lambda}. \tag{A.6}$$

Since $\partial \tilde{U}(\lambda)/\partial \lambda$ is a mechanical property that can easily be measured in a computer simulation, the concept of thermodynamic integration can be used for calculating the

difference between the Helmholtz free energy of the system of interest $F$ and the reference system $F_{\mathrm{ref}}$. Integration of Eq. (A.6) gives

$$\begin{aligned} F &= F_{\mathrm{ref}} + \tilde{F}(\lambda=0) - \tilde{F}(\lambda=1) \\ &= F_{\mathrm{ref}} - \int_{\lambda=0}^{\lambda=1} \mathrm{d}\lambda \left\langle \frac{\partial \tilde{U}(\lambda)}{\partial \lambda} \right\rangle_{\lambda} \\ &= F_{\mathrm{ref}} - \int_{\lambda=0}^{\lambda=1} \mathrm{d}\lambda \left\langle \Delta U \right\rangle_{\lambda}, \end{aligned} \tag{A.7}$$

with $\Delta U = U_{\mathrm{ref}} - U$.

## A.3. Application to solids

For applying the coupling parameter method to free energy calculations of solids, the Einstein crystal is a convenient choice for a reference system. The atoms in a classical Einstein crystal do not interact with each other, instead they are coupled harmonically to their equilibrium lattice positions $\mathbf{r}_{0,i}$ via a spring constant $\alpha$. The potential energy function $U_{\mathrm{E}}$ of the Einstein crystal of $N$ atoms then reads

$$U_{\mathrm{E}}(\mathbf{r}^N) = \frac{1}{2}\alpha \sum_{i=1}^{N} \left(\mathbf{r}_i - \mathbf{r}_{0,i}\right)^2. \tag{A.8}$$

Since the atoms in an Einstein crystal do not experience any intermolecular interactions, no pressure can be defined and calculations can only be carried out in the $N, V, T$ ensemble.

According to Eq. (A.3), an arbitrary solid can be coupled to an Einstein crystal by writing

$$\tilde{U}(\mathbf{r}^N) = U(\mathbf{r}_0^N) + (1-\lambda)\left[U(\mathbf{r}^N) - U(\mathbf{r}_0^N)\right] + \lambda U_{\mathrm{E}}(\mathbf{r}^N). \tag{A.9}$$

The term $U(\mathbf{r}_0^N)$ denotes the static contribution to the potential energy, i.e. the potential energy of the solid when all atoms occupy their equilibrium lattice positions. Applying Eq. (A.7), the free energy of the solid can be calculated by the thermodynamic integration

$$F = F_{\mathrm{E}} - \int_0^1 \mathrm{d}\lambda \left\langle \Delta U(\mathbf{r}^N) \right\rangle_{\lambda}, \tag{A.10}$$

where $\Delta U(\mathbf{r}^N)$ is given by $U_{\mathrm{E}}(\mathbf{r}^N) - U(\mathbf{r}^N) + U(\mathbf{r}_0^N)$ and $F_{\mathrm{E}}$ is the free energy of the Einstein crystal.

The value of $F_{\mathrm{E}}$ in Eq. (A.10) can be calculated analytically. The Hamiltonian of an atom bound to its lattice position by a spring constant $\alpha$ is given by $H = \mathbf{p}^2/2m + \alpha\mathbf{r}^2/2$

and the one particle partition function $Z_1$ is obtained by integration over the whole phase space $\Gamma$:

$$\begin{aligned} Z_1 &= \frac{1}{h^3} \iint_{\Gamma} \mathrm{d}\mathbf{p}\mathrm{d}\mathbf{r} \exp\left(-\beta H\right) \\ &= \left(\frac{m}{\hbar^2 \beta^2 \alpha}\right)^{\frac{3}{2}}. \end{aligned} \tag{A.11}$$

In an Einstein crystal of $N$ atoms, all atoms are distinguishable, because each atom is assigned to its own equilibrium lattice position. The partition function of the Einstein crystal $Z_N$ can therefore be written as $Z_N{=}Z_1^N$ and its free energy is given by

$$\begin{aligned} F_{\mathrm{E}} &= -\frac{1}{\beta} \ln Z_N \\ &= -\frac{3N}{2\beta} \ln\left(\frac{m}{\hbar^2 \beta^2 \alpha}\right) \\ &= -3Nk_{\mathrm{B}}T \ln\left(\frac{T}{T_{\mathrm{E}}}\right), \end{aligned} \tag{A.12}$$

where $T_{\mathrm{E}}$ is the Einstein temperature, $T_{\mathrm{E}}{=}\sqrt{\hbar^2\alpha/{k_{\mathrm{B}}}^2 m}$.

In practice, the integrand in Eq. (A.10) is evaluated by a series of simulations at different values for $\lambda$ and the integral is evaluated numerically. The accuracy of the numerical integration can be enhanced by assuring that the integrand is a smooth function within the integration limits. This can be achieved by adjusting the value of the spring constant $\alpha$ in a way that the Einstein crystal behaves as much like the original solid as possible. A quantitative measure for this similarity is the mean square displacement of the atoms in the Einstein crystal $\langle \Delta r_{\mathrm{E}}^2 \rangle$, which should be the same as the mean square displacement $\langle \Delta r^2 \rangle$ in the original solid [33]. The latter value has to be determined by simulation, while the mean square displacement of the Einstein crystal can be calculated analytically. In the canonical ensemble it is given by

$$\langle \Delta r_{\mathrm{E}}^2 \rangle = \frac{4\pi \int_0^{\infty} r^4 \exp\left(-\alpha\beta r^2/2\right) \mathrm{d}r}{4\pi \int_0^{\infty} r^2 \exp\left(-\alpha\beta r^2/2\right) \mathrm{d}r} = \frac{3}{\beta\alpha}, \tag{A.13}$$

and one obtains the optimal value for the spring constant

$$\alpha = \frac{3}{\beta \langle \Delta r^2 \rangle}. \tag{A.14}$$

Another issue when sampling the integrand in Eq. (A.10) is that for $\lambda \to 0$ the atoms are free to move away from their equilibrium positions in the Einstein crystal and the solid as a whole can move. This leads to a sharp peak of the integrand for small $\lambda$ values, which in turn requires a finer sampling interval in order to guarantee a sufficient accuracy of the numerical quadrature. This problem can be avoided if the calculations are performed under the fixed center of mass constraint, which ensures that the atoms always oscillate around their equilibrium positions defined in the Einstein crystal [33, 166]. However, keeping the center of mass of the system fixed reduces the number of degrees of freedom. As a consequence, the free energy of the constrained solid differs from the unconstrained case and Eq. (A.10) has to be corrected for the difference. Polson *et al.* present a derivation of the correction terms in Ref. [167]. Their final expression for the free energy of the unconstrained solid of interest reads:

$$\begin{aligned}\frac{F}{Nk_\mathrm{B}T} &= -\frac{3}{2}\ln\left(\frac{{k_\mathrm{B}}^2T^2m}{\hbar^2\alpha}\right) \\ &\quad -\frac{1}{Nk_\mathrm{B}T}\int_0^1 \mathrm{d}\lambda \left\langle \Delta U(\mathbf{r}^N)\right\rangle_\lambda^{\mathrm{CM}} \\ &\quad -\frac{3}{2N}\ln\left(\frac{\alpha}{2\pi k_\mathrm{B}T}\right) \\ &\quad -\frac{3}{2N}\ln N + \frac{1}{N}\ln\frac{N}{V}. \end{aligned} \tag{A.15}$$

Here, $V$ is the volume of the system and the superscript CM denotes that the ensemble average is calculated under the fixed center of mass constraint. (In Ref. [167] Planck's constant is omitted in the first term on the right hand side).

## A.4. Phase stability of bcc and fcc iron

The schemes described above for calculating entropy related properties of a solid have been applied for determining the temperature dependent phase stability of bcc and fcc iron for different analytical potentials (see Sec. 3.4). The methodology used to this end is described in the following.

In order to compare the thermodynamic stabilities of the bcc and fcc phases of the analytic potentials, the phase with the lower Gibbs free energy has to be identified. If the equilibrium volume of a system at pressure $P$ and temperature $T$ is given by $V_{P,T}$, then the Gibbs free energy can be written as

$$G(N,P,T) = F(N,V_{P,T},T) + PV_{P,T}. \tag{A.16}$$

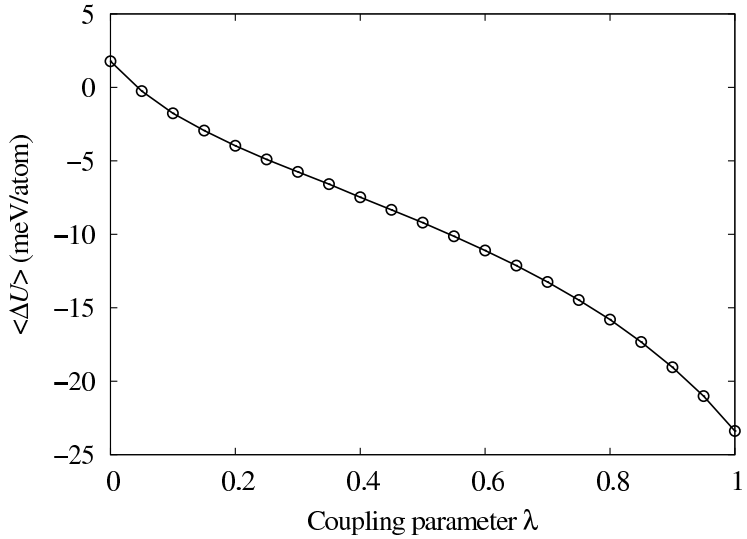


**Figure A.1:** *Integrand of Eq. (A.15) sampled at 300 K for the bcc phase of the Fe bond-order potential.*

At zero pressure, the Gibbs free energy $G$ therefore equals the Helmholtz free energy $F$, if the latter is determined at the appropriate equilibrium volume. This allows the calculation of $G$ with the coupling parameter method using the Einstein crystal as the reference system, despite its restriction to the $N, V, T$ ensemble: As a first step, the equilibrium volume $V_0$ at temperature $T_0$ and zero pressure is determined by a MD simulation run. The spring constant $\alpha$ of the reference Einstein crystal is then adjusted using Eq. (A.14), with $\langle \Delta r^2 \rangle$ obtained from a MC simulation at constant $V_0$ and coupling parameter $\lambda$=0. The integrand in equation Eq. (A.15) is then evaluated by a series of fixed center of mass MC simulations for $\lambda$ varying from 0 to 1 with an interval of $\Delta\lambda$=0.05. The system sizes used for the calculations are $8 \times 8 \times 8$ unit cells for the bcc lattice and $6 \times 6 \times 7$ unit cells for the fcc lattice, which corresponds to 1024 and 1008 atoms, respectively. For each $\lambda$, the value of $\Delta U(\mathbf{r}^N)$ is sampled over at least 5000 MC steps after allowing the system to equilibrate for 500 MC steps. An example of data obtained by this method is given in Fig. A.1 for the bcc phase of the Fe bond-order potential.

The temperature dependence of the Gibbs free energy can in principle be obtained by applying the coupling parameter method at different temperatures $T_0$. Alternatively, the Gibbs-Helmholtz equation offers a computationally more efficient approach: Once the Gibbs free energy has been determined by the coupling parameter method at an arbitrary $T_0$, Eq. (A.2) can be used to calculate the free enthalpy at any other temperature. In contrast to $\langle \Delta U \rangle$, the enthalpy $H(T)$ appearing in Eq. (A.2) can be obtained by a single MD simulation in the $N, P$=0$, T$ ensemble. In this work, the Gibbs free energies of the bcc and fcc iron phases have been determined by applying the coupling parameter method once for $T_0 = 300\,\mathrm{K}$ or alternatively 600 K and by integrating the Gibbs-Helmholtz equation for

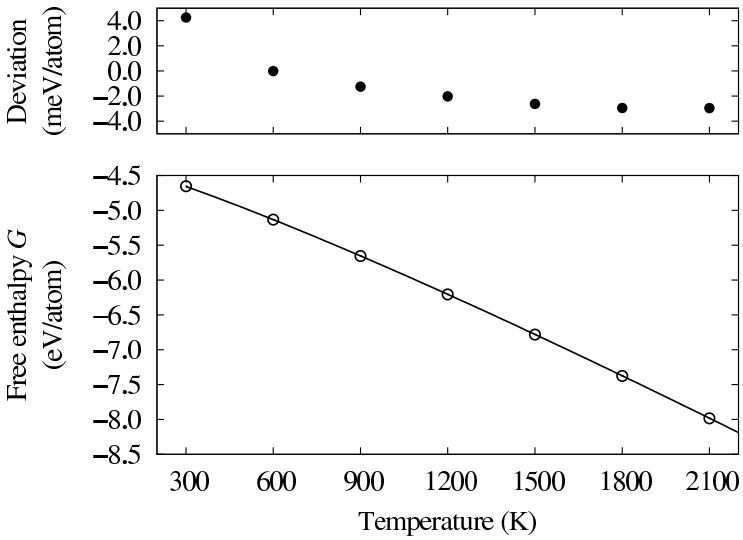


**Figure A.2:** *Lower panel: Gibbs free energy of the bcc Fe phase of the bond-order potential. Open circles denote data obtained by the coupling parameter method, the solid line denotes data obtained by integrating the Gibbs-Helmholtz equation with $T_0 = 600\,K$. Upper panel: Deviation between the two methods. Note the different units of the energy axis.*

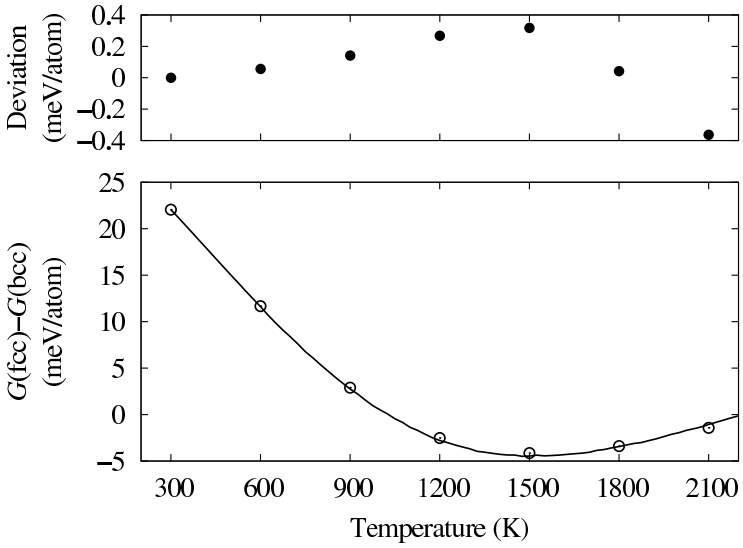


**Figure A.3:** *Lower panel: Gibbs free energy difference between the fcc and bcc iron phases of the bond-order potential. Open circles denote data obtained by the coupling parameter method, the solid line denotes data obtained by integrating the Gibbs-Helmholtz equation with $T_0 = 600\,K$. Upper panel: Deviation between the two methods.*

other temperatures using $H(T)$ data gained from MD simulations in 25 K intervals up to the melting point.

The accuracy of the integration and moreover the correctness of the implementation of the coupling parameter method can be verified by repeating the coupling parameter method at a few selected temperatures, which provides Gibbs free energy data from two independent sources. This is demonstrated in Fig. A.2, where the temperature variation of the Gibbs free energy of the bcc Fe phase is plotted as obtained from a repeated application of the coupling parameter method and from an integration of the Gibbs-Helmholtz equation with $T_0 = 600\,\mathrm{K}$. The maximum deviation between the two methods is less than

5 meV/atom. Furthermore, for Gibbs free energy *differences* between two solid phases, the deviation is less than 0.4 meV/atom, as demonstrated in Fig. A.3.

# Danksagung – Acknowledgments

An dieser Stelle möchte ich mich bei allen bedanken, die zum Gelingen dieser Arbeit beigetragen haben.

Mein Dank gilt insbesondere Herrn Professor Karsten Albe für die intensive Betreuung der Arbeit und das entgegengebrachte Vertrauen. Durch die hervorragende Arbeitsatmosphäre im Fachgebiet Materialmodellierung und der Offenheit für Fragestellungen abseits der vorgegebenen Thematik hat er maßgeblich zu meiner Motivation und zum Gelingen dieser Arbeit beigetragen.

Herrn Professor Horst Hahn möchte ich für die Begutachtung meiner Arbeit danken.

Bei meinen Bürokollegen Dr. Paul Erhart und Johan Pohl bedanke ich mich für unzählige fachliche Diskussionen und für die angenehme Zeit. Paul Erhart gebührt besonderer Dank für die Unterstützung bei der Potentialentwicklung.

Bei Herrn Dr. Bernd Rellinghaus vom IFW Dresden möchte ich mich für anregende Diskussionen bedanken, ebenso bei den *Mechanikern* Oliver Goy und Professor Ralf Müller von der TU Darmstadt.

I am very grateful to Kai Nordlund and his group at the University of Helsinki for their hospitality during my stays in Helsinki.

I wish to thank Brent Kraczek and Duane Johnson from the University of Illinois for communicating their calculations on defect energies in FePt.

Generous grants of computer time by the Center for Scientific Computing at the Johann Wolfgang Goethe-University in Frankfurt is gratefully acknowledged.

Über das Thema dieser Dissertation hinaus hatte ich die Gelegenheit auch an anderen Fragestellungen zu arbeiten. Für intensive und ausdauernde Diskussionen über die Modellierung organischer Halbleiter bedanke ich mich besonders bei Dr. Yuri Genenko und den *Organikern* aus der Gruppe von Professor Heinz von Seggern, allen voran Frederik Neumann, Arne Fleißner, Dr. Marcus Ahles, Dr. Torsten Finnberg und Dr. Christian Melzer. Bei Professor Thomas Michely und Dr. Karsten Busse von der RWTH Aachen möchte ich mich für die gute Zusammenarbeit auf dem Thema des Schichtwachstums bedanken.

Allen Mitgliedern des Gemeinschaftslabors Nanomaterialien und der ehemaligen Arbeitsgruppe Dünne Schichten möchte ich für die gemeinsamen Kaffeepausen, Betriebsausflüge und Konferenzreisen sowie für ihre mittägliche Geduld in der Mensa danken.

Bei meinen Eltern und meiner Freundin bedanke ich mich herzlich für ihre vielfältige Unterstützung während meines gesamten Studiums und der Promotion.

# Erklärung – Disclaimer

Die vorliegende Arbeit wurde im Zeitraum von Juli 2003 bis Dezember 2006 im Fachgebiet Materialmodellierung am Institut für Materialwissenschaft der Technischen Universität Darmstadt bei Herrn Prof. Dr. rer. nat. Karsten Albe angefertigt.

Hiermit versichere ich an Eides statt, dass ich die vorliegende Arbeit selbständig und nur unter Verwendung der angegebenen Hilfsmittel angefertigt habe. Von mir wurde weder an der Technischen Universität Darmstadt noch an einer anderen Hochschule ein Promotionsversuch unternommen.

Darmstadt, den 5. Dezember 2006

Michael Müller

# Curriculum Vitae

**Education**

PhD student,
Materials Modeling Division, Institute of Materials Science,
Technische Universität Darmstadt, since July 2003 – December 2006

Diploma in Materials Science and Engineering (*Dipl.-Ing.*),
Technische Universität Darmstadt, May 2003

High School Graduation (*Abitur*),
Hermann-Staudinger-Gymnasium, Erlenbach, June 1997

**Research experience**

Research scientist,
Materials Modeling Division, Institute of Materials Science,
Technische Universität Darmstadt, since July 2003

Research assistant,
Thin Films Division, Institute of Materials Science,
Technische Universität Darmstadt, August 2000 – November 2002

**Publications based on the present dissertation**

1. M. Müller and K. Albe, *Lattice Monte Carlo simulations of FePt nanoparticles: Influence of size, composition, and surface segregation on order-disorder phenomena*, Phys. Rev. B **72**, 094203 (2005).
2. M. Müller, P. Erhart and K. Albe, *Analytic bond-order potential for bcc and fcc iron - comparison with established EAM potentials*, submitted to Phys. Rev. B.
3. M. Müller, P. Erhart and K. Albe, *Thermodynamics of $L1_0$ ordering in FePt nanoparticles studied by Monte-Carlo simulations based on an analytic bond-order potential*, submitted to Phys. Rev. B.
4. M. Müller and K. Albe, *Concentration of thermal vacancies in metallic nanoparticles*, Acta Mater. accepted for publication
5. M. Müller and K. Albe, *Structural stability of multiply twinned FePt nanoparticles*, submitted to Acta Mater.
6. K. Albe, P. Erhart, M. Müller, *Analytical interatomic potentials for metals and metal compounds: A brief overview*, Proceedings des Abschlusskolloquiums SFB 370, RWTH Aachen, Wiley-VCH (2006), in print
7. K. Albe and M. Müller, *Größe entscheidet - Magnetische Nanopartikel in der Computersimulation*, thema Forschung **2/2006**, 52 (2006)

**Other publications**

1. C. Busse, C. Polop, M. Müller, K. Albe, U. Linke and T. Michely, *Stacking-fault nucleation on Ir(111)*, Phys. Rev. Lett. **91**, 056103 (2003).
2. M. Müller, K. Albe, C. Busse, A. Thoma and T. Michely, *Island shapes, island densities, and stacking-fault formation on Ir(111): Kinetic Monte Carlo simulations and experiment*, Phys. Rev. B **71**, 075407 (2005).
3. K. Albe and M. Müller, *Cluster diffusion and island formation on fcc(111) metal surfaces*, Int. Series Num. Math. **149**, 19 (2005).

# Bibliography


[1] J. Shi, S. Gider, K. Babcock and D. Awschalom, *Magnetic clusters in molecular beams, metals, and semiconductors*, Science **271**, 937 (1996).

[2] C. N. Ramachandra, G. U. Kulkarni, P. J. Thomas and P. P. Edwards, *Metal nanoparticles and their assemblies*, Chem. Soc. Rev. **29**, 27 (2000).

[3] M. J. Yacamán, J. A. Ascencio, H. B. Liu and J. Gardea-Torresdey, *Structure shape and stability of nanometric sized particles*, J. Vac. Sci. Technol. B **19**, 1091 (2001).

[4] F. Kim, J. H. Song and P. Yang, *Photochemical synthesis of gold nanorods*, J. Am. Chem. Soc. **124**, 14316 (2002).

[5] G. Schmid, *Large clusters and colloids. Metals in the embryonic state*, Chem. Rev. **92**, 1709 (1992).

[6] J. P. Borel, *Thermodynamical size effect and the structure of metallic clusters*, Surf. Sci. **106**, 1 (1981).

[7] F. Baletto and R. Ferrando, *Structural properties of nanoclusters: Enrgetic, thermodynamic,and kinetic effects*, Rev. Mod. Phys. **77**, 371 (2005).

[8] C. Q. Sun, prog. Sol. Stat. Chem., in press .

[9] R. C. Cammarata and K. Sieradzki, *Surface and interface stresses*, Annu. Rev. Mater. Sci. **24**, 215 (1994).

[10] L. D. Marks, *Experimental studies of small particle strutures*, Rep. Prog. Phys. **57**, 603 (1994).

[11] S. Ino, *Stability of multiply-twinned particles*, J. Phys. Soc. Jpn. **27**, 941 (1969).

[12] C. L. Cleveland and U. Landman, *The energetics and structure of nickel clusters: Size dependence*, J. Chem. Phys. **94**, 7376 (1991).

[13] K. Koga, T. Ikeshoji and K. Sugawara, *Size- and temperature-dependent structural transitions in gold nanoparticles*, Phys. Rev. Lett. **92**, 115507 (2004).

[14] S. Sun, C. B. Murray, D. Weller, L. Folks and A. Moser, *Monodisperse FePt nanoparticles and ferromagnetic FePt nanocrystal superlattices*, Science **287**, 1989 (2000).

[15] B. D. Terris and T. Thomson, *Nanofabricated and self-assembled magnetic structures as data storage media*, J. Phys. D: Appl. Phys. **38**, R199 (2005).

[16] S. Sun, *Recent advances in chemical synthesis, self-assembly, and applications of FePt nanoparticles*, Adv. Mater. **18**, 393 (2006).

[17] D. Weller, A. Moser, L. Folks, M. E. Best, W. Lee, M. F. Toney, M. Schwickert, J. U. Thiele and M. F. Doerner, *High $K_u$ materials approach to 100 GBits/in*$^2$, IEEE Trans. Magn. **36**, 10 (2000).

[18] S. Stappert, B. Rellinghaus, M. Acet and E. F. Wassermann, *Gas-phase preparation of L10 ordered FePt nanoparticles*, J. Cryst. Growth **252**, 440 (2003).

[19] *Landolt-Börnstein: Numerical data and Functional Relationships in Science and Technology*, edited by H. Ullmaier (Springer-Verlag, Heidelberg, 1991), No. 5.

[20] B. Bian, Y. Hirotsu, K. Sato, T. Ohkubo and A. Makino, *Structures and magnetic properties of oriented Fe/Au and Fe/Pt nanoparticles and a-Al2O3*, J. Electron Microscopy **48**, 753 (1999).

[21] Y. K. Takahashi, T. Koyama, M. Ohnuma, T. Ohkubo and K. Hono, *Size dependence of ordering in FePt nanoparticles*, J. Appl. Phys. **95**, 2690 (2004).

[22] B. Stahl, J. Ellrich, R. Theissmann, M. Ghafari, S. Bhattacharya, H. Hahn, N. S. Gajbhiye, D. Kramer, R. N. Viswanath, J. Weissmüller and H. Gleiter, *Electronic properties of 4-nm FePt particles*, Phys. Rev. B **67**, 4422 (2003).

[23] Z. R. Dai, S. Sun and Z. L. Wang, *Shapes, multiple twins and surface structures of monodisperse FePt magnetic nanocrystals*, Surf. Sci. **505**, 325 (2002).

[24] Z. R. Dai, S. Sun and Z. L. Wang, *Phase Transformation, coalescence, and twinning of monodisperse FePt nanocrystals*, Nano Lett. **1**, 443 (2001).

[25] Y. K. Takahashi, T. Ohkuba, M. Ohnuma and K. Hono, *Size effect on the ordering of FePt granular films*, J. Appl. Phys. **93**, 7166 (2003).

[26] D. L. Peng, T. Hihara and K. Sumiyama, *Structure and magnetic properties of FePt alloy cluster-assembled films*, J. Magn. Magn. Mater. **277**, 201 (2004).

[27] C. Y. Tan, J. S. Chen, B. H. Liu and G. M. Chow, *Microstructure of FePt nanoparticles produced by nanocluster beam*, J. Cryst. Growth **293**, 175 (2006).

[28] O. Dmitrieva, B. Rellinghaus, J. Kästner, M. O. Liedke and J. Fassbender, *Ion beam induced destabilization of icosahedral structures in gas phase prepared FePt nanoparticles*, J. Appl. Phys. **97**, 10N112 (2005).

[29] W. Press, S. Teukolsky, W. Vetterling and B. Flannery, in *Numerical Recipies in Fortran* (Cambridge University Press, Cambridge, 1992), Chap. 10.

[30] D. P. Landau and K. Binder, *A guide to Monte Carlo simulations in statistical physics* (Cambridge University Press, Cambridge, 2000).

[31] A. R. Leach, *Molecular Modelling, principles and applications* (Pearson Education, Harlow, 2001).

[32] N. Metropolis, A. W. Rosenbluth, M. N. Rosenbluth, A. H. Teller and E. Teller, *Equation of state calculations by fast computing machines*, J. Chem. Phys. **21**, 1087 (1953).

[33] D. Frenkel and B. Smit, *Understanding Molecular Simulation: From Algorithms to Applications* (Academic, New York, 1996).

[34] A. B. Bortz, M. H. Kalos and J. L. Lebowitz, *New algorithm for Monte-Carlo simulations of Ising spin systems*, J. Comp. Phys. **17**, 10 (1975).

[35] K. A. Fichthorn and W. H. Weinberg, *Theoretical foundations of dynamical Monte Carlo simulations*, J. Chem. Phys. **95**, 1090 (1991).

[36] A. F. Voter, F. Montalenti and T. C. Germann, *Extending the time scale in atomistic simulation of materials*, Annu. Rev. Mater. Res. **32**, 321 (2002).

[37] M. Müller, K. Albe, C. Busse, A. Thoma and T. Michely, *Island shapes, island densities, and stacking-fault formation on Ir(111): Kinetic Monte Carlo simulations and experiment*, Phys. Rev. B **71**, 075407 (2005).

[38] J. Hafner, C. Wolverton and G. Ceder, *Toward computational materials design: The impact of density functional theory on materials research*, MRS Bulletin **31**, 659 (2006).

[39] P. Hohenberg and W. Kohn, *Inhomogeneous eletron gas*, Phys. Rev. **136**, B864 (1964).

[40] W. Kohn and L. J. Sham, *Self-consistent equations including exchange and correlation effects*, Phys. Rev. **140**, A1133 (1965).

[41] G. Kresse and J. Furthmüller, *Efficient iterative schemes for ab initio total-energy calculations using a plane-wave basis set*, Phys. Rev. B **54**, 11169 (1996).

[42] M. S. Daw and M. I. Baskes, *Embedded-atom method: Derivation and application to impurities, surfaces, and other defects in metals*, Phys. Rev. B **29**, 6443 (1984).

[43] M. I. Baskes, *Modified embedded-atom potentials for cubic materials and impurities*, Phys. Rev. B **46**, 2727 (1992).

[44] G. C. Abell, *Empirical chemical pseudopotential theory of molecular and metallic bonding*, Phys. Rev. B **31**, 6184 (1985).

[45] J. Tersoff, *New empirical approach for the structure and energy of covalent systems*, Phys. Rev. B **37**, 6991 (1988).

[46] D. W. Brenner, *Empirical potential for hydrocarbons for use in simulating the chemical vapor-deposition of diamond films*, Phys. Rev. B **42**, 9458 (1990).

[47] K. Albe, K. Nordlund and R. S. Averback, *Modeling the metal-semiconductor interaction: Analytical bond-order potential for platinum-carbon*, Phys. Rev. B **65**, 195124 (2002).

[48] N. Juslin, P. Erhart, P. Traskelin, J. Nord, K. Henriksson, K. Nordlund, E. Salonen and K. Albe, *Analytical interatomic potential for modeling nonequilibrium processes in the W-C-H system*, J. Appl. Phys. **98**, 3520 (2005).

[49] A. Zunger, L. G. Wang, G. L. W. Hart and M. Sanati, *Obtaining Ising-like expansions for binary alloys from first principles*, Model. Simul. Mater. **10**, 685 (2002).

[50] K. Binder, J. L. Lebowitz, M. K. Phani and M. H. Kalos, *Monte Carlo study of the phase diagrams of binary alloys with face centered cubic lattice structure*, Acta Metall. **29**, 1655 (1981).

[51] J. Tersoff, *Empirical interatomic potential for silicon with improved elastic properties*, Phys. Rev. B **38**, 9902 (1988).

[52] J. Tersoff, *Empirical interatomic potential for carbon, with applications to amorphous carbon*, Phys. Rev. Lett. **61**, 2879 (1988).

[53] D. W. Brenner, *Relationship between the embedded-atom method and tersoff potentials*, Phys. Rev. Lett. **63**, 1022 (1989).

[54] P. Erhart, N. Juslin, O. Goy, K. Nordlund, R. Müller and K. Albe, *Analytic bond order potential for atomistic simulations of zinc oxide*, J. Phys. Cond. Mat. **18**, 6585 (2006).

[55] K. Albe, K. Nordlund, J. Nord and A. Kuronen, *Modeling of compound semiconductors: Analytical bond-order potential for Ga, As, and GaAs*, Phys. Rev. B **66**, 035205 (2002).

[56] I. J. Robertson, V. Heine and M. C. Payne, *Cohesion in aluminum systems: a first-principles assessment of "glue" schemes*, Phys. Rev. Lett. **70**, 1944 (1993).

[57] Y. Mishin, D. Farkas, M. J. Mehl and D. A. Papaconstantopoulos, *Interatomic potentials for monoatomic metals from experimental data and ab initio calculations*, Phys. Rev. B **59**, 3393 (1999).

[58] P. Erhart and K. Albe, *Pontifix/Pinguin: A program package for fitting interatomic potentials of the bond-order type*, submitted to Comp. Mater. Sci., `http://www.mm.mw.tu-darmstadt.de/`.

[59] F. Cleri and V. Rosato, *Tight-binding potentials for transition metals and alloys*, Phys. Rev. B **48**, 22 (1993).

[60] P. Ehrhart, *Landolt-Börnstein: Numerical data and Functional Relationships in Science and Technology* (Springer-Verlag, Heidelberg, 1991), No. 25.

[61] H. Hasegawa and D. G. Pettifor, *Microscopic theory of the temperature-pressure phase diagram of iron*, Phys. Rev. Lett. **50**, 130 (1983).

[62] G. Simonelli, R. Pasianot and E. J. Savino, *Embedded-atom-method interatomic potentials for bcc-iron*, Mat. Res. Soc. Symp. Proc. **291**, 567 (1993).

[63] G. J. Ackland, D. J. Bacon, A. F. Calder and T. Harry, *Computer simulation of point defect properties in dilute Fe-Cu alloy using a many-body interatomic potential*, Phil. Mag. A **75**, 713 (1997).

[64] R. Meyer and P. Entel, *Martensite-austenite transition and phonon dispersion curves of Fe1-xNix studied by molecular-dynamics simulations*, Phys. Rev. B **57**, 5140 (1998).

[65] Y. N. Osetsky and A. Serra, *Computer-simulation study of high-temperature phase stability in iron*, Phys. Rev. B **57**, 755 (1998).

[66] M. I. Mendelev, S. Han, D. J. Srolovitz, G. J. Ackland, D. Y. Sun and M. Asta, *Development of new interatomic potentials appropriate for crystalline and liquid iron*, Philos. Mag. **83**, 3977 (2003).

[67] S. L. Dudarev and P. M. Derlet, *A 'magnetic' interatomic potential for molecular dynamics simulations*, J. Phys.: Cond. Mat. **17**, 7097 (2005).

[68] H. Chamati, N. Papanicolaou, Y. Mishin and D. Papaconstantopoulos, *Embedded-atom potential for Fe and its application to self-diffusion on Fe(100)*, Surf. Sci. **600**, 1793 (2006).

[69] B. J. Lee, M. I. Baskes, H. Kim and Y. K. Cho, *Second nearest-neighbor modified embedded atom method potentials for bcc transition metals*, Phys. Rev. B **64**, 184102 (2001).

[70] G. Simonelli, R. Pasianot and E. J. Savino, *Phonon dispersion curves for transition metals within the embedded-atom and embedded-defect methods*, Phys. Rev. B **55**, 5570 (1997).

[71] Y. Mishin, M. Mehl and D. Papaconstantopoulos, *Phase stability in the Fe-Ni system: Investigation by first-principles calculations and atomistic simulations*, Acta Mater. **53**, 4029 (2005).

[72] P. E. Blöchl, *Projector augmented-wave method*, Phys. Rev. B **50**, 17953 (1994).

[73] G. Kresse and D. Joubert, *From ultrasoft pseudopotentials to the projector augmented-wave method*, Phys. Rev. B **59**, 1758 (1999).

[74] J. P. Perdew, in *Electronic structure of solids*, edited by P. Ziesche and H. Eschrig (Akademie Verlag, Berlin, 1991).

[75] F. Birch, *Finite strain isotherm and velocities for single-crystal and polycrystalline NaCl at high pressures and 300° K*, J. Geograph. Res. **83**, 1257 (1978).

[76] H. C. Herper, E. Hoffmann and P. Entel, *Ab initio full-potential study of the strutural and magnetic phase stability of iron*, Phys. Rev. B **60**, 3839 (1999).

[77] H. C. Herper, E. Hoffmann and P. Entel, *Ab inition study of iron and Cr/Fe(001)*, Phase Transitions **75**, 185 (2002).

[78] M. Acet, H. Zähres, E. F. Wassermann and W. Pepperhoff, *High-temperature moment-volume instability and anti-Invar of gamma-Fe*, Phys. Rev. B **49**, 6012 (1994).

[79] H. Purdum, P. A. Montano, G. K. Shenoy and T. Morrison, *Extended-x-ray-absorption-fine-structure study of small Fe molecules isolated in solid neon*, Phys. Rev. B **25**, 4412 (1982).

[80] A. R. Miedema and K. A. Gingerich, *On the formation enthalpy of metallic dimers*, J. Phys. B **12**, 2081 (1979).

[81] G. L. Gutsev, M. D. Mochena, P. Jena, C. W. Bauschlicher Jr. and H. Partridge III, *Periodic table of 3d-metal dimers and their ions*, J. Chem. Phys. **121**, 6785 (2004).

[82] L. Lian, C. X. Su and P. B. Armentrout, *Collision-induced dissociation of Fe+n (n=2-19) with Xe: Bond energies, geometric structures, and dissociation pathways*, J. Chem. Phys. **97**, 4072 (1992).

[83] M. Moskovits and D. P. DiLella, *Di-Iron and Nickeliron*, J. Chem. Phys. **73**, 4917 (1980).

[84] C. Kittel, *Introduction to Solid State Physics*, 6th Ed. (Wiley, New York, 1986).

[85] *Handbook of Chemistry and Physics*, 85th Ed., edited by D. R. Lide (CRC Press, Boca Raton, 2004).

[86] S. Chen and B. Sundman, *Modeling of thermodynamic properties for bcc, fcc, liquid, and amorphous iron*, J. Phase Equilibria **22**, 631 (2001).

[87] J. Zarestky and C. Stassis, *Lattice dynamics of gamma-Fe*, Phys. Rev. B **35**, 4500 (1987).

[88] D. M. Clatterbuck, D. C. Chrzan and J. W. Morris, Jr., *The ideal strength of iron in tension and shear*, Acta Mater. **51**, 2271 (2003).

[89] W. R. Tyson and W. A. Miller, *Surface free energies of solid metals: Estimation from liquid surface tension measurements*, Surf. Sci. **62**, 267 (1977).

[90] M. J. S. Spencer, A. Hung, I. K. Snook and I. Yarovsky, *Density functional theory study of the relaxation and energy of iron surfaces*, Surf. Sci. **513**, 389 (2002).

[91] J. A. Yan, C. Y. Wang and S. Y. Wang, *Generalized-stacking-fault energy and dislocation properties in bcc Fe: a first principles study*, Phys. Rev. B **70**, 174105 (2004).

[92] E. M. Lopasso, M. Caro, A. Caro and P. Turchi, *Phase diagram of an empirical potential: The case of Fe-Cu*, Phys. Rev. B **68**, 214205 (2003).

[93] A. Caro, M. Caro, E. M. Lopasso, P. E. A. Turchi and D. Farkas, *Thermodynamics of Fe-Cu alloys as described by a classic potential*, J. Nuclear Mat. **349**, 317 (2006).

[94] S. Klotz and M. Braden, *Phonon dispersion of bcc iron to 10 GPa*, Phys. Rev. Lett. **85**, 3209 (2000).

[95] C. Domain and C. S. Becquart, *Ab initio calculations of defects in Fe and dilute Fe-Cu alloys*, Phys. Rev. B **65**, 024103 (2002).

[96] C. C. Fu, F. Willaime and P. Ordejón, *Stability and mobility of mono- and di-interstitials in alpha-Fe*, Phys. Rev. Lett. **92**, 175503 (2004).

[97] F. Maury, M. Biget, P. Vajda, A. Lucasson and P. Lucasson, *Anisotropy of defect creation in electron-irradiated iron crystals*, Phys. Rev. B **14**, 5303 (1976).

[98] J. N. Lomer and M. Pepper, *Anisotropy of defect production in electron irradiated iron*, Phil. Mag. **16**, 1119 (1967).

[99] K. Nordlund, J. Wallenius and L. Malerba, *Molecular dynamics simulations of threshold displacement energies in Fe*, Nucl. Instr. Meth. Phys. Res. B **246**, 322 (2006).

[100] C. S. Becquart, C. Domain, A. Legris and J. C. van Duysen, *Influence of interatomic potentials on molecular dynamics simulations of displacement cascades*, J. Nucl. Mater. **280**, 73 (2000).

[101] C. S. Becquart, C. Domain, A. Legris and J. C. van Duysen, *Influence of Interatomic Potentials in MD Investigation of Ordering in alpha-SiC 4*, Mat. Res. Soc. Symp. Proc. **650**, R3.24.1 (2001).

[102] K. Nordlund, private communication.

[103] S. M. Kim and W. J. L. Buyers, *Vacancy formation energy in iron by positron annihilation*, J. Phys. F: Metal Phys. **8**, L103 (1978).

[104] D. Nguyen-Manh, A. P. Horsfield and S. L. Dudarev, *Self-interstitial atom defect in bcc transition metal: Group specific trends*, Phys. Rev. B **73**, 020101(R) (2006).

[105] F. Willaime, C. Fu, M. Marinica and J. Dalla Torre, *Stability and mobility of self-interstitials and small interstitial clusters in alpha-iron: ab initio and empirical potential calculations*, Nucl. Instr. Meth. Phys. Res. B **228**, 92 (2005).

[106] N. Bernstein and E. B. Tadmor, *Tight-binding calculations of stacking energies and twinnability in fcc metals*, Phys. Rev. B **69**, 4116 (2004).

[107] R. E. Macfarlane, J. A. Rayne and C. K. Jones, *Anomalous temperature dependence of shear modulus c44 for platinum*, Physics Letters **18**, 91 (1965).

[108] P. Alinaghian, S. R. Nishitani and D. G. Pettifor, *Shear constants using angularly dependent bond order potentials*, Phil. Mag. B **69**, 889 (1994).

[109] D. M. Ceperley and B. J. Alder, *Ground-state of the electron-gas by a stochastic method*, Phys. Rev. Lett. **45**, 566 (1980).

[110] J. P. Perdew and A. Zunger, *Self-interaction to density-functional approximations for many-electron systems*, Phys. Rev. B **23**, 5048 (1981).

[111] M. B. Airola and M. D. Morse, *Rotationally resolved spectroscopy of Pt2*, J. Chem. Phys. **116**, 1313 (2002).

[112] J. Anton, T. Jacob, B. Fricke and E. Engel, *Relativistic Density Functional calculations for Pt2*, Phys. Rev. Lett. **89**, 3001 (2002).

[113] *Metal Reference Book*, edited by C. Smith (Butterworths, London, 1976).

[114] P. Ehrhart, K. H. Robrock and H. R. Schober, in *Physics of Radiation Effects in Crystals*, edited by R. A. Johnson and A. N. Orlov (Elsevier, Amsterdam, 1986), S. 3.

[115] P. van Beurden and G. J. Kramer, *Parametrization of modified embedded-atom-method potentials for Rh, Pd, Ir, and Pt based on density functional theory calculations, with applications to surface properties*, Phys. Rev. B **63**, 165106 (2001).

[116] S. M. Foiles, M. I. Baskes and M. S. Daw, *Embedded-atom-method functions for the fcc metals Cu, Ag, Au, Ni, Pd, Pt and their alloys*, Phys. Rev. B **33**, 7983 (1986).

[117] V. Vítek, *Theory of the core structures of dislocations in body-centered-cubic metals*, Cryst. Latt. Defects **5**, 1 (1974).

[118] H. Cox, *Potential energy functions for platinum and palladium solids and their application to surfaces*, Surf. Sci. **397**, 374 (1998).

[119] D. C. Wallace, *Thermodynamics of Crystals* (Dover, Mineola, NY, 1998).

[120] Y. Chen, S. Iwata and T. Mohri, *First-principles calculation of L10-disorder phase diagram in Fe-Pt system within the first and second nearest neighbor pair interaction energies*, Calphad **26**, 583 (2002).

[121] P. Fredriksson and B. Sundman, *A thermodynamic assessment of the Fe-Pt system*, Calphad **25**, 535 (2001).

[122] J. Kim, Y. Koo and B. J. Lee, *Modified embedded-atom method interatomic potential for the Fe-Pt alloy system*, J. Mater. Res. **21**, 199 (2006).

[123] O. Beckstein, J. E. Klepeis, G. L. W. Hart and O. Pankratov, *First-principles elastic constants and electronic structure of alpha-Pt2Si and PtSi*, Phys. Rev. B **63**, 134112 (2001).

[124] S. H. Wei, L. G. Ferreira, J. E. Bernard and A. Zunger, *Electronic properties of random alloys: Special quasirandom structures*, Phys. Rev. B **42**, 9622 (1990).

[125] A. V. Ruban, S. I. Simak, S. Shallcross and H. L. Skriver, *Local lattice relaxations in random metallic alloys: Effective tetrahedron model and supercell approach*, Phys. Rev. B **67**, 4302 (2003).

[126] B. Kraczek and D. D. Johnson, (private communication).

[127] J. S. Kim, Y. M. Koo, B. J. Lee and S. R. Lee, *The origin of (001) texture evolution in FePt thin films on amorphous substrates*, J. Appl. Phys. **99**, 053906 (2006).

[128] S. H. Whang, Q. Feng and Y. Q. Gao, *Ordering, deformation and microstructure in L10 type FePt*, Acta mater. **46**, 6485 (1998).

[129] A. Kußmann and G. von Rittberg, *Untersuchung über die Umwandlungen im System Platin-Eisen*, Z. Metallk. **41**, 470 (1950).

[130] M. Toney, W. Lee, J. Hedstrom and A. Kellock, *Thickness and growth temperature dependence of structure and magnetism in FePt thin films*, J. Appl. Phys. **93**, 9902 (2003).

[131] O. G. Mouritsen, *Computer studies of phase transitions and critical phenomena* (Springer-Verlag, Berlin, 1984).

[132] S. Hong and M. H. Yoo, *Surface energy anisotropy of FePt nanoparticles*, J. Appl. Phys. **97**, 084315 (2005).

[133] F. C. Nix and W. Shockley, *Order-disorder transformations in alloys*, Rev. Mod. Phys. **10**, 1 (1938).

[134] M. K. Phani, J. L. Lebowitz, M. H. Kalos and C. C. Tsai, *Monte Carlo study of an ordering alloy on an fcc lattice*, Phys. Rev. Lett. **42**, 577 (1979).

[135] G. Gompper and D. M. Kroll, *Wetting in fcc Ising antiferromagnets and binary alloys. II. A Monte Carlo and renormalization-group study*, Phys. Rev. B **38**, 459 (1988).

[136] C. Frontera, E. Vivies, T. Castán and A. Planes, *Monte Carlo study of the growth of L12-ordered domains in fcc A3B binary alloys*, Phys. Rev. B **55**, 212 (1997).

[137] M. Kessler, W. Dieterich and A. Majhofer, *Monte Carlo simulation of subsurface ordering kinetics in an fcc alloy model*, Phys. Rev. B **64**, 125412 (2001).

[138] K. Binder, D. Landau and M. Müller, *Monte Carlo studies of wetting, interface localization and capillary condensation*, J. stat. phys. **110**, 1411 (2003).

[139] B. Yang, M. Asta, O. N. Mryasov, T. J. Klemmer and R. W. Chantrell, *Equilibrium Monte Carlo simulations of A1-L10 ordering in FePt nanoparticles*, Script. Mat. **53**, 417 (2005).

[140] R. V. Chepulskii and W. H. Butler, *Temperature and particle size dependence of the equilibrium order parameter of FePt alloys*, Phys. Rev. B **72**, 134205 (2005).

[141] B. Yang, M. Asta, O. N. Mryasov, T. J. Klemmer and R. W. Chantrell, *The nature of A1-L10 ordering transitions in alloy nanoparticles: A Monte Carlo study*, Acta Mater. **54**, 4201 (2006).

[142] K. Binder, *Ordering of the face-centered-cubic lattice with nearest-neighbor interaction*, Phys. Rev. Lett. **45**, 811 (1980).

[143] D. F. Styer, M. K. Phani and J. L. Lebowitz, *Multiatom interactions in the fcc Ising binary alloy: Low-temperature behavior and Monte Carlo simulations*, Phys. Rev. B **34**, 3361 (1986).

[144] M. K. Phani, J. L. Lebowitz and M. H. Kalos, *Monte Carlo studies of an fcc Ising antiferromagnet with nearest- and next-nearest-neighbor interactions*, Phys. Rev. B **21**, 4027 (1980).

[145] P. Beccat, Y. Gauthier, R. Baudoing-Savois and J. C. Bertolini, *Monotonous concentration profile and reconstruction at Pt80Fe20(111): LEED study of a catalyst*, Surf. Sci. **238**, 105 (1990).

[146] C. Creemers and P. Deurinck, *Platinum segregation on the (111) surface of ordered Pt80Fe20: LEIS results and model simulations*, Surf. Inter. Anal. **25**, 177 (1997).

[147] R. Defay, I. Prigogine and A. Bellemans, *Surface tension and adsorption* (Longmans, London, 1966).

[148] A. L. Mackay, *A dense non-crystllographic packing of equal spheres*, Acta Cryst. **15**, 916 (1962).

[149] A. Howie and L. D. Marks, *Elastic strains and the energy balance for multiply twinned particles*, Phil. Mag. **49**, 95 (1984).

[150] N. A. Schclar, *Anisotropic Analysis using Boundary Elements* (Computational Mechanics Publications, vol. 20, Topics in Engineering, Southampton UK and Boston USA, 1994).

[151] M. Müller and K. Albe, *Lattice Monte Carlo simulations of FePt nanoparticles: Influence fo size, composition, and surface segregation on order-disorder phenomena*, Phys. Rev. B **72**, 094203 (2005).

[152] J. P. K. Doye and F. Calvo, *Entropic effects on the structure of Lennard-Jones clusters*, J. Chem. Phys. **116**, 8307 (2002).

[153] G. H. Vineyard, *Theroy of order-disorder kinetics*, Phys. Rev. **102**, 981 (1956).

[154] J. Philibert, *Atom movements - Diffusion and mass transport in solids* (Les Éditions de Physique, Les Ulis, 1991).

[155] N. T. Gladkikh and O. P. Kryshtal, *On the size dependence of the vacancy formation energy*, Functional Materials **6**, 823 (1999).

[156] W. H. Qi and M. P. Wang, *Vacancy formation energy of small particles*, J. Mat. Sci. **39**, 2529 (2004).

[157] D. Xie, M. P. Wang and L. F. Cao, *Comment on "Vacancy formation energy of small particles"*, J. Mat. Sci. **40**, 3565 (2005).

[158] W. H. Qi, M. P. Wang, M. Zhou and W. Y. Hu, *Surface-area-difference model for thermodynamic properties of metallic nanocrystals*, J. Phys. D: Appl. Phys. **38**, 1429 (2005).

[159] D. Reinhard, B. D. Hall, P. Berthoud, S. Valkealahti and R. Monot, *Size-dependent icosahedral-to-fcc structure change confirmed in unsupported nanometer-sized copper clusters*, Phys. Rev. Lett. **79**, 1459 (1997).

[160] J. W. Cahn, *Surface stress and the chemical equilibrium of small crystals - I. the case of the isotropic surface*, Acta Metall. **28**, 1333 (1980).

[161] R. C. Cammarata, *Surface and interface stress effects in thin films*, Prog. Surf. Sci. **46**, 1 (1994).

[162] J. Weissmüller, *Comment on "Lattice contraction and surface stress of fcc nanocrystals"*, J. Phys. Chem. B **106**, 889 (2002).

[163] R. Kozubski, *Thermal vacancies in B2 and L12 ordering alloys*, Acta metall. mater. **41**, 2565 (1993).

[164] P. Gumbsch and M. S. Daw, *Interface stresses and their effects on the elastic moduli of metallic multilayers*, Phys. Rev. B **44**, 3934 (1991).

[165] R. A. Ristau, K. Barmak, L. H. Lewis, K. R. Coffey and J. K. Howard, *On the relationship of high coercivity and L10 ordered phase in CoPt and FePt thin films*, J. Appl. Phys. **86**, 4527 (1999).

[166] D. Frenkel and A. J. C. Ladd, *New Monte Carlo method to compute the free energy of arbitrary solids. Application to the fcc and hcp phases of hard spheres*, J. Chem. Phys. **81**, 3188 (1984).

[167] J. M. Polson, E. Trizac, S. Pronk and D. Frenkel, *Finite-size corrections to the free energies of crystalline solids*, J. Chem. Phys **112**, 5339 (2000).